Capacitive Power Transfer Field Excitation with an Integrated Resolver for Synchronous Machines

by

Marisa J.T. Liben

A dissertation submitted in partial fulfillment of
the requirements for the degree of

Doctor of Philosophy

(Electrical and Computer Engineering)

at the

UNIVERSITY OF WISCONSIN–MADISON

2023

Date of final oral examination: 3 May 2023

The dissertation is approved by the following members of the Final Oral Committee:

Daniel C. Ludois, Associate Professor, Electrical and Computer Engineering
Bulent Sarlioglu, Professor, Electrical and Computer Engineering
Eric L. Severson, Assistant Professor, Electrical and Computer Engineering
Joseph Andrews, Assistant Professor, Mechanical Engineering

ABSTRACT

Permanent magnet synchronous machines currently dominate traction motor applications such as electric vehicles. However, wound field synchronous machines offer a comparable alternative in terms of performance and efficiency without the unpredictable prices and high carbon emissions of mining and manufacturing permanent magnets. These machines are ubiquitous at megawatt levels, especially in power plants, but require high-performance, low-cost excitation systems in order to be attractive as traction motors. This work continues research into capacitive power transfer (CPT) as a suitable wireless excitation method for wound field synchronous machines. Here, a capacitive power transfer system is scaled beyond previous work to achieve a $> 3X$ increase in power transfer over previous work by increasing the frequency to $\geqslant 6.78\text{MHz}$. A peak output power of 2.3kW at a DCDC efficiency of 88.5% is reached in this system.

The system features a minimal part count series tank resonant topology with the inverter redesigned for megahertz level operation with special consideration for stray inductance verified in Ansys Q3D FEA. Likewise, the coupler structure's rectifier is updated to reduce the total parts count by half and handle kilowatt output power with a current-stiff rectifier. The current stiff rectifier features a large DC filter inductor on the output to maintain continuous conduction operation of the diodes. Using SiC Schottky diodes the rectifier has superior performance over conventional voltage-stiff rectifiers to achieve the 2.3kW output power to the load.

Additionally, a capacitive resolver is developed to be integrated around the rotating rectifier of any wireless exciter and also around the CPT coupler boards. This solution reduces the machine cost for traction applications by removing the cost of an external rotor position sensor. The capacitive resolver is made to be a drop-in replacement for conventional magnetic resolvers and compatible with their existing demodulation strategies. The general integrated resolver and rectifier is tested with a digital demodulation kit, AD2S1210 from Analog Devices, and achieves a maximum angle error of 0.3°. The carrier excitation frequency is 20kHz as is standard for magnetic resolvers. For the CPT-integrated resolver and rectifier, the excitation frequency is $\geqslant 6.78\text{MHz}$ and demodulation with an analog multiplier is used instead. A maximum rotor angle error of 10° is achieved. Overall, the integrated capacitive resolver and rectifier provides an additional pathway to reduce the wound field synchronous machine system cost for adoption in traction applications.

ACKNOWLEDGMENTS

Professor Daniel C. Ludois has been a truly exceptional advisor with an endless stream of new and creative ideas. I am grateful for his guidance to develop my confidence and intuition as an engineer and researcher from first principles and back of the envelope calculations.

I would like to thank the Wisconsin Electric Machines and Power Electronics Consortium (WEMPEC) and the Department of Energy for their support of my research.

Recognition and thanks also go to the defense committee members, Prof. Bulent Sarlioglu, Prof. Eric Severson, and Prof. Joseph Andrews who provided valuable feedback and insight for my work. I would also like to thank all of the WEMPEC faculty and staff and the student community for a welcoming work environment especially Kathy Young, Kyle Hanson, and Pia Strampp. Additionally, the members of the Ludois group have provided camaraderie, testing assistance, and welcome distractions during set backs in the lab. I am thankful that so many work acquaintances have become life-long friendships.

I would like to thank all of my friends and family who have supported me throughout these last years. My parents, Lynn and Greg Tisler, have been a constant support in my life and have always encouraged me to pursue my non-technical and academic interests. In particular, I want to acknowledge my friend Claire Griesbach. From grade school through to finishing our PhDs together, it has been a joy and great pleasure being friends and academic partners these last twenty or so years.

Finally, and most importantly, I would like to thank my husband Max who has been my grounding rock throughout graduate school. From working on homework together to commiserating with my failures and celebrating my successes in the lab, I am blessed to have found a life partner that understands and shares my passion for power engineering.

CONTENTS

LIST OF TABLES

LIST OF FIGURES

Symbols

f_{res}	Resonant frequency of LC coupler [Hz]
f_{sw}	Switching frequency of the inverter [Hz]
L	Inductor Inductance [H]
C	Capacitor capacitance [F]
R_{field}	Equivalent series resistance of field winding, also called R_{load} [Ω]
L_{field}	Equivalent series inductance of field winding [H]
P_{out}	DC Output Power [W]
$V_{DC,in}$	Input bus voltage to the inverter [V]
$I_{DC,in}$	Input current to the inverter [A0]
$V_{DC,out}$	DC output voltage to the field windings [V]
$I_{DC,out}$	DC output current to the field windings [A]
η	DCDC system efficiency [%]
i_{tank}	LC tank current [A]
$v_{inverter}$	Output voltage of the inverter [V]
$v_{rectifier}$	Input voltage to the rectifier [V]
α	Dead time angle [rad]
β	Inverter power factor angle [rad]
t_d	dead time [s]
v_{gs}	Inverter gate-to-source voltage [V]
C_{DC}	DC filter capacitor [F]
C_j	Equivalent diode capacitance [F]
R_e	Equivalent resistance of the rotor field reflected across the rectifier [Ω]
C_e	Equivalent rectifier capacitance [F]
L_e	Input inductance to the rectifier [H]
γ	Phase between the inverter and rectifier voltages [rad]

φ	Rectifier power factor angle [rad]
v_f	Diode forward voltage drop [V]
μ_o	Permeability of free space $4\pi * 10^{-7}$ [H/m]
C_{iss}	Input switch capacitance $C_{gd} + C_{gs}$ [F]
Q_g	Switch gate charge [C]
C_p	Parasitic capacitance [F]
L_p	Parasitic inductance [H]
ω_{ex}	Resolver input excitation frequency, carrier frequency [Hz]
ω_r	Shaft rotor speed $[\frac{rad}{s}]$
$v_{carrier}$	Resolver input voltage, also called v_{ex} [V]
v_{mod}	Resolver output modulated voltage, not filtered [V]
v_{dm}	Resolver output demodulated voltage waveform, carrier removed [V]
θ	Rotor shaft angle calculated from the resolver [rad] or [°]

Abbreviations

CPC	Capacitive Power Coupler
CPT	Capacitive Power Transfer
EMI	Electromagnetic Interference
ESR	Equivalent Series Resistance
FEA	Finite Element Analysis
GaN	Gallium Nitride
IPT	Inductive Power Transfer
ISM	Industrial, Scientific, and Medical
LPF	Low Pass Filter
PCB	Printed Circuit Board
SiC	Silicon Carbide
WFSM	Wound Field Synchronous Machine
ZVS	Zero Voltage Switching
ZCS	Zero Current Switching

Chapter One

Introduction and State of the Art

1.1 The Importance of Wound Field Synchronous Machines

The electrification of vehicles and aircraft heavily rely upon permanent magnet synchronous machines (PMSMs) with performance and efficiency far exceeding asynchronous induction machines. However, the rapid increase of PM machines in everything from electric vehicles and wind turbines to the vibrators in cell phones has become an area of political [9–11], economic [12, 13], environmental [14–16], and ethical [17–19] concern. Common permanent magnets that contain rare earth metals are samarium-cobalt (SmCo) and neodymium-iron-boron (NdFeB), of which the latter often also contains dysprosium. The mining and extraction of these materials can be toxic not only to those working in the mines but can also leech into the ground water supply, affecting much larger populations. In cobalt and copper mines like those in the Democratic Republic of the Congo, child labor, unfair compensation, hazardous working conditions, and lack of proper protective equipment have been and continue to be an issue despite the work of such groups as the Fair Cobalt Alliance. Studies have shown increased risk of birth defects from fathers exposed to mining-related pollution where there is little government regulation and accountability [17].

Rare earth metal mining is dominated by a few countries that control much of the world's supply. As the demand for electric vehicles (EVs) skyrockets, so too does the demand for these magnets which has caused unpredictable and fluctuating prices to the point that EV companies are moving to reduce total magnet volume in their motors by combining aspects of synchronous reluctance machines. The global supply of EVs could increase upwards of 36% [11] within the

next decade, and with it a surge in the required supply of PMs. Thus, it is imperative to transition towards machine topologies that offer high performance, high efficiency, and that do not rely on these cost prohibitive materials. The wound field synchronous machine (WFSM) provides a good and comparable alternative to the PMSM in terms of performance and efficiency.

Wound field synchronous machines (WFSMs) have been around for over one hundred thirty years and are today still the preferred machine in many applications such as industrial power plant generators, grid-connected applications, commercial flight, and MW-level propulsion systems [1]. Instead of using a permanent magnet to produce rotor flux, WFSMs have rotor windings that are separately excited with direct current to create rotating electromagnets. Figure 1.1 shows the long history of the WFSM rotor excitation topology development starting from mechanical brushed methods to wireless excitation methods.

Lately, WFSMs are being researched for their use in electric vehicles as a replacement for PMSMs. While these wound field machines can compete with the performance and efficiency of permanent magnet machines, in EVs their adoption relies on an economical and robust field excitation structure. More broadly, all parts of the EV powertrain must be cost optimized, especially the electric machine and its position sensor (whether it be a magnetic resolver, optical encoder, or any of the many other sensor topologies).

For many decades WFSMs dominated in areas where PMSM technology fell short; however, in the EV market where PMs are ideally suited, the challenge now lies in the design of the field excitation structure. It is necessary to develop a cost-effective wireless excitation method to transfer kilowatts of power to the rotor field winding to produce the torque necessary for traction applications. In the following review of the state of the art, a small selection of WFSM rotor excitation methods is discussed that would be most relevant for adoption in traction applications.

1.2 Types of WFSM Rotor Excitation

A conventional permanent magnet machine relies on magnets to create a permanent rotating rotor flux; however, in a wound field synchronous machine, the rotor consists of windings to form externally excited electromagnets. There are many methods used for the external excitation, but they all have the goal of applying a controllable direct current to the rotor field windings. The

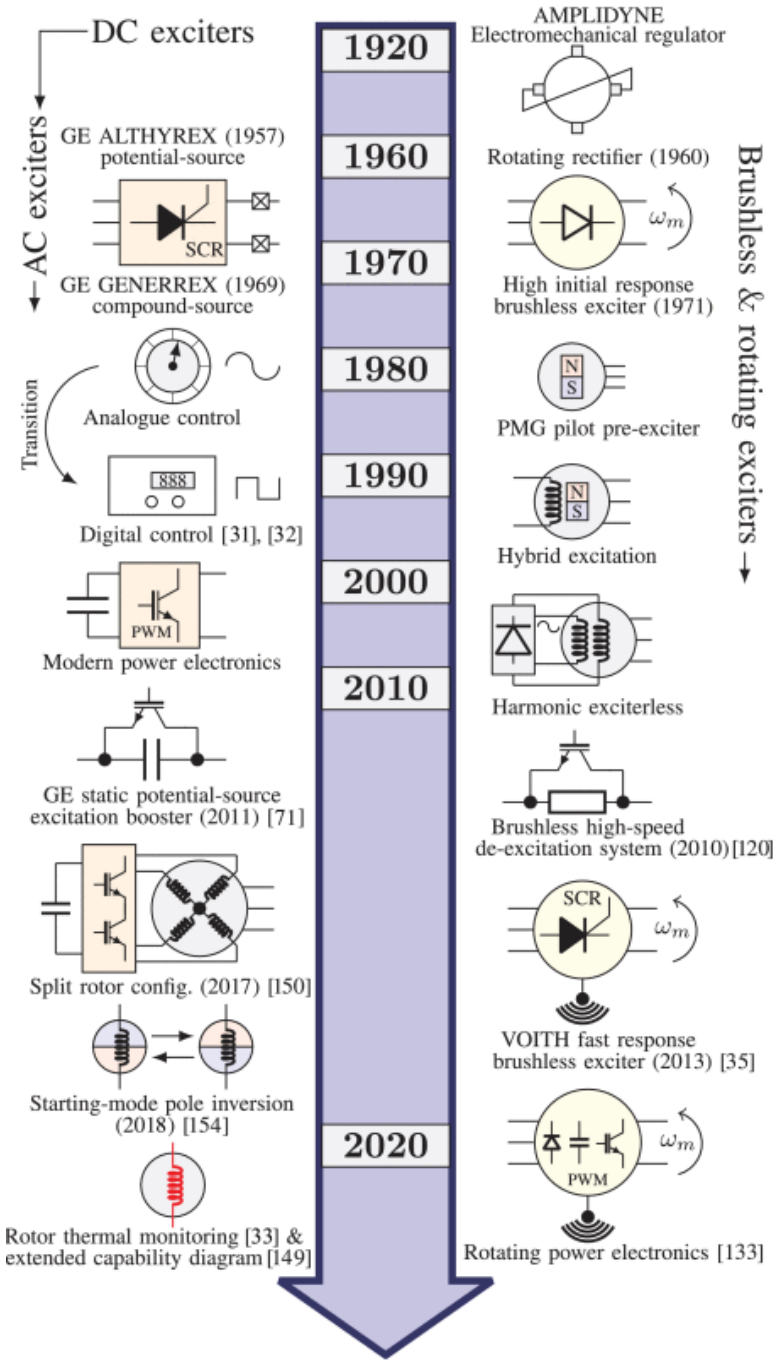

Figure 1.1: History of WFSM excitation systems [1]

topology allows for the machine itself to be controlled by adjusting a direct current on the rotor windings instead of a full power electronics drive on the stator. Thus, even before the age of modern semiconductors, a mega-watt WFSM could be controlled without the need of a mega-watt inverter or sophisticated drive system, which in the present day remains an attractive topology to save on

cost and complexity.

In general, WFSM exciters can be discussed in three main categories: external brushed systems, external brushless systems, and embedded, integrated systems. Slip rings are discussed for external brushed systems, harmonic injection is discussed for embedded systems, and brushless exciters, transformers, inductive power transfer (IPT), and CPT are discussed for external brushless systems. The comparison of dynamic performance and fault tolerance of these WFSM excitation systems are not discussed here and are out of the scope of this document but have been extensively discussed in the literature [1, 20]. Likewise, the WFSM outside of its excitation system will not be discussed, but research continues on the machine itself [21–26].

1.2.1 Slip Rings

For as long as DC and wound field machines have been around, so too have brushes and slip rings for transmitting DC and AC power. Brushes and slip rings refer to the large class of mechanical contact exciters for machines that are ubiquitous for being a cheap and straightforward excitation method. Figure 1.2 shows an example of brushes on rotating slip rings. Over time the brushes wear, resulting in the possibility of faults and maintenance issues that has been extensively researched in the literature [27–31].

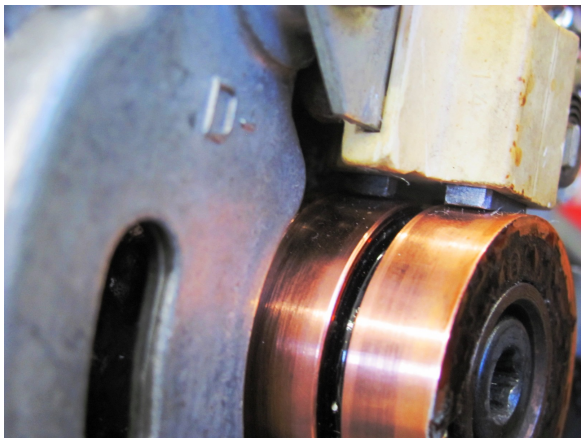

Figure 1.2: Picture of brushes on rotating slip rings [2]

Typically, slip rings are made from materials such as copper, brass, bronze, or steel while the brushes are commonly made of carbon in the form of graphite. The wear on brushes comes not only from mechanical friction, but also on electrical, thermal, and chemical factors. Current transmitted

through the contacts erodes material over time, and high motor temperatures further accelerate wear rates. Likewise, contamination and moisture inevitably produce metal oxide films that lead to uneven current distribution and brush wear. While brushes and slip rings are a cost-effective solution, in traction applications they would require regular maintenance and replacement for the consumer.

1.2.2 Brushless Exciter

Brushless exciters encompass a large range of topologies that refer to excitation systems that do not require mechanical contact to the rotating field windings, or in other words, provide wireless excitation through an airgap. In this document, a few different brushless exciter systems are highlighted specifically for traction applications, but it should be noted that these represent a small portion of schemes available for the wide array of WFSM use cases.

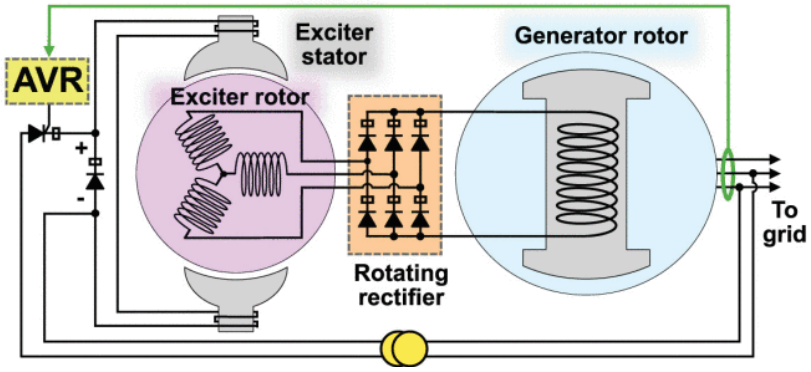

Figure 1.3: Diagram of a common brushless exciter system [1]

The common topology for a brushless exciter is shown in Figure 1.3 with a rotating exciter connected directly to the WFSM rotor shaft. In this figure, the WFSM is acting as a generator. The exciter is similar to a DC machine where direct current is supplied to the stator winding to excite a rotating three phase winding across the air gap. Through a rotating rectifier, the exciter rotor's three-phase AC becomes DC applied to the WFSM rotor winding. There are many variations on this topology such as replacing the excitatory stator windings with permanent magnets for improved transient and fault handling [32, 33]. In this case, the exciter essentially functions as a permanent magnet generator. Furthermore, the exciter can also take the form of an asynchronous induction generator [34]. Overall, the external exciter provides three-phase current to the WFSM rotor with a

rotating rectifier required to convert to DC power. In large power plant applications, mega-watt rated exciters can be found controlling giga-watt level WFSM generators. In these cases, instead of passive diodes, a thyristor bridge is typically employed to handle the appropriate rotor current [35, 36].

The brushless exciter is a versatile topology, but in all cases needs a rotating rectifier of some sort. Additionally, the topologies presented above all require the WFSM to have a smaller machine, acting as a generator, attached to the shaft to power the rotor windings. This excitation power is derived from the shaft power and requires some prime mover to spin the shaft on startup as well. In many applications, this additional space and cost requirement is trivial, but in traction applications both present pertinent issues. The cost of the additional excitation generator must be comparable to the cost of permanent magnets and must justify the extra needed space. So far, brushless exciters have found their place in large mega-watt to giga-watt applications, but a different topology may be better suited for traction vehicle applications.

1.2.3 Harmonic Injection

As with brushless exciters and slip rings, many forms of WFSM rotor excitation focus on adding an external unit to the rotor windings; however, another technique involves integrating the exciter into the motor windings [37]. Here the term harmonic injection is used to refer to a class of integrated excitation systems, whether brushed or brushless. Recently, there has been a good amount of research regarding the use of the stator winding itself to induce an excitation current on dedicated excitation windings in the rotor. There are two main approaches: third harmonic injection [38–42] and subharmonic injection [43, 44] on the fundamental torque-producing frequency. The stator winding drive is designed such that it produces not only a fundamental torque-producing frequency that couples to the main rotor field winding, but also produces an additional "injected" frequency that couples with a second rotor excitation or "harmonic" winding.

In a balanced three-phase system with a Y-connected neutral point there is no zero-sequence component and thus the triplen harmonics of the fundamental frequency cancel out. With the ability to control the neutral point, any desired fixed and pulsating frequency can be injected into the stator winding. Figure 1.4 shows the two topologies proposed for controlling injected frequencies onto the stator [34]. In either case, the harmonic winding is connected to the field winding via a

full-bridge rectifier. In Figure 1.4a, the stator winding is open with a full three-phase inverter at both ends to fully control the stator current while simultaneously injecting arbitrary amplitudes of the desired excitation harmonics, but this requires twice the number of semiconductor switches and controls as a typical motor drive. Figure 1.4b shows a modified version with a reduced amount of power electronics components and controls to solely manipulate the neutral point.

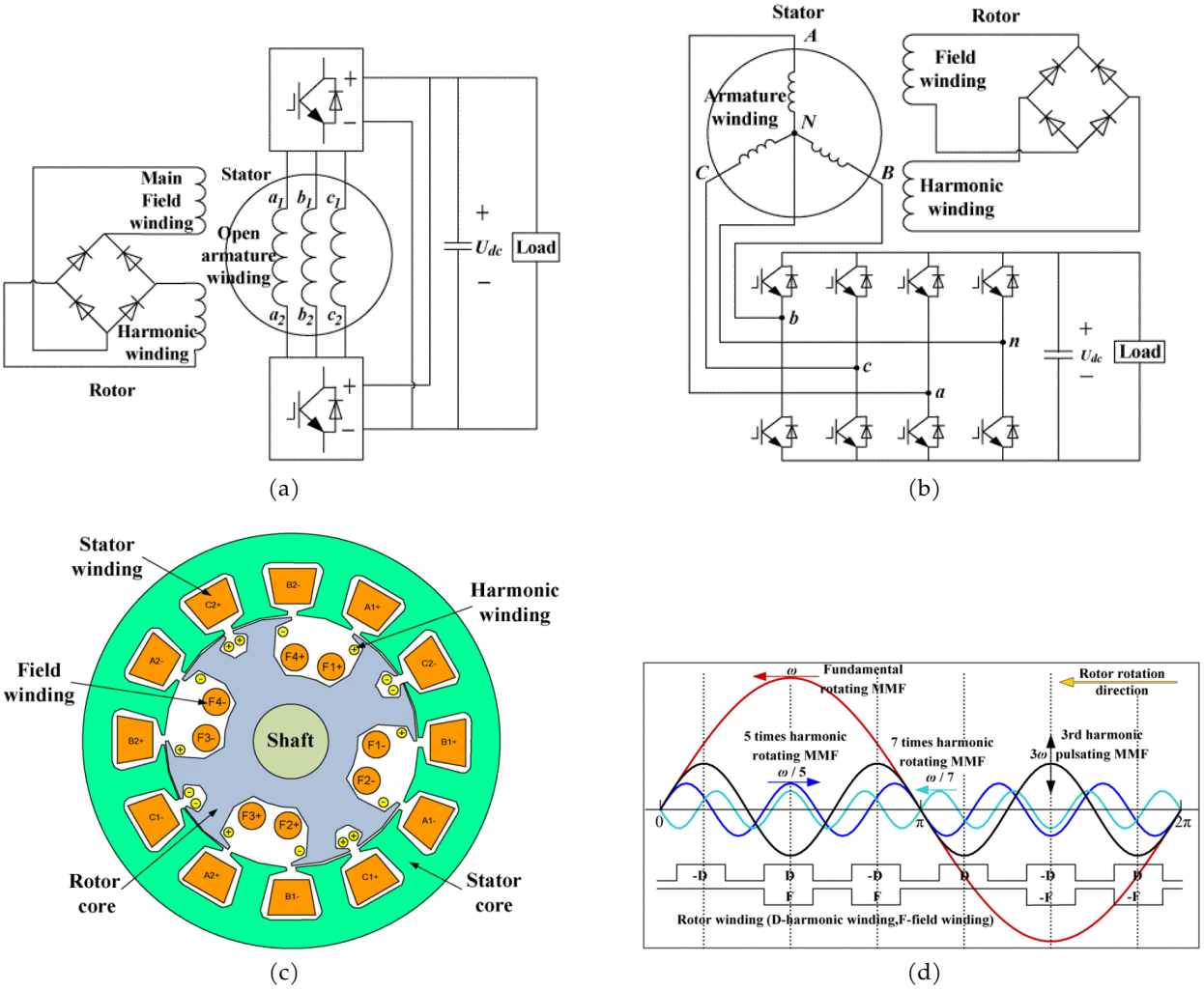

Figure 1.4: Diagram of proposed third-harmonic injection motor topology with (a) an open stator winding and (b) a modified semi-open stator winding. The (c) stator and rotor winding configuration and (d) equivalent winding functions are shown, as well.

From here, a zero-sequence third harmonic of the electrical frequency is injected and coupled with the third spatial harmonic of the rotor's harmonic, or excitation, winding. The third harmonic is chosen because it is the lowest harmonic present above the fundamental, and as such has the

least iron losses and the highest amplitude of the possible harmonics. Figure 1.4c-Figure 1.4d show the stator and rotor winding topology as well as the development of the spatial harmonics coupling with the rotor windings. The main four pole field winding (labeled "F") is shown in orange as well as the yellow excitation winding (labeled "D"), which is laid out such that it has a twelve-pole winding function harmonic. The current induced in the harmonic winding is connected back to the field winding via a rotating rectifier. Unfortunately, this design necessarily induces a higher order harmonic which will increase iron losses that are proportional to frequency.

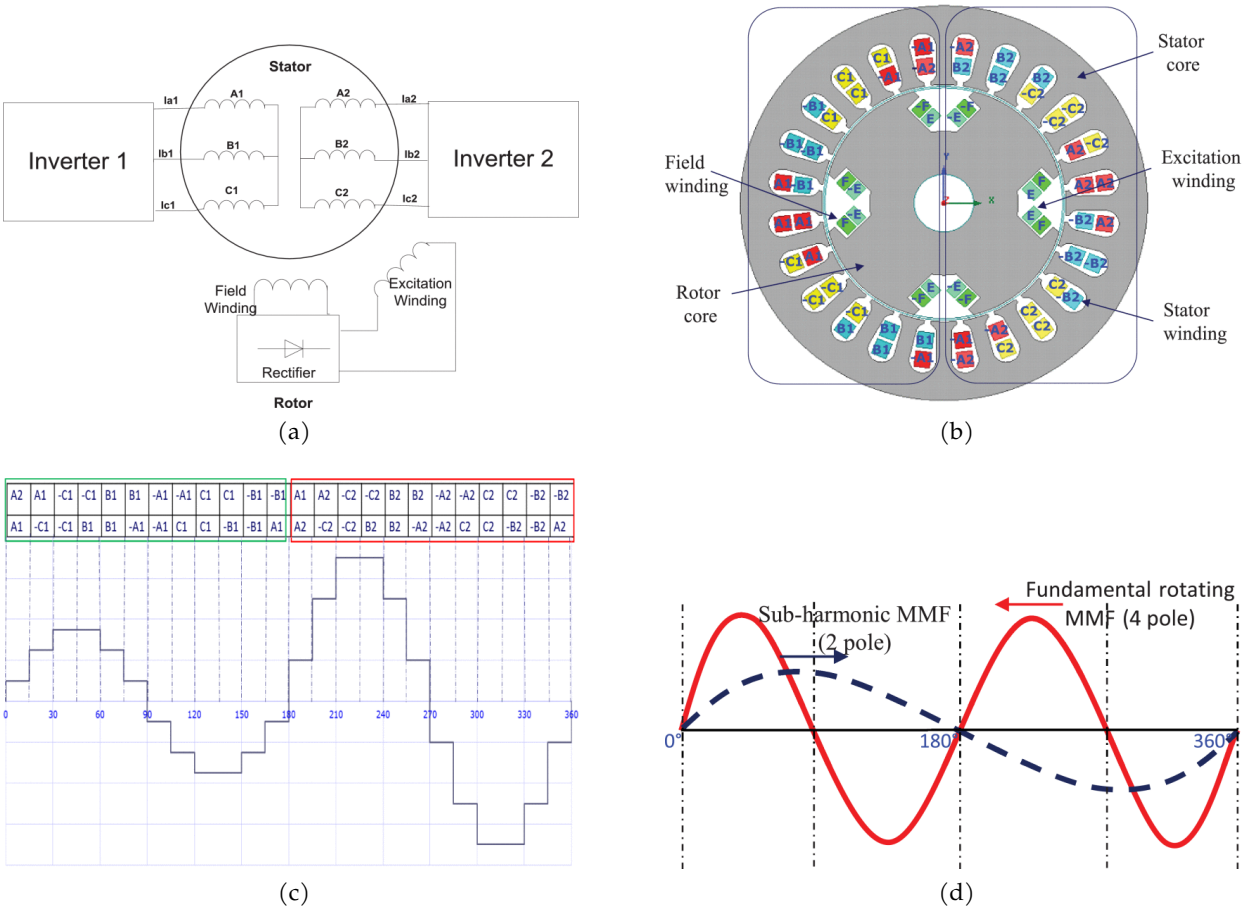

Figure 1.5: Diagram of proposed subharmonic injection motor topology with (a) dual inverter layout, (b) stator and rotor winding configuration along with the (c) winding function and (d) equivalent results winding function harmonics.

Figure 1.5 shows the second approach to harmonic injection, which is similar but reduces the complexity of the controls for the stator coil. In this case the two inverters drive the same frequency and phase, but simply have different magnitudes. The two inverters are connected to two

separate windings – each drives half of the stator as in Figure 1.5a. With a correct offset, there is the torque fundamental frequency and then also a spatial subharmonic frequency induced. For this motor the optimal determined topology is a four pole twenty-four slot machine with the winding configuration in Figure 1.5b. The four-pole spatial harmonic in the rotor is the torque-producing harmonic given by the field winding. Both inverters are still operating at the electrical frequency of the four-pole winding; however, there is a second winding on the rotor as well that is a two-pole excitation winding. This 2-pole winding is excited as the spatial subharmonic with the mismatching stator winding currents. Figure 1.5c-Figure 1.5d show the generated winding function and the resulting four-pole fundamental and a two-pole subharmonic. The excitation winding in this case will inevitably lead to asymmetric saturation in the rotor with the four-pole versus two-pole configuration. As with the third-harmonic injection, the excitation winding is likewise connected to the field winding via a full-bridge rotating rectifier.

In both approaches there are two separate windings in the rotor. Unfortunately, this means that the excitation winding is taking up space, or in other words, reducing the fill factor of the rotor field winding and subsequently the amount of torque (via the amount of flux) it can produce. While these excitation schemes are integrated into the machine, they necessarily require a specially designed synchronous machine and cannot simply be used as a drop-in replacement for slip rings or a brushless exciter. The limitation in machine design and requirement for an entirely new design are serious drawbacks of harmonic injection and create friction for industry adoption.

1.2.4 Transformers and Inductive Power Transfer (IPT)

Rotary transformers and inductive power transfer (IPT) excitation systems transfer power wirelessly via magnetic fields. Figure 1.6 shows a general diagram of an inductive-based excitation system featuring a rotating rectifier and field winding represented by L_f and R_f. An AC power source or an inverter is necessary for the system. These systems have been around for many decades and represent a common drop-in replacement system for brushes and slip rings in terms in terms of power scalability and cost [45].

In general, rotary transformers are grouped by having a characteristically high mutual inductance and strong coupling, with transformer designs containing ferrite or steel cores and high flux concentrations [26], [46–54]. These systems can operate down to the 50Hz range but are typically

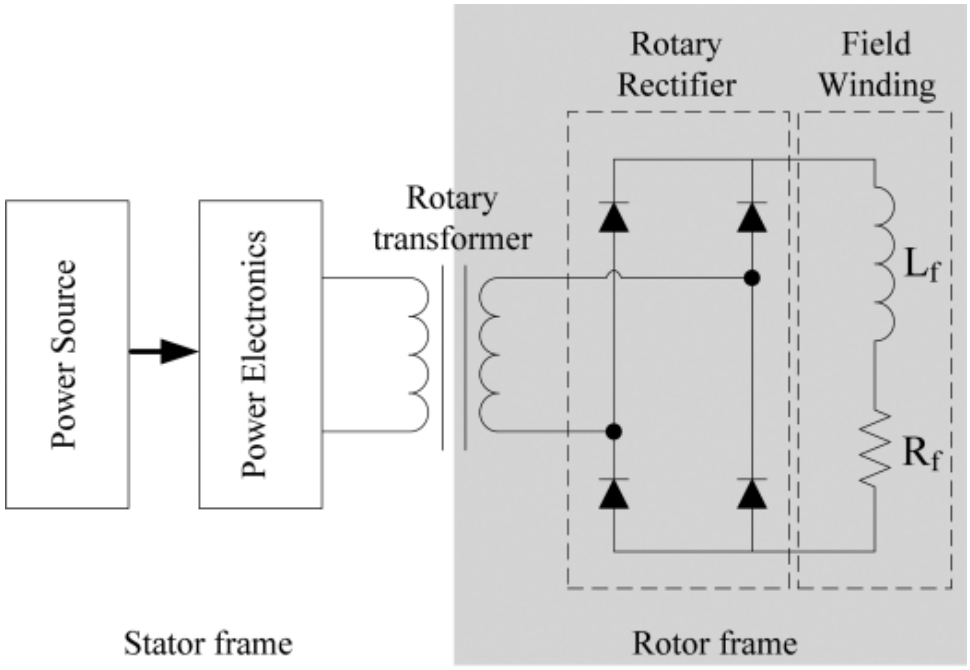

Figure 1.6: General diagram of a transformer and IPT system

in the 10's to 100's of kHz range. Conversely, IPT has loose coupling [55–62], utilizing either air core transformers or gapped ferrite cores that require external compensation. The ideal wireless power transfer system, shown in Figure 1.6, has infinite mutual inductance. With loosely coupled inductors, the mutual inductance is commonly compensated with a resonant capacitor. These resonant systems can operate up into the MHz range with dedicated development of the power electronics for the AC power source. For both of these systems, there are many papers discussing optimal designs for cored transformers. [63–73]. Likewise, these systems all require a rotating rectifier to create DC for the field winding.

The power requirements of rotary transformers for WFSMs in traction applications also vary greatly. A design by General Motors required 5kW of field power for a 70kW machine [26], while another research paper required 750W of field power to power a 45.3kW machine [50], and yet further transformer designs suggest a target of 10kW continuous field power [65]. In any case, field power on the order of kilowatts will be required for traction machines and is a good benchmark goal for any wireless excitation method.

1.2.5 Capacitive Power Transfer (CPT)

Overview of Capacitive Power Transfer

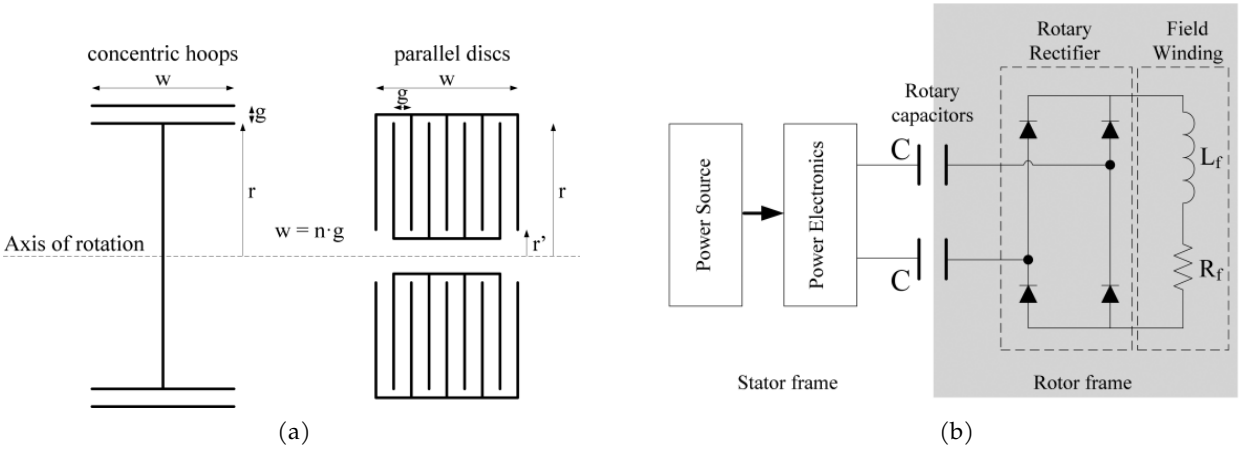

Figure 1.7: (a) General diagram of CPT system and (b) diagram of radial and axial configurations [3]

Analogous to IPT transferring power via magnetic fields, capacitive power transfer (CPT) works on the principle of transferring power across an air gap through an electric field. Although rotating transformers as an excitation scheme have been around for many decades, the concept of CPT for synchronous machine excitation is relatively recent within the last decade. The first CPT for WFSM excitation prototype was proposed in 2011 [3, 74] as an alternative to the rotary transformer and IPT. Unlike IPT, CPT does not suffer from high power loss from surrounding metal components such as the synchronous machine rotor. Similarly, the majority of the electric field in CPT is necessarily contained between the two plates with less possibility of high EMI interference.

Figure 1.7a shows the general diagram for this excitation system. For a WFSM, the stator side would be stationary, while the greyed rotor side would be rotating and connected to the field windings represented by R_f and L_f. Two separate capacitors are required in the forward and return path in order to create a wireless exciter. The two capacitors are also referred to as a capacitive coupler. Likewise, these capacitors can be arranged in an axial or a radial format as shown in Figure 1.7b [75, 76]. On the primary side, an arbitrary front-end power source is required that can be supplied either directly from an AC source, or a DC source with the appropriate converter power electronics.

Between two electrodes, there is some maximum allowable voltage determined by the breakdown electric field strength of the gap, which is typically $3\frac{kV}{mm}$ for air. The general equation for a capacitor is given in eq. (1.1)

$$C = \frac{\varepsilon_o \varepsilon_r A}{d} \tag{1.1}$$

where ε_r is the relative permittivity, $\varepsilon = 8.854 * 10^{-12}$, A is the electrode surface area and d is the distance between them. The voltage across the gap between the electrodes is

$$V_c = Ed \tag{1.2}$$

where E is the electric field, and the magnitude of the current through the capacitor is given in

$$I_c = \omega C V_c \tag{1.3}$$

Together, these equations produce an $\frac{A}{Hz}$ rating to characterize this capacitive coupler in eq. (1.4)

$$\frac{I_{c,pk}}{f} = 2\pi C V_{c,pk} \tag{1.4}$$

Given a certain capacitor operating with the maximum electric field, eq. (1.4) creates the operating space boundary to determine the current transferred across the capacitor. For WFSM excitation, the goal is to transfer a certain amount of direct current to the rotor, so a rotating rectifier is necessary between the coupler and field windings as with all other discussed forms of wireless excitation.

Within CPT there are two main areas of research: small-gap and large-gap power transfer. Figure 1.8 shows a typical axial coupler configuration with the matrix of capacitances between all four plates. The main desired capacitance for transferring power between the like-colored plates is denoted by C_{13} and C_{24}. All four other capacitances in the matrix are undesired leakage pathways. Typically, the leakage capacitances, C_{34}, C_{23}, C_{14}, and C_{12}, are on the order of single $pF's$ whereas the main pathway is on the order of 100's of $pF's$ to 10's of $nF's$. It is desirable that the main pathway capacitances are many orders of magnitude above the leakage capacitances. In small-gap CPT where the electrode plates are close together, this is the case; however, in large-gap CPT all six

capacitances would be in the similar order of magnitude. In this work, only small-gap CPT will be considered for WFSM excitation, whereas one application for large-gap CPT is in wireless vehicle charging that requires special compensation strategies [77–82]. For small-gap power transfer, CPT and IPT are comparable in terms of power density [83].

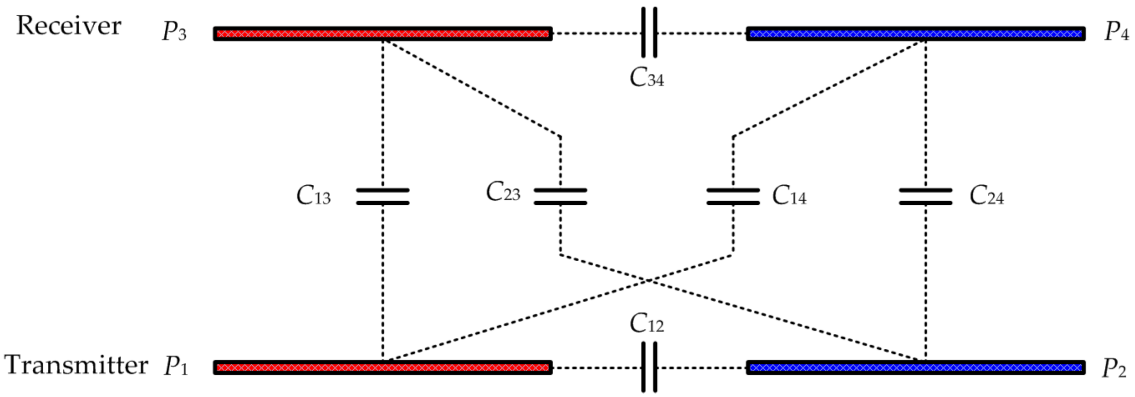

Figure 1.8: Capacitance coupling matrix of a four-plate coupler. [4]

The impedance of a capacitor is inversely proportional to the capacitance, so it follows that with typical values of coupling capacitance, it is necessary to find ways to compensate for the high impedance coupler. Operating the coupler at resonance to minimize the impedance with carefully added inductors is a popular method of compensation.

Review of Current CPT Research for WFSM excitation

The capacitive coupler presented in this section is described in detail in [84], [85, 86] which uses a series tank inductor. Specifically, Figure 1.9 shows the derived values of the capacitive coupler matrix for an airgap of 1mm. In this case, the capacitors in position C_{12} and C_{34} at 288pF and 268pF, respectively, are the intended main transmission path. The coupler has an approximate amps/hertz rating of 2 $\frac{A_{pk}}{MHz}$ with an air gap of one millimeter and therefore requires the system and power electronics to operate in the megahertz range.

Figure 2.3 shows the amps-per-hertz rating of the CPC with a star denoting the 1.7MHz switching frequency from prior research. The tank current refers to the current through the capacitor coupler and compensation inductor. The output power is mapped to various system frequencies with a field winding approximated as an RL load of 40Ω and 3H. The tank current is related to the load current by reflecting across the rectifier as $I_{pk,tank} = (\frac{\pi}{2})I_{out,DC}$. With a given rotor field impedance, the field power is limited by the switching frequency. A buck converter was added on the output of the

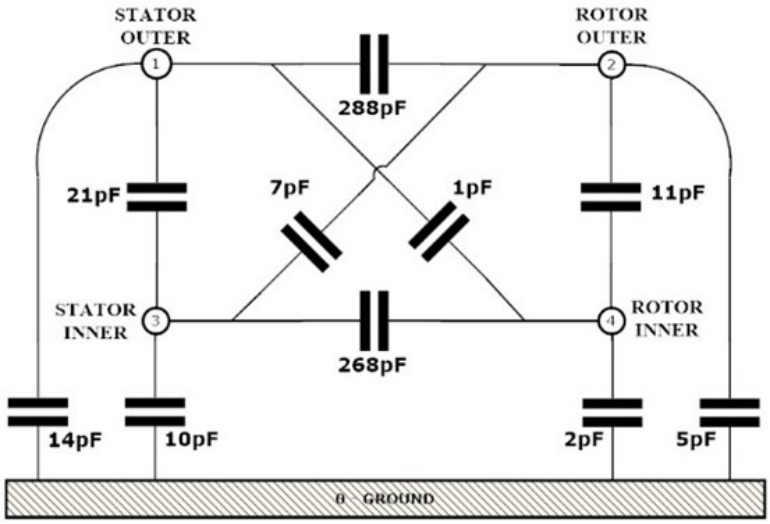

Figure 1.9: Capacitive Coupler Matrix

rectifier as an impedance converter, and the CPC achieved a maximum field power of 675W at a frequency of 1.7MHz. Dynamometer testing confirmed power can be transmitted while spinning. To reduce the system complexity and increase output power capability $> 1kW$, it is necessary to operate at a higher frequency. This work details the design and testing of a CPT system for wireless excitation of wound field synchronous machine windings operating at the 6.78MHz ISM band frequency.

Current CPT research areas include CPT modeling and simulation [87–90] and compensation strategies [91–94, 5]. Figure 1.10 shows a summary of the recent coupler topologies specifically for WFSM excitation.

Figure 1.10a shows the first proof of concept CPT excitation system with multiple metal parallel plates in an axial configuration [3, 74], [24]. To increase the coupling capacitance, there are many sets of stator and rotor discs electrically connected together to achieve 900 pF of capacitance. Likewise, to compensate for the low capacitance, an inductor was added in series with the forward direction capacitor to resonate at 626 kHz and minimize the series impedance. Once rectified, the first prototype system transferred less than 10W of power to the WFSM at 94% efficiency. In [95], further research into the AC power source and compensation yields 1034W transferred to a 75Ω load resistor at 90.3% efficiency using the same coupler in a static setup. The AC source is generated using a buck-boost resonant converter at 200 kHz.

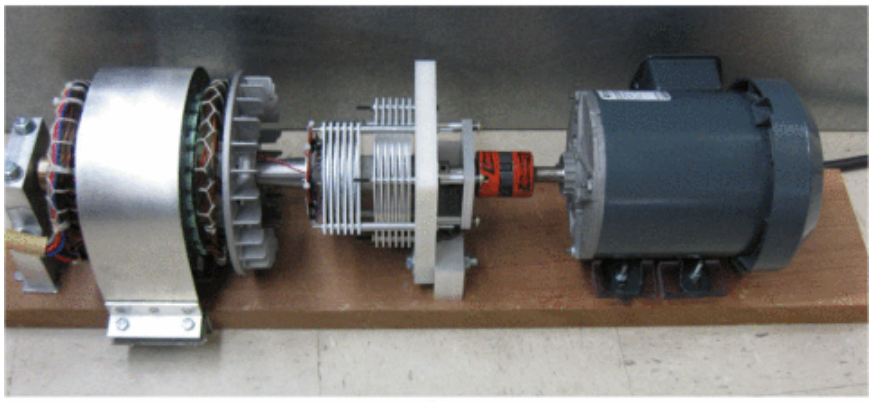

(a)

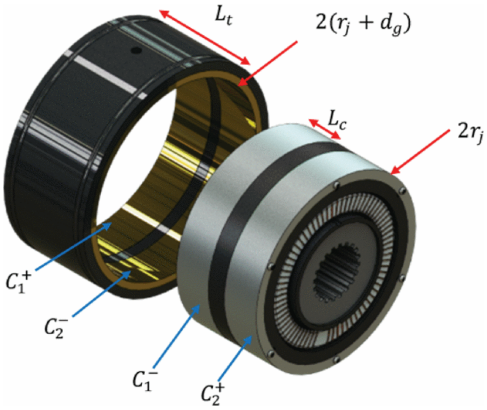

(b)

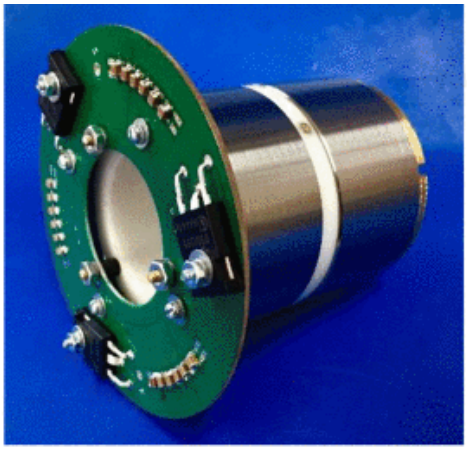

(c)

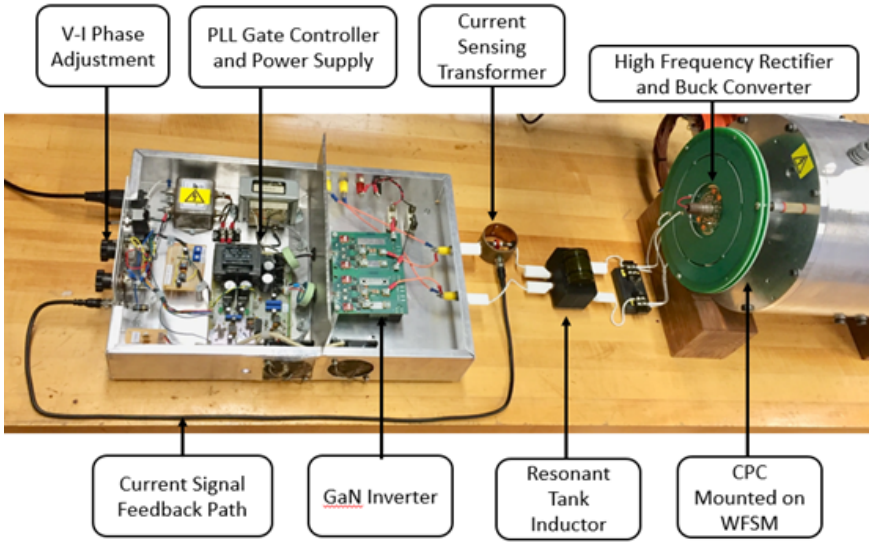

(d)

Figure 1.10: Summary of CPT couplers for WFSM excitation that use (a) many thin metal plates connected in parallel with the electric field between the plates in the axial direction, (b)-(c) a journal bearing with the coupling capacitance between the cylindrical surface areas, and (d) coupler made from PCBs with resonance in the MHz range.

The next concept in Figure 1.10b is a radial CPT design with journal bearings used to excite a synchronous generator [96, 97]. The cylindrical bearing surfaces offer high surface area with 2nF of coupling capacitance; however, the coupling capacitance was shown to change with shaft speed to an asymptotic point closer to 1.7nF. The bearings are commercially available with the rotor rings made of hardened steel and the stator rings made of ceramic-coated aluminum with a lubricating oil acting as a dielectric. The AC input power is created using a push-pull class-E resonant inverter operating at 765 kHz. Additionally, an inductor is added in series with the coupler in both the forward and return paths set to resonate at the converter switching frequency. This compensation reduces the system impedance and allows the converter to utilize soft-switching, which reduces the switching losses at near-MHz frequencies. For the full system, 2.5A DC, corresponding to 340W of power, is transferred to the field winding at 85% efficiency. The journal bearing approach provides a CPT system with many commercially available components and small overall size.

The third and most recent CPT system in Figure 1.10d features a capacitive power coupler (CPC) made from printed circuit boards for ease of manufacturing, integration with the rotating rectifier, and low cost [85, 84]. This system is similar to the axial coupler in A, but instead features just three boards: two stator boards and one rotor board. Each board has two concentric copper plates that correspond to the forward and returning coupling electrodes. The stator boards are connected in parallel to double the capacitance. This coupler also has the lowest coupling capacitance, just under 290 pF, and as a result requires compensation with series inductors and a high system resonant frequency. Initially, air-core inductors were used for compensation, but ultimately compact, high-frequency inductors were designed using [66]. From eq. (1.4), this coupler's $\frac{\mathrm{amps}}{\mathrm{hertz}}$ rating is $2\frac{\mathrm{A}}{\mathrm{MHz}}$ which means a mega-hertz resonant point is required for high power operation. The CPT system's AC power source comes from a full-bridge class-D resonant inverter operating at 1.7 MHz. This system was tested during operation of a WFSM and transferred a peak power of 675W, 4A DC, at 90.3% efficiency. While series compensation was used, at a 1.7 MHz operating frequency it was necessary to incorporate a buck converter between the output of the rectifier and the field winding to effectively increase the load impedance for the CPC. The buck converter operated as an impedance transformer to allow the CPC to operate within its current capability but transfer higher power than the fixed rotor winding resistance would otherwise allow. As mentioned in section 1.2.4 on rotary transformers and IPT, current research suggests field power in the kilowatt

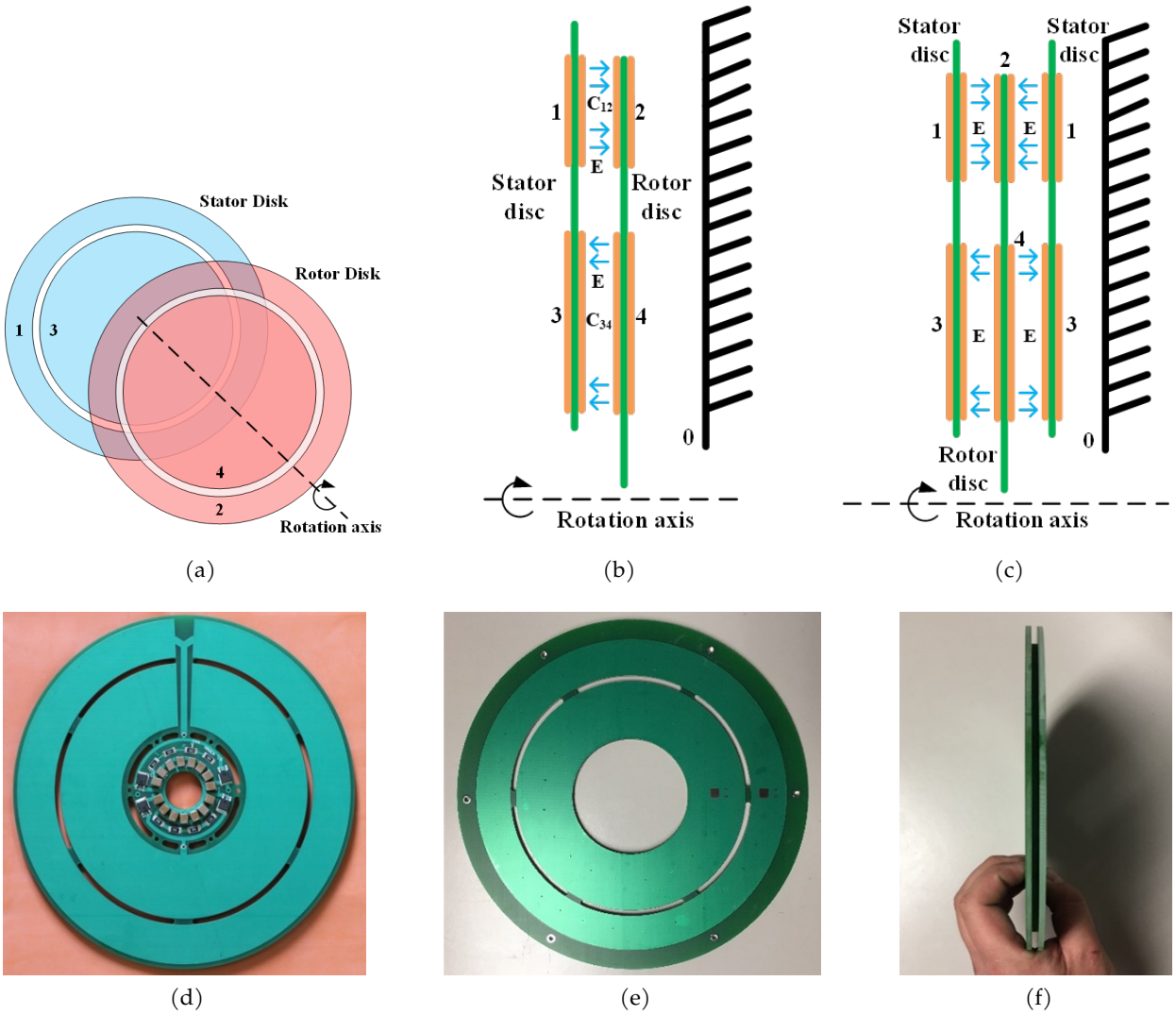

Figure 1.11: Detailed explanation of most recent CPT coupler topology [94]. (a) shows a general diagram of the coupler axis of rotation along with the side-view (b) two board and (c) three board configurations. (d)-(f) show pictures of the assembled stator board, rotor board, and side view of the coupler together, respectively.

range is required for traction machine adoption. This CPC prototype does not currently meet this standard and will require future improvements to achieve the minimum goal of 1kW of field power.

1.3 Capacitive Position Sensors

As stated in section 1.1, the successful adoption of EVs by consumers will only happen when they are economically preferable to traditional combustion-engine vehicles. Therefore, the WFSM can

further its cost-competitiveness with PM motors by providing additional pathways to reduce the cost of its wireless excitation system and the synchronous machine overall. All traction motors have a separate, physical position sensor that are purchased from one of numerous resolver and encoder companies and sensor products on the market; however, this necessary sensor adds per unit cost to every motor. If the already present excitation system could absorb the sensor cost as well, the WFSM could become more economically viable. Thus, chapter 4 of this work proposes the design of a new topology of capacitive resolver to be integrated into the rotating rectifier of the capacitive coupler boards. This section on capacitive position sensors will explain their basic operation and current research topologies.

The first use of capacitive sensors was proposed as an alternative to strain gauges when higher reliability and sensitivity were needed for measurements in six degrees of freedom [98, 99]; however, in the late 1980's and 1990's researchers started to develop prototypes for capacitive sensors to measure radial position [100]. While capacitive sensors are commonly used for linear position as well, in this review, only position sensors for radial position are discussed. A summary of sensor topologies as well as a discussion on common design issues and solutions is presented below.

1.3.1 Capacitive Sensors Overview

A capacitive sensor operates on the principle that an AC input voltage applied to a varying capacitance, thus a varying impedance, will output a predictable and varying output voltage. The capacitance changes by some physical movement, specifically rotation, for encoder and resolver applications. The primary goal of the sensor design is to create an output voltage that varies linearly with rotational position by understanding and mitigating the nonlinear pathways in the electrode plate design. Consider a simple circular parallel plate capacitor shown in Figure 1.12. If fringing is neglected in the ideal case, the capacitance would be calculated using eq. (1.1). However, a nonideal capacitor experiences fringing effects between the edges of the electrode plates and has leakage paths between each electrode plate and any nearby surfaces.

One compensation factor simply increases the total surface area, A, by the distance between the plates, d. Thus, as the distance between the plates is decreased, so would the fringing effects. Another way to approach this is to reduce fringing effects by maximizing the $\frac{A}{d}$ ratio in a sensor design. One common technique used to mitigate the fringing field effects [98, 99, 101] are guard

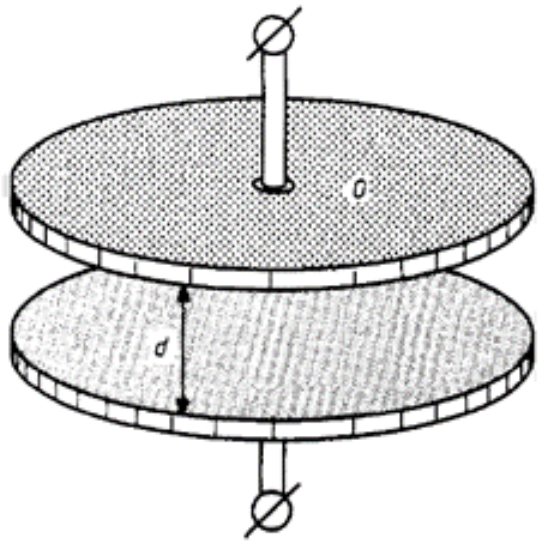

Figure 1.12: Parallel plate capacitor example

electrodes. In , guard electrodes, also called grounding electrodes, would appear as outer rings on both electrode plates that are connected to ground and shield the edges of the electrodes from fringing effects.

Conversely, another consideration for sensor design concerns the manufacturability and flatness of the electrode plates. Any warp or tilt in the electrode plates would cause unexpected and nonlinear changes in the capacitance as it rotates that would then affect the desired linear output voltage [102]. The effect of manufacturing defects decreases as the distance between the plates increases or by minimizing the $\frac{A}{d}$ ratio in the sensor design. However, minimizing this ratio would also reduce the maximum capacitance and measurement sensitivity of the plates which typically falls in the pF to 10's pF range. As such, minimizing fringing effects while also minimizing the effects of manufacturing tolerances presents a challenge due to the competing design factors. Alongside the development of the physical capacitive sensor design, there has also been much research on demodulation algorithms for converting a pF change in capacitance to a linear and predictable position [103–106].

1.3.2 Capacitive Encoder and Resolver Topologies

In general, radial capacitive position sensors, where the parallel electrode surfaces rotate relative to each other, can be grouped into two main categories: two-plate sensors and three-plate sensors.

For all designs, stationary boards are referred to as stator boards and rotating boards are referred to as rotor boards and all consist of a transmitter, receiver, and a varying capacitance component. Figure 1.11 shows a summary of capacitive sensor topologies compatible with machine position- and speed-sensing, organized in chronological order of their proposed design development.

Capacitive Sensor Topology A

Initially, in 1989 Peters [100] developed a linear rotary differential capacitance transducer as a capacitive counterpart to the linear variable differential transformer (LVDT) shown in Figure 1.13a. The design consists of one stator transmitting plate and one rotor receiving plate that have two half circles of electrodes. With a single-phase voltage applied across the stator half circle electrodes, the changing capacitance creates a changing differential output voltage across the rotor electrodes. Assuming no stray loss, the differential output voltage corresponds linearly to the relative position between the plates. This sensor is designed such that the measurement electronics are on the rotating plate which restricts movement to 180 degrees and therefore cannot be continuously rotated. Although the capacitance transducer cannot operate as a motor encoder, it shows the potential to create a linearly varying capacitance sensor.

Capacitive Sensor Topology B

To solve the issue of capacitance measurements on the rotor, two board sensors, by nature of having two sets of electrodes on the rotor and stator instead of just one, improved upon the linear rotary differential capacitance transducer Figure 1.13b shows a two-board sensor capable of full rotation [102]. The stator has four driving electrodes excited with equal amplitude sinusoidal voltages at 90° phase offsets. The four identical “pick-up” electrodes on the rotor result in a single sinusoidal voltage on the outer ring that is coupled back to the stator outer ring and measured. The four excitation and pick-up electrode shapes are mathematically designed such that the total capacitance is constant over a full rotation to maintain linearity with position.

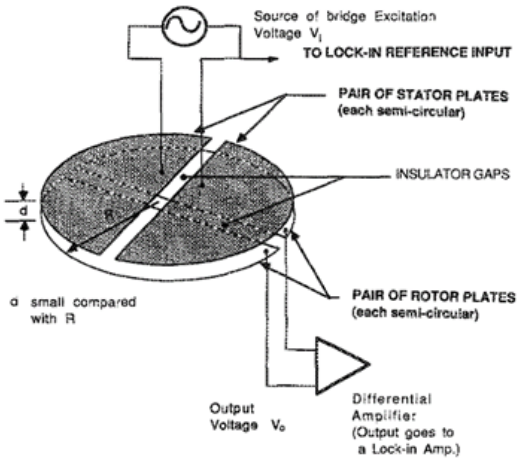
Source of bridge Excitation Voltage V_i
TO LOCK-IN REFERENCE INPUT
PAIR OF STATOR PLATES (each semi-circular)
INSULATOR GAPS
d
R
d small compared with R
PAIR OF ROTOR PLATES (each semi-circular)
Output Voltage V_o
Differential Amplifier (Output goes to a Lock-in Amp.)

(a)

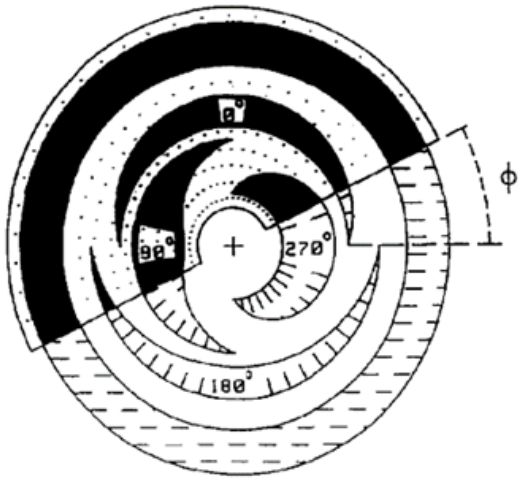
0°
90°
270°
180°
ϕ

(b)

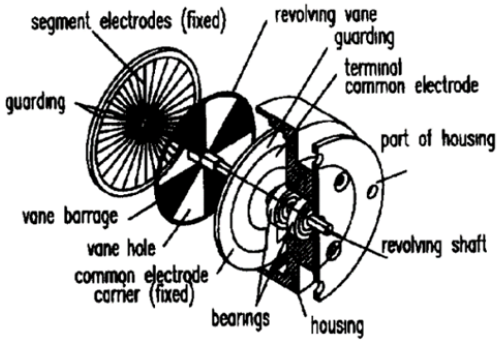
segment electrodes (fixed)
revolving vane
guarding
terminal common electrode
guarding
part of housing
vane barrage
vane hole
revolving shaft
common electrode carrier (fixed)
bearings
housing

(c)

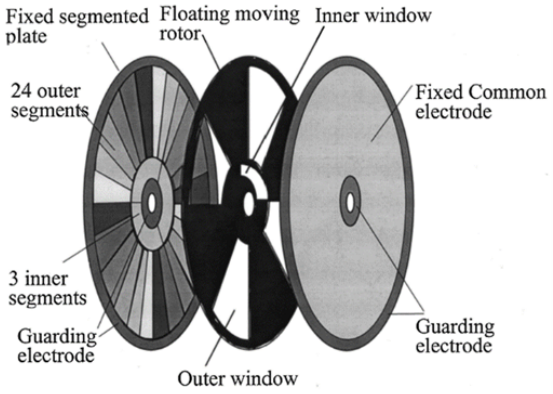
Fixed segmented plate
Floating moving rotor
Inner window
24 outer segments
Fixed Common electrode
3 inner segments
Guarding electrode
Guarding electrode
Outer window

(d)

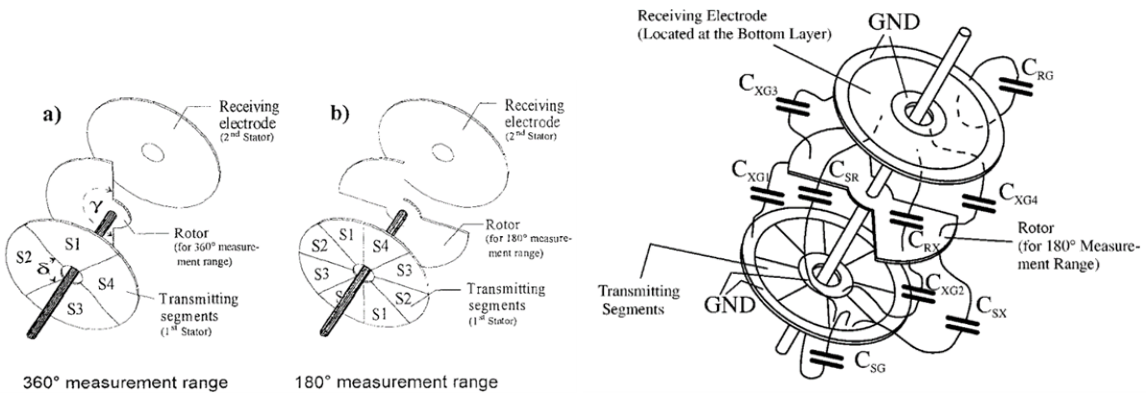
a)
Receiving electrode (2nd Stator)
Rotor (for 360° measurement range)
Transmitting segments (1st Stator)
S1
S2
S3
S4
b)
Receiving electrode (2nd Stator)
Rotor (for 180° measurement range)
Transmitting segments (1st Stator)
360° measurement range
180° measurement range
Receiving Electrode (Located at the Bottom Layer)
GND
C_{XG3}
C_{RG}
C_{XG1}
C_{SR}
C_{XG4}
C_{RX}
Rotor (for 180° Measurement Range)
Transmitting Segments
GND
C_{XG2}
C_{SX}
C_{SG}

(e)

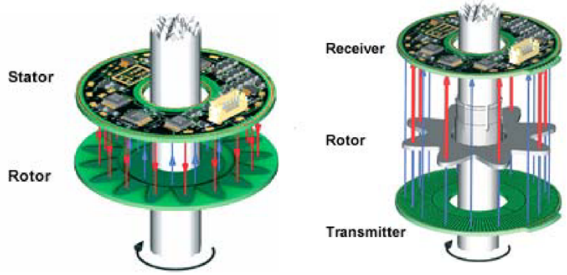
Stator
Rotor
Receiver
Rotor
Transmitter

(f)

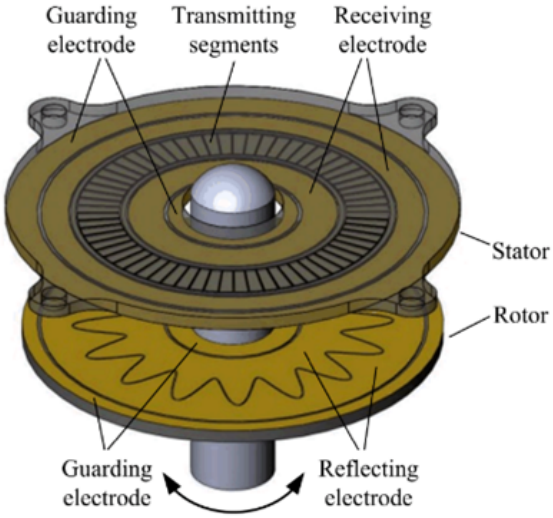
Guarding electrode
Transmitting segments
Receiving electrode
Stator
Rotor
Guarding electrode
Reflecting electrode

(g)

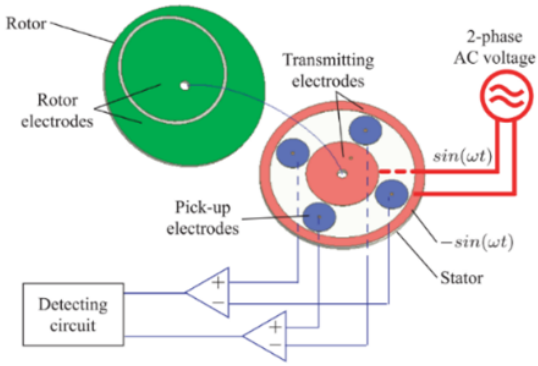
Rotor
Rotor electrodes
Transmitting electrodes
2-phase AC voltage
$sin(\omega t)$
Pick-up electrodes
$-sin(\omega t)$
Stator
Detecting circuit

(h)

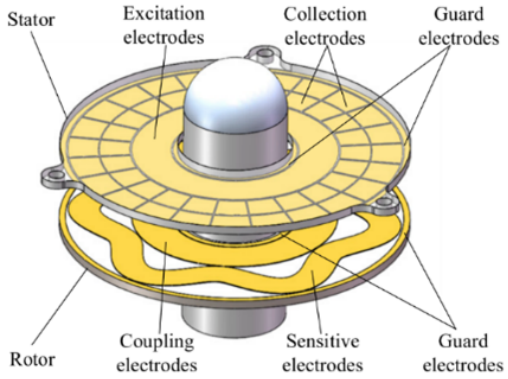
Stator
Excitation electrodes
Collection electrodes
Guard electrodes
Rotor
Coupling electrodes
Sensitive electrodes
Guard electrodes

(i)

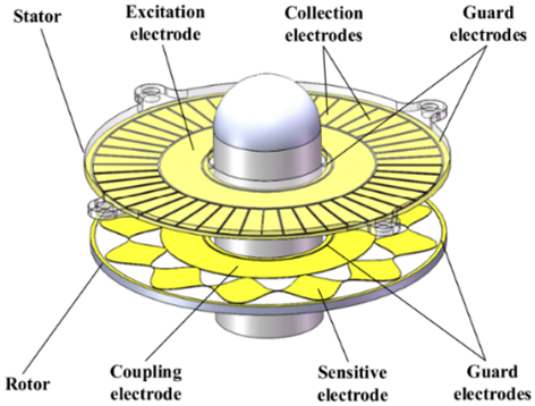
Stator
Excitation electrode
Collection electrodes
Guard electrodes
Rotor
Coupling electrode
Sensitive electrode
Guard electrodes

(j)

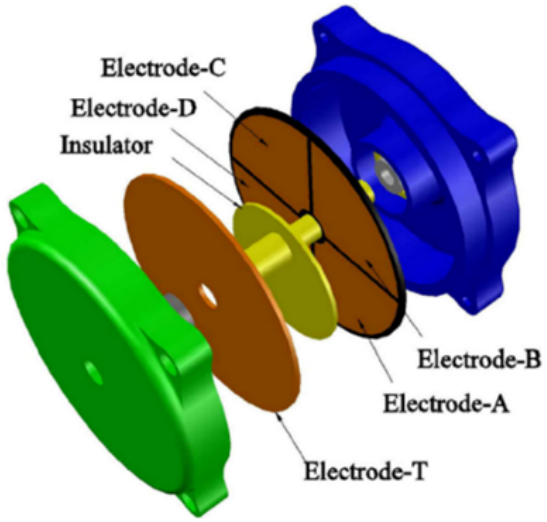
Electrode-C
Electrode-D
Insulator
Electrode-B
Electrode-A
Electrode-T

(k)

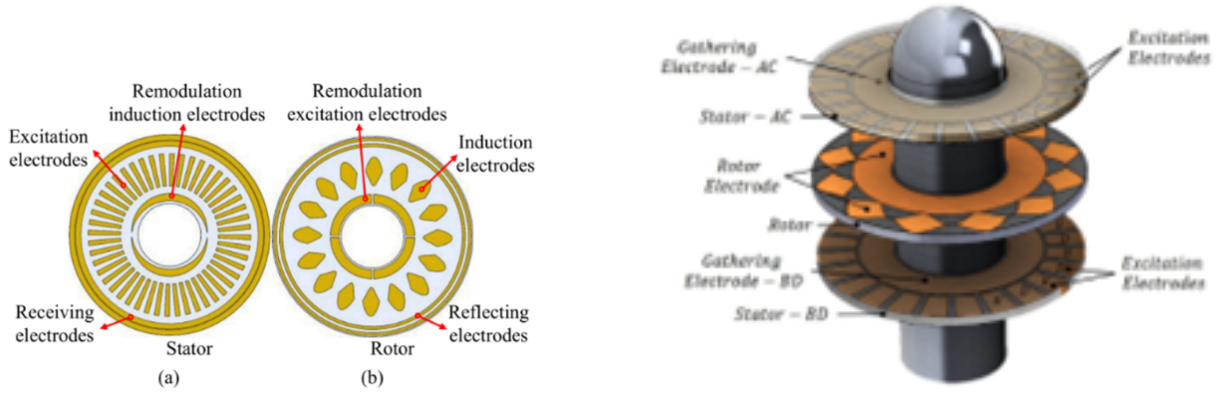

(l) (m)

Figure 1.11: Overview of capacitive position and speed sensor topologies.

Capacitive Sensor Topology C

Figure 1.13c shows the first three-board version of a capacitive sensor [107] with two stator boards and one rotor board. The transmitting stator board is excited with a single-phase sinusoidal voltage, and the receiving stator board is made up of twenty-four segments of electrodes. The twenty-four sensing segments are in six groups of four electrodes that are electrically connected. The rotor board, also called a vane in this paper, consists of four blocking, mechanically grounded segments that will adjust the coupling capacitance between the transmitting and receiving board electrodes as it rotates. The position can only be known within a 90° range as the receiving electrode arrangement has six repeating segments. This topology is likewise novel because it measures the position over the entire circle and effectively reduces capacitance errors from misaligned or warped boards.

Capacitive Sensor Topology D

The topology in Figure 1.13d is heavily derived from the previous topology while updating it to give a position measurement over the full 360° range [108, 109]. This design has the same excitation strategy but adds a second blocking scheme and sensing scheme on the inner radius of the rotor and receiving stator boards, respectively. These extra blocking vanes and sensing electrodes give information on the exact 90° quadrant of the current sensor position and are referred to as a "course" measurement in addition to the twenty-four electrode "fine" measurement. Likewise, this design includes guard electrodes on the outside radius of all three boards that are virtually grounded without mechanical contact to mitigate fringing. With twenty-four segments, topology C

and D are able to achieve high positional accuracy to less than one-tenth of a degree.

Capacitive Sensor Topology E

Figure 1.13e shows modified and simplified topologies from D that concentrate on high-speed, cost-effective sensing while compromising on lower positional sensitivity and complicated electronics [104], [110, 110–112]. In these topologies, the transmitting stator board has four to six transmitting electrodes with DC voltage applied instead of sinusoidal voltages. The DC voltages are applied to create a rough, pseudo-alternating voltage. Depending on the number of transmitting electrodes, the mechanically or virtually grounded rotor board is designed for either a 360° or 180° measurement range. Additionally, all boards can feature an outside grounded guard electrode to reduce the effect of fringing.

Capacitive Sensor Topology F

Figure 1.12f features a two-board and three-board topology that led to commercially available capacitive rotary Caps from Netzer Precision [113, 114]. These sensors feature a new petal type of blocking scheme. In both configurations, several sinusoidal phase-offset voltages are applied to the transmitting stator board that couple through a blocking petal configuration on the rotor to create a single sinusoidal voltage that is coupled back to the receiving side. The pedal configuration creates a new way to predictably vary the capacitance with radial position.

Capacitive Sensor Topology G

The topology in Figure 1.12g is roughly the inverse of the previous topology where the stator has multiple transmitting electrodes is groups of four that are offset by 90° [115]. The rotor in this case has two large coupling and reflecting electrodes that allow for two “pick-up” electrodes on the stator board. These two electrodes allow for an encoder that is more compatible with magnetic rotary resolver algorithms with a sine and cosine voltage output.

Capacitive Sensor Topology H

Figure 1.12h proposes an entirely new rotary position sensor design that aims to be a nearly drop-in replacement for standard magnetic-based resolvers [116]. The stator is excited with two sinusoidal AC voltages that have a 90° phase offset, and the resulting differential measured outputs are sine and cosine voltages to give position. As with previous two-board designs, the stator board acts as both a transmitter and couples back as a receiver while the rotor board modulates the capacitance with position.

Capacitive Sensor Topology I-J

The sensor topologies in Figure 1.12i-Figure 1.12j feature a petal-like rotor electrode structure that creates extremely high precision position measurements [105, 106], [117–119]. The transmitter has single phase AC voltage excitation with four sets of pick-up electrodes that, through differential measurements, result in sine and cosine output voltages. The resulting position resolution is below one thousandth of a degree.

Capacitive Sensor Topology K

Figure 1.12k shows another topology that focuses on speed sensing and cost rather than high precision with a rotating off-center, circular rotor board [120]. The transmitter is excited with single phase AC voltage and there are only four receiving electrodes. This design is not conducive for applications where high positional accuracy nor linearity is needed but is a simple and cost-effective solution.

Capacitive Sensor Topology L

Figure 1.11l is a further topology that stresses high resolution and has an additional set of electrodes to create an absolute encoder over the full 360° [121, 122].

Capacitive Sensor Topology M

Figure 1.11m is the same as topology J except with a third board for redundancy and increased resolution [123, 124].

1.4 Conclusion

This work deals with wound field synchronous machine wireless excitation and the removal of barriers for its widespread adoption in traction applications via achieving comparable cost and performance to the permanent magnet synchronous machine. WFSMs for traction applications are intended to meet similar power densities and efficiencies to PMSMs without the need for permanent magnets. Specifically, they are designed to eliminate rare earth elements that have high mining carbon emissions, ethical concerns, and unstable prices. However, WFSM wireless excitation methods, although numerous, are often large additions to the motor, mechanically and electrically complex, and can be cost prohibitive in comparison to even the fluctuating permanent magnet prices. In this work, the capacitive power coupler system will be improved and optimized

to help realize the potential of WFSM in traction applications by providing an easily manufacturable and compact wireless excitation system. Additionally, the WFSM will become more economically advantageous with the development of the proposed capacitive resolver integrated into the rotating rectifier board. Not only will the integrated resolver improve the viability of the current CPC excitation system for traction motor adoption, but of all possible wireless excitation methods in general.

1.4.1 Research Opportunities

While the initial CPT prototypes were suitable to transfer up to 675W of power, it is necessary to achieve kilowatt-level power transfer. Specifically for traction motors above 100kW, the goal is to achieve 1.5-2kW transferred to the field for a 2x-3x improvement from the current level. Many challenges exist to achieve this new power level. Unlike other wireless power transfer research where the load is chosen, the WFSM rotor winding is not designed to achieve a certain resistance. Thus, the system resonant frequency must be increased to 6.78MHz to lower the capacitive power coupler impedance and transfer more current, for more power, to the field windings. At 6.78MHz, the system will fall into the ISM band of frequencies reserved for industrial, scientific, and medical purposes free for EMI/EMC pollution, but the efficient operation also becomes extremely sensitive to any stray inductance and capacitance. Furthermore, higher coupler currents will naturally lead to thermal and cooling concerns and challenges to create a compact design.

To further the goal of reducing the prohibitive cost of WFSM wireless excitation methods in consumer traction applications such as electric vehicles, the cost of the machine's resolver can be absorbed into the excitation system. All forms of noncontact excitation utilize a rotating rectifier of some sort which is typically placed on a printed circuit board. As described in detail previously, there are a variety of capacitive-based encoders and resolvers that likewise are built on printed circuit boards with small overall footprints in comparison to the size of a motor endcap. Thus, with the larger rotating rectifier circuit board already present for the excitation, the resolver cost is virtually eliminated by reducing the number of unique PCBs in the system.

Chapter Two

Resonant System Design

Chapter 2 and Chapter 3 of this work intend to continue and improve upon the capacitive power transfer (CPT) design that achieved a peak output power of 675W with an efficiency of 90.3% [84]. The main drawbacks of the current CPT system are as follows:

1. The resonant tank uses large and expensive custom ferrite core inductors
2. The rectifier requires a buck converter to compensate for the field impedance.
3. The rectifier and buck converter board experiences thermal failure above 675W of output power.

Beyond these issues, the main goal for the CPT system is to achieve output powers > 1kW and reduce the size of the system. Ultimately, the coupler's low amps/hertz rating limits its maximum power capability before voltage breakdown occurs across the coupler air gap. In keeping the same coupler design, the only variable that can be manipulated to improve the output power limit is the frequency. Thus, the challenges in the improvements for this system design are rooted in the need to significantly increase the operating frequency while maintaining the overall efficiency. All components in this system have losses that scale with frequency and it will be necessary to re-evaluate and re-design each section. Consequently, increasing the operating frequency will also aid in the goal to reduce the size and complexity of the system. This chapter discusses the basics of the capacitive power transfer system design that will be tested and evaluated in Chapter 3.

2.1 Resonant System Overview

In capacitive power transfer it is often necessary to use a resonant system to compensate the capacitive coupler's large reactance for adequate power throughput as shown in the general diagram in Figure 2.1. In this figure, the matching network may be added on both sides of the capacitive coupler and contain both a gain and compensation element. The voltage and current gain blocks will step-up and step-down the voltage, respectively, for efficient power transfer across a gap. A large variety of compensation strategies exist [125] by using inductors and capacitors in combinations of series, parallel, or series-parallel configurations such as LC [80, 82, 126, 127], LCLC [77], LCL [81, 128], and CLLC [129]. Typically, more complex compensation circuits are required with large-gap capacitive power transfer. Air gaps greater than 10mm are considered large. In large gap applications such as wireless charging, the coupling capacitance is on the order of single to tens of picofarads, and the same order of magnitude as the coupler's stray capacitances.

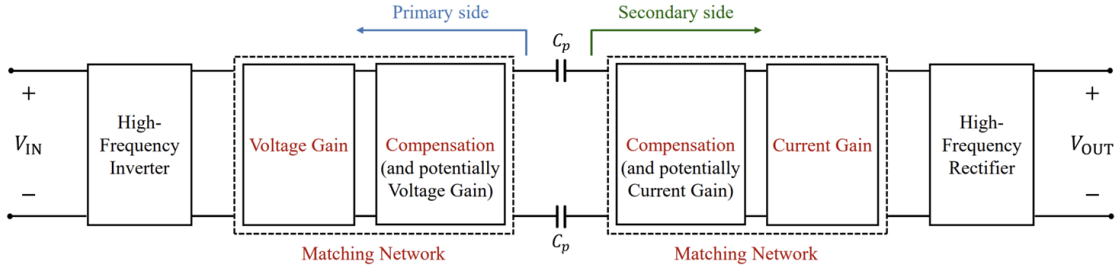

Figure 2.1: General diagram of a capacitive power transfer system with the general matching network power flow [5]

This work uses small-gap wireless power transfer with air gaps on the order of $\approx 1\text{mm}$ and coupling capacitances in the 100's of picofarads. A series resonant compensation strategy is chosen to minimize the number of components, not necessarily for peak efficiency. The series resonant system features a series inductor sized to resonate with the capacitive coupler near the system excitation frequency. There are a few advantages of this compensation strategy: there are no compensation elements required on the rotating post-capacitor side of the coupler, and single inductors add the least number of unique components to minimize space and cost.

Figure 2.2a shows the general power flow for the CPT rotor excitation method. An inductor placed in series with the capacitive coupler on both the forward and return paths constitutes the resonant "tank" of the system. The inductors are designed to be identical as the forward and return

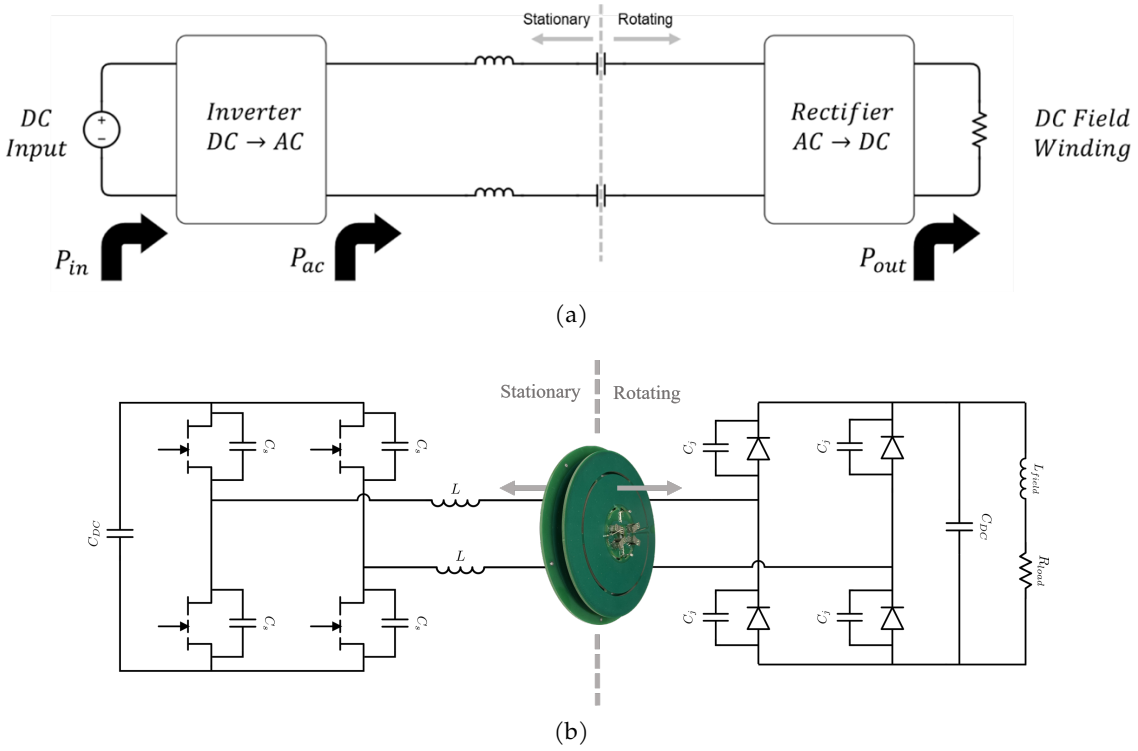

Figure 2.2: (a) Power flow overview of CPT power conversion excitation system and (b) detailed inverter and rectifier converters

capacitances are designed to be the same. The full series resonant system in Figure 2.2b is setup as a DCDC converter. A class-D resonant full-bridge inverter converts DC to AC power while on the rotating side the full-bridge rectifier converts back to DC power for the field winding. The field winding is simplified as an equivalent series RL load. The inductor value, L, determines the resonant point of the tank given in eq. (2.1) and thus the operating frequency of the surrounding power electronics.

$$f_{res} = \frac{1}{2\pi\sqrt{LC}} \tag{2.1}$$

The LC resonant tank has a resonance point that is independent of the load impedance. With the inverter simplified as an ideal sinusoidal AC voltage source and an ideal rectifier, the quality factor of the system is shown in eq. (2.2).

$$Q = \frac{1}{R_{field}}\sqrt{\frac{L}{C}} \tag{2.2}$$

The quality factor describes the "peakiness" of the resonance point, or in other words, the level of damping in the resonant tank. A higher quality factor will have less damping. At the exact point of resonance, the series tank appears as a resistive load to the inverter and the output voltage and current of the inverter will exactly match the input voltage and current to the rectifier. The impedance of the tank at resonance will only be the equivalent series resistance (ESR) of the tank components and wire connections.

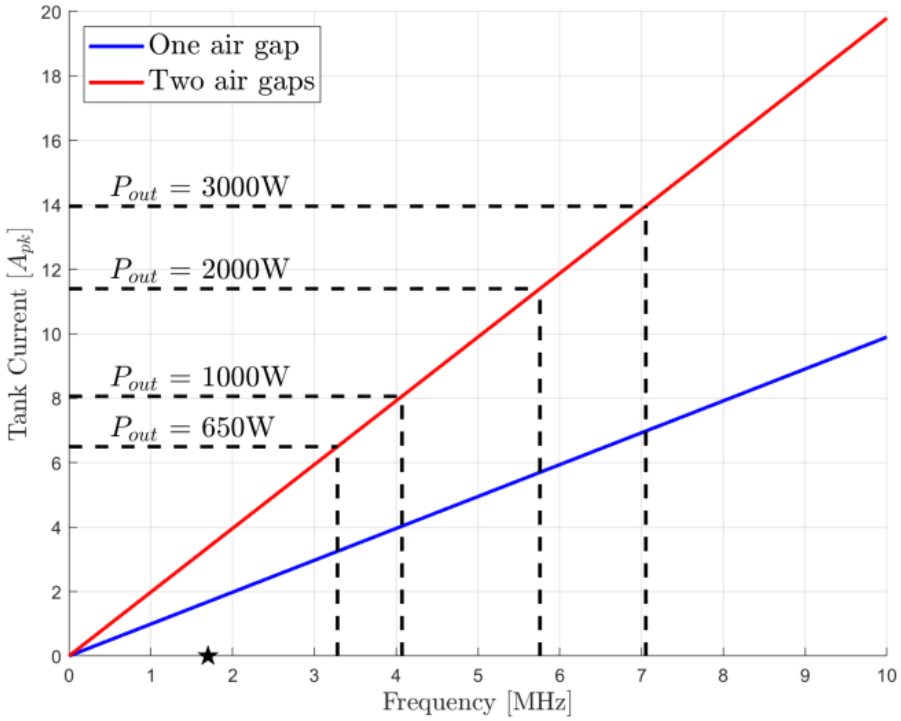

Figure 2.3: Amps-per-Hertz rating of the PCB-based capacitive coupler for a three-board system (2 air-gaps) and a two-board system (1 airgap).

The capacitive coupler presented in this section is described in detail in subsection 1.2.5 [84–86]. The coupler's performance is quantified by an amps/hertz rating of $\approx 2\frac{\mathrm{A_{pk}}}{\mathrm{MHz}}$ with two air gaps of one millimeter each. Figure 2.3 shows the amps-per-hertz rating of the CPC with a star denoting the 1.7MHz switching frequency from prior research. The tank current refers to the current through the capacitor coupler and compensation inductor.

The output power is mapped to various system frequencies with the rotor field winding approximated as 40Ω and 3H RL load. Assuming an ideal series resonant system, the output field current is given in eq. (2.3). Then the tank current can be approximated by reflecting the output

current across the rectifier in eq. (2.4). With a series resonant system, the tank current is the same as the coupler current and the terms are used interchangeably in this work. eq. (2.4) assumes that the rectifier is ideal with a unity power factor; however, this is not necessarily the case as will be seen in later sections.

$$I_{DC,out} = \sqrt{\frac{P_{out}}{R_{field}}} \tag{2.3}$$

$$\begin{aligned} I_{tank,pk} &= \frac{\pi}{2} I_{DC,out} \\ I_{tank,rms} &= \frac{\pi}{2\sqrt{2}} I_{DC,out} \end{aligned} \tag{2.4}$$

The intended goal for power transmission to the field windings of the wound field synchronous machine under test is to reach $> 1.5kW$. The denoted 1.7MHz point in Figure 2.3 cannot achieve this output power goal. Two paths forward exist to achieve higher power transmission: operate the system at a higher frequency or artificially increase the load resistance of the coupler to transfer the same power at a lower tank current. The previous state-of-the-art design increased the coupler load impedance by adding a buck converter after the rectifier to artificially increase the impedance by changing the duty ratio of the switch. However, this work focuses on increasing the system frequency to 6.78MHz in the ISM (industrial, scientific, and medical) reserved band frequencies chosen for future automotive compatibility. The higher system frequency allows for easier EMI/EMC compliance.

2.1.1 Resonant System Modeling

Equation (2.1) gives the inductance needed to resonate at 6.78MHz with the resonant coupler, but the actual switching frequency of the inverter will be different. The voltage source inverter inverter switches just above resonance in a zero voltage switching (ZVS) turn-on condition to reduce switching losses that are proportional to the switching frequency. As will be shown, the deadtime between the top and bottom switch in each half-bridge also affects the relationship between resonance and switching frequency.

The dead time angle, α, is defined by eq. (2.5) where t_d is the dead time, and f_{sw} is the

switching frequency. Figure 2.4 shows α in the context of the inverter diagram where $v_{gs,1}$ and $v_{gs,2}$ are the complementary inverter gate drive signals. According to [130], the minimum phase angle, β, between the inverter output voltage and current to maintain ZVS is given by eq. (2.6). This condition ensures that the current does not cross zero during the deadtime period. Otherwise, the voltage polarity will reverse rapidly during deadtime and create a short unintended pulse, or "notch," in the inverter output voltage waveform.

$$\alpha = 2\pi f_{sw} t_d \tag{2.5}$$

$$\beta \geqslant \frac{\alpha}{2} \tag{2.6}$$

The power factor for the inverter can also be expressed as:

$$PF_{inverter} = \cos(\beta) \tag{2.7}$$

The inverter operates with 50% duty cycle, meaning the output will look like a square wave. Considering the dead time and GaN output capacitance, the inverter output voltage is better approximated as a trapezoidal wave shown in solid blue in Figure 2.4b. Thus, the fundamental of the inverter output voltage is given in terms of the DC input voltage in eq. (2.8).

$$v_{fund,pk} = \left(\frac{4}{\pi}\right) \frac{\sin(\frac{\alpha}{2})}{\frac{\alpha}{2}} V_{DC,in} \tag{2.8}$$

From the equivalent system diagram in Figure 2.4a, the tank current can be described by eq. (2.9). This then leads to the derivation of β from the equivalent RLC load in eq. (2.10).

$$i_{tank,pk} = \frac{V_{inverter,fund,pk}}{|2j\omega L + \frac{2}{j\omega C} + R_{load}|} = \frac{V_{inverter,fund,pk}}{R_{load}} \cos(\beta) \tag{2.9}$$

$$\cos(\beta) = \frac{R_{load}}{\sqrt{\left(2j\omega L + \frac{2}{j\omega C}\right)^2 + R_{load}^2}} \tag{2.10}$$

Substituting in eq. (2.5) and eq. (2.6) to eq. (2.10), the resonant tank inductance is solved in

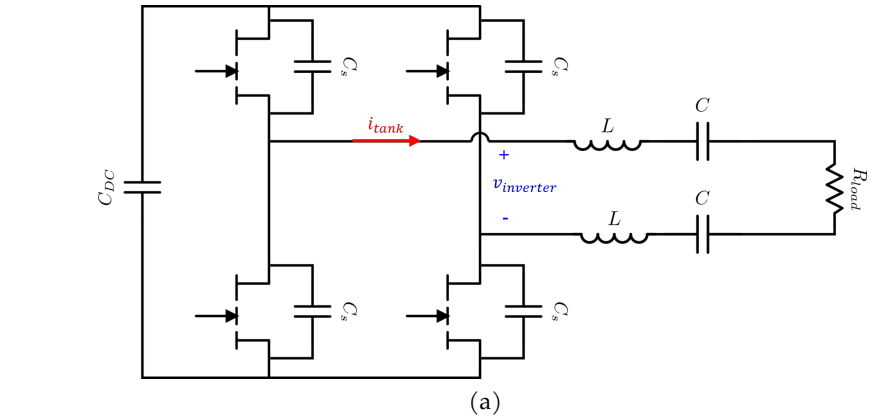

(a)

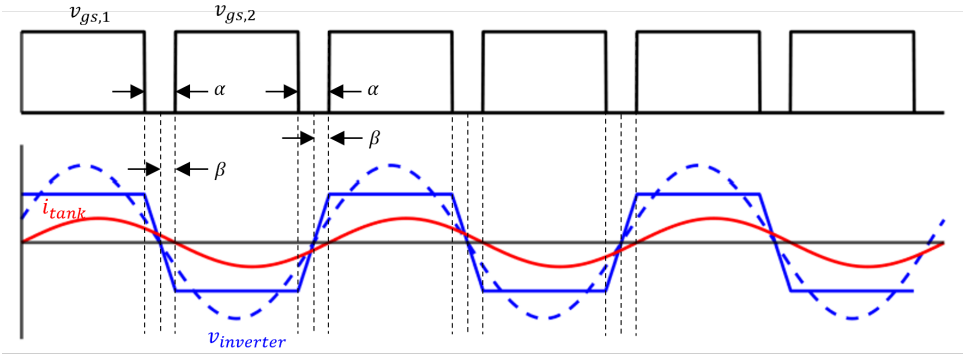

(b)

Figure 2.4: (a) Diagram of the inverter and resonant tank with a resistive load, and (b) plots of the ideal complementary gate signals with the output inverter voltage and current waveforms.

terms of the desired switching frequency, deadtime, and the coupler capacitance. All of these are known quantities. Of the two possible inductances, only one is real and valid.

$$L = \frac{\pi^2 \cos(\pi f_{sw} t_d) \pm \sqrt{C^2\pi^6 \cos^2(\pi f_{sw} t_d) R_{load}^2 f_{sw}^2 - C^2\pi^6 R_{load}^2 f_{sw}^2}}{4\pi^4 \cos(\pi f_{sw} t_d) f_{sw}^2 C} \tag{2.11}$$

The inductance given in eq. (2.11) is valid assuming the rectifier is ideal and the load of the capacitive coupler can be modeled as purely resistive. However, at mega-hertz frequencies, the diodes cannot be considered ideal. Instead, the equivalent diode capacitance must be included in the model. The rectifier diagram in Figure 2.5a shows passive diodes in parallel with their equivalent capacitance, C_j. From [131], the individual capacitances can be grouped into one input equivalent capacitance, C_e, and resistance, R_e, using eq. (2.12) and eq. (2.13) where C_j is a single diode's equivalent parallel capacitance. In Figure 2.5b, the full non-ideal rectifier turns into an equivalent circuit with the equivalent capacitance and resistance as the input to an ideal rectifier.

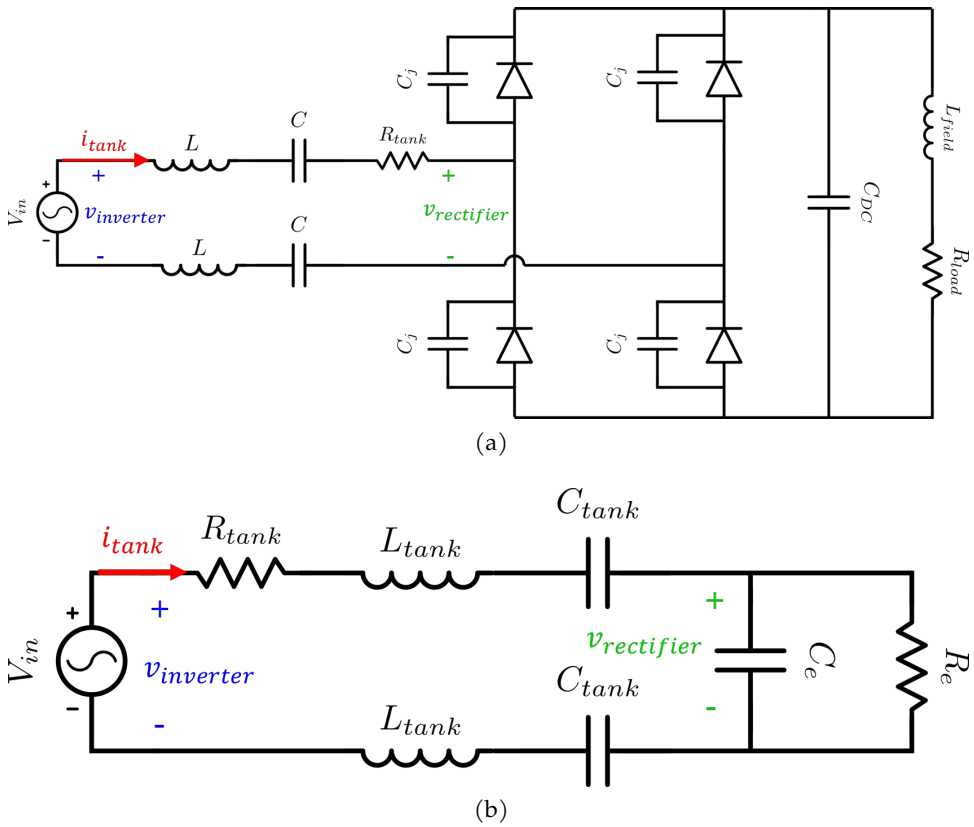

(a)

(b)

Figure 2.5: (a) Diagram of the resonant tank and rectifier. The inverter is represented as an ideal AC voltage source. (b) Equivalent CPT circuit assuming an ideal AC voltage source and the rectifier with the field winding as an equivalent parallel capacitance, C_e and resistance, R_e.

An additional resistance, R_{tank}, is added to account for the ESR of the resonant tank components. The field resistance, R_{load}, is reflected across the rectifier from the DC to the AC and is included in the R_e term. Equation (2.12) - eq. (2.16) are derived in [131].

$$R_e = \frac{8R_{load}}{\pi^2}\left(a + \frac{b^2}{a}\right) \approx \frac{8R_{load}}{\pi^2} \tag{2.12}$$

$$C_e = \frac{\pi b}{16 f R_{load}\,(a^2 + b^2)} \tag{2.13}$$

Where:

$$a = \frac{\sin^2(\theta)}{16 f R_{load} C_j} \tag{2.14}$$

$$b = \frac{\sin(2\theta) - 2\theta}{32 f R_{load} C_j} \tag{2.15}$$

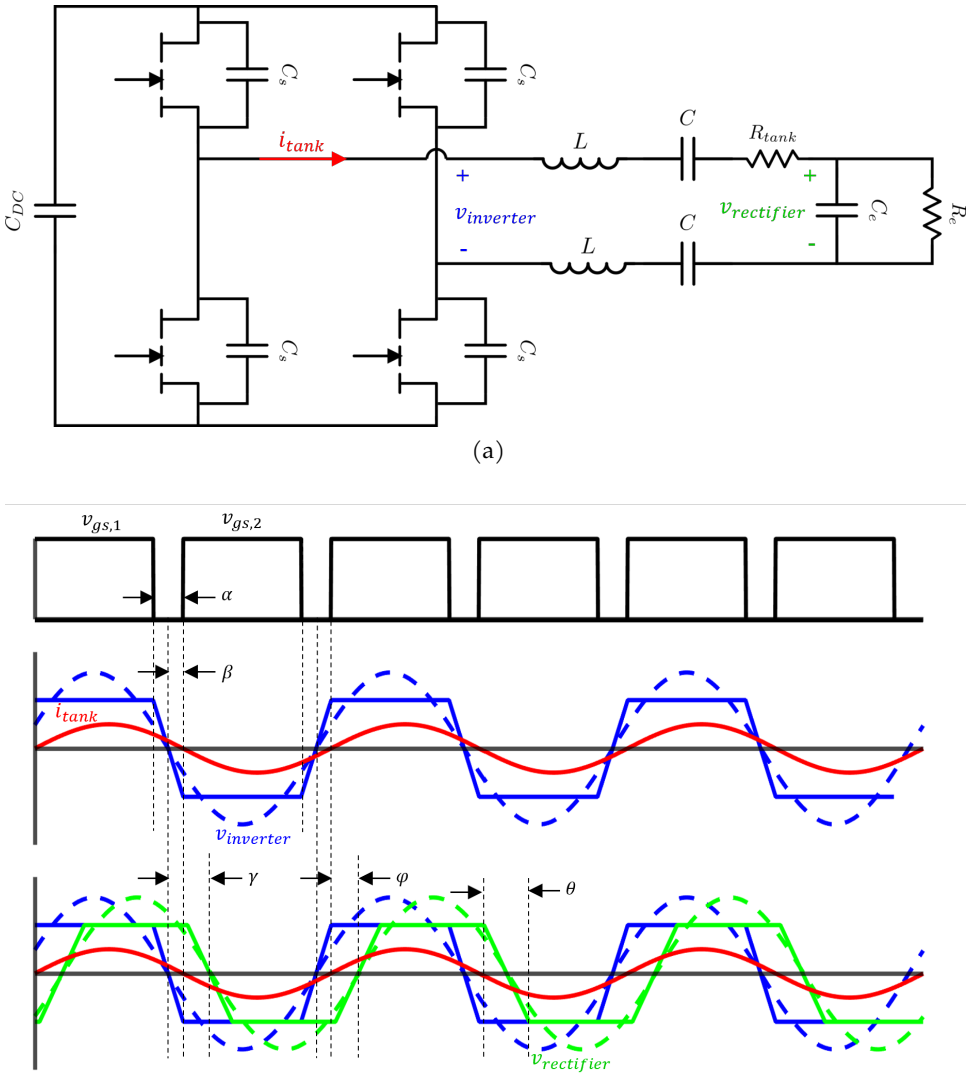

Figure 2.6: (a) Diagram of the inverter and resonant tank assuming the rectifier load is an equivalent parallel capacitance, C_e, and resistance R_e from the rectifier and field winding. (b) The corresponding inverter output and rectifier input waveforms with reference to the gain signals. All angles between the voltages and current are denoted.

$$\theta = \cos^{-1}\left(\frac{1-4fR_{load}C_j}{1+4fR_{load}C_j}\right) = \omega\tau_{diode} \tag{2.16}$$

The angle term, θ, in eq. (2.16) refers to the commutation angle of the diode and can be derived from to the time constant, τ_{diode}, for charging the equivalent diode capacitance. Angle θ is denoted in the context of the tank waveforms in Figure 2.6b.

An improved analysis of the series resonant system now includes the effect of the diode capaci-

tance along with the tank ESR. Figure 2.6a looks back at the inverter with the rectifier non-idealities properly taken into account. Equation (2.17) shows the updated form of inverter current from eq. (2.9).

$$i_{tank,pk} = v_{inverter,fund,pk}\left(\frac{1}{\frac{R_e}{1+j\omega R_e C_e} + \frac{2}{j\omega C} + 2j\omega L + R_{tank}}\right) \tag{2.17}$$

Likewise, the updated β is derived in eq. (2.18)

$$\begin{aligned}\beta &= \angle\left(\frac{1}{\frac{R_e}{1+j\omega R_e C_e} + \frac{2}{j\omega C} + 2j\omega L + R_{tank}}\right)\\ \beta &= \tan^{-1}\left[\frac{2CC_e^2LR_e^2\omega^4 - 2 - (C_e(C+2C_e)R_e^2 - 2CL)\omega^2}{(C_e^2R_e^2R_{tank}\omega^2 + R_e + R_{tank})\omega C}\right]\end{aligned} \tag{2.18}$$

where C_e is the equivalent rectifier capacitance. Now substituting eq. (2.18) and eq. (2.5) into eq. (2.6), the optimal series resonant inductance for the system is found in eq. (2.19).

$$L = \frac{C\omega(C_e^2R_e^2R_{tank}\omega^2 + R_e + R_{tank})\tan(\frac{\omega}{2}t_d) + 2 + C_eR_e^2(C+2C_e)\omega^2}{2\omega^2C(C_e^2R_e^2\omega^2+1)} \tag{2.19}$$

With the inductance known, the voltage gain across the LC tank is also known. The rectifier voltage is found with a simple voltage divider in eq. (2.20). Equation (2.21) defines γ as the phase between the fundamental component of the inverter and rectifier voltages.

$$\frac{v_{rectifier,fund,pk}}{v_{inverter,fund,pk}} = \left(\frac{\frac{R_e}{1+j\omega RC_e}}{\frac{R_e}{1+j\omega RC_e} + \frac{2}{j\omega C} + 2j\omega L + R_{tank}}\right) \tag{2.20}$$

$$\gamma = \tan^{-1}\left(-\frac{CC_eR_eR_{tank}\omega^2 + 2\omega^2LC - 2}{\omega(2CC_eLR_e\omega^2 - CR_e - CR_{tank} - 2C_eR_e)}\right) \tag{2.21}$$

From here, angle φ in eq. (2.22) corresponds to the phase of the rectifier between the current and voltage inputs.

$$\varphi = \gamma - \beta \tag{2.22}$$

Equation (2.4) then can be improved to include the rectifier power factor in eq. (2.23).

$$I_{tank,pk} = \frac{\pi}{2\cos(\varphi)} I_{DC,out} \tag{2.23}$$

Equation (2.23) makes the assumption that the diode capacitance is the only non-ideality in the rectifier. The diodes also have significant forward voltage drops, v_f, that will be a main source of rectifier loss. If the the solid green rectifier input voltage waveform in Figure 2.6b has a peak voltage $v_{rectifier,pk}$, it will be related to the DC output voltage by eq. (2.24).

$$V_{rectifier,pk} = V_{DC,out} + 2v_f \tag{2.24}$$

Now, by using the AC tank current can be calculated with the inclusion of the diode forward voltage drop. in

$$\begin{aligned} V_{rectifier,pk} &= \frac{1}{C_j} \int_0^{\tau_{diode}} I_{tank,pk} \sin(\omega t)\, d\omega t \\ V_{rectifier,pk} &= \frac{I_{tank,pk}}{2\pi f_{sw} C_j} (1 - \cos(\theta)) \\ I_{tank,pk} &= \frac{4\pi f_{sw} C_j}{1 - \cos(\theta)} V_{rectifier,pk} \end{aligned} \tag{2.25}$$

Equation (2.25) will give a slightly higher current than eq. (2.23) to account for loss from the diode conduction loss from forward voltage drop. Then the fundamental component of the rectifier is determined:

$$V_{rectifier,fund,pk} = \left(\frac{4}{\pi}\right) \left(\frac{\sin\left(\frac{\theta}{2}\right)}{\frac{\theta}{2}}\right) V_{rectifier,pk} \tag{2.26}$$

The overall system voltage gain is simply:

$$v_{gain} = \frac{V_{DC,out}}{V_{DC,in}} \tag{2.27}$$

2.2 Resonant Inductor Design

For the simple LC series resonant system, the tank inductance can simply be calculated from eq. (2.28).

$$L_{tank} = \frac{1}{(2\pi f_{res})^2 C_{tank}} \tag{2.28}$$

For the 1.7MHz CPT system, the two series resonant inductors are both 27µH. These custom ferrite inductors were wound onto a single quasi-distributed air gap core [132]. The design for this inductor is taken from [66]. At resonance, the voltages across the tank inductance and coupler capacitance are equal in magnitude and 180 degrees phase shifted according to eq. (2.29). Therefore, the tank inductors must be rated for the same $1500V_{pk}$ as the coupler.. Teflon insulation was used for high voltage isolation on the 18AWG silver-plated copper wire.

$$V = \left| \frac{-j}{\omega C} i_{tank} \right| = |j\omega L i_{tank}| \tag{2.29}$$

Using simplified equations, a 4x increase in frequency to 6.78MHz means the inductor size will be reduced by $\approx \frac{1}{16}$ from eq. (2.28). Given the cost of custom ferrite pieces, the smaller inductors are made using the same ferrite cores as in [132]. For a 1.5kW target and assuming $9.6A_{pk}$ or $6.8A_{rms}$ from Figure 2.3, the inductor design also needs to supply at least 3.7kVAR and withstand $777V_{pk}$.

Another consideration for the inductor design is the skin effect. As the frequency increases, the current is pushed to conduct on the outer edge. This effect decreases the available conducting cross sectional area. Equation (2.30) describes the skin depth of a conductor:

$$\delta = \sqrt{\frac{\rho}{\pi f \mu_r \mu_o}} \tag{2.30}$$

where ρ is the resistivity and μ_r is the relative permeability of the material, and $\mu_o = 4\pi * 10^{-7}$ is the permeability of free space. The skin depth is defined as the point where the current density is reduced to $\approx 37\%$ of its peak at the conductor's edge. If all current is assumed to flow through the skin depth of a conductor, quadrupling the system frequency from 1.7MHz to 6.78MHz effectively doubles the system equivalent series resistance (ESR) loss in the copper wire connections.

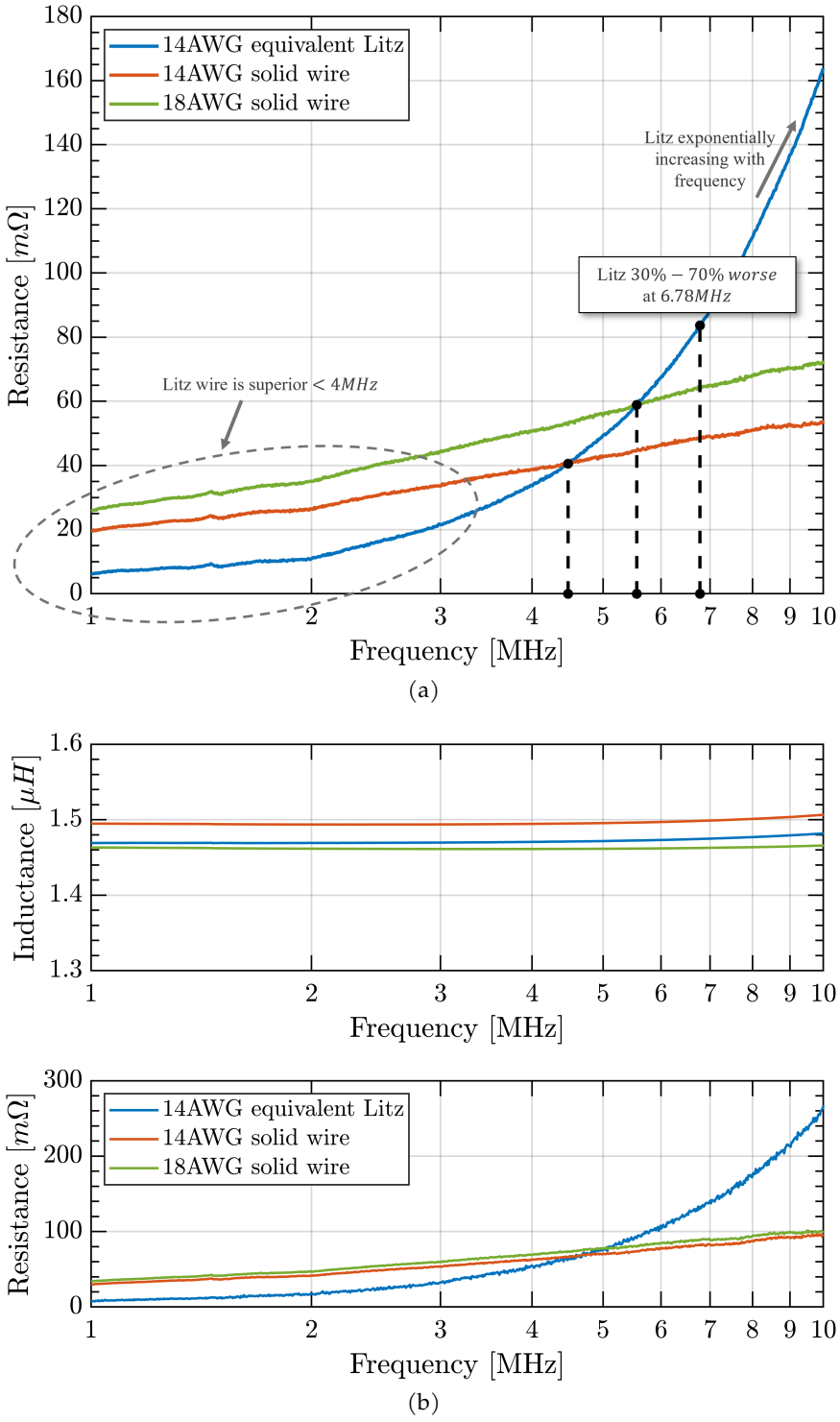

Figure 2.7: (a) Comparison of equal lengths of solid 18AWG silver-plated copper wire, solid 14AWG copper wire, and 14AWG-equivalent Litz wire with individually insulated 48AWG strands. (b) Comparison of three inductors wound with 14 AWG and 18 AWG solid wire, and 14 AWG-equivalent Litz wire.

It can be helpful to use Litz wire to reduce the equivalent resistance of the tank system at high frequencies [133]. Litz wire is made of small, individually insulated wires that are transposed within a bundle so that all wires experience equal flux from all other wires. However, each individual wire in the bundle still experiences the skin effect. For copper, the skin depth at 6.78MHz is approximately one thousandth of an inch, or 25μm. To account for the skin depth, an equivalent 14 AWG Litz wire with 2700 48-gauge (30.5μm diameter) individually insulated wires is tested for use in all connections and series inductors. 48-gauge Litz wire is currently the smallest commercially available strand size, but is only recommended in applications up to 2.8MHz [134].

In order to evaluate the Litz wire, Figure 2.7a compares the resistances of three equal $\approx$ 0.5m lengths of wire. The wires are measured as half-loops of wire in the impedance analyze. The previously used 18AWG silver-plated solid copper wire is compared with the 14AWG-equivalent Litz wire described above and 14AWG solid copper wire. At frequencies below four megahertz the Litz wire is superior and is up to 2x and 3x better than the 14AWG and 18AWG solid wire, respectively. However, the solid wire trends are mostly linear over this frequency range while the Litz wire resistance exponentially increases. The cross-over points where the solid wire has lower resistance are at $\approx$4.5MHz and $\approx$5.5MHz. By the 6.78MHz point, the Litz wire is 30-70% worse than the solid wire.

It is known that the effectiveness of Litz wire diminishes in the megahertz range [133]. With many small diameter wires bundled together, the wire capacitance can be significant. Additionally, eddy current losses (proportional to f^2) are induced in the wire that can negate any benefits from the Litz wire. It is possible that 50AWG or 52AWG Litz wire bundles would perform better at 6.78MHz, but these are not commercially available standard sizes.

This effect is also observed for the individual inductors. Figure 2.7b compares the same three versions of wire at the same length, now as two-turn inductors. Core loss is now included in resistance value as well as proximity losses between the two turns. The inductances are similar among the three types of wire, but again the Litz wire has a significantly higher resistance at 6.78MHz than the solid wire. Figure 2.8 gives examples of the inductors wound with the original 18AWG wire, and the 14AWG-equivalent Litz wire. In order to achieve the same voltage standoff rating as the blue Teflon insulation, Kapton tape is wound around the Litz wire and 14AWG solid wire before being wound around the core.

(a) (b)

Figure 2.8: Resonant inductors for the 6.78MHz resonant tank made with (a) 18 AWG solid copper wire, and (b) 14 AWG-equivalent Litz wire

2.3 High Frequency Inverter Design

The inverter in this resonant system is a class-D converter with high switch utilization [95, 135]. Ideally, the inverter switches at the resonant frequency of the tank, 6.78MHz, with a 50% duty cycle. At megahertz switching frequencies, wide-band gap (WBG) switches are used. Gallium nitride (GaN) devices are chosen over silicon carbide (SiC) as GaN HEMT switches typically have more than an order of magnitude lower gate charge than their SiC counterparts. This significantly reduces the power necessary to drive the switch as the power scales with frequency according to eq. (2.31).

$$P_{drive} = Q_g v_{gs} f_{sw} = C_{iss} v_{gs}^2 f_{sw} \tag{2.31}$$

Additionally, GaN HEMT devices have the anti-parallel diode functionality without an explicit diode present. This eliminates the loss associate with diode free-wheeling. Although SiC MOSFETs have lower output capacitance across the drain-to-source, the loss associated with this capacitance only becomes an issue in the 10's megahertz range [136, 137]. The GS66508T GaN Systems E-HEMT top-side cooled switch is chosen with 650V voltage blocking, 50mΩ on-state resistance, and a gate charge of 6.1nC.

The gate drive integrated circuit (IC) chip is also chosen specifically for megahertz frequencies and GaN devices. GaN HEMT switches can have faster turn-on and turn-off speeds (slew rates)

than SiC MOSFETs and thus their driving ICs must have higher common-mode transient immunity (CMTI). The isolated gate drive IC from Silicon Labs, SI8271, is specifically designed for GaN devices and short deadtimes with CMTI $> 350\frac{V}{ns}$.

Each switch in the full-bridge inverter is separately isolated for driving the high-side and maintaining an identical layout for each switch. In this design, a 5V isolated DCDC converter from RECOM, RHV2-0505S/R20, is used with a low isolation capacitance of 4pF. The low isolation capacitance is necessary to prevent high frequency content and voltage spikes coupling back to the low-voltage, non-isolated side of the inverter and affecting the control signal. Additionally, a common mode choke is added to the input of the DCDC converter to remove high frequency content.

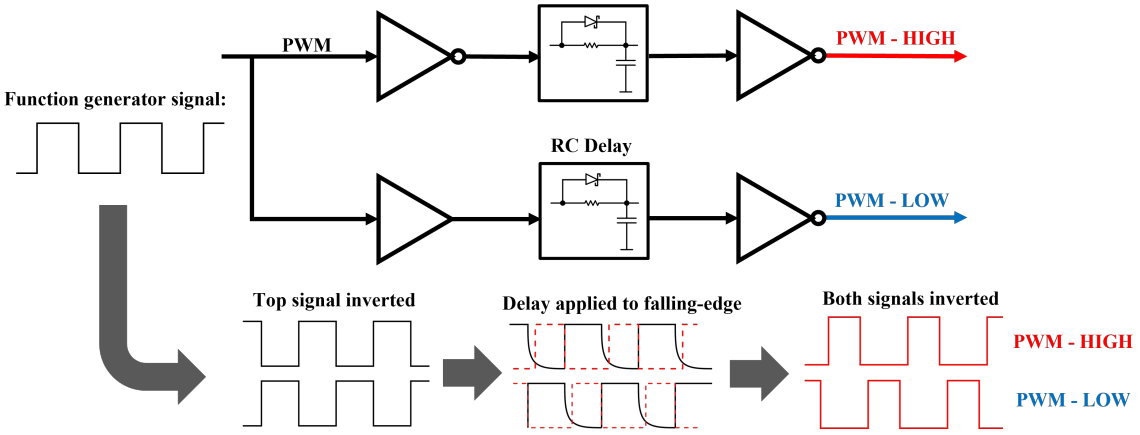

Figure 2.9: Block diagram of the circuity to produce two complementary signals with deadtime from one reference square wave.

The inverter does not have a microcontroller for control. Instead, a single square wave signal from a waveform generator is used for the gate drive control signal. As shown in Figure 2.9, analog PWM circuitry splits the single square wave signal into two complementary signals with a specified deadtime using Schmitt trigger inverters and an RC delay. The added non-inverting buffer stage is necessary to match the propagation delay for all the ICs to maintain consistent dead time. The propagation delay for these devices is in the range of 4-5ns and therefore it is critical they are identical. As will be discussed in section 3.2, the deadtime is set as low as 15ns.

The deadtime between switches in the half-bridge must be set such that it is a shorter period than the free-wheeling diode conduction action of the switches. Figure 2.10 shows that the choice of deadtime has consequences for the full system design. In this plot, the switching frequency is

set to 6.78MHz for all conditions. The simple LC resonant frequency of the tank is adjusted using eq. (2.19) as the load resistance and dead time is varied. As the deadtime and/or load resistance increases, the ratio of switching frequency to LC resonant frequency must increase. It is important to note that even without deadtime, the interaction from the equivalent diode capacitance means that the switching frequency must be above resonance. Knowing the desired switching frequency of 6.78MHz and achievable dead time for ZVS, the appropriate target for the resonant frequency can be determined.

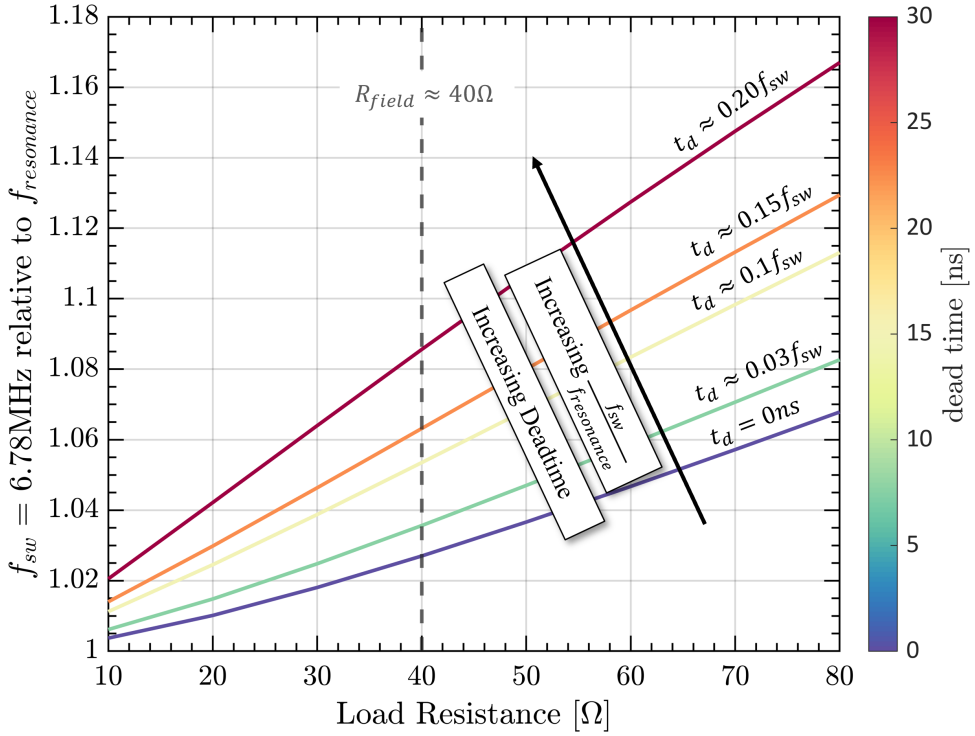

Figure 2.10: Plot showing how the resonant tank frequency changes to maintain minimum zero voltage switching (ZVS) conditions in terms of the load resistance and inverter deadtime. The inverter switching frequency is held constant at 6.78MHz.

Soft switching is employed to reduce the switching loss component in converters and to reduce the switch voltage overshoot and ringing. In zero current switching (ZCS), Figure 2.11a, the inverter output current leads the voltage when the switching frequency is below the tank resonance and thus creates a capacitive load for the inverter. The switches turn off when the current is zero, but still have a hard turn on that creates a voltage spike. In zero voltage switching (ZVS), Figure 2.11b, the inverter output current lags the voltage when the switching frequency is above the tank resonance and the load is inductive. In this case, the switch turns on when the voltage is zero and has a hard

turn-off that can create a voltage spike. The turn-off voltage spike is often lessened by an additional output capacitor across the drain-source of the switch denoted as C_s in Figure 2.2b. The output capacitance of the GaN switch, C_{oss}, may be enough or an external capacitor can be added as a snubber. During testing, it is determined that the capacitance of the GaN switch is sufficient.

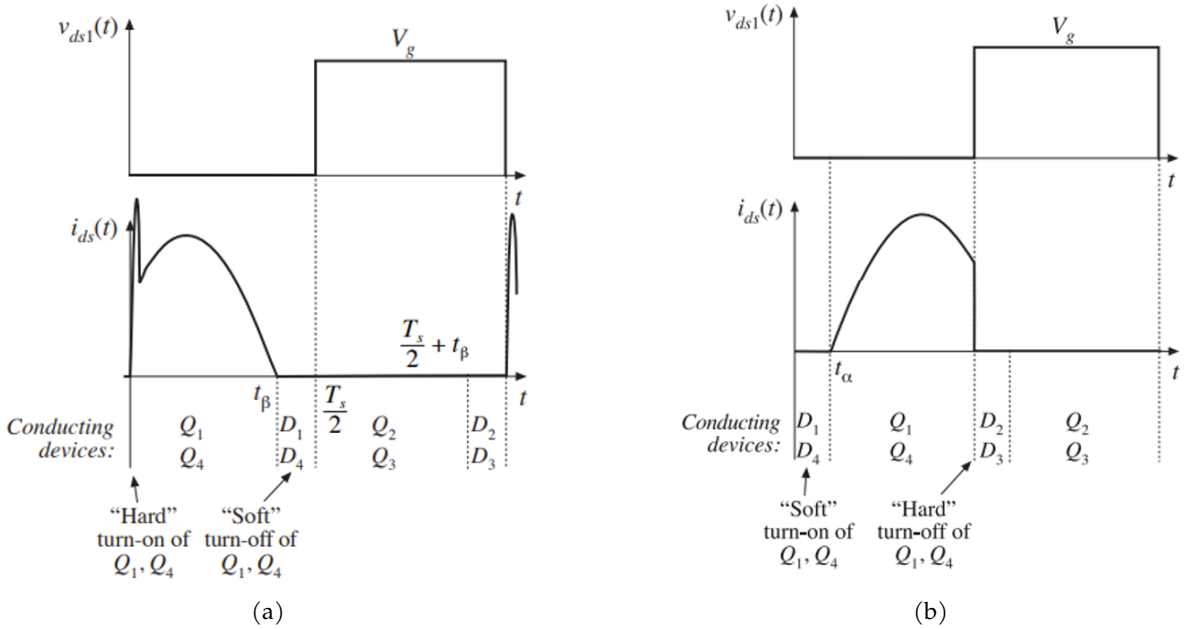

Figure 2.11: (a) Zero current switching and (c) zero voltage switching waveform diagrams taken from [6]. Q and D refer to switch and its body diode. Q1 & Q2 are the top and bottom switches of one half-bridge, and Q3 & Q4 are the top and bottom switches of the second half-bridge.

The inverter PCB layout is designed to reduce parasitic inductance in the half-bridge and gate loops by reducing trace lengths and loop areas. At megahertz switching frequencies, the effects of parasitic inductances and capacitances can never be eliminated, only mitigated. The input to the inverter should be a voltage stiff DC source; however, parasitic inductance in the traces causes noise on the line. In order to reduce the parasitic inductance, an additional DC link capacitor is added as close as possible across each half-bridge and the loop area is kept as small as possible.

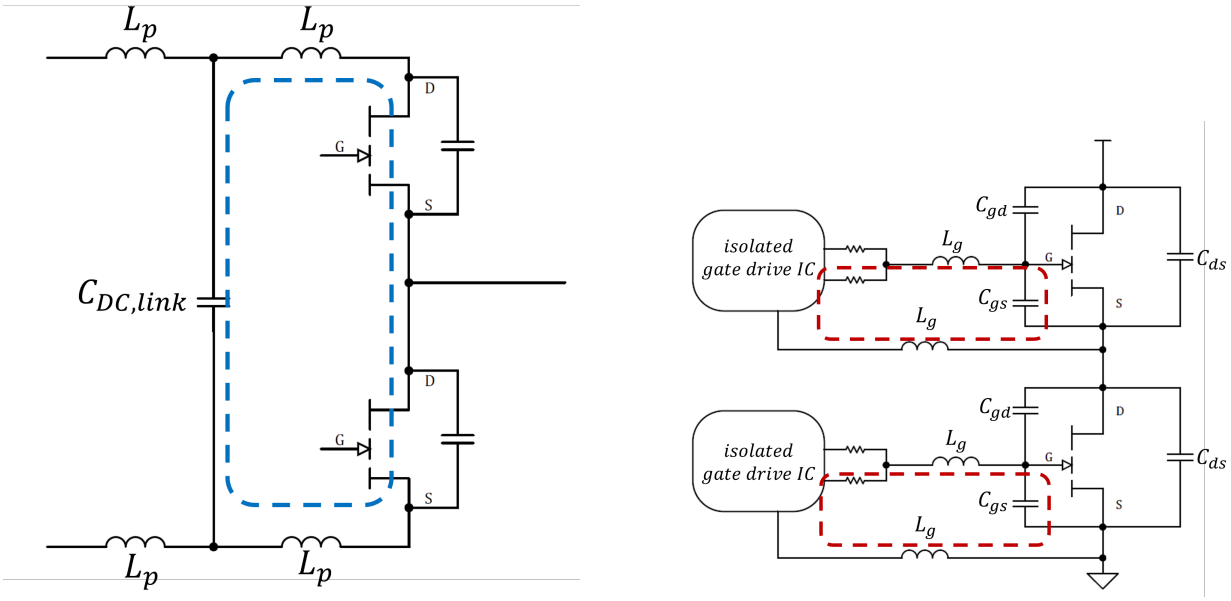

Figure 2.12: (a) Diagram of a single half-bridge emphasizing the DC-link loop with parasitic inductances. (b) Diagram showing the commutation loop inductance of each gate drive in a half-bridge.

Figure 2.12 shows the two main pathways with problematic stray inductance: the half-bridge loop and the gate loop. The half-bridge loop in Figure 2.12a necessarily has some stray inductance between the DC link capacitor and the two GaN switches resulting from the PCB trace lengths. Figure 2.13 compares the DC-link placement layout between the two prototypes. In the first prototype surface mount DC link capacitors are placed on the top side of the board. The second prototype shows that the DC filter capacitors are placed on the bottom of the board so that the loop only has the thickness of the board instead of being placed around the output phase connector. Both layouts are imported to Ansys Q3D for parasitic loop inductance analysis.

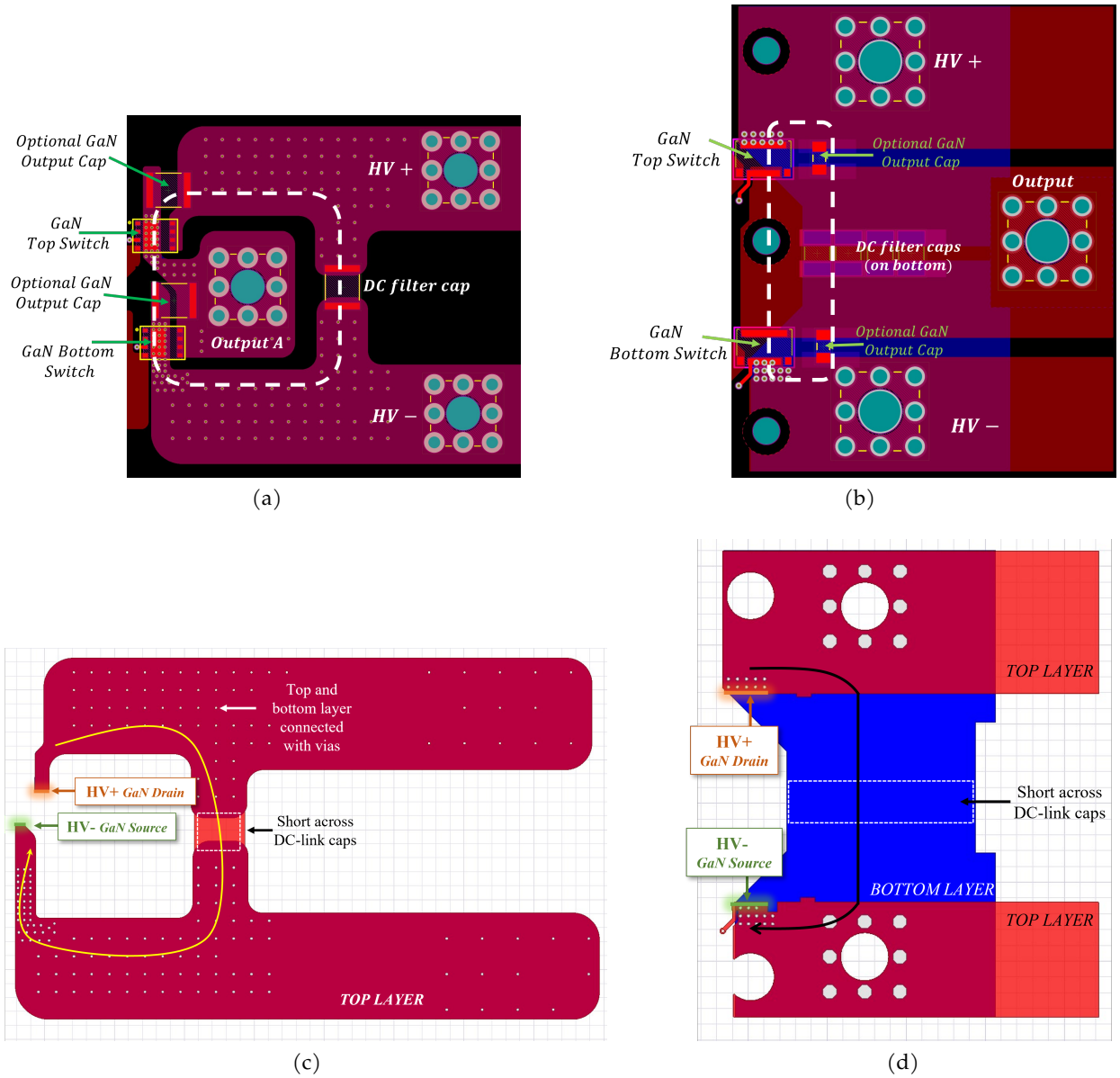

Figure 2.13: Half-bridge PCB layout diagrams in Altium for (a) top-side (1^{st} prototype), and (b) bottom-side (2^{nd} prototype) placements of DC-link capacitors. The corresponding layouts for (c) top-side and (d) bottom-side capacitor placements are added to Ansys Q3D to calculate the half-bridge parasitic loop inductances.

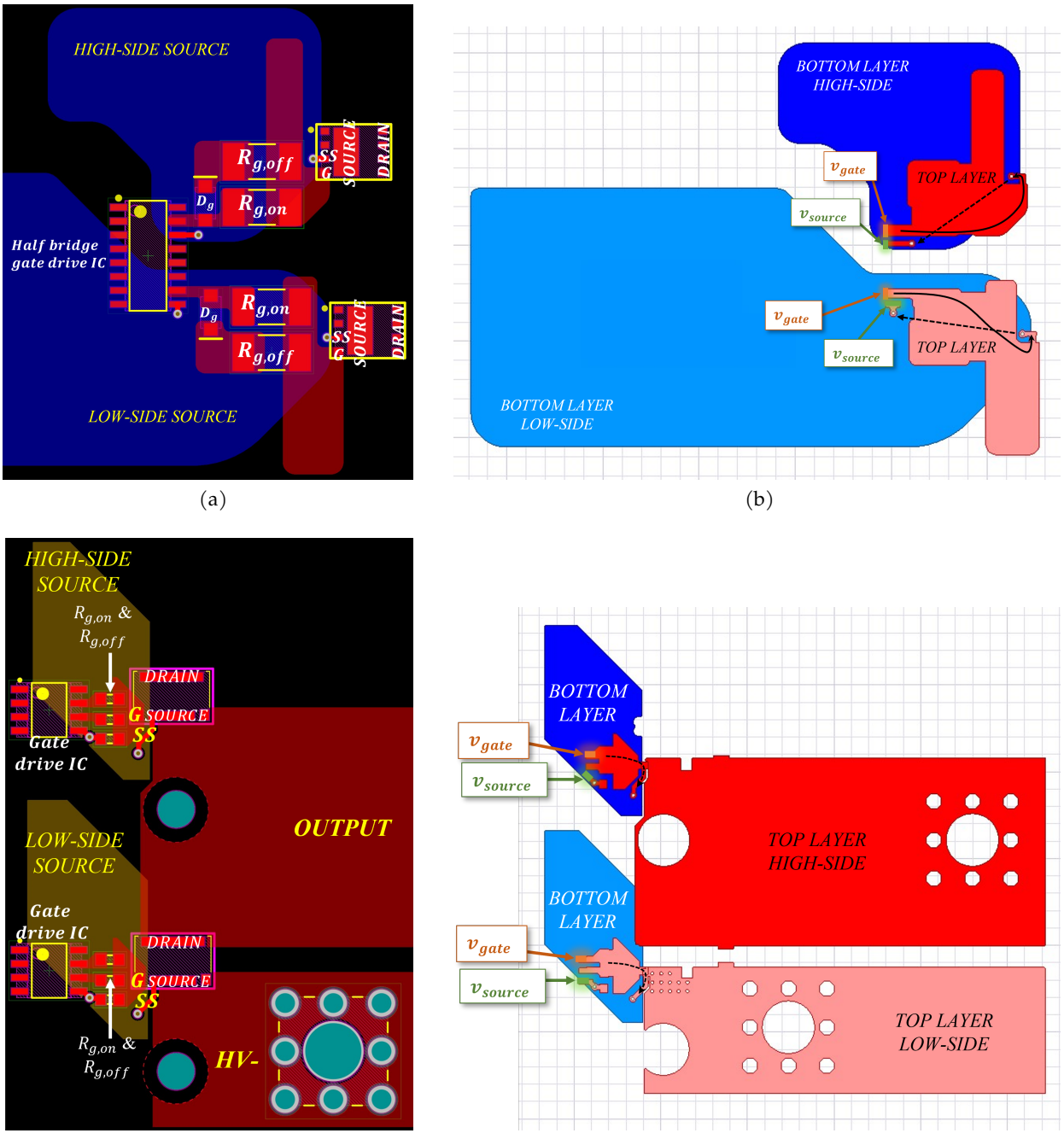

Figure 2.14: Gate-loop PCB layout diagrams in Altium for the (a) 1st prototype and (b) corresponding Ansys Q3D simulation, as well as the (c) 2nd prototype and (d) its corresponding FEA simulation.

Figure 2.12b shows the DC-link half-bridge and gate loop diagrams of the inverter with parasitic inductances. The first prototype utilized a gate-drive IC with a single gate signal output. Separate turn-on and turn-off paths were implemented with the use of a diode and an additional TVS diode

was added across the gate-to-source to limit the overshoot from the high slew rates of the GaN switch. The second prototype emphasized reducing the complexity, part count, and parasitic loop inductances. Individually isolated gate drive ICs were used that had separate turn-on and turn-off pins and only small gate resistors were used in the loop. In Figure 2.14 the gate drive loops for both prototypes are shown. Stray inductance is reduced by keeping all traces as short as possible and creating a separate low inductance return path from the main GaN source pin. GaN switches have distinctly low gate charge, in the single nanocoulombs range, resulting in a low gate driving power that make them ideal for megahertz switching frequencies. Additionally, a gate drive IC is chosen with the capability to supply the full driving current, up to 4A, and have dedicated output high and output low pins. In this way, there is no additional need for additional driving circuitry, such as a push-pull configuration or additional diodes required to create two separate outputs from one output pin. The reduction in complexity and part count is at the crux of reducing stray inductance in this gate loop path.

Table 2.1 summarizes the parasitic inductance FEA results from Ansys Q3D. For both prototypes the gate loop inductances are comparable, but the biggest improvement comes from the half-bridge DC-link capacitor loop. Placing the capacitors on the bottom of the board below the GaN switches results in a 3x reduction in loop inductance. This improvement reduces the voltage ripple and overshoot present on the inverter output voltage waveforms.

	1^{st} Prototype	2^{nd} Prototype
Gate Loop Inductances	5.3nH	4.4nH
Half-Bridge Loop Inductance	45.5nH	14.2nH

Table 2.1: Ansys Q3D parasitic inductance FEA results for the half-bridge and gate drive loops as shown in Figure 2.12

The inverter board is shown in Figure 2.15. Two green connectors provide 5V input power and the reference PWM signal from a function generator. The blocks on the bottom of the board are the individual isolated DCDC converters. Each switch has a solid copper block soldered to its top, source, thermal pad with a heatsink and fan attached across each half-bridge of set of switches. Sheets of Kapton isolate the two thermal pads from each other. The inverter manufacturing process is further described in section 3.2.

The switching loss is assumed to be negligible with the resulting power losses summarized in

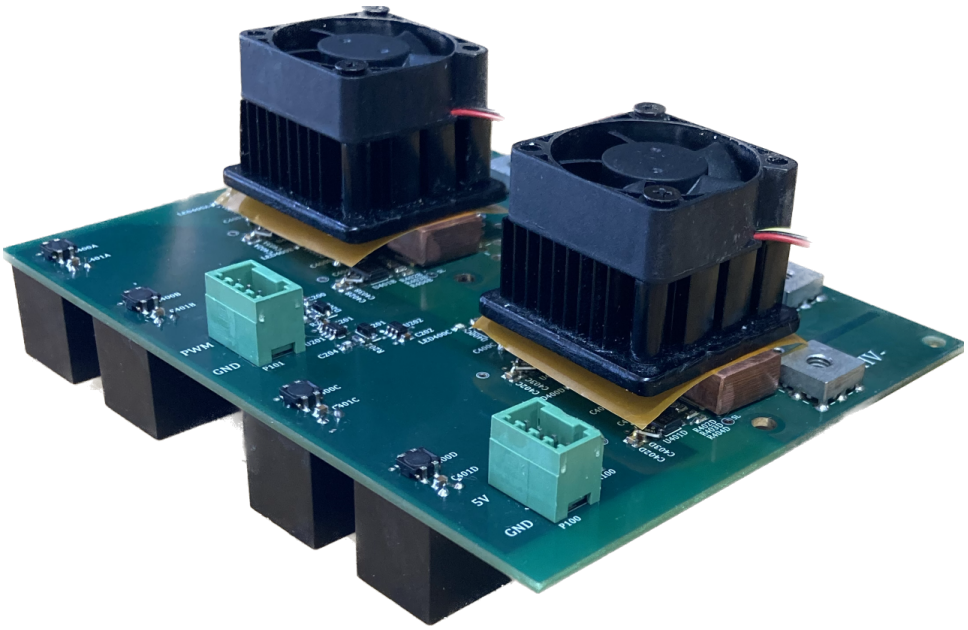

Figure 2.15: Picture of the final prototype of the 6.78MHz full-bridge inverter.

eq. (2.32). Specifically, the output capacitance charge quantity, E_{Coss} comes from [138] where the same GaN device used here was characterized.

$$\begin{aligned} P_{loss,inverter} &= P_{conduction} + P_{Coss} \\ P_{loss,inverter} &= 4I_{rms,GaN}^2 R_{ds,on} + 4E_{Coss} f_{sw} \end{aligned} \tag{2.32}$$

where

$$E_{Coss} = \left(0.049 \left(\frac{f_{sw}}{10^6}\right)^{0.2} V_{in}^{1.16}\right) 10^{-9} \tag{2.33}$$

$$I_{rms,GaN} = \frac{I_{tank,pk}}{2} \tag{2.34}$$

2.4 High Frequency Rectifier Design

2.4.1 Voltage Stiff Design

A passive full-bridge rectifier is necessary to convert the AC coupler power to DC for exciting the field windings. This rectifier is categorized as a voltage stiff design with a large capacitance on the

output to filter high frequency harmonics from the DC voltage. The rotating rectifier is made to fit in the center radius of the rotating CPC board. Figure 2.16 shows the diodes on the inside of the rotating coupler PCB. For the SiC Schottky diodes, the equivalent capacitance is nonlinear as a function of the reverse voltage applied to the diode. 1200V SiC schottky diodes, IDM08G120C5, from Infineon are chosen for the full-bridge rectifier as they have negligible reverse recovery loss and withstand high $\frac{dv}{dt}$. The rectifier input power in eq. (2.35) is a function of the power factor previously discussed in section subsection 2.1.1.

$$P_{rectifier,in} = V_{rectifier,rms} I_{tank,rms} \cos(\varphi) \tag{2.35}$$

The main loss mechanism for the diodes comes from the conduction loss.

$$P_{rectifier,conduction} = 4 v_f i_{avg,diode} \tag{2.36}$$

where

$$i_{diode,avg} = \frac{I_{tank,pk}}{\pi} \tag{2.37}$$

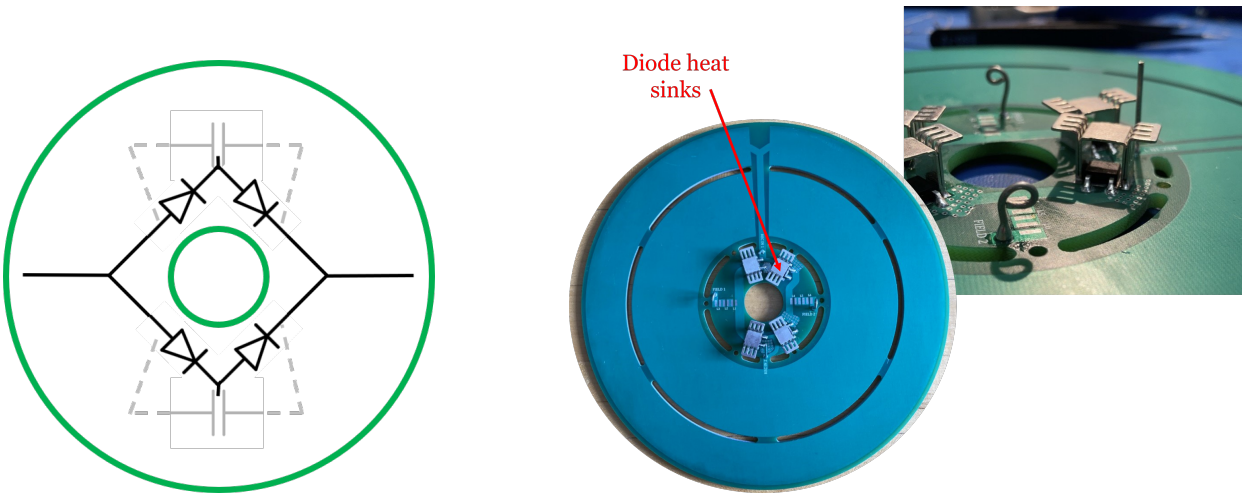

(a) (b)

Figure 2.16: (a) Diagram of the rectifier layout and (b) the assembled rectifier PCB with heatsinks for each diode.

The diodes also have a nonlinear equivalent capacitance of 50pF at 100V down to 26pF at

400V. At megahertz frequencies, the equivalent diode capacitance contributes significantly to the performance of the system as it is on the same order of magnitude as the main coupling capacitance. With the addition of the equivalent diode capacitance, the resonant system changes from a primarily LC series resonant to an LCC resonant system. Different methods are employed to compensate for this capacitance. One method involves adding an inductor, L_e, across the input of the rectifier to create a parallel resonance with the diode capacitance that is sized to resonate at the same frequency of the series LC tank [139]. The inductor value is set as a power factor correction term for C_e in the rectifier. Essentially, the equivalent diode capacitance is decoupled from the resonant tank. Figure 2.17 shows the same series resonant system with the addition of the power factor correcting inductor in parallel to the input of the rectifier. Adding this compensation inductor can improve the power factor, $\cos(\varphi)$, and efficiency of the rectifier, but also adds an additional large and potentially lossy component to the high frequency rotating side of the system.

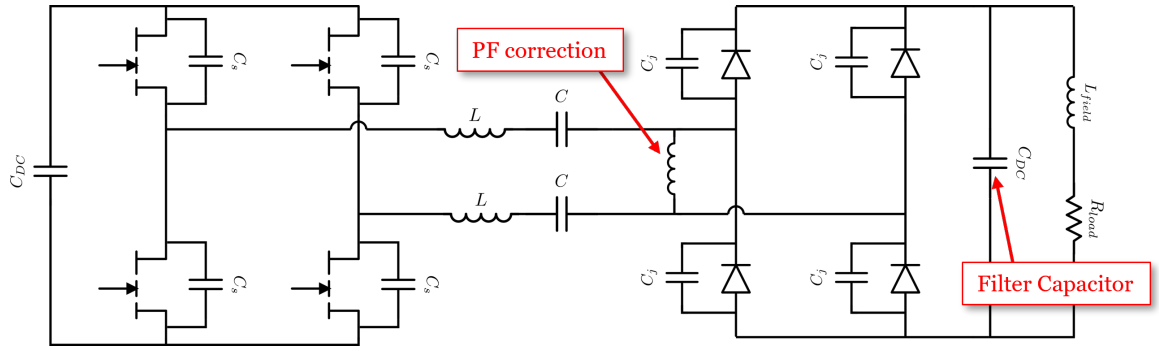

Figure 2.17: Diagram of the full CPT system with the voltage-stiff rectifier featuring a power factor correcting inductor in parallel with the input to the rectifier.

Figure 2.18 looks at the resonance of the full resonant converter system with a voltage-stiff rectifier under a few different conditions. The swept frequency is normalized to the simplified resonance of just the main LC tank. The black curve shows the baseline condition of a simple RLC series-resonant system (not including C_e or L_e). Figure 2.18a specifically shows the equivalent circuit, equation and plots for the input impedance as the rectifier capacitance, C_e, changes. As C_e increases the full system resonant frequency increases, as well. The value of C_e changes with reverse voltage; therefore, as the output power to the field winding changes, so too will the value of C_e. Additionally, the system equivalent load resistance decreases as the rectifier capacitance increases.

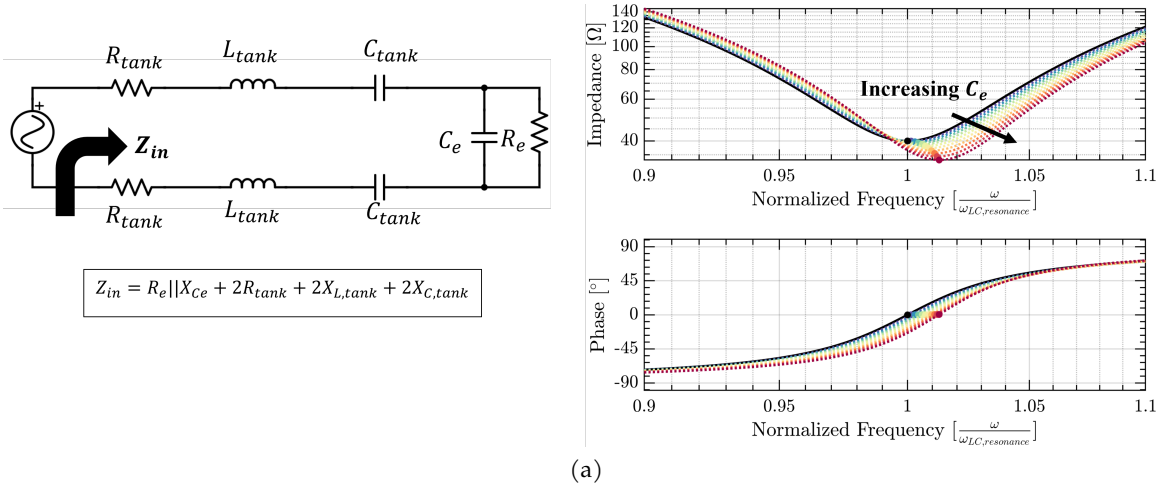

(a)

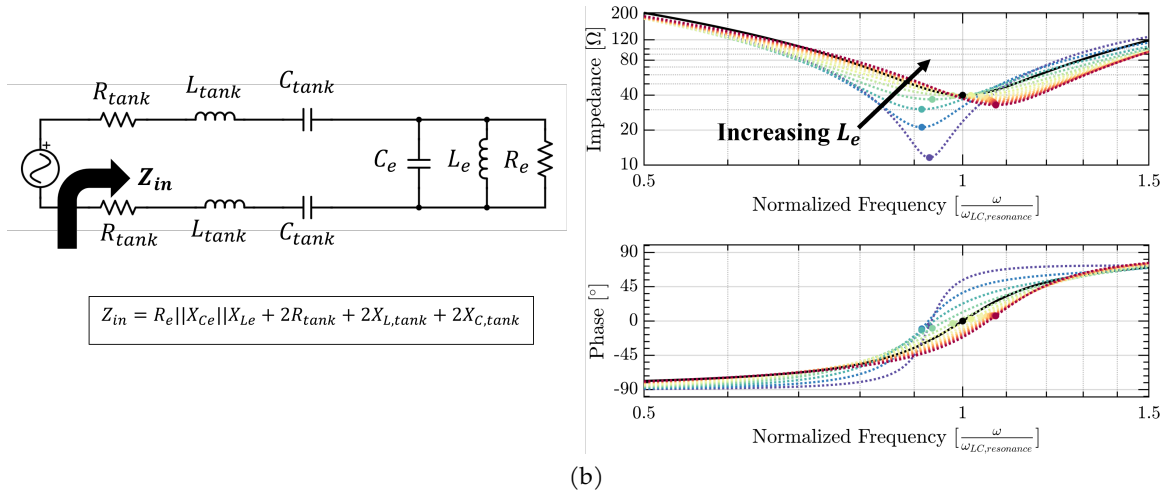

(b)

Figure 2.18: Input impedance and phase calculations of the equivalent system from Figure 2.5b looking at the sensitivity of components in the voltage-stiff rectifier. In (a) the equivalent rectifier capacitance, C_e is varied and in (b) the compensation inductance, L_e is varied showing general trends in the system resonance

Figure 2.18b considers the addition of the parallel power factor correcting inductor, L_e. This inductance is a fixed value for all power operating conditions of the system. As the value of L_e cannot change as the output power changes, the plot shows the case when there is an error in L_e relative to the resonance point with C_e. As L_e increases, so too does the resonance point. When L_e is too small to decouple C_e completely, the overall system resonant point decreases.

For the actual rectifier layout, there are more considerations than just the diode capacitance. Any small traces between the diodes creates parasitic inductances that can resonate with the diode capacitance as shown in Figure 2.19a. Typically, the traces are on the order of nH's of inductance

that create high frequency ripples in the 10's of megahertz range. Ideally, filter capacitors would be placed as close as possible across each pair of diodes but any short trace will have some parasitic inductance effect. It is not possible to filter out all harmonics, only to mitigate their effects.

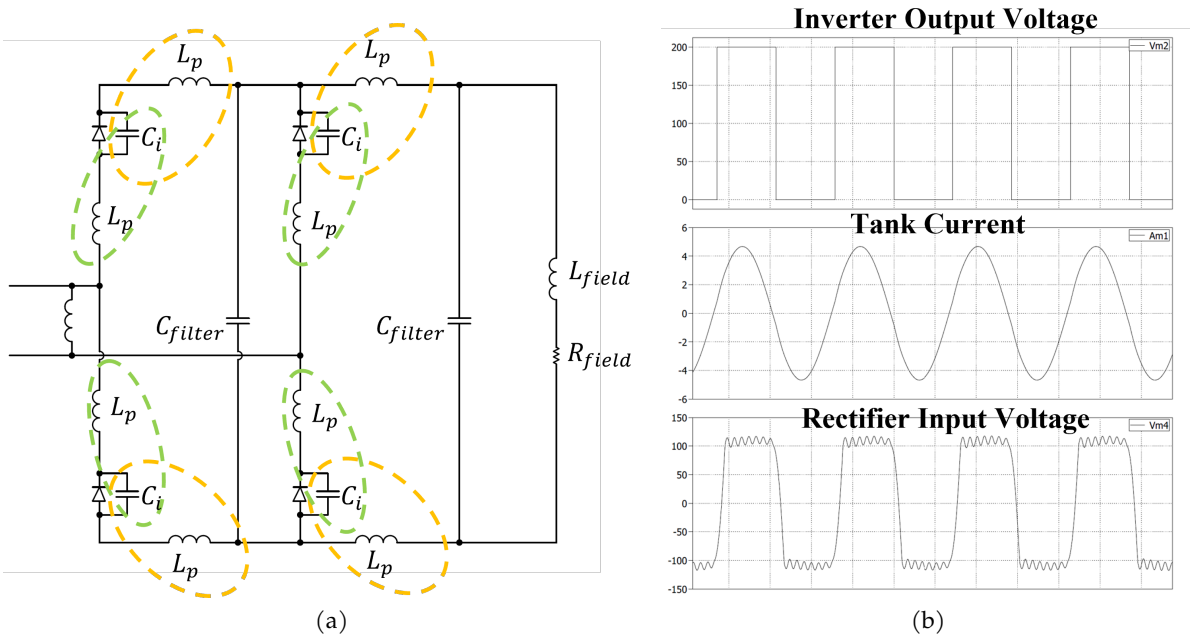

(a) (b)

Figure 2.19: (a) Voltage-stiff rectifier diagram highlighting the parasitic inductances that could be creating high-frequency harmonic with the diode equivalent capacitance. (b) LTspice simulation results showing high-frequency rippled on the rectifier input voltage from the addition of parasitic inductance in the rectifier circuit.

In fig. 2.19b, the circuit is simulated using LTspice to look at the effect of the stray inductance. As previously stated, in an ideal series resonant converter without diode capacitance and parasitic components, at the tank resonance the input voltage of the rectifier should be identical to the output voltage of the inverter. In the bottom plot there is a high frequency ripple on the rectifier input voltage. Negligible parasitic resistance was added into the simulation so that the ripple is under damped instead of displaying the familiar damped response seen in practice. The rectifier input voltage plot also shows that the diode equivalent capacitance turns the waveform from a square wave to a trapezoidal waveform.

The main constraint for the rectifier PCB layout is the small space allotted in the center radius of the capacitive coupler boards. The donut shape does not lend itself to a tight, low parasitic layout as shown in Figure 2.16 where the diodes are stacked on top and the capacitors on the bottom. To help

mitigate thermal issues, surface mount heatsinks are placed around each diode and compressed air is blown across the top.

2.4.2 Current Stiff Design

Another rectifier design approach utilizes the inherent input capacitance to reduce diode switching losses as a result of discontinuous output current. In contrast with voltage stiff rectifiers that have a main output filter capacitor, current stiff rectifiers have large output filter inductors to ensure continuous conduction mode for each passive diode as described in [7]. A large DC filter inductance is added before the output filter capacitor to create a current-stiff rectifier output. It is still necessary to have a capacitive filter after the inductor in order to filter the output voltage. A diagram of this system is shown in Figure 2.20 where L_{DC} and C_{DC} are the output filter components and L_p, C_p, and R_p are parasitic components useful for simulation. In megahertz passive rectifiers, the parasitic components cause distortion in the waveforms that result in poor efficiency and discontinuous output currents. Specifically, discontinuous current through the diode during a conduction period leads to unnecessary diode switching and loss.

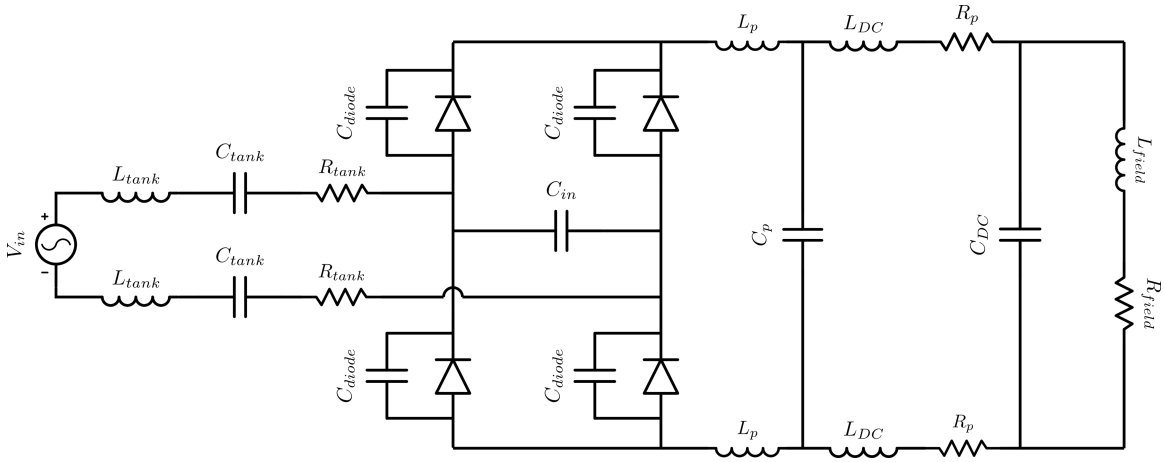

Figure 2.20: Diagram of current stiff rectifier with DC filter inductors post-rectifier along with parasitic components [7].

The current stiff system analogously requires a parallel capacitor, or commutation capacitor, C_{in} on the terminal inputs to the rectifier to filter out higher frequency harmonics in the input voltage waveform. The values for both the filter inductor and input commutation capacitor are largely determined via simulations and experimentation with the full CPC system.

Simulations using PLECS sweep different parameter variables in the current-stiff rectifier design. Figure 2.21 investigates the effect of the variable L_{DC} while C_{in} is kept constant. Specifically, the input rectifier voltage and rectifier diode current are plotted against L_{DC}, which has been swept by several orders of magnitude. In the diode current plot, values of L_{DC} below 1µH clearly have many oscillations in this discontinuous condition that contribute to large amounts of loss for each diode. It is desirable to have a continuous output current to reduce diode loss. In the voltage plot, as the inductance increases, so too does the sinusoidal shape of the waveforms. The ideal waveform for a current-stiff rectifier is a sinusoidal input voltage. Increasing the inductance above the continuous conduction mode produces diminishing returns.

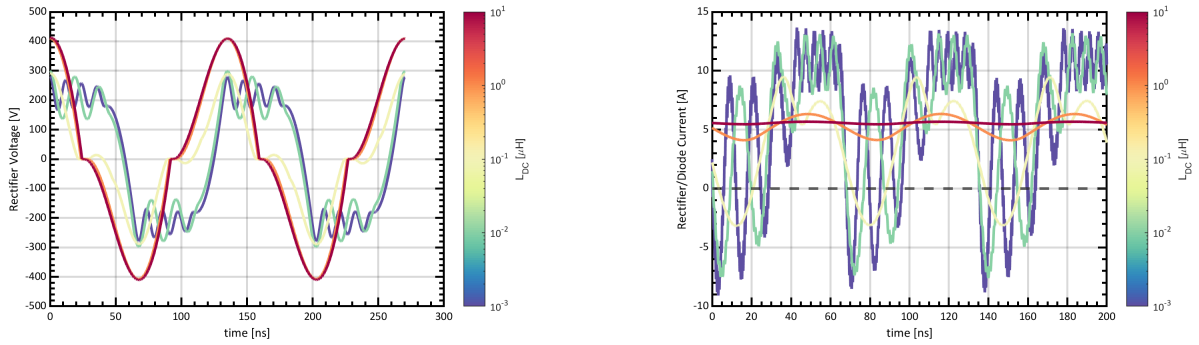

(a) (b)

Figure 2.21: PLECS simulations sweeping L_{DC} in the full current-stiff rectifier system against (a) input rectifier voltage, and (b) output rectifier current.

The inherent parasitic inductance of the rectifier traces with the equivalent diode capacitance creates high frequency ringing on the voltage waveforms. The current-stiff rectifier is preferable to limit the voltage overshoot on the rectifier voltage waveforms and ultimately lower the voltage utilization of the diodes.

2.5 Example 6.78MHz CPT System Design Calculations

This section walks through the analysis developed in this chapter for a single power point of the 6.78MHz CPT system. This will give an estimate of the efficiency and expected loss from each section at a specific operating point of 1.5kW. The testing results in chapter 3 will discuss how this analysis compares to the real system and also where it falls short. Table 2.2 lists the known system

design conditions and constraints.

Condition	Variable	System Value
Power Output	P_{out}	1500 W
Switching frequency	f_{sw}	6.78 MHz
Dead time	t_d	15 ns
Coupler capacitance	C	300 pF
Field resistance	R_{field}	40 Ω
System ESR	R_{tank}	1 Ω
Diode capacitance	C_j	50 pF
Diode Forward Voltage Drop (150°C)	v_f	2.25V
GaN HEMT on resistance (150°C)	$r_{ds,on}$	129mΩ

Table 2.2: CPT Example Circuit Parameters

Now to go through the main calculations from the equations:

Parameter	Variable	Equation Reference	Result	Unit
Deadtime angle	α	eq. (2.5)	37	°
Inverter power factor	$PF_{inverter}$	eq. (2.7)	0.95	
Equivalent rectifier+load resistance	R_e	eq. (2.12)	32	Ω
Equivalent rectifier capacitance	C_e	eq. (2.13)	242	pF
Resonant tank inductance	L	eq. (2.19)	2.06	μ H
Tank LC resonant frequency	f_res	eq. (2.1)	6.395	MHz
Field winding current	$I_{DC,out}$	eq. (2.3)	6.1	A
Rectifier power factor	$PF_{rectifier}$	eq. (2.22)	0.95	
Rectifier diode current	$I_{ave,diode}$	eq. (2.37)	3.3	A
Tank current	$I_{tank,pk}$	eq. (2.25)	10.38	A_{pk}
GaN switch current	$I_{GaN,RMS}$	eq. (2.34)	5.2	A_{RMS}
Input bus voltage	$V_{DC,in}$	eq. (2.8)	260	V
System voltage gain	v_{gain}	eq. (2.27)	0.94	$[\frac{V}{V}]$

Table 2.3: CPT example system calculation results.

In the above calculations the capacitive coupler is assumed to purely be two equivalent capacitances. In reality the coupler is a matrix of capacitances that will change the current magnitude and phase across the PCB boards.The loss from the rectifier diode switching is also not captured. Theoretically SiC have no reverse recovery loss so this is negligible. There will be some small amount of switching loss considering that the switching frequency is above the resonant frequency

Power	Variable	Result	Unit
Rectifier Conduction Loss	$P_{loss,rectifier}$	50.7	W
Tank ESR Loss	$P_{loss,ESR}$	53.8	W
Inverter Loss	$P_{loss,inverter}$	15.5	W
Total System Loss	$P_{loss,tot}$	120	W
Total System Efficiency	η_{system}	92.6	%

Table 2.4: CPT example calculated loss from each subsection and total system efficiency.

that is not captured in the above analysis. Figure 2.22 shows the individual loss components from Table 2.4. It is clear that the majority of the loss comes from the system ESR and the rectifier diodes. The biggest efficiency improvements come from reducing the system ESR and having excellent cooling for the rectifier. The hot forward voltage drop at 150°C is 2.25V compared to 1.65V at 25°C.

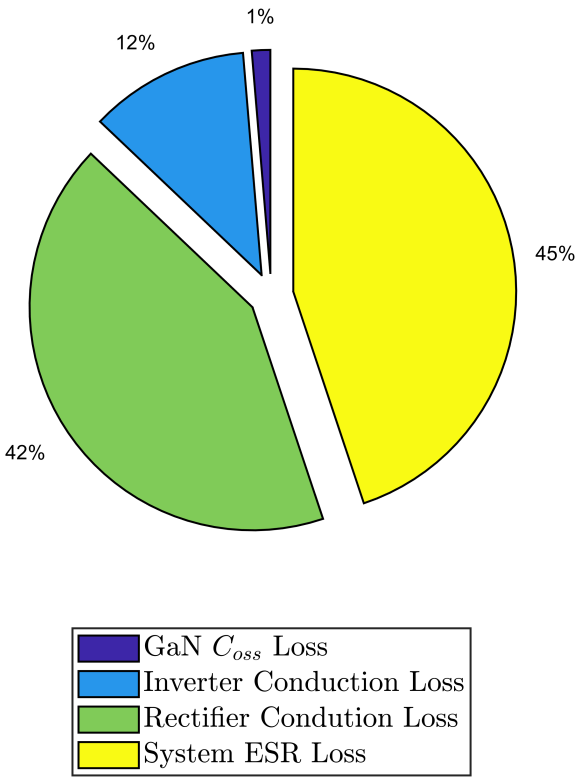

Figure 2.22: Pie chart of the estimated loss breakdown of the CPT system example calculations

2.6 Concluding Remarks

The motivation for improvements and redesign of the CPT system are rooted in the need to achieve higher output powers > 1kW by increasing the operating frequency. The scope of this work is not to redesign the capacitive coupler, but to optimize its performance through the surrounding power and compensation circuitry. This chapter has gone through the design assumptions and analytical calculations to optimize the high frequency soft-switching inverter, resonant tank, and rectifier subsystems. The following is a summary of the main design improvements:

- **4x increase in operating frequency from 1.7MHz to 6.78MHz**

This addresses issues #1 and #2 to reduce the resonant inductor size and eliminate the post-rectifier buck converter, respectively. A smaller inductor is needed to resonate at a higher frequency with the same coupling capacitance. Additionally, the current rating of the coupler is 4x higher with a 4x increase in frequency from the proportional amps/hertz rating. There is no longer a need for the buck converter impedance compensation.

Although the inverter from the 1.7MHz was not limiting the maximum output power of the system, it nonetheless was redesigned to manage parasitics and losses at a 4x higher frequency. One main issue at megahertz switching frequencies is that any stray inductance or capacitance can affect the performance and efficiency of the system significantly. This work has taken the approach to simplify and minimize the number of components creating compact circuit layouts to reduce trace lengths and loop areas and confirmed in FEA using Ansys Q3D.

- **Investigation of different rectifier topologies and compensation strategies to reduce the losses and diode voltage utilization.**

This addresses issue #3 to prevent thermal failure of the diodes on the rectifier board. It is clear that any small amount of stray inductance will create ringing in the voltage stiff rectifier design and stray trace inductance is inherent to any PCB layout. The current stiff rectifier design appears to be superior in that it prevents large overshoot or ringing from current spikes by placing a large inductor on the output. The goal is that the reduction of ringing on the rectifier will reduce the individual diode loss and mitigate thermal issues. The following chapter will expand on these designs to evaluate their potential for kilowatt-level wireless power transfer to field windings.

Chapter Three

Resonant System Testing

This chapter develops the platform testing protocol for evaluating the designs in chapter 2 and provides an overview of the current system capability in terms of output power and temperature handling. The following sections focus on testing the inverter, resonant tank, and rectifier sections separately to identify their successes and areas of future improvement. The capacitive power transfer system achieved a peak output power of 2.3kW with an efficiency of 88.5%. This a 3.4x power improvement over the previous 1.7MHz-based CPT design [84].

3.1 Overall System Description

Figure 3.1a shows a diagram of the full CPT system with the wound field synchronous rotor field winding as an RL load. The rotating rectifier rotor board design is described in further detail below, but the capacitive coupler system is shown in Figure 3.1b. The inverter and the tank inductors are contained together in a housing that holds a fan to force air over the inverter switch heat sinks. The two red and blue touch-safe connectors into the housing are for the low voltage 5V input to power the low voltage deadtime and square wave control circuitry. A common-mode choke is necessary on the input to the 5V isolated DCDC converter to prevent noise from coupling back through to the low-voltage side. This inverter is driven with a square-wave signal generator controlled by the user to set the inverter to operate at zero voltage switching. Likewise, the frequency is adjusted during testing to achieve the optimal efficiency as the system reaches thermal steady state and the field resistance changes. This setup is sufficient for bench testing where the boards do not rotate.

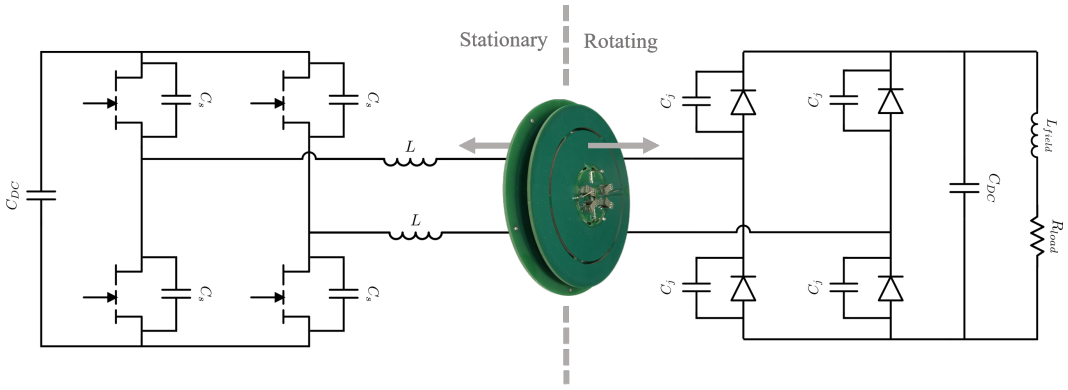

(a)

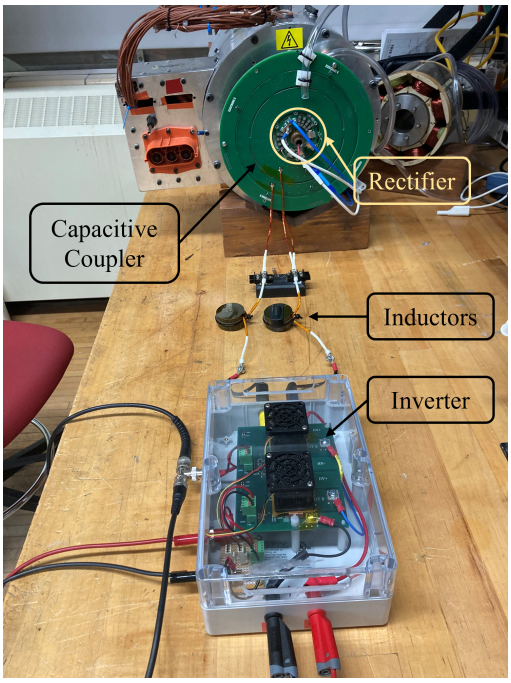

(b)

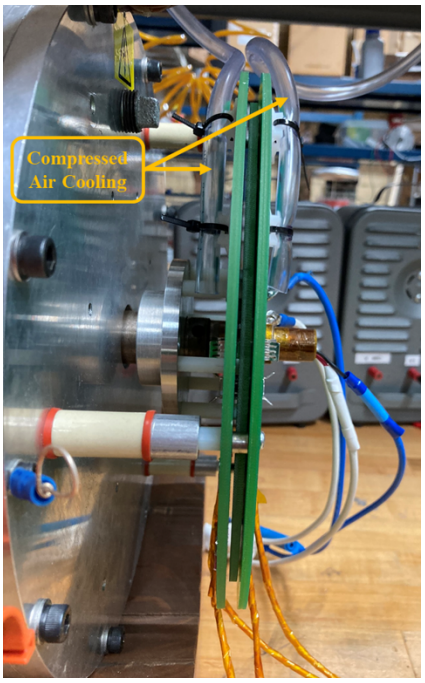

(c)

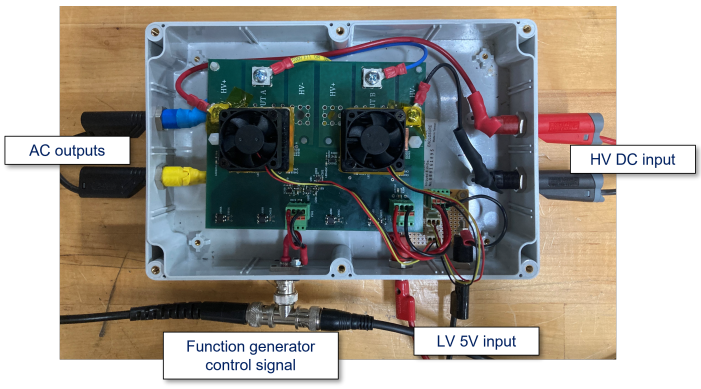

(d)

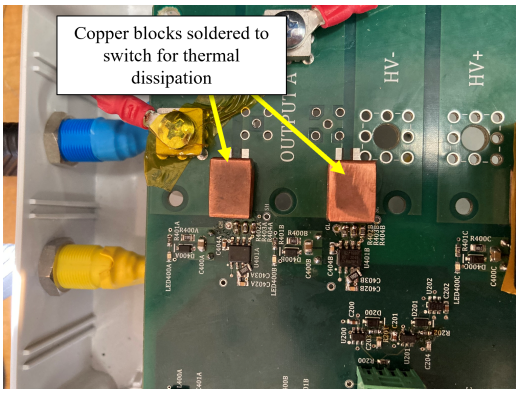

(e)

Figure 3.1: (a) Diagram of the CPC system along with pictures of (b) the overall CPC system, (c) the rectifier and resonant inductors, and (d) the tubes for compressed air to cool the rotating diodes

3.2 Inverter Testing

Figure 3.2 shows the top and bottom views of the final assembled inverter. The switches from GaN Systems (GS66508T) are top side cooled. The switches' top side thermal pads are connected to the source pin. In order to increase the thermal mass of each switch, copper blocks are soldered directly to the source thermal pad as shown in Figure 3.1e. The small blocks are cut out of 6.5mm thick copper stock to cover the full thermal pad. The inverter is first assembled and soldered with the switches by themselves, then solder paste is applied to the thermal pad and the copper blocks are added and baked in a reflow oven. The soldered connection provides a direct thermal connection without added thermal resistance from thermal paste or other insulating pads. Likewise, the copper blocks add thermal mass to reduce the rate of the GaN junction temperature rise.

An integrated fan and heatsink block meant for microcontroller cooling is placed across each half-bridge of switches. Since the copper blocks are electrically connected to the switch source, each switch has an isolation sheet between its thermal pad and the heatsink to keep the components electrically isolated from each other. The heatsink fans are powered from the same 5V power supply as the inverter controls.

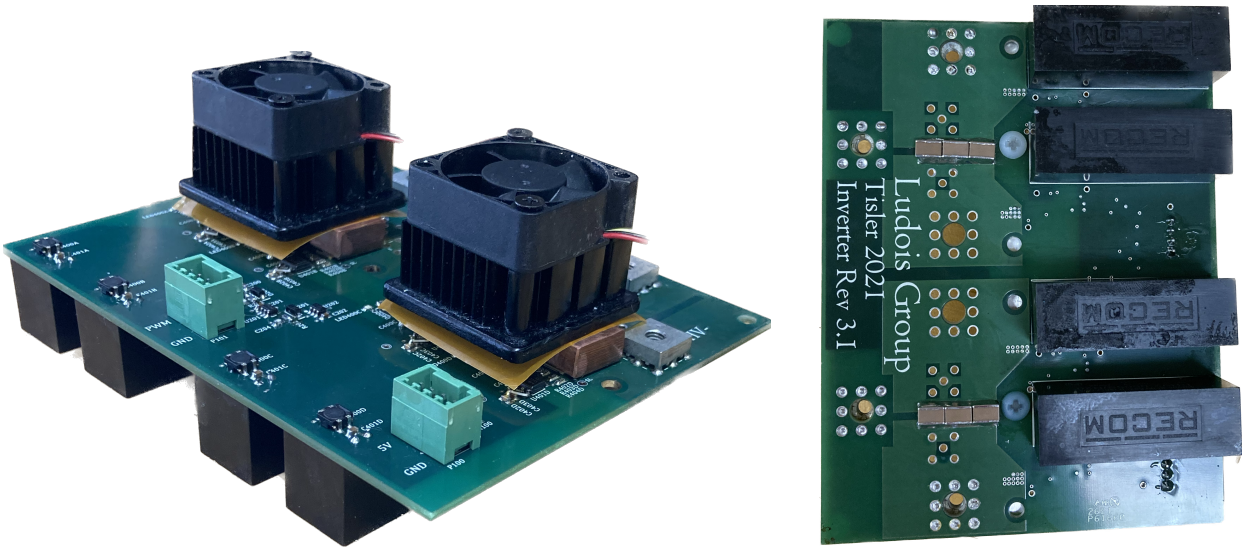

(a) (b)

Figure 3.2: Pictures of assembled inverter from (a) top view and (b) bottom view

The gate drive IC for the inverter by Silicon Labs, SI8271GBD-IS, is automotive qualified and has an integrated "deglitcher" that ignores any noise for fifteen nanoseconds after a command signal

is given. This prevents one switch in the half-bridge from being turned on during the deadtime period due to noise from the turn-off of the other switch. Separate gate drive ICs were chosen for the high and low side instead of a combined half-bridge IC to keep all four gate driver circuits as identical as possible.

Figure 3.3a shows the GaN switch gate signals for a half-bridge from an oscilloscope waveform capture with no load. The waveforms are captured using single-ended probes with bandwidths $>$ 400MHz on the high and low sides to achieve the highest possible quality and accuracy. The deadtime time measurement is taken when the gate signal equals 1.7V which is listed on the datasheet as the v_{GS} threshold voltage. The deadtime during testing is tuned to be $\approx 15ns$ using the RC delay in Figure 2.9. This is a 2.5x reduction in deadtime from the 40ns minimum for the previous 1.7MHz inverter. Additionally, each inverter must be tuned separately since the propagation delays in each Schmitt trigger inverter and buffer can vary by nanoseconds.

Figure 3.3b shows the same gate-to-source signals when the system is operating at its maximum recorded operating output power of 2.3kW. The measurement was taken courtesy of Teledyne-Lecroy using new high-bandwidth and common-mode-rejection differential probe prototypes. Two different probes were used for the high-side and low-side measurements, so that can account for differences in the high frequency harmonics. The high-side gate signal remains largely the same, but the low-side has a slower turn-off with a deadtime that is smaller than expected.

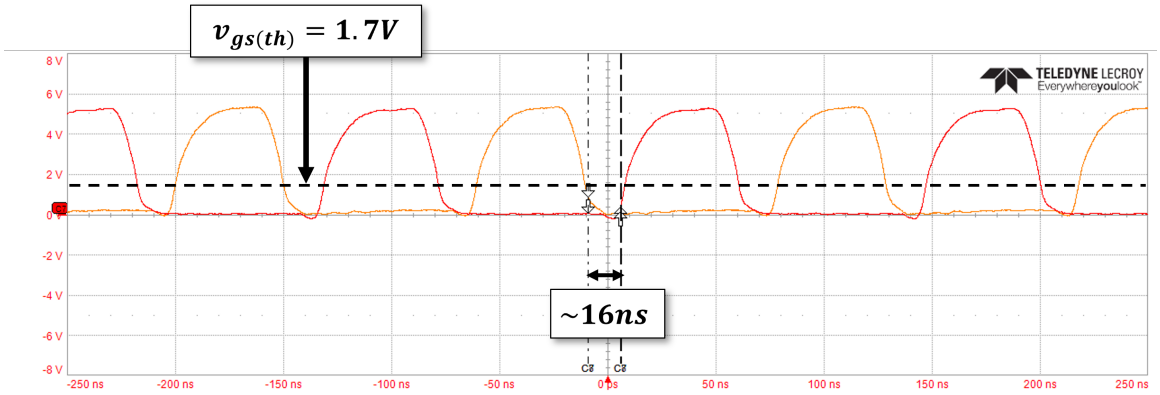

(a)

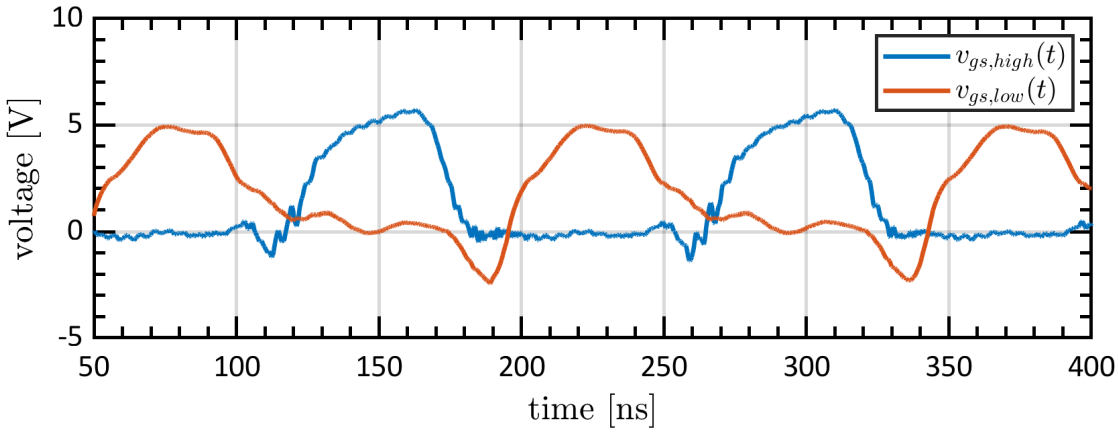

(b)

Figure 3.3: Oscilloscope capture of half-bridge gate signals (a) not under load with a deadtime of $\approx$ 16ns, and (b) under maximum load at $P_{out} = 2.3kW$

Without the use of a power analyzer capable of megahertz range analysis, it is not possible to accurately measure the inverter efficiency (DC-in to AC-out). The input and output inverter waveforms can be captured on an oscilloscope, but the measurement circuits and probes are not intended for extremely high accuracy. As a result, calculated efficiencies are nonsensical and can erroneously be over one hundred percent in some situations. Assuming the inverter loss is solely from conduction, the efficiency is $>$ 99% and therefore is not considered to be a large factor in improving the overall DCDC system efficiency.

3.3 Resonant Tank System Testing

The new set of inductors that are designed for a system resonance of 6.78MHz are shown in Figure 3.4, with and without Litz wire. Both inductors are identical quasi-distributed air gapped inductors made of segmented ferrite core segments with 2 thousandths of an inch of Kapton sheets in between each segment to maintain the air gap. The original inductors in Figure 3.4a are made with 18 AWG solid copper wire plated with silver for high-frequency performance and initially designed for the 1.7 MHz CPC prototype on the left. The wire is insulated with PTFE for high-voltage breakdown strength. The Litz wire inductor version in Figure 3.4b is made with 14 AWG-equivalent Litz wire with individually insulated 48 AWG wires. It is not necessary for the individually isolated wires to be rated for high voltages, only the overall bundle insulation. However, the Litz wire bundle is only wrapped with a nylon cloth and does not provide high voltage isolation. Kapton tape, shown in orange, is wrapped around the wire before assembly of the inductor for high voltage isolation. Unfortunately, the significantly larger gauge wire and Kapton wrap means that the outer ferrite core segments do not sit flush with the endcap pieces with a ring of bare ferrite exposed.

Figure 3.5 compares the original 1.7MHz system ESR with the new 6.78MHz system ESR. It is important to note that the system ESR is determined by shorting together the input of the rectifier. Therefore, the equivalent diode capacitance is not considered for these impedance analyzer measurements and the system resonance point is solely determined from the tank inductor and capacitive coupler. As shown from simulations in section 2.4.1, the rectifier diode capacitance will increase the resonance point of the coupler compensation system.

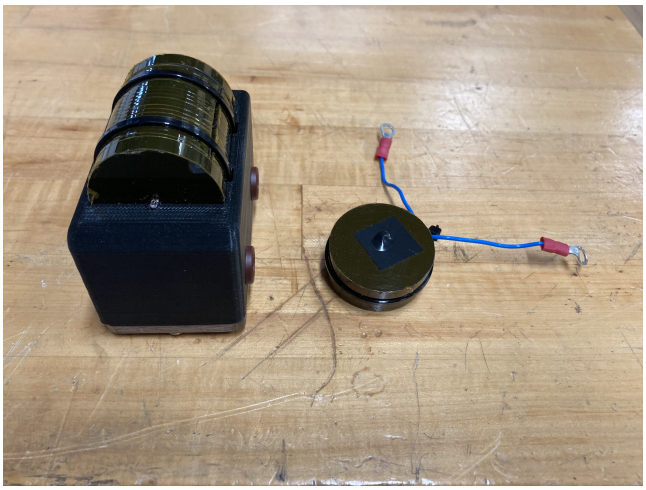

(a)

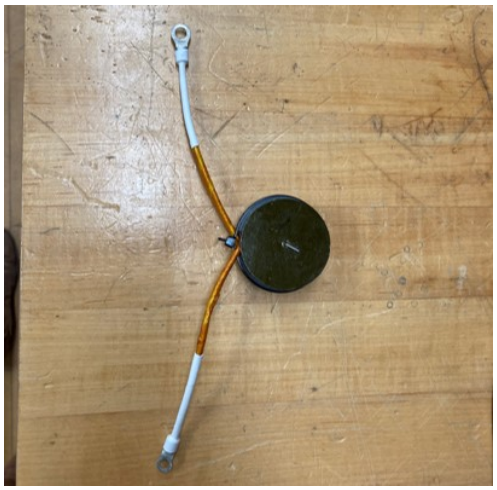

(b)

Figure 3.4: Pictures of assembled tank inductors (a) comparing the 1.7MHz and 6.78MHz solid copper wire versus the (b) Litz wire wound versions

The new 6.78MHz system ESR in Figure 3.5b improved significantly, nearly 1/3 lower, even considering the higher frequency and skin depth. The ESR is significantly affected by the total length of wire in the system simply due to smaller resonant tank inductors with much fewer turns and less wire. Additionally, a mistake was found in the original CPC rotor board where it was lacking vias between the front and back side copper pours. Without vias, there is an additional resistance between the CPC boards. While most of the system resistance comes from the connection wires and inductors, the capacitive coupler plates also have real resistive loss. The ESR improvement will reduce the resistive loss; however, it also reduces the damping of high frequency oscillations above the fundamental.

In order to maintain zero voltage switching (ZVS) such that the inverter devices are soft switching, the switching frequency must be above the tank resonance frequency. The system modeling from subsection 2.1.1 aims to predict the minimum switching frequency required for ZVS given the machine load impedance and the inverter deadtime. Specifically, Figure 2.10 plots the ratio of switching frequency over resonant frequency versus load resistance and deadtime.

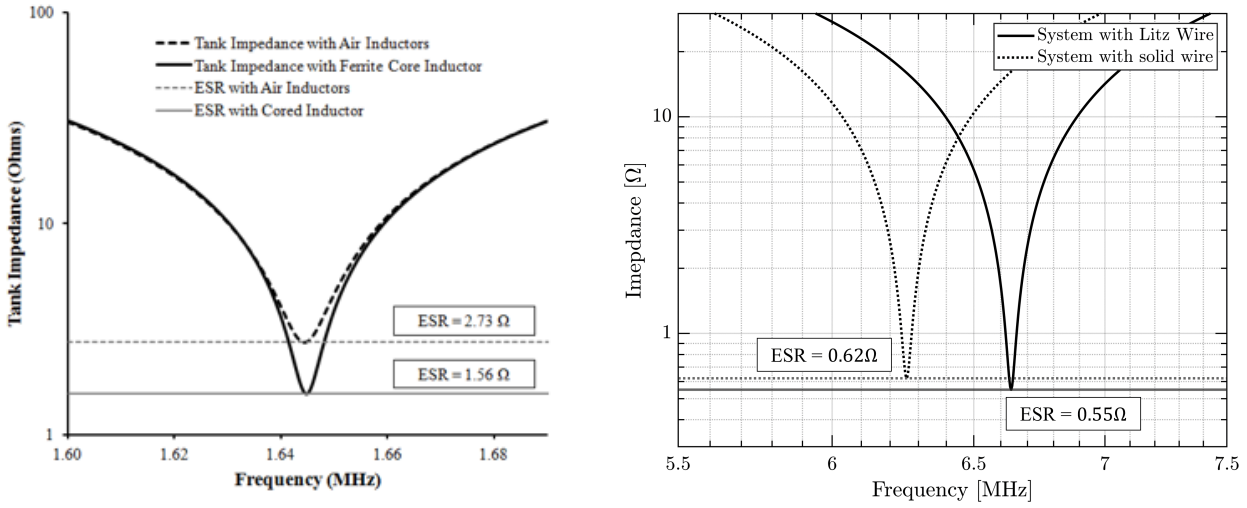

Figure 3.5: Comparison of (a) the 1.7MHz system ESR [94] and (b) the new 6.78MHz system ESR with and without Litz wire

Figure 3.5b plots the CPT system impedance with the rectifier shorted across its input terminals. These plots show the series LC tank resonance points for all solid wire and all Litz wire in the system. The impedance at the resonance point is the system equivalent series resistance (ESR), meaning the Litz wire version will have lower ESR loss. With Litz wire, the system LC resonance is at 6.62MHz.

Table 3.1 uses the analytical calculations from chapter 2 to determine the minimum switching frequency of the inverter with the assumption that the LC tank resonance is at 6.62MHz and the deadtime is 15ns. The switching frequency is calculated assuming two different output powers since the diode capacitance is nonlinear with blocking voltage. At 250W, the diode blocking voltage is roughly 100V, and at 4kW it is roughly 400V. The switching frequency increases with power given that the diode equivalent capacitance increases with blocking voltage. For testing, the inverter switching frequency will not actually be at 6.78MHz. Instead, it will roughly be in the range of 7.1-7.2MHz.

	$P_{out} \approx 250W$	$P_{out} \approx 4000W$
LC Resonant Frequency	6.62MHz	6.62MHz
Switching Frequency	7.15MHz	7.19MHz

Table 3.1: Table showing the theoretical minimum switching frequency as the output power changes. The tank resonance is assumed constant.

3.4 Rectifier Testing

The rotating rectifier board is an important and necessary component of any WFSM wireless excitation method. In this work, two different types of rectifiers are analyzed. "Voltage-stiff" and "current-stiff" rectifier designs refer to the method of filter used on the DC output whether capacitive or inductive, respectively. Both are compared based on how well they reduce the loss and stress on the passive diodes in the megahertz operating region.

3.4.1 Voltage Stiff Rectifier

The first rectifier designed and tested is the classic voltage-stiff version where a large DC filter capacitor is placed on the output to create a smooth DC voltage. Figure 3.6 shows pictures of the assembled rotating rectifier board as described in section 2.4.1. As is shown in Figure 3.6b, the filter capacitor is actually many capacitors in parallel. At 7MHz, the impedance of capacitors in the μF range are dominated by stray inductance and would not have the ability to filter out higher frequencies of voltage ripple. As a solution to this issue, many 100nF capacitors were put in parallel, each of which has a self-resonance just above 30MHz.

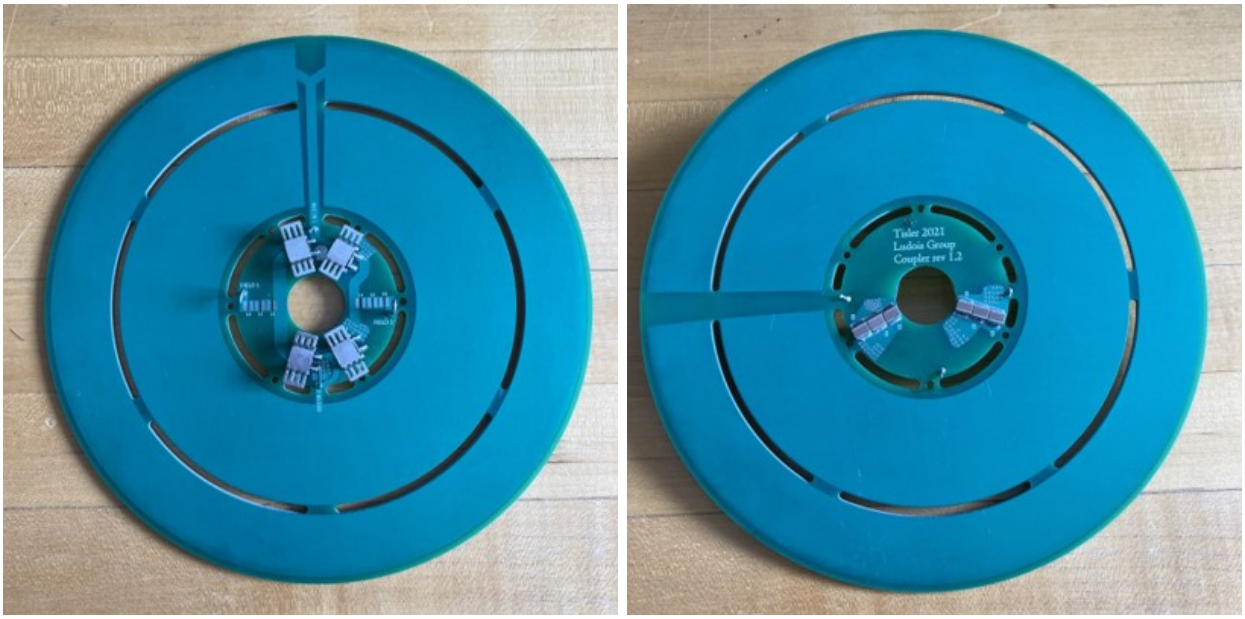

(a) (b)

Figure 3.6: Pictures of the (a) front and (b) back of the rotor coupling board with voltage-stiff rectifier.

The diodes are placed on the top side with DC filter capacitors directly behind each half-bridge to keep the loop area as small as possible and mitigate stray inductance. The SiC Schottky diodes used in this design are 1200V-rated devices from Infineon, IDM08G120C5. Each diode has a surface-mount heatsink specific to DPAK packages. The heatsinks are chosen to be the width of the rectifier radial area and a small profile for rotating. The choice to use surface-mount (as opposed to through-hole) heatsinks and diodes was driven by the limited area on the CPC board for the rotating rectifier and the high-speed nature of the board. However, as shown in Figure 3.1c, compressed air is forced across the diodes, providing sufficient cooling. Eight total diodes with two diodes each in parallel can also reduce the individual loss of each diode for cooling without changing the loss of the system.

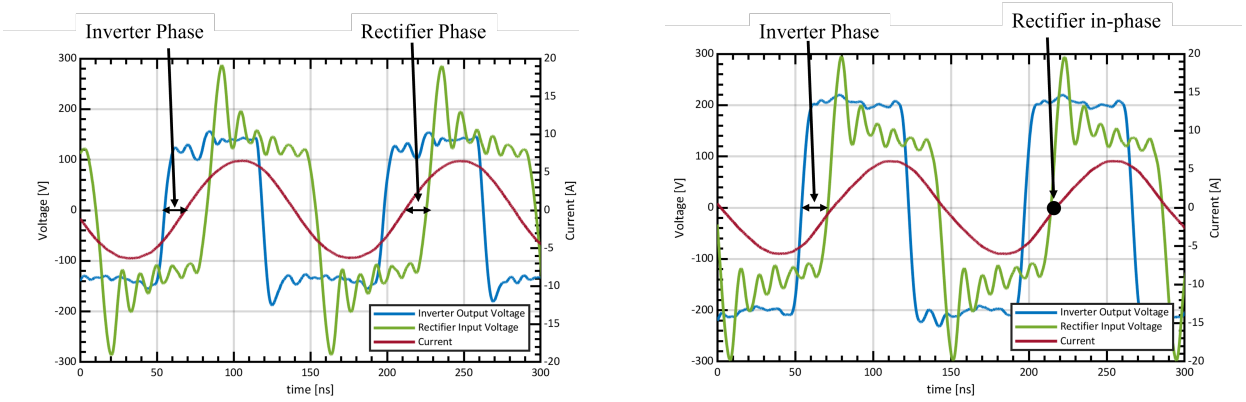

Figure 3.7: System waveforms showing the inverter voltage, tank current, and rectifier voltage for both the voltage-stiff rectifier (a) without and (b) with inductor compensation.

Figure 3.7 plots the oscilloscope waveforms where during testing the system is operated above resonance to achieve ZVS. In both figures, the blue curve is the output voltage from the inverter and the red is the output current, otherwise known as the tank current. The green waveform is the input voltage to the rectifier. From the resonant system analysis in chapter 2, the blue and green waveforms are expected to look trapezoidal. Additionally, there is a voltage gain between the inverter and rectifier voltage waveforms from the presence of the rectifier equivalent capacitance. The large overshoot and ringing in the rectifier voltage comes from stray inductance in the half-bridge loop resonating with the equivalent diode capacitance. In both plots, the current lags the inverter voltage indicating the inverter sees an inductive load as desired in ZVS. In Figure 3.7a without

the compensation inductor, the tank current leads the rectifier voltage, indicating a large input capacitance from the equivalent diode capacitance. The addition of the input rectifier capacitance pushes the resonant frequency and the voltage gain higher. In the initial 1.7MHz prototype, it was determined that the optimal efficiency occurs when the switching frequency is set such that the current splits the inverter and rectifier phase equally.

In Figure 3.7b it is shown that the addition of a parallel input inductor can help decouple the effects of the diode capacitance. The parallel input inductance is a power factor corrector for the rectifier. Ideally, the inductance is set such that it resonates with the diode capacitance at the tank frequency. Figure 3.8 shows different air core inductors wound from solid magnet wire. The equivalent rectifier capacitance is 230 ± 20pF, so at 6.62MHz the inductance should be around 2.5µH. Any small change to the system drastically changes the resonant point so this inductance value is best determined experimentally.

It is important to note that there is negligible overshoot on the blue inverter voltage waveforms. There was a significant effort made in Figure 2.13 and Figure 2.14 to mitigate the parasitic inductance in the half-bridge and gate-drive loops to reduce the overshoot on the inverter waveforms. Typically, a 50% headroom is given between the DC input voltage and the power switch rating. However, the the low overshoot present on these waveforms means the 650V GaN devices do not need 50% headroom and have excellent voltage utilization.

Figure 3.7b shows a sample waveform of the system with the compensation inductor included. In this case, the waveforms keep the same general shape as without compensation except the phase shifts change. The inverter still has an inductive load with the voltage leading the current; however, the rectifier voltage is now nearly in-phase with the current. This shift aims to reduce the stress on the diodes by moving it towards the condition of zero-current switching with a power factor closer to one.

The full system is tested and analyzed with the two different voltage-stiff rectifier versions, with and without compensation. Table 3.2 and Table 3.3 show a few of the best data points from bench testing. All bench testing was done with open-loop control by manually adjusting the inverter switching frequency to achieve the highest efficiency. Without compensation, the diode capacitance increased the resonant frequency of the system, and the switching frequency was set between 7.3-7.35MHz. With inductor compensation, however, the switching frequency was set between

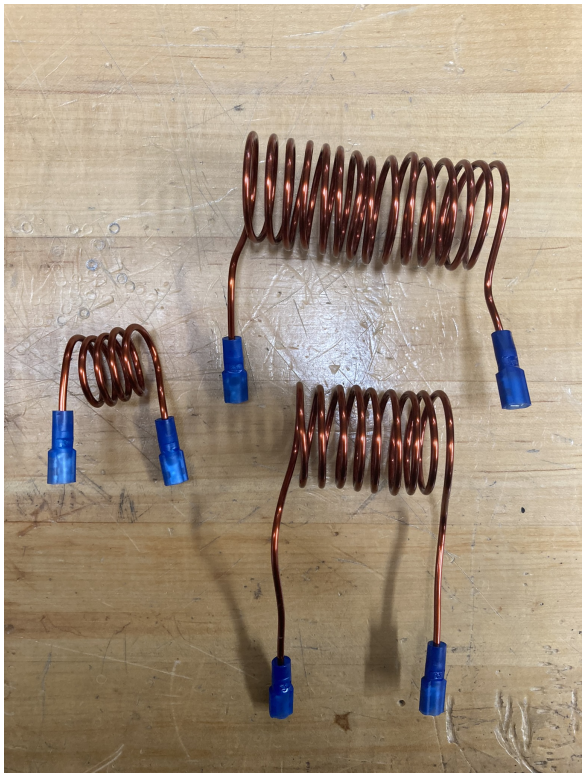

Figure 3.8: Picture of different power factor corrector inductor sizes

6.9-7.1MHz to be above the resonance to maintain ZVS.

Table 3.2 contains data collected while the rectifier was operated without compensation, while Table 3.3 contains data collected while the rectifier was operated with the power factor correction inductor. The field of the WFSM works as the load in all voltage-stiff rectifier testing. The power supply is used for the input voltage and current data and two digital multimeters are used for the output current and voltage data. Unfortunately, the oscilloscope waveforms are not reliable enough to provide useful efficiency data. Without any compensation, a peak power of 508W was achieved at 90.4% efficiency. Likewise, with inductor compensation, a peak power of 871W was achieved at 90.5% efficiency.

The efficiency of the inverter and rectifier cannot be measured accurately at 7MHz, but an estimate can be made from datasheet parameters. For the inverter, the switching loss is minimal due to soft-switching and thus the loss can be assumed to all be from conduction and output capacitance loss. At room temperature, 25°C, $r_{ds,on} = 50m\Omega$ while the "hot" value at 150°C is $r_{ds,on} = 129m\Omega$, corresponding to the nominal and hot values that are the primary drivers of

inverter efficiency. Overall, the inverter efficiency is estimated to be greater than or equal to 99%. While this is quite good, cooling still presents a challenge for the inverter because it is difficult to remove heat effectively from the small GaN dies and any small amount of switching loss adds up quickly at switching frequencies of 7MHz.

Similar to the inverter $r_{ds,on}$ value, the rectifier forward voltage drop also changes significantly with temperature. The nominal forward voltage drop is $v_f = 1.65$V whereas the "hot" value can be as high as $v_f = 2.85$V. The rectifier can be assumed to have mostly conduction loss as the SiC Schottky diode is marketed with "no reverse recovery current," but with the equivalent diode capacitance at 7MHz there will be some turn-on and turn-off loss as well; this loss mechanism cannot be calculated accurately nor easily. For the rectifier efficiency, at best it is above 97% and at worst it is above 94%.

$V_{DC,in}$	$I_{DC,in}$	$V_{DC,out}$	$I_{DC,out}$	P_{in}	P_{out}	η	$I_{AC,tank}$
[V_{DC}]	[A_{DC}]	[V_{DC}]	[A_{DC}]	[W]	[W]	[%]	[A_{rms}]
150	2.56	125.7	2.77	384.2	348.2	90.6	4.3
160	2.76	136.4	2.94	442.1	400.7	90.7	4.6
180	3.13	154.4	3.29	562.5	508.4	90.4	5.1

Table 3.2: Measured data from testing voltage-stiff rectifier without compensation

$V_{DC,in}$	$I_{DC,in}$	$V_{DC,out}$	$I_{DC,out}$	P_{in}	P_{out}	η	$I_{AC,tank}$
[V_{DC}]	[A_{DC}]	[V_{DC}]	[A_{DC}]	[W]	[W]	[%]	[A_{rms}]
175	3.1	150	3.20	542.5	480.0	88.5	4.4
200	3.3	170	3.54	660.0	601.0	91.0	5.7
225	3.56	185	3.84	800.3	710.4	88.8	6.3
250	3.85	205	4.25	962.5	871.3	90.5	6.8

Table 3.3: Measured data from testing voltage-stiff rectifier with inductor compensation

The current seen by the GaN switches and SiC Schottky diodes is assumed to be a direct transformation of the tank current. However, it is clear that the power factor for both the inverter and rectifier is less than unity with circulating reactive power. It is evident that as the power increases, the relative impact of conduction loss as a fraction of the total loss in both converters is reduced.

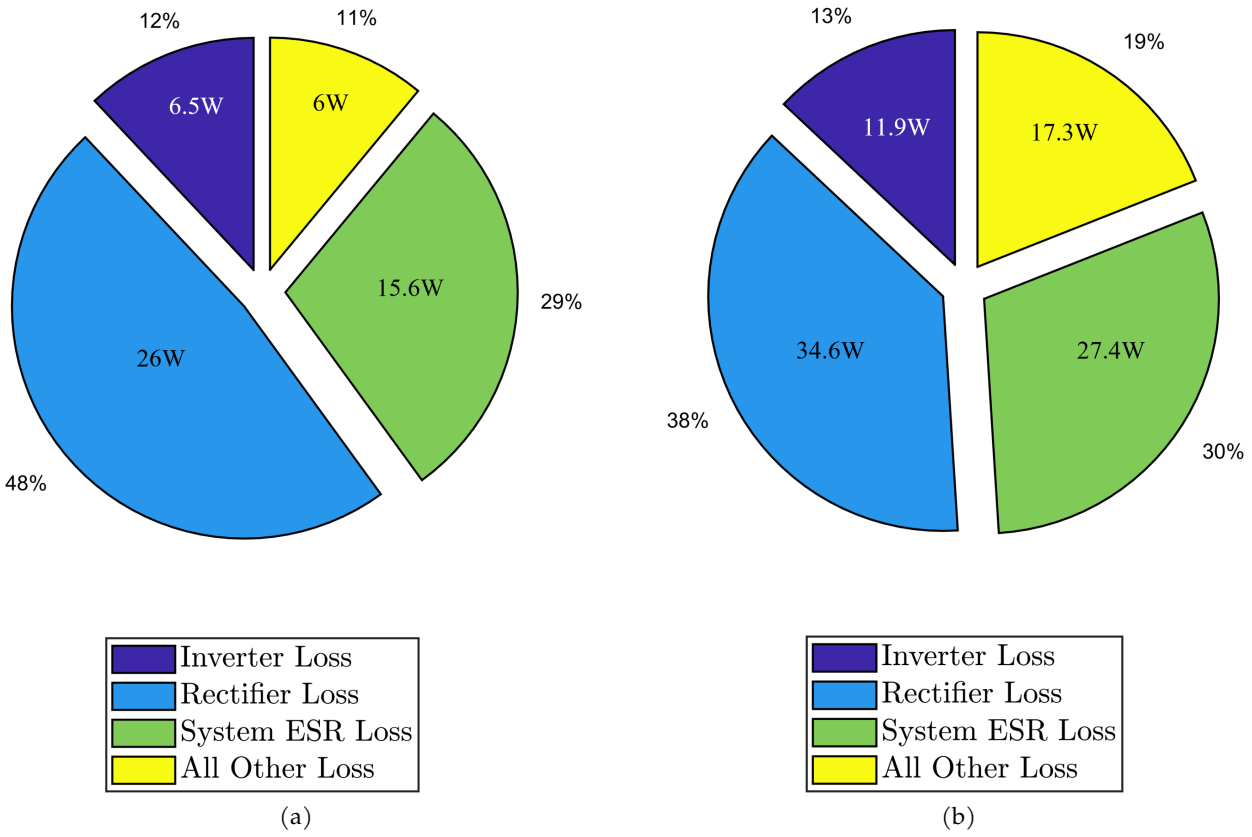

Figure 3.9: Power loss breakdown for the rectifier (a) without and (b) with compensation for the highest output power data point in each condition.

Figure 3.14 summarizes all the voltage-stiff rectifier bench testing data and shows general trends with and without the inductor compensation added. Every time the CPC system is adjusted and reassembled the system parameters change. Multiple days of testing are shown with slightly different system parameters resulting in different efficiency results Figure 3.14a shows the crucial relationship between efficiency vs. output power. As output power is increased, the efficiency begins to level off between 88-91%. While at first this may appear to span a large range, it must be noted that since a power analyzer was not used it is possible to have efficiency measurement error in the 1-2% range. Interestingly, the efficiency is not better with the inductor compensation than without. Although the rectifier is near zero current switching mode, the compensation inductor shunts current from the rectifier and creates its own additional losses.

In Figure 3.14b, the voltage overshoot for both the inverter and rectifier is analyzed with respect to the output power. For the inverter, the overshoot is the maximum output voltage of the ringing

normalized to the input voltage, whereas the rectifier overshoot is normalized to the output voltage for a fair comparison. The compensation inductor does not appear to strongly affect the inverter voltage overshoot; however, it does appear to produce consistently lower rectifier voltage overshoot. The rectifier overshoot in any case is over two times the output voltage for a low diode voltage utilization. This indicates a 1200V diode is required with 650V GaN switches. Even when attempting to eliminate as much stray inductance as possible from the rectifier loop, the small amount that remains is enough to create substantial ringing.

At low power, the system was allowed to reach a steady state to achieve a true measurement of the heatsink temperature at that operating point. However, as the output power reached operating points above 600W, the system was only brought up to the power momentarily to capture the data point and then brought back down to cool, which is not representative of the steady-state temperature at that operating point. The fact that the diodes were able to still reach nearly 90°C in seconds shows that the cooling approach is limited on the diodes.

3.4.2 Current Stiff Rectifier

The second rectifier designed and tested is the current-stiff version. Figure 3.10 shows the top and bottom sides of the rectifier board. Large DC filter inductors are placed on the two rectifier outputs to maintain a continuous switching current for the diodes in Figure 3.10b. Twelve CoilCraft surface mount inductors are placed in series on both sides of the rectifier output to be $\approx 2\mu H$ per side. Additionally, multiple filter capacitors are placed in parallel after the output to create a smooth DC voltage. These capacitors also have self-resonances above 30MHz. On the front side in Figure 3.10a, a single capacitor,C_{in}, is placed between the inputs to the rectifier to filter the input voltage. The same 1200V-rated Schottky diodes from Infineon are used (IDM08G120C5) and compressed air is likewise used to cool their heatsinks.

The most crucial design element for the current-stiff rectifier is the input capacitance, C_{in}. This capacitance serves the purpose of filtering out ripple harmonics in the input rectifier voltage, resulting in a sinusoidal waveform. It is difficult to analytically derive this value outside of simulations to get a sense of the appropriate order of magnitude. From Figure 3.11, different values of C_{in} ranging from 100pF to 400pF are tested and compared. The waveform becomes more sinusoidal, and the initial switching spike reduces by increasing the value of capacitance; however, at 400pF

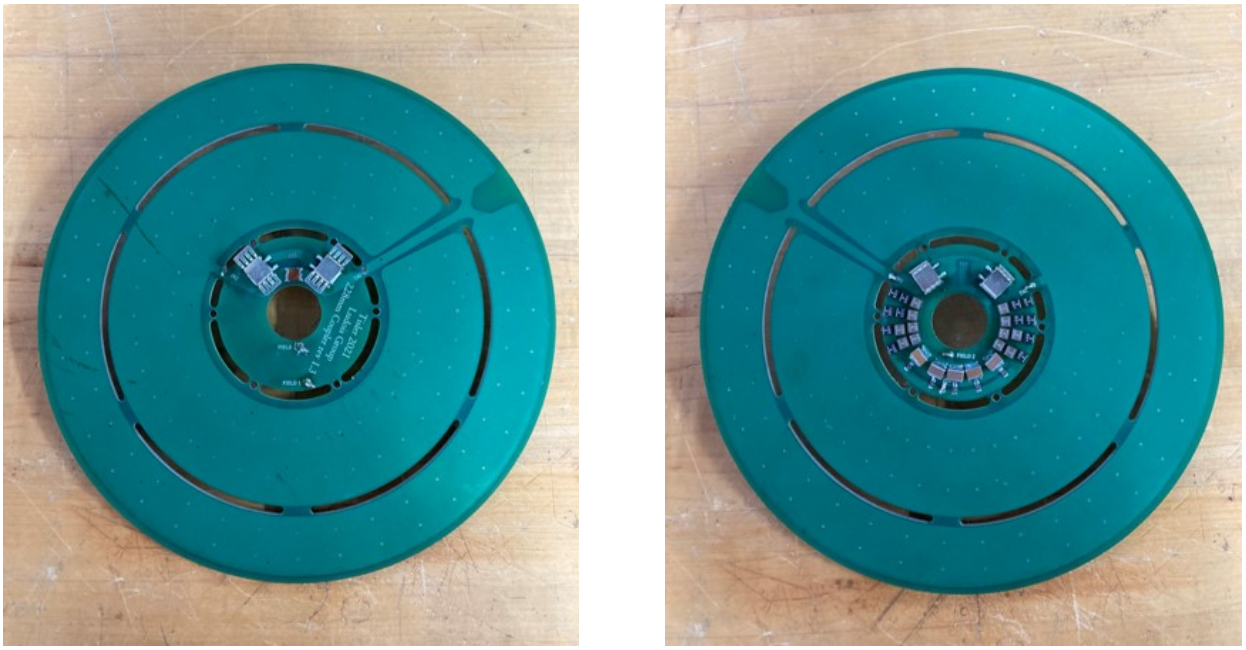

(a) (b)

Figure 3.10: Pictures of the (a) front and (b) back of the rotor coupling board with current-stiff rectifier.

there is a new ripple component on top of the waveform. With $C_{in} = 200pF$ both the overshoot and efficiency are generally at their optimal values of any capacitance even though data was not collected at all switching frequencies. Low frequency oscillations were an issue at 200pF, but it was determined to be a good tradeoff to adjust the switching frequency range for better performance overall. Thus, all current-stiff rectifier data was collected with $C_{in} = 200pF$.

With the input capacitance value determined, the same open loop system bench tests were performed. Figure 3.12 shows plots of the full system with the current-stiff rectifier at the peak output power of 2.3kW, with a resistive bank and inductor as the load to avoid damaging the WFSM field winding insulation. For some tests at output powers below 1kW, the rotor was used for the load. Typically, the WFSM would be oil-cooled, however during bench testing the rotor was not actively cooled in any way and the CPC was providing enough power to potentially damage the insulation of the field windings. The rotor temperature was not measured directly, but by recording the output voltage and current, the equivalent "hot" field resistance can directly indicate the rotor temperature as in eq. (3.1):

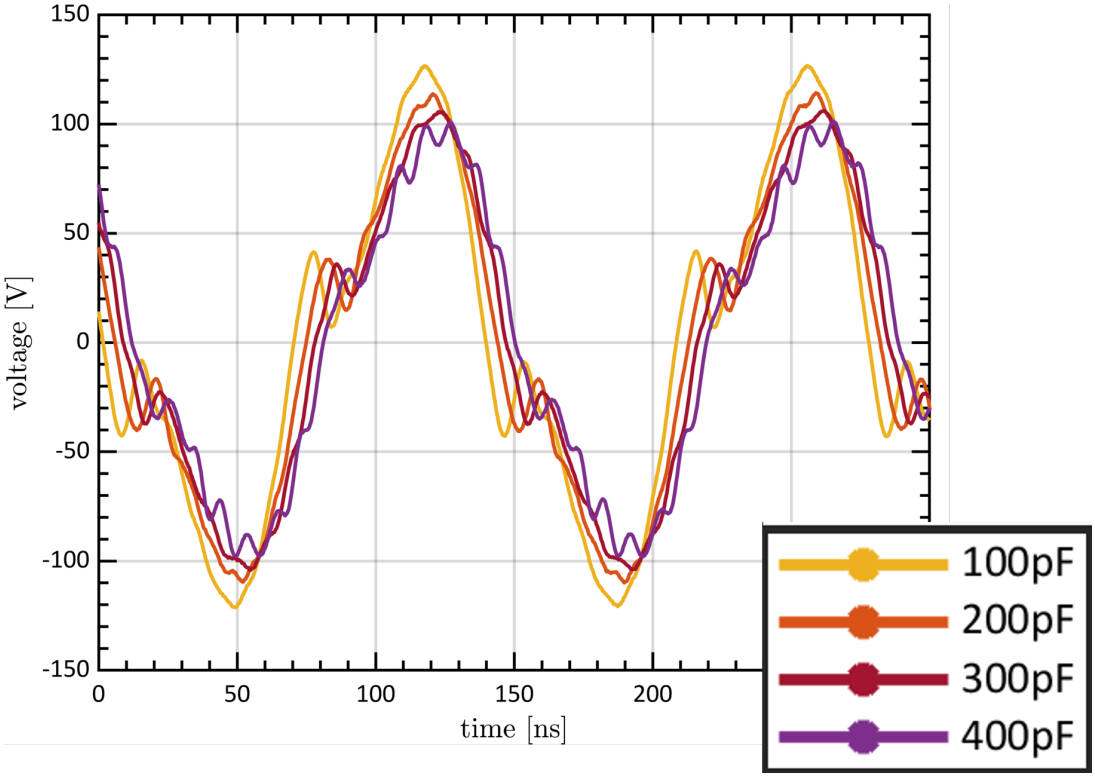

Figure 3.11: Plots comparing C_{in} values to determine optimal input rectifier capacitance.

$$T_{avg} = \frac{\frac{R_{hot}}{R_{nom}} - 1}{\alpha_{cu}} + T_{nom} \tag{3.1}$$

where R_{nom} and T_{nom} are unloaded field resistance and temperature, respectively, and $\alpha_{cu} = 3.81 * 10^{-3} \frac{1}{^{\circ}C}$, the temperature coefficient of copper. At room temperature, the field is roughly 39Ω and 3H.

Table 3.4 summarizes the highest power testing with the current-stiff rectifier with a separate inductor and resistive bank used as the load. During the preliminary testing with the voltage-stiff and current-stiff rectifiers, the inverter was the limiting factor as the GaN switches would fail from overheating. The copper blocks and fan heatsink provided adequate cooling for the inverter and the system was able to reach 2.3kW output power without inverter thermal issues.

Figure 3.14 includes the current-stiff data compared with the voltage-stiff rectifier with and without compensation with a variety of metrics. All testing was completed with open loop inverter control using a function generator output square voltage. The switching frequencies were between 7.1-7.3MHz in order to maintain peak efficiency.

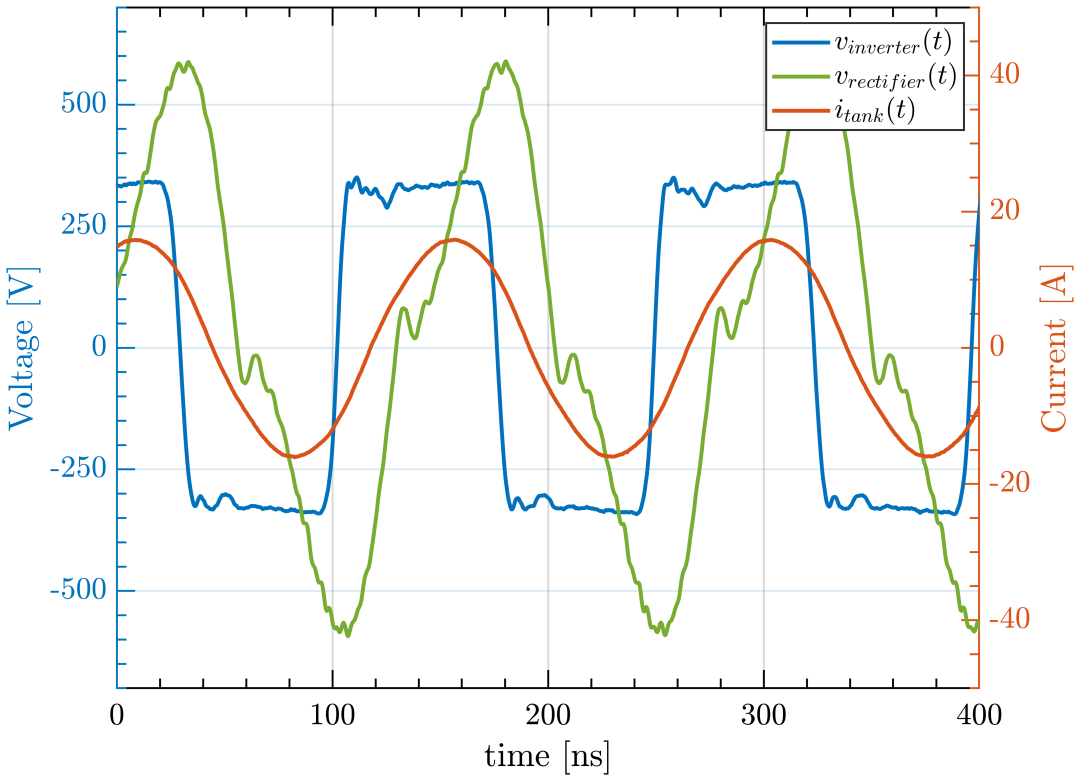

Figure 3.12: System waveforms showing the inverter voltage, tank current, and rectifier voltage the current-stiff rectifier at 2.3kW output power

$V_{DC,in}$ [V_{DC}]	$I_{DC,in}$ [A_{DC}]	$V_{DC,out}$ [V_{DC}]	$I_{DC,out}$ [A_{DC}]	P_{in} [W]	P_{out} [W]	η [%]	$I_{AC,tank}$ [A_{rms}]
310	6.9	270.5	7.0	1995	1896	88.6	10.3
320	7.1	279.6	7.25	2282	2027	88.8	10.6
330	7.7	290.5	7.5	2475	2190	88.5	11.1
340	7.7	300	7.7	2618	2316	88.5	11.4

Table 3.4: Measured data from testing current-stiff rectifier with $C_{in} = 200pF$ with resistive bank and inductor as the load

For the efficiency in Figure 3.14a, the current-stiff rectifier is very comparable, reaching peak efficiency near 91% and steadying out between 88-89% above 1kW. However, in Figure 3.14b, the current-stiff rectifier performs significantly better in terms of inverter and rectifier voltage overshoot for all output powers. The current-stiff rectifier overshoot is 10-20% better than the voltage-stiff rectifier versions with less harmonic content as well. Specifically, the inverter overshoot is below 10% for output powers > 1kW. The GaN switches have excellent voltage utilization from the careful PCB layout made to mitigate parasitic inductances in the half-bridge and gate-drive commutation

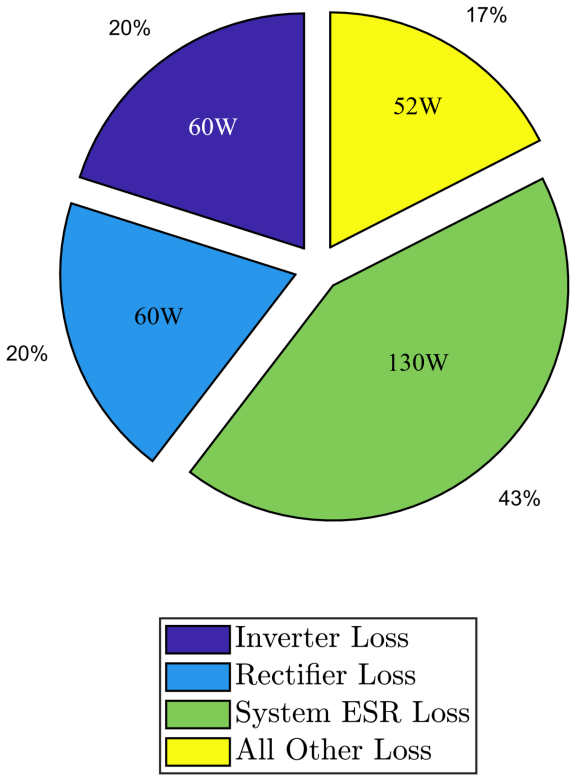

Figure 3.13: Power loss breakdown for the rectifier with the resistive bank as load for the highest output power data point in each condition.

loops.

Even with the rectifier input voltage being changed to a sinusoidal curve, the peak ringing of the typical square is still higher than the peak sine amplitude. From this parameter alone, it appears that the new current-stiff rectifier reduces stress on the individual diodes. Additionally, for the testing done with the current-stiff rectifier, the inverter overshoot is <10% as is evident from Figure 3.12.

Figure 3.14c shows the plot of output power versus expected field resistance for results with the rotor as the field winding. This can also be though of as a correlation between field temperature and power. At a field resistance of 50Ω the winding temperature would be ≈ 97°C and with a 60Ω field resistance the temperature would be ≈ 163°C. The field winding insulation is rated to 180°C, so it was necessary to use an equivalent RL load to avoid damaging the motor. The resistive bank was set to 38Ω and the closest large inductor readily available from the lab was 0.5H. The RL load held a constant resistance for the duration of the high power testing.

As expected, the field resistance increases as output power is increased, and the field winding

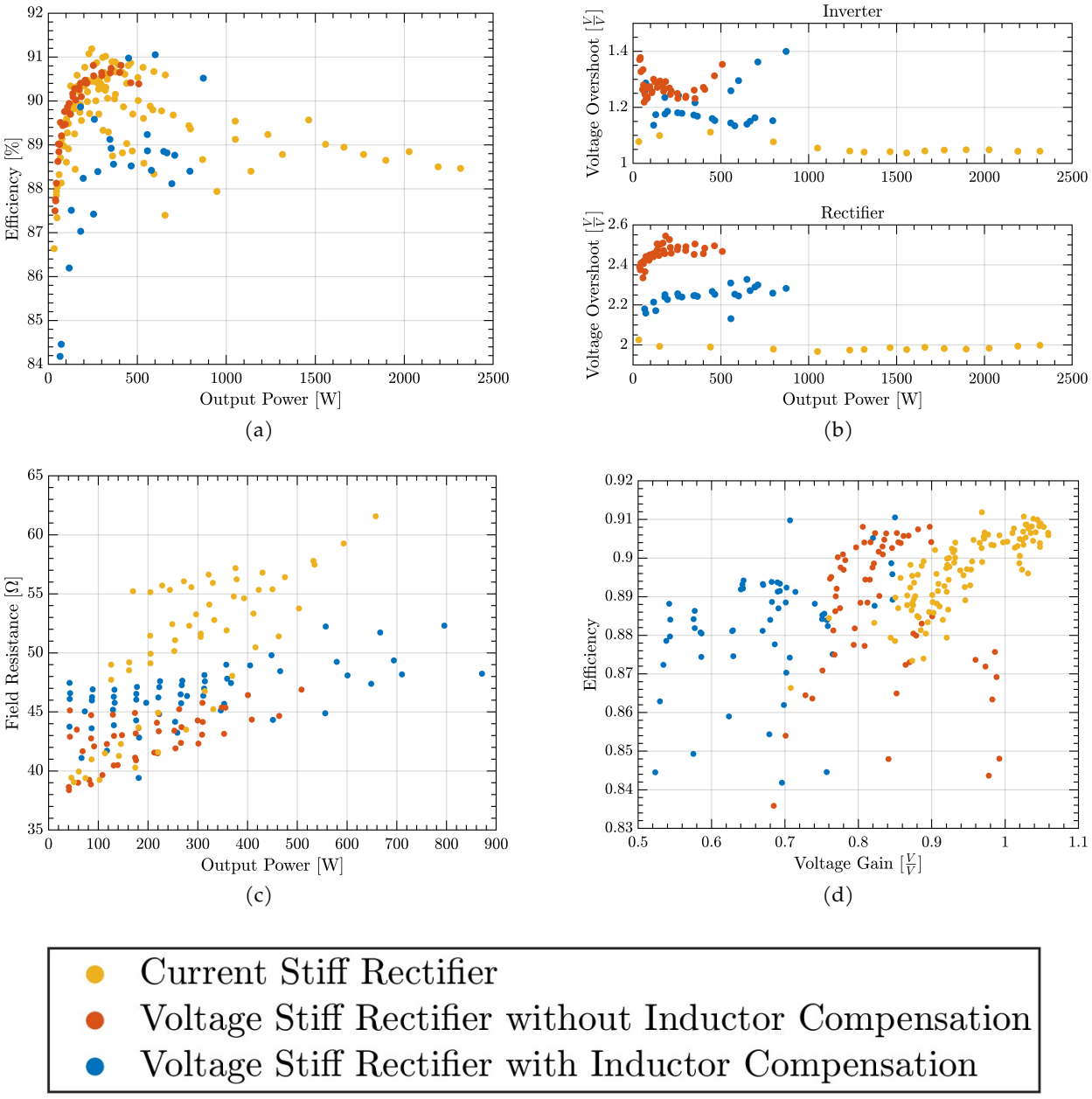

Figure 3.14: Summary of all voltage-stiff and current-stiff rectifier data comparing (a) efficiency vs. output power, (b) voltage overshoot vs. output power, (c) load field resistance vs. output power, and (d) efficiency vs. voltage gain for various parameters.

must dissipate this without active cooling. In the current-stiff rectifier case, the field is getting hotter because the system was not allowed to cool in between testing operating points. The system was held at the output power condition and allowed to come to steady state. As the field resistance increases, the switching frequency also changes making repeatable runs very difficult. With active

cooling employed for dynamometer testing, the field resistance would stay relatively constant and close to its nominal value, and this would be less of an issue.

3.5 Concluding Remarks

Overall, the full capacitive power transfer system with the current-stiff rectifier successfully achieved 2.3kW of output power at an efficiency of 88.5%. This represents a nearly 3.5x output power improvement over the previous CPT system operating at 1.7MHz with a peak output power of 675W and an efficiency of 90.3%.

The testing and results detailed in this chapter validate the design and analysis from chapter 2 to reach 2.3kW. The main achievements validated in testing are as follows:

1. The inverter PCB layout was optimized to reduce the parasitic inductances in the half-bridge and gate-loop commutation loops and validated in FEA using Ansys Q3D. During testing, the inverter overshoot was <50% for all data points and system conditions. With the current stiff rectifier the inverter voltage overshoot was at or below 10% with minimal harmonic content.

2. The inverter dead time was successfully reduced by 60% from matching propagation delays in the ICs and tuning the delay in the lab. The dead time is reduced from 40ns with the inverter for 1.7MHz operation to 16ns for operation above 7MHz and 2.3kW. The deadtime is roughly 11% of the total switching period.

3. Copper blocks were soldered to the top-side thermal pad of each GaN device along with a dedicated heatsink and fan across each half-bridge of switches. This increased the thermal performance of the inverter to be able to output 2.3kW

4. Two types of rectifiers were evaluated: the voltage-stiff and the current-stiff rectifier based on their DC filtering strategy of an output capacitive or inductive filter, respectively. The voltage-stiff rectifier had high voltage overshoot and large amounts of harmonic content. Conversely, the current-stiff rectifier had lower voltage utilization and harmonic content while maintaining a similar or better efficiency performance.

Chapter Four

Integrated Capacitive Resolver and Rectifier Design

The goal from this work is to reduce the cost of wireless exciters for wound field synchronous machines to be able to replace permanent magnet machines in traction applications. chapter 2 and chapter 3 focus on optimizing and improving the performance of a capacitive power transfer exciter. The use of printed circuit boards (PCBs) greatly reduces the system's overall cost and allows the rotating rectifier to easily be integrated with the capacitive coupler design. Additionally, the wireless rotor excitation system can be taken a step further by integrating other necessary but otherwise costly machine components into its design.

The focus of the next two chapters is on combining the wireless exciter's rectifier with the machine's rotor position sensor. In this chapter, a capacitive resolver is designed on printed circuit boards to be integrated around the rotating rectifier circuitry and connected to the field winding of the rotor. This new design can be added to the capacitive coupler CPT boards, or as a drop-in replacement for any wireless excitation method. The ultimate goal is to remove the position sensor cost from the total motor budget.

The capacitive resolvers proposed in this work rely on varying the capacitance between two electrodes on printed circuit boards as a function of rotor position. A high frequency, constant amplitude voltage is applied as a carrier signal. As the shaft rotates, the capacitance changes and modulates the amplitude of the carrier input voltage. Then, the envelope of the modulated

waveform can be extracted and used along with other channels to derive the shaft position and speed.

Specifically, the capacitive resolver described in this chapter is designed to be a drop-in replacement and an analog to conventional magnetic resolvers with a single phase carrier input and two sinusoidal waveforms 90° apart. It will give absolute rotor position. Another capacitive resolver design tracks the saliency between stationary and rotating electrodes and is further discussed in Appendix A. This design creates a three-phase output and will give absolute electrical position only. Although both are valid resolver designs, it is most important to provide a design that is compatible with existing resolver and control software.

4.1 Magnetic Resolver Transformer Action

Magnetic resolvers are one such analog sensor that can give absolute mechanical rotor position. The accuracy of magnetic resolvers is largely based on the demodulation algorithm used by the manufacturer, but typically are in the range of 5' to 50', or 0.08° to 0.8° [140–142].

Figure 4.1a shows a simplified diagram of a magnetic resolver with two poles. An AC voltage acting as a carrier, or excitation, signal of frequency ω_{ex} is applied to a spinning coil, rotor, that inductively couples like a transformer with sensor coils on the stator, spatially located 90° apart from each other. As the carrier coil spins, it inductively couples with the sensor coils. The receiving coil voltages are thus modulated according to the angular speed of the rotor. The variable ω_r will be used to denote the rotor mechanical speed with the assumption that the resolvers have two poles. More accurately, the electrical rotor speed, ω_{re}, and the mechanical speed, ω_r, are related through the number of resolver poles, N_{poles} according to eq. (4.1). Note: the terms rotor speed and rotor angular frequency will be used interchangeably with units of $[\frac{rad}{s}]$.

$$\omega_{re} = \left(\frac{N_{poles}}{2}\right)\omega_r \tag{4.1}$$

The resulting differential output voltages have sine and cosine envelopes according to eq. (4.2)

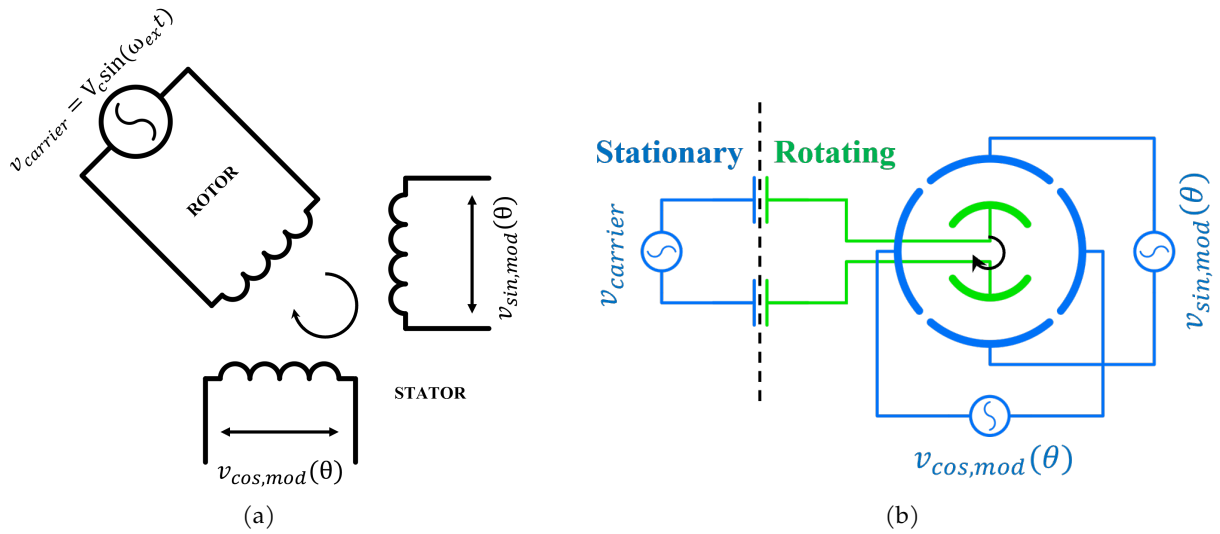

Figure 4.1: Comparison of (a) a simplified two-pole magnetic resolver, and (b) a capacitive resolver

$$\begin{aligned} v_{sin,mod}(\theta) &= V_k \sin(\omega_{ex} t) \sin(\omega_r t + \phi) \\ v_{cos,mod}(\theta) &= V_k \sin(\omega_{ex} t) \cos(\omega_r t + \phi) \end{aligned} \tag{4.2}$$

where V_k is determined by the carrier frequency magnitude and the voltage gain of the resolver. The resolver may also have a phase delay, ϕ, that will be addressed further in chapter 5. Through an analog and/or digital demodulation scheme [143], the high frequency carrier is removed in eq. (4.3) and the resulting shaft angle is determined in eq. (4.4).

$$\begin{aligned} v_{sin,dm}(\theta) &= V \sin(\omega_r t) \\ v_{cos,dm}(\theta) &= V \cos(\omega_r t) \end{aligned} \tag{4.3}$$

$$\theta = \tan^{-1}\left(\frac{v_{sin,dm}(\theta)}{v_{cos,dm}(\theta)}\right) \tag{4.4}$$

Then the speed of the rotor electrical frequency would be:

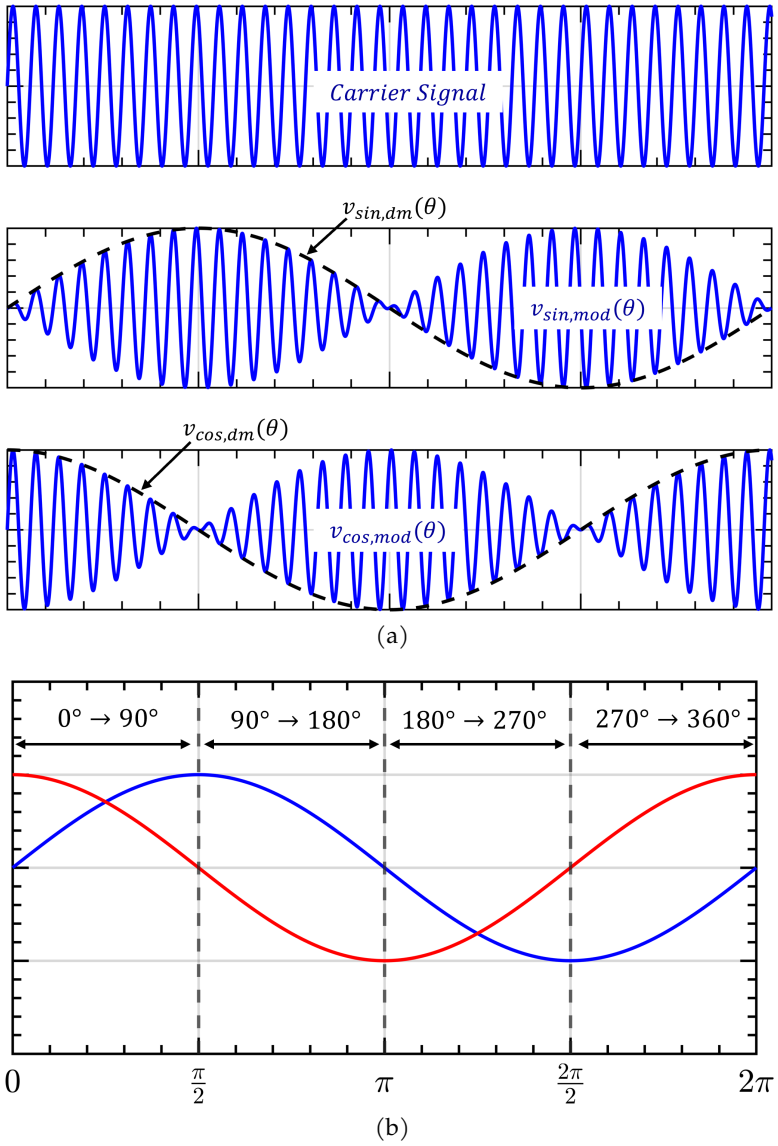

Figure 4.2: (a) Plots of the resolver input carrier waveform and the corresponding sine and cosine modulated output waveforms. (b) Demodulated sine and cosine waveforms showing the resulting shaft position.

$$\begin{aligned}\omega_r &= \frac{\dot{v}_{sin,dm}}{v_{cos,dm}} = \frac{V\omega_r \cos(\omega_r t)}{V\cos(\omega_r t)} \\ &= -\frac{\dot{v}_{cos,dm}}{v_{sin,dm}} = -\left(-\frac{V\omega_r \sin(\omega_r t)}{V\sin(\omega_r t}\right)\end{aligned} \tag{4.5}$$

Figure 4.2 shows the two modulated stator coil voltage waveforms. The dashed black lines are the sine and cosine envelops extracted to calculate position and speed. While eq. (4.4) only gives

angles from -90° to $+90^\circ$, Figure 4.2b shows how a full 360° is achieved based on whether the sine or cosine waveforms are in their positive or negative half cycle.

While there are many ways [143–146] to extract the envelope from the modulated sine and cosine waves, one common method is using multiplier demodulation. Ignoring any phase delay from the resolver, the modulated waveforms in eq. (4.2) are multiplied by the carrier frequency in eq. (4.6) and eq. (4.7) to yield a low frequency component and a component at double the initial carrier frequency. As will be discussed further in chapter 5, the multiplication can be done digitally or with an analog multiplier. Likewise, either an analog or digital low pass filter (LPF) is then applied to extract the low frequency rotor speed.

$$\begin{aligned} v_{sin,dm}(\theta) &= V_k \sin(\omega_{ex} t) \sin(\omega_r t) * V_c \sin(\omega_{ex} t) \\ &= \frac{V_k V_c}{2} \sin(\omega_r t) - \frac{V_k V_c}{2} \cos(2\omega_{ex} t) \sin(\omega_r t) \\ \text{LPF} \Rightarrow & \frac{V_k V_c}{2} \sin(\omega_r t) \end{aligned} \tag{4.6}$$

$$\begin{aligned} v_{cos,dm}(\theta) &= V_k \sin(\omega_{ex} t) \cos(\omega_r t) * V_c \sin(\omega_{ex}) \\ &= \frac{V_k V_c}{2} \cos(\omega_r t) - \frac{V_k V_c}{2} \cos(2\omega_{ex} t) \cos(\omega_r t) \\ \text{LPF} \Rightarrow & \frac{V_k V_c}{2} \cos(\omega_r t) \end{aligned} \tag{4.7}$$

4.2 Capacitive Resolver Analysis

There are many forms of capacitive position sensors, but the first capacitive drop-in replacement to the magnetic resolver was developed in [116]. Figure 4.1b shows the general operation of the capacitive resolver in comparison to the magnetic resolver. All electrodes colored in blue are on the stationary board and all electrodes in green are on the rotating board. Figure 4.3 has cartoon diagrams of both boards of the capacitive resolver proposed, designed, and tested in this work. The stationary-side board is hereafter referred to as the resolver's stator, whereas the rotating-side board is referred to as the resolver's rotor.

Two complementary AC voltages, eq. (4.8), are applied to two "excitation" electrodes on the

stator seen in 4.3a in dark and light grey. These ring electrodes on the stator capacitively couple to the corresponding electrodes on the rotor board in 4.3b.

$$\begin{aligned} v_{excite,1} &= V_{ex}\sin(\omega_{ex}) \\ v_{excite,2} &= V_{ex}\sin(\omega_{ex}+\pi) \end{aligned} \tag{4.8}$$

As the rotor spins, the excitation electrodes capacitively couple back to the overlapping stator "pick-up" electrodes, or petals, in blue and red. Figure 4.3c shows how the rotor wave electrodes overlap with the stator. The rotor lobes are designed to be the same peak amplitude and width as each individual stator electrode petal. The two modulated sine and cosine waveforms come from the differential voltage signals between the pair of blue petals and red petals. Figure 4.3a shows two resistors with voltages V_A and V_B, that would be going to analog or digital filter circuitry for demodulation.

The outer edge of the stator "pick-up" electrodes determines the modulation envelope. As the rotor lobes couple with the stator petals, the varying capacitance produces varying voltage amplitudes. The outer edge, r_o, is designed to be a rectifier sine wave. In a way, the demodulation method "un-rectifies" the voltage envelope to achieve the ideal sine wave.

Shown in mint green at the center of the rotor board is an area designated for a rotating rectifier. This capacitive resolver is designed to be integrated into a wireless exciter for a wound field synchronous machine. Thus, the resolver is meant to be integrated around the rotating rectifier and on the same boards to save space and money. The leads from the rotor field winding would attach to the rectifier area and the rotor board could be mounted against the motor housing for cooling of the rectifier diodes. This functionality will be further discussed in detail in chapter 5.

4.2.1 Resolver Capacitance Matrix

The main, desirable capacitances in the resolver are between like stator and rotor excitation electrodes, and the rotor excitation electrodes to the stator petals directly beneath them. However, among all eight separate electrodes there are capacitances formed between each combination. Parasitic capacitances are also formed to the surroundings, but these are not included in this analysis.

Figure 4.4 numbers all of the electrodes for future reference and shows some of the capacitances formed. There are board-to-board capacitances as well as undesirable coupling between electrodes on the same board. There are six electrodes on the stator board and two on the rotor board. There are 64 total permutations of capacitances, but considering $C_{nm} = C_{mn}$ where m and n are the numbers of electrodes, there are only 36 unique capacitances.

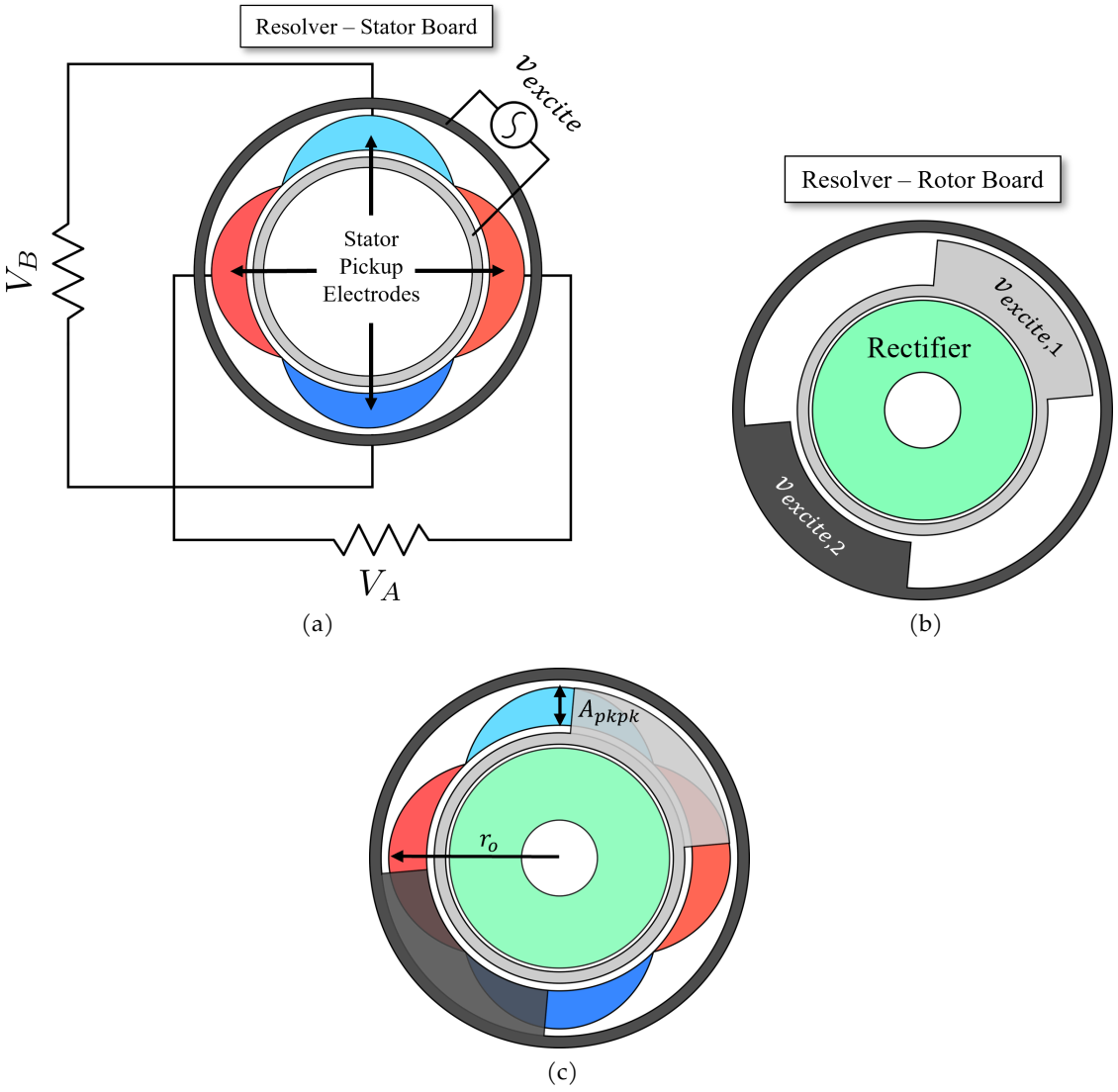

Figure 4.3: Diagrams of the capacitive resolver (a) stator board, (b) rotor board, and (c) the two boards overlapped.

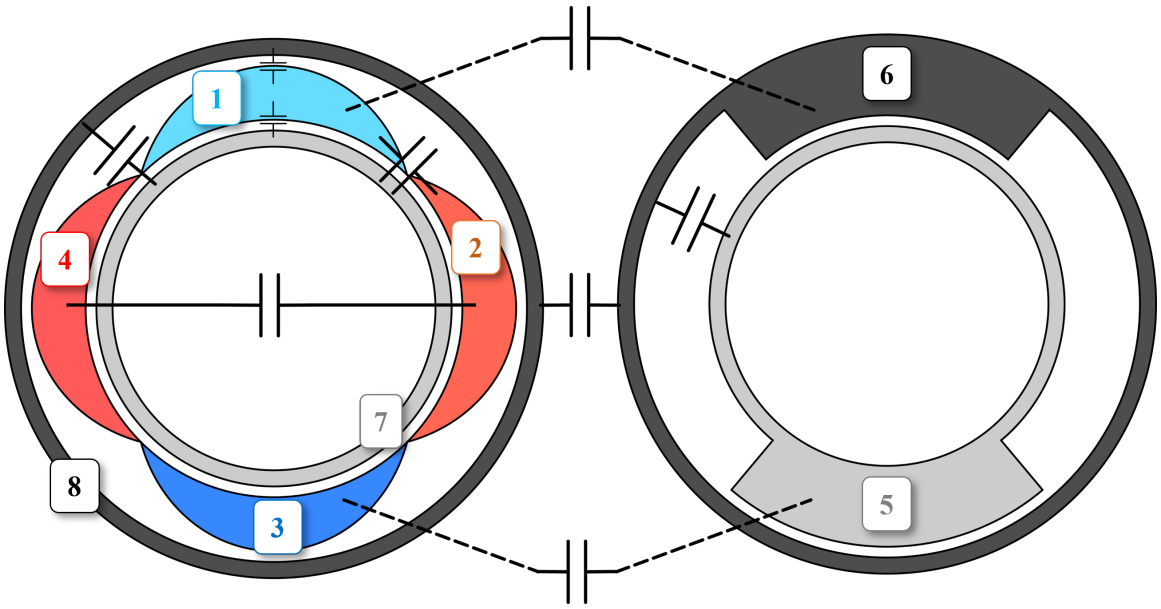

(a)

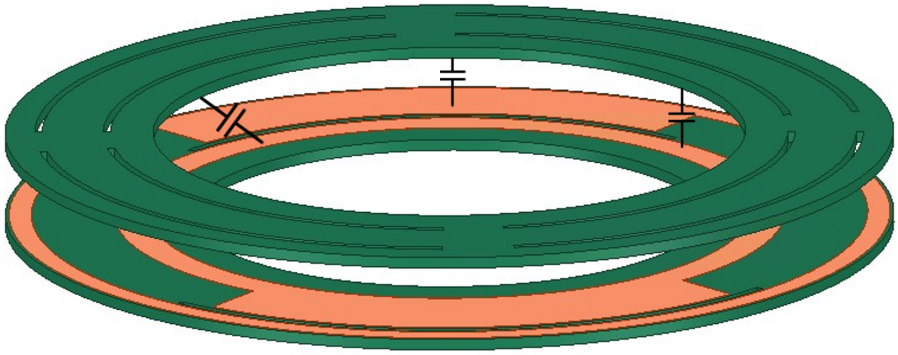

(b)

Figure 4.4: (a) Cartoon diagram labeling all 8 resolver electrodes and their mutual capacitances. (b) 3D view of the resolver with example board-to-board mutual capacitances.

$$
\begin{bmatrix} C_{11} & \dots & C_{18} \\ \vdots & \ddots & \\ C_{81} & & C_{88} \end{bmatrix} =
$$

		Stator Petals				*Rotor Excite*		*Stator Excite*	
		C_{11}	C_{12}	C_{13}	C_{14}	C_{15}	C_{16}	C_{17}	C_{18}
	Stator	C_{21}	C_{22}	C_{23}	C_{24}	C_{25}	C_{26}	C_{27}	C_{28}
	Petals	C_{31}	C_{32}	C_{33}	C_{34}	C_{35}	C_{36}	C_{37}	C_{38}
		C_{41}	C_{42}	C_{43}	C_{44}	C_{45}	C_{46}	C_{47}	C_{48}
	Rotor	C_{51}	C_{52}	C_{53}	C_{54}	C_{55}	C_{56}	C_{57}	C_{58}
	Excite	C_{61}	C_{62}	C_{63}	C_{64}	C_{65}	C_{66}	C_{67}	C_{68}
	Stator	C_{71}	C_{72}	C_{73}	C_{74}	C_{75}	C_{76}	C_{77}	C_{78}
	Excite	C_{81}	C_{82}	C_{83}	C_{84}	C_{85}	C_{86}	C_{87}	C_{88}

$=$

		Stator Petals				*Rotor Excite*		*Stator Excite*	
		$C_{s,s}$	$C_{ss,m}$	$C_{ss,m}$	$C_{ss,m}$	$C_{sr,m}$	$C_{sr,m}$	$C_{ss,m}$	$C_{ss,m}$
	Stator	$C_{ss,m}$	$C_{s,s}$	$C_{ss,m}$	$C_{ss,m}$	$C_{sr,m}$	$C_{sr,m}$	$C_{ss,m}$	$C_{ss,m}$
	Petals	$C_{ss,m}$	$C_{ss,m}$	$C_{s,s}$	$C_{ss,m}$	$C_{sr,m}$	$C_{sr,m}$	$C_{ss,m}$	$C_{ss,m}$
		$C_{ss,m}$	$C_{ss,m}$	$C_{ss,m}$	$C_{s,s}$	$C_{sr,m}$	$C_{sr,m}$	$C_{ss,m}$	$C_{ss,m}$
	Rotor	$C_{sr,m}$	$C_{sr,m}$	$C_{sr,m}$	$C_{sr,m}$	$C_{r,s}$	$C_{rr,m}$	$C_{sr,m}$	$C_{sr,m}$
	Excite	$C_{sr,m}$	$C_{sr,m}$	$C_{sr,m}$	$C_{sr,m}$	$C_{rr,m}$	$C_{r,s}$	$C_{sr,m}$	$C_{sr,m}$
	Stator	$C_{ss,m}$	$C_{ss,m}$	$C_{ss,m}$	$C_{ss,m}$	$C_{sr,m}$	$C_{sr,m}$	$C_{s,s}$	$C_{ss,r}$
	Excite	$C_{ss,m}$	$C_{ss,m}$	$C_{ss,m}$	$C_{ss,m}$	$C_{sr,m}$	$C_{sr,m}$	$C_{ss,r}$	$C_{s,s}$

(4.9)

where: $C_{s,s}$ = stator self capacitance

$C_{r,s}$ = rotor self capacitance

$C_{ss,m}$ = stator-stator mutual capacitance

$C_{sr,m}$ = stator-rotor mutual capacitance

$C_{rr,m}$ = rotor-rotor mutual capacitance

The capacitance matrix in eq. (4.9) organizes all the capacitances by their location and function according to the numbering in Figure 4.4. Additionally, it labels each capacitance as self capacitances, board-to-board capacitances, or within-board capacitances. The variables in red are the spatially varying capacitances that create the modulated waveforms, and the variables in blue, are the main, constant, excitation capacitances. Equation (4.10) is used as the basis to analyze the resolver capacitance matrix and derive the output modulated voltage waveforms.

$$\boldsymbol{Q} = \boldsymbol{C}\boldsymbol{V} \tag{4.10}$$

$$\begin{bmatrix} q_1 \\ q_2 \\ q_3 \\ q_4 \\ q_5 \\ q_6 \\ q_7 \\ q_8 \end{bmatrix} = \begin{bmatrix} C_{11} & \dots & C_{18} \\ \vdots & \ddots & \\ C_{81} & & C_{88} \end{bmatrix} \begin{bmatrix} v_1 \\ v_2 \\ v_3 \\ v_4 \\ v_5 \\ v_6 \\ V_{ex}\sin(\omega_{ex}t) \\ -V_{ex}\sin(\omega_{ex}t) \end{bmatrix} \tag{4.11}$$

Equation (4.11) shows the vector of charges and voltages present on each electrode. Currently, there are fourteen unknown variables in this system. It is assumed that the voltage is dropped across the high impedance load so charge (and voltage) on the capacitors is negligible. The following simplification can be made where:

$$\boldsymbol{Q} = [0, 0, 0, 0, 0, 0, q_7, q_8] \tag{4.12}$$

so that eq. (4.11) then has eight unknowns with eight equations. The voltages on all electrodes can easily be solved knowing the capacitance matrix of the resolver. The resulting output modulated voltages are determined by:

$$\begin{aligned} v_{sine}(\theta) &= v_3 - v_1 \\ v_{cosine}(\theta) &= v_4 - v_2 \end{aligned} \tag{4.13}$$

The capacitance matrix is not made up of coefficients. In reality, each capacitance, $C_{nm}(\theta)$ is a function of the rotor position, θ, relative to the stator. There are a few useful simplifications that can made to simplify this system. First, the stator-side excitation electrodes only exist because voltage cannot be applied to a rotating board directly. The capacitances C_{75} and C_{86} are assumed to be large and constant so that:

$$\begin{aligned} v_{stator,ex1} &= v_{rotor,ex1} \\ v_{stator,ex2} &= v_{rotor,ex2} \end{aligned} \tag{4.14}$$

and rows 7 and 8 can be removed. It is important to note that the excitation coupling capacitances need to be equal in order to make sure that the rotor-side excitation electrodes are both at the same potential given eq. (4.15).

$$\begin{aligned} V_{rotor,ex1} &= V_{stator,ex1} - \frac{i}{j\omega C_{57}} \\ V_{rotor,ex2} &= V_{stator,ex2} - \frac{i}{j\omega C_{68}} \end{aligned} \tag{4.15}$$

Additionally, all unwanted parasitic capacitances are assumed to be negligible compared to the main rotor-to-stator coupling path. Equation (4.11) then becomes eq. (4.16).

$$\begin{bmatrix} q_1 \\ q_2 \\ q_3 \\ q_4 \\ q_5 \\ q_6 \end{bmatrix} = \begin{bmatrix} C_{6x6} \end{bmatrix} \begin{bmatrix} v_1 \\ v_2 \\ v_3 \\ v_4 \\ V_{ex}\sin(\omega_{ex}t) \\ -V_{ex}\sin(\omega_{ex}t) \end{bmatrix} \tag{4.16}$$

where

$$\begin{bmatrix} C_{6x6} \end{bmatrix} = \begin{bmatrix} C_{s,s} & 0 & 0 & 0 & C_m(\theta) & C_m(\theta-\pi) \\ 0 & C_{s,s} & 0 & 0 & C_m(\theta-\frac{\pi}{2}) & C_m(\theta+\frac{\pi}{2}) \\ 0 & 0 & C_{s,s} & 0 & C_m(\theta-\pi) & C_m(\theta) \\ 0 & 0 & 0 & C_{s,s} & C_m(\theta+\frac{\pi}{2}) & C_m(\theta-\frac{\pi}{2}) \\ C_m(\theta) & C_m(\theta-\frac{\pi}{2}) & C_m(\theta-\pi) & C_m(\theta+\frac{\pi}{2}) & C_{r,s} & 0 \\ C_m(\theta-\pi) & C_m(\theta+\frac{\pi}{2}) & C_m(\theta) & C_m(\theta-\frac{\pi}{2}) & 0 & C_{r,s} \end{bmatrix}$$

In the 6x6 capacitance matrix, $C_{s,s}$ refers to the stator self-capacitances and $C_{r,s}$ refers to the rotor self-capacitances, all of which are assumed to be constant with rotor position. $C_m(\theta)$ refers to the main rotor excitation to stator petal mutual capacitances. The mutual capacitances are all the same function but each shifted by $\pm 90°$ or $\pm 180°$. Similar to above, the charge vector can be simplified assuming a high-impedance load:

$$\boldsymbol{Q} = [0, 0, 0, 0, q_5, q_6] \tag{4.17}$$

Now, eq. (4.16) can be solved with the simplified following series of equations:

$$
\begin{aligned}
0 &= C_{ss}v_1 + C_m(\theta)V_{ex}\sin(\omega_{ex}t) - C_m(\theta-\pi)V_{ex}\sin(\omega_{ex}t) \\
0 &= C_{ss}v_2 + C_m(\theta-\frac{\pi}{2})V_{ex}\sin(\omega_{ex}t) - C_m(\theta+\frac{\pi}{2})V_{ex}\sin(\omega_{ex}t) \\
0 &= C_{ss}v_3 + C_m(\theta-\pi)V_{ex}\sin(\omega_{ex}t) - C_m(\theta)V_{ex}\sin(\omega_{ex}t) \\
0 &= C_{ss}v_4 + C_m(\theta+\frac{\pi}{2})V_{ex}\sin(\omega_{ex}t) - C_m(\theta-\frac{\pi}{2})V_{ex}\sin(\omega_{ex}t) \\
q_5 &= C_m(\theta)v_1 + C_m(\theta-\frac{\pi}{2})v_2 + C_m(\theta-\pi)v_3 + C_m(\theta+\frac{\pi}{2})v_4 + C_{rs}V_{ex}sin(\omega_{ex}t) \\
q_6 &= C_m(\theta-\pi)v_1 + C_m(\theta+\frac{\pi}{2})v_2 + C_m(\theta)v_3 + C_m(\theta-\frac{\pi}{2})v_4 - C_{rs}V_{ex}sin(\omega_{ex}t)
\end{aligned}
\tag{4.18}
$$

$$
\begin{aligned}
v_1 &= -\frac{\sin(\omega_{ex}t)V_{ex}\left[C_m(\theta) - C_m(\theta-\pi)\right]}{C_{ss}} \\
v_2 &= -\frac{\sin(\omega_{ex}t)V_{ex}\left[C_m(\theta-\frac{\pi}{2}) - C_m(\theta+\frac{\pi}{2})\right]}{C_{ss}} \\
v_3 &= \frac{\sin(\omega_{ex}t)V_{ex}\left[C_m(\theta) - C_m(\theta-\pi)\right]}{C_{ss}} \\
v_4 &= \frac{\sin(\omega_{ex}t)V_{ex}\left[C_m(\theta-\frac{\pi}{2}) - C_m(\theta+\frac{\pi}{2})\right]}{C_{ss}}
\end{aligned}
\tag{4.19}
$$

$$
\begin{aligned}
v_{sine}(\theta) = v_3 - v_1 &= \frac{2\sin(\omega_{ex}t)V_{ex}\left[C_m(\theta) - C_m(\theta-\pi)\right]}{C_{ss}} \\
v_{cosine}(\theta) = v_4 - v_2 &= \frac{2\sin(\omega_{ex}t)V_{ex}\left[C_m(\theta-\frac{\pi}{2}) - C_m(\theta+\frac{\pi}{2})\right]}{C_{ss}}
\end{aligned}
\tag{4.20}
$$

If $C_m(\theta)$ is set such that the expressions $[C_m(\theta) - C_m(\theta-\pi)]$ and $[C_m(theta-\frac{\pi}{2}) - C_m(\theta+\frac{\pi}{2})]$ are equal to $\sin(\theta)$ and $\cos(\theta)$, respectively, then, eq. (4.20) will resemble the desired equations in eq. (4.2). In other words, $C_m(\theta)$ should ideally look like a half sine wave as in Figure 4.5.

The general equations used to create half sine wave electrodes are described in eq. (4.21). The series of equations describes four outer radii, one for each stator petal. The angles are given in 90° increments, but in reality each segment will be shorter than 90° so that the neighboring electrodes do not touch. Figure 4.3c denotes r_o and A_{pkpk} on the stator. Since the voltage measurements are taken as differential pairs, there will be twice as many stator petals as poles of the resolver. For example, an eight pole resolver would be sixteen stator petals but electrically connected to still yield

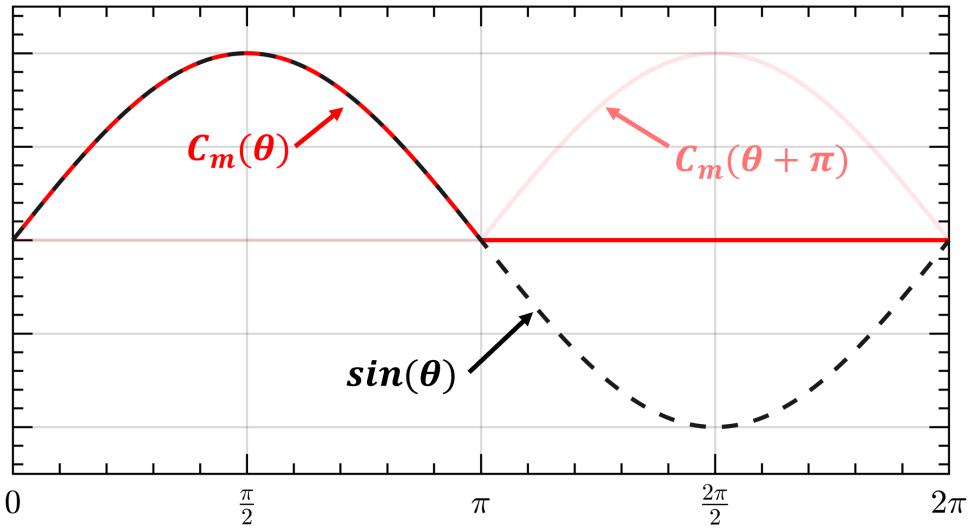

Figure 4.5: Plot showing the stator-to-rotor mutual capacitances 180° out of phase that create the modulated sinusoidal voltage waveforms

only four distinct petals. The rotor side lobes are of constant amplitude with the same angle span of the stator petals.

$$\begin{cases} r_1 = (r_o - A_{pkpk}) - A_{pkpk}\sin(2\varphi + \pi) & 0 \leqslant \varphi \leqslant \frac{\pi}{2} \\ r_2 = (r_o - A_{pkpk}) - A_{pkpk}\sin(2\varphi) & \frac{\pi}{2} \leqslant \varphi \leqslant \pi \\ r_3 = (r_o - A_{pkpk}) - A_{pkpk}\sin(2\varphi + \pi) & \pi \leqslant \varphi \leqslant \frac{3\pi}{2} \\ r_4 = (r_o - A_{pkpk}) - A_{pkpk}\sin(2\varphi) & \frac{3\pi}{2} \leqslant \varphi \leqslant 2\pi \end{cases} \tag{4.21}$$

The capacitance for two stator petals as in Figure 4.5 are derived in eq. (4.22) and eq. (4.23). It is important that while the outer edge of the petal shape has a $\sin(\theta)$ term, the resulting capacitance has a $\sin^2(\theta)$ term.

$$C_m(\theta) = \begin{cases} \frac{\varepsilon \frac{1}{2} \int_0^{\theta} [r_1 - (r_o - A_{pkpk})]^2 \, d\theta}{d} & \theta = 0 \ldots \frac{\pi}{2} \\ \frac{\varepsilon \frac{1}{2} \int_{\left(\theta - \frac{\pi}{2}\right)}^{\frac{\pi}{2}} [r_1 - (r_o - A_{pkpk})]^2 \, d\theta}{d} & \theta = \frac{\pi}{2} \ldots \pi \\ 0 & \theta = \pi \ldots \frac{3\pi}{2} \\ 0 & \theta = \frac{3\pi}{2} \ldots 2\pi \end{cases} \tag{4.22}$$

$$C_m(\theta+\pi) = \begin{cases} 0 & \theta = 0 \dots \frac{\pi}{2} \\ 0 & \theta = \frac{\pi}{2} \dots \pi \\ \frac{\varepsilon \frac{1}{2} \int_0^{\theta} [r_3 - (r_o - A_{pkpk})]^2 \, d\theta}{d} & \theta = \pi \dots \frac{3\pi}{2} \\ \frac{\varepsilon \frac{1}{2} \int_{\left(\theta - \frac{\pi}{2}\right)}^{\frac{\pi}{2}} [r_3 - (r_o - A_{pkpk})]^2 \, d\theta}{d} & \theta = \frac{3\pi}{2} \dots 2\pi \end{cases} \tag{4.23}$$

For another example, eq. (4.24) and eq. (4.25) derive the equations assuming the stator petals are constant amplitude so that they look exactly like the rotor electrodes. This creates a triangular waveform.

$$C_m(\theta) = \begin{cases} \frac{\varepsilon \frac{1}{2} \int_0^{\theta} [(r_o + g) - (r_o - A_{pkpk} - g)]^2 \, d\theta}{d} & \theta = 0 \dots \frac{\pi}{2} \\ \frac{\varepsilon \frac{1}{2} \int_{\left(\theta - \frac{\pi}{2}\right)}^{\frac{\pi}{2}} [(r_o + g) - (r_o - A_{pkpk} - g)]^2 \, d\theta}{d} & \theta = \frac{\pi}{2} \dots \pi \\ 0 & \theta = \pi \dots \frac{3\pi}{2} \\ 0 & \theta = \frac{3\pi}{2} \dots 2\pi \end{cases} \tag{4.24}$$

$$C_m(\theta+\pi) = \begin{cases} 0 & \theta = 0 \dots \frac{\pi}{2} \\ 0 & \theta = \frac{\pi}{2} \dots \pi \\ \frac{\varepsilon \frac{1}{2} \int_0^{\theta} [(r_o + g) - (r_o - A_{pkpk} - g)]^2 \, d\theta}{d} & \theta = \pi \dots \frac{3\pi}{2} \\ \frac{\varepsilon \frac{1}{2} \int_{\left(\theta - \frac{\pi}{2}\right)}^{\frac{\pi}{2}} [(r_o + g) - (r_o - A_{pkpk} - g)]^2 \, d\theta}{d} & \theta = \frac{3\pi}{2} \dots 2\pi \end{cases} \tag{4.25}$$

Figure 4.6 shows the predicted capacitance in picofarads for the sinusoidal and constant amplitude petal shapes derived in eq. (4.22) and eq. (4.23). The constant amplitude is also referred to as the triangle petal shape derived in eq. (4.24) and eq. (4.25). Additionally, Figure 4.7 shows the analytically calculated error in degrees for the sinusoidal and triangle shapes compared to a perfect sine wave shown in black. The theoretical peak degree errors from ideal are 11.8° for the sinusoidal petal shape and 4.1° for the constant amplitude petals, also referred to as the triangle shape. These angles are quite high, however they are only considering the main coupling capacitance without any parasitic capacitance effect. It is interesting that the constant amplitude/triangle shape has a lower predicted error. The following section uses FEA to understand how the parasitic capacitances can affect the modulation equations.

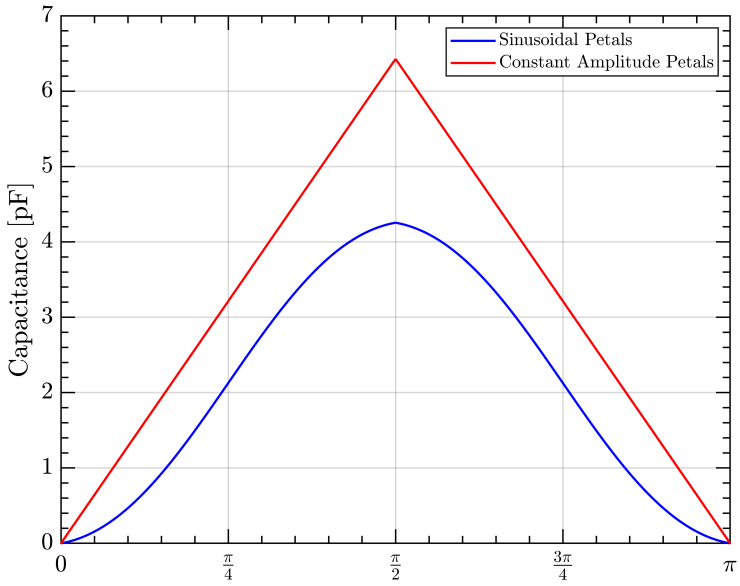

Figure 4.6: Plots of the capacitance calculations from eq. (4.22) and eq. (4.24).

4.3 Capacitive Resolver FEA

As mentioned above, in order to analyze the capacitive resolver it is necessary to know the full capacitance matrix. A simplified version is helpful to determine the general stator electrode petal shape, but the parasitic capacitances can also affect the resulting resolver output voltage waveforms in significant ways. FEA is necessary to get a full picture of a given resolver design. In this work, FEA was carried out using the 3D electrostatic solver in Ansys Maxwell. The electrostatic solver is limited to DC excitation. While an electric transient solver was available, the additional complexity was deemed unnecessary to rapidly evaluate different resolver designs and their predicted performance.

Figure 4.8 shows diagrams of example stator and rotor boards along with dimensions in Ansys Maxwell. The dimensions shown are for the final resolver design. There were a few different iterations as will be seen in the following FEA. The copper excitation electrodes are in black and white for the rotor and stator boards. Additionally, the four copper stator petals are shown in copper. The FR4 material of the stator and rotor PCBs is colored in green. 1mm-wide cutouts are added on both the rotor and stator boards to mitigate parasitic capacitances between electrodes on the same board. Each board is shown from a front on view to show the electrodes, but in the simulation, the two boards are facing each other as shown in Figure 4.8c with a 1mm air gap. The PCBs are of standard 0.062in (1.6mm) thickness.

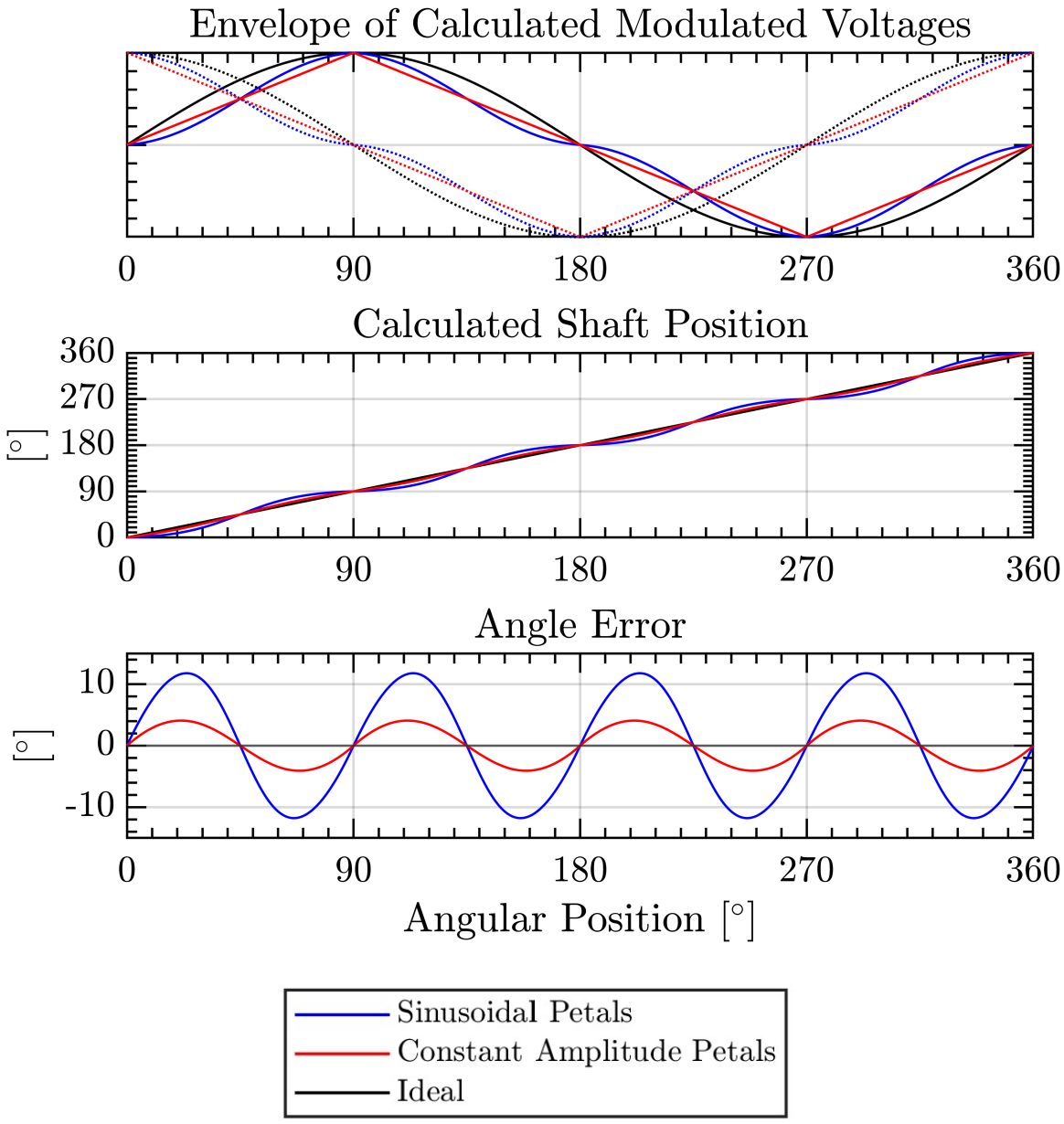

Figure 4.7: Plots of the analytically derived voltage modulation envelope and predicted error in degrees for sinusoidal and constant amplitude stator petal shapes.

During the 3D simulation, the rotor board is rotated about the z-axis and all the capacitance matrix values in eq. (4.9) are captured at 5° increments. Over a full 360° rotation, a $C(\theta)$ function can be approximated for each capacitance. Then, using MATLAB all of the resolver output voltages can be solved for exactly using eq. (4.11). Figure 4.9 shows an example of the resolver output voltage calculated using eq. (4.13). The excitation frequency is 20kHz with a 100Hz rotational frequency.

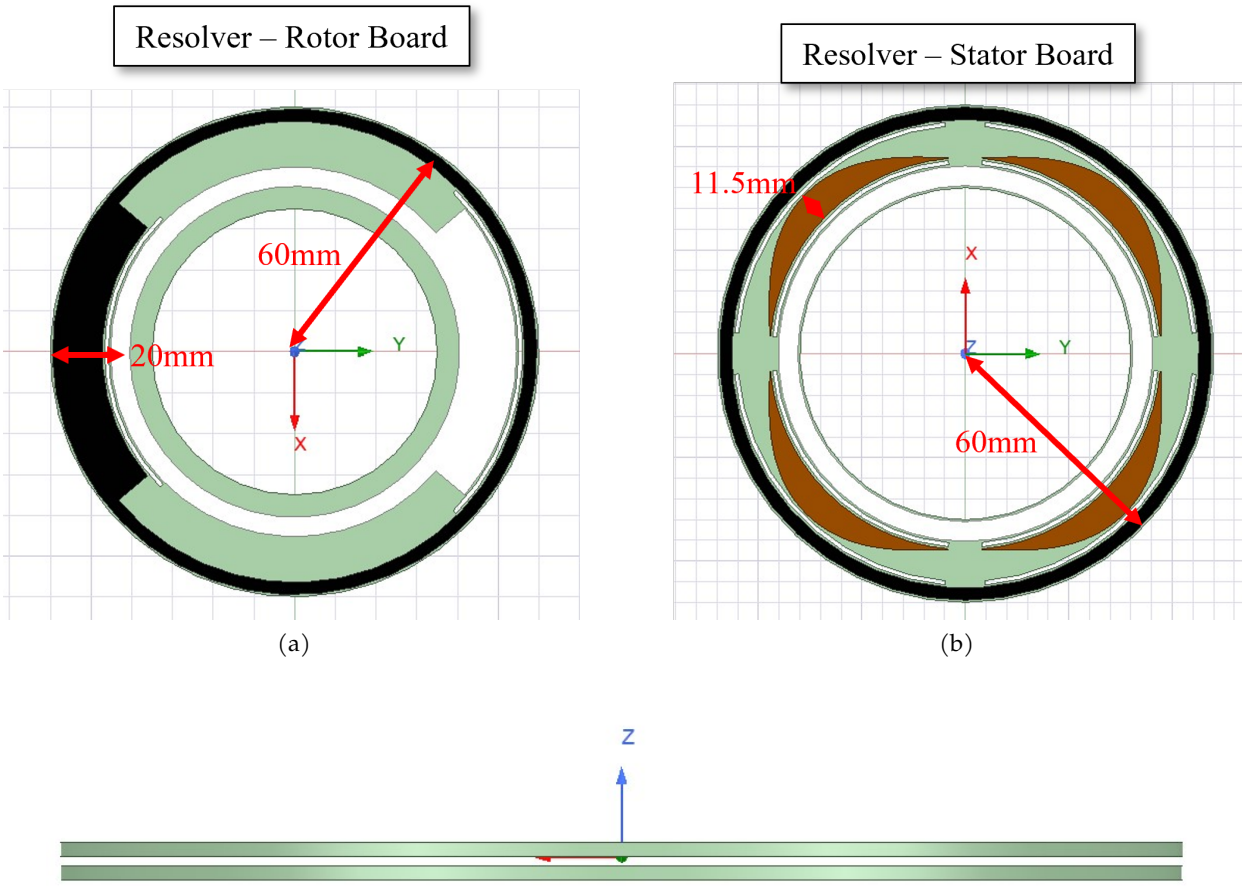

Figure 4.8: Annotated screenshots from FEA in Ansys Maxwell of the resolver (a) rotor board, (b) stator board, and (c) the 3D side view with a 1mm air gap.

Many different iterations are shown below with a need to quantify the accurateness of a given resolver design. Ultimately, the best resolver design will have the lowest position angle error. The best design would be the closest to producing ideal sine and cosine envelopes. Using Fourier analysis, an FFT generates all of the harmonics present for a given resolver design. By extracting the fundamental component, the design can be compared to its ideal reference without harmonics.

The MATLAB FFT gives magnitude, M_h, frequency, f_h, and phase, ϕ_h for all h harmonics present in the differential voltage waveform. The ideal waveform only contains the fundamental component:

$$v_{h=1} = M_1 \cos(2\pi f_1 t + \phi_1) \tag{4.26}$$

The reference position is then calculated using eq. (4.4).

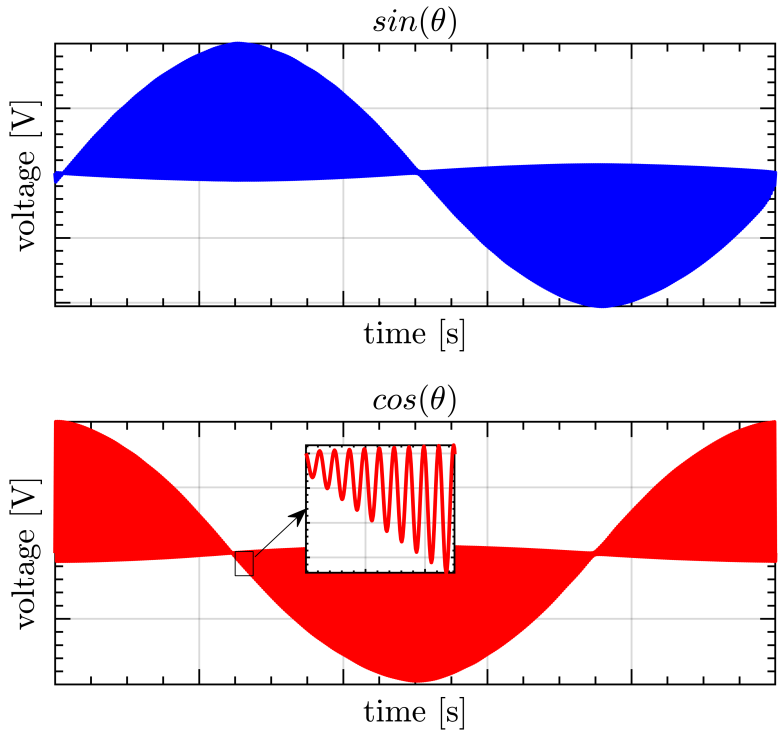

Figure 4.9: Plots from MATLAB calculating the modulated sine and cosine voltage waveforms derived from the full 8x8 capacitance matrix in FEA.

$$\theta_{reference} = \tan^{-1}\left(\frac{M_{sin,1}\cos(2\pi f_{sin,1}t + \phi_{sin,1})}{M_{cos,1}\cos(2\pi f_{cos,1}t + \phi_{cos,1})}\right) \tag{4.27}$$

Then to find the actual angle for a given FEA simulation run, the first 100 harmonics, or however many are desired to include, are used in eq. (4.28).

$$\theta_{FEA} = \tan^{-1}\left(\frac{\sum_{n=1}^{100} M_{sin,n}\cos(2\pi f_{sin,n}t + \phi_{sin,n})}{\sum_{n=1}^{100} M_{cos,n}\cos(2\pi f_{cos,n}t + \phi_{cos,n})}\right) \tag{4.28}$$

If the voltage waveforms had perfect sine and cosine envelopes, they would give the position exactly. Using the above analysis quantifies how the parasitic capacitances that produce the higher-order harmonics negatively affect the resolver accuracy.

The following simulations look at how well the resolver petal shape responds to mechanical mounting or alignment issues. The resolver will never be mounted perfectly, so it is important to see how the design is affected by alignment issues. Figure 4.10 shows the two alignment issues considered. Figure 4.10a exaggerates the two boards tilted relative to each otherİn the simulation, with a 1mm air gap, the rotor board is rotated along the y-axis at an angle of 0.5°. Figure 4.10b

shows a shift of the rotor board, dark green, in the xy-plane.

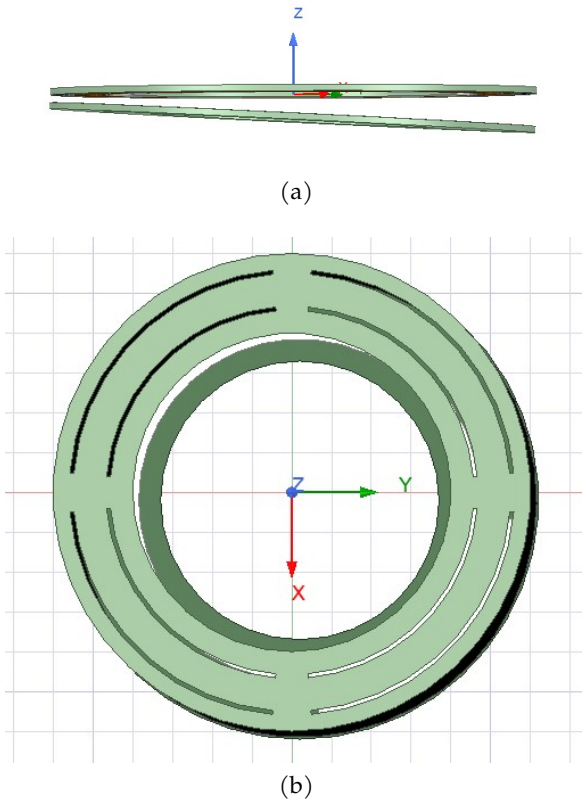

Figure 4.10: Screenshots from Ansys Maxwell showing the resolver boards with (a) tilt, and (b) XY-plane displacement.

The first design comparison looks at the relative magnitudes between the stator petals and rotor excitation lobes. Initially, it was hypothesized that the resolver could reject disturbances from mechanical alignment better if the rotor amplitude electrodes were larger than the stator petals. In this way, the rotor could move as it was rotating but still fully cover the stator petals as intended. The oversized rotor electrode condition is called the "overhang" design; whereas the original design is referred to as "no overhang." Figure 4.11 summaries the FEA from comparing the two designs. Figure 4.11a and Figure 4.11b show the resulting sine and cosine voltage envelopes, the plotted actual vs. reference angular position and then the expect angular error for two revolutions. The calculated angular position is solid black with the reference position overlayed in grey. It is evident that the small oscillations around the reference position translate into large expected errors.

Figure 4.11c and Figure 4.11d show the FFT of the no-overhang and overhang designs for the first ten harmonics. The harmonic magnitudes are scaled to the fundamental, $M_1 = 1$, which is not

shown. Higher order harmonics $> M_{10}$ are included in the position error calculation, but are not shown here for clarity. For both designs only odd harmonics are present in the waveform, with a dominant third harmonic. The third harmonic can clearly be seen in the differential voltages by the flat region present in each waveform.

Table 4.1 shows a summary of the expected peak angular position errors for each mechanical alignment issue. Specifically, resolver topologies are considered with and without electrode overhang. As anticipated, the overhang version appears to have lower error for all cases with and without alignment issues. Interestingly, the mechanical alignment issues do not appear to negatively affect the overall error and the presence of a slight y-axis tilt actually improves the error. It is possible that from the symmetry of the boards, any misalignment issues are mitigated when taking the differential of the output voltages.

	No Overhang	**Overhang**
Aligned	$\pm 10.3°$	$\pm 7.3°$
XY-Plane Displacement	$\pm 8.4°$	$\pm 6.2°$
Tilt	$\pm 10.5°$	$\pm 7.5°$
Displacement+Tilt	$\pm 8.7°$	$\pm 6.1°$

Table 4.1: Calculated peak position errors in degrees from Ansys Maxwell FEA simulations. Comparing different types of board misalignments.

The next condition to consider came about after the design and testing of first round of resolver PCBs. All of the stator petal voltages must be able to be connected to external filtering circuitry in some way. The first attempt was to route traces from each stator petal to a common connector on the back-side of the board opposite to the electrode side. This connector would also provide the two voltage signals for the excitation electrodes. Figure 4.12a and Figure 4.12b show two different methods for connecting the traces to a connector on the upper right hand side of each board. The view is looking at the bottom of the board with the FR4 PCB mostly transparent to see the stator electrodes on the top-side. Figure 4.12a aimed to keep the length of each return trace equal whereas Figure 4.12b aimed to keep the return paths as symmetric/identical as possible for each electrode. In either case, the additional electrodes significantly increased the error of the resolver.

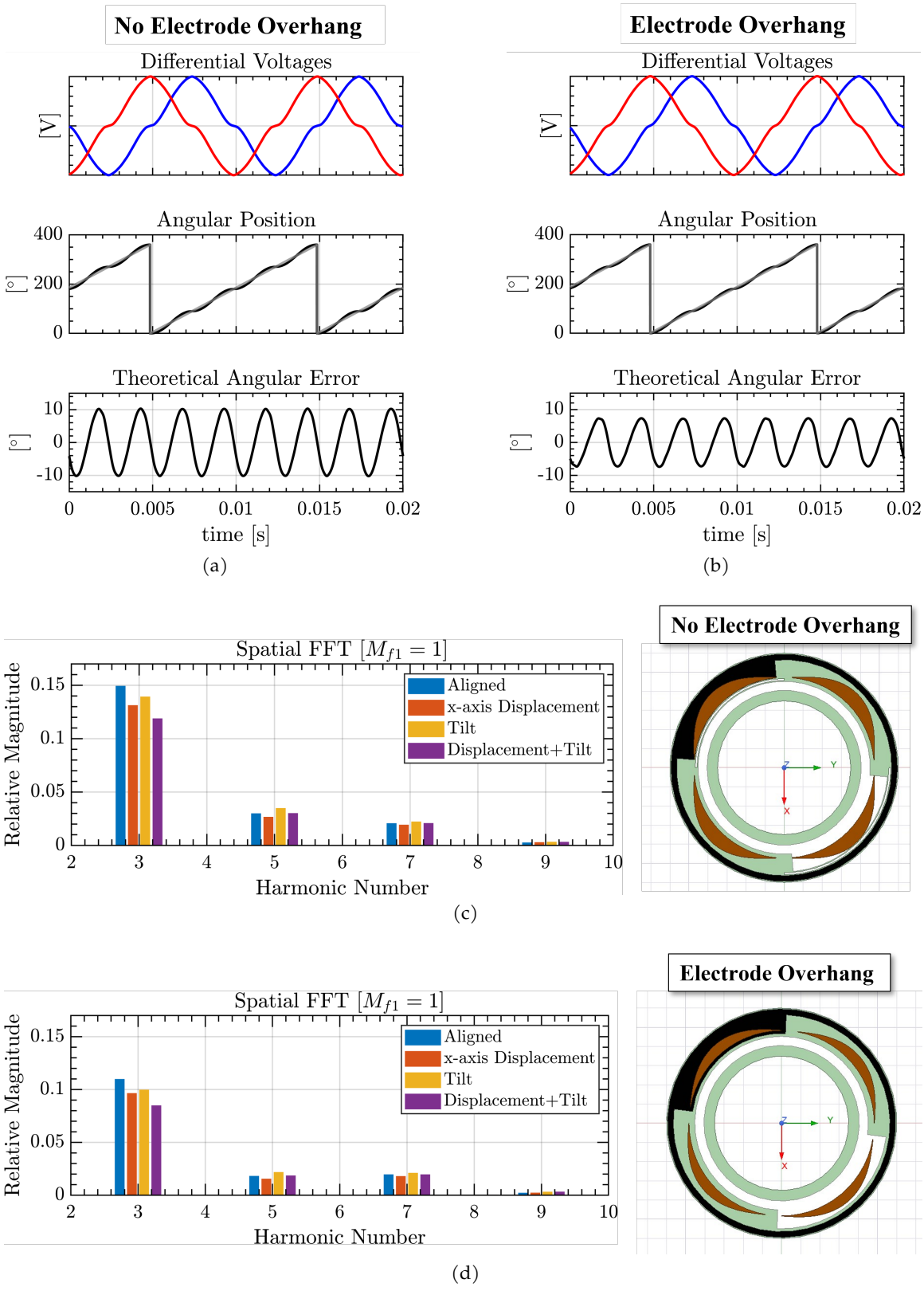

Figure 4.11: Summary of FEA results looking at designs with and without overhang between the rotor and stator pick-up electrodes.

The next step changed the stator board from a 2-layer to a 4-layer PCB to add in ground (GND) planes to act as a quasi Faraday cage for the return electrodes. The layer configuration is detailed in Table 4.2.

	4-Layer Stator Stackup
Layer 1	Resolver Electrodes
Layer 2	-GND Plane-
Layer 3	Return Traces
Layer 4	- GND Plane-

Table 4.2: Layer stack-up of the stator board with connector return traces and ground planes.

Visually, the top waveforms in Figure 4.12c and Figure 4.12d are far from ideal and the amplitudes are different as if the excitation path capacitances are no longer equal. From the FFT in Figure 4.12e, the waveform distortion arises from small amounts of even harmonics present. While the addition of the ground plane makes two differential voltages nearly identical, it also significantly increases the third harmonic. Additionally, the ground plane significantly reduces the amplitude of the output resolver signals. Table 4.3 summarizes the expected position errors for each of the four cases. The errors are significantly worse than the original case in Figure 4.11 so much so that traces are avoided for all future design iterations. Instead all connections are made using board-to-board connectors.

	Non-Symmetric	**Symmetric**
2-Layer Board	$\pm 14.2^\circ$	$\pm 24.3^\circ$
4-Layer with GND Planes	$\pm 19.0^\circ$	$\pm 18.9^\circ$

Table 4.3: Calculated peak position errors in degrees from Ansys Maxwell FEA simulations. Comparing stator boards with connector traces and additional grounding planes.

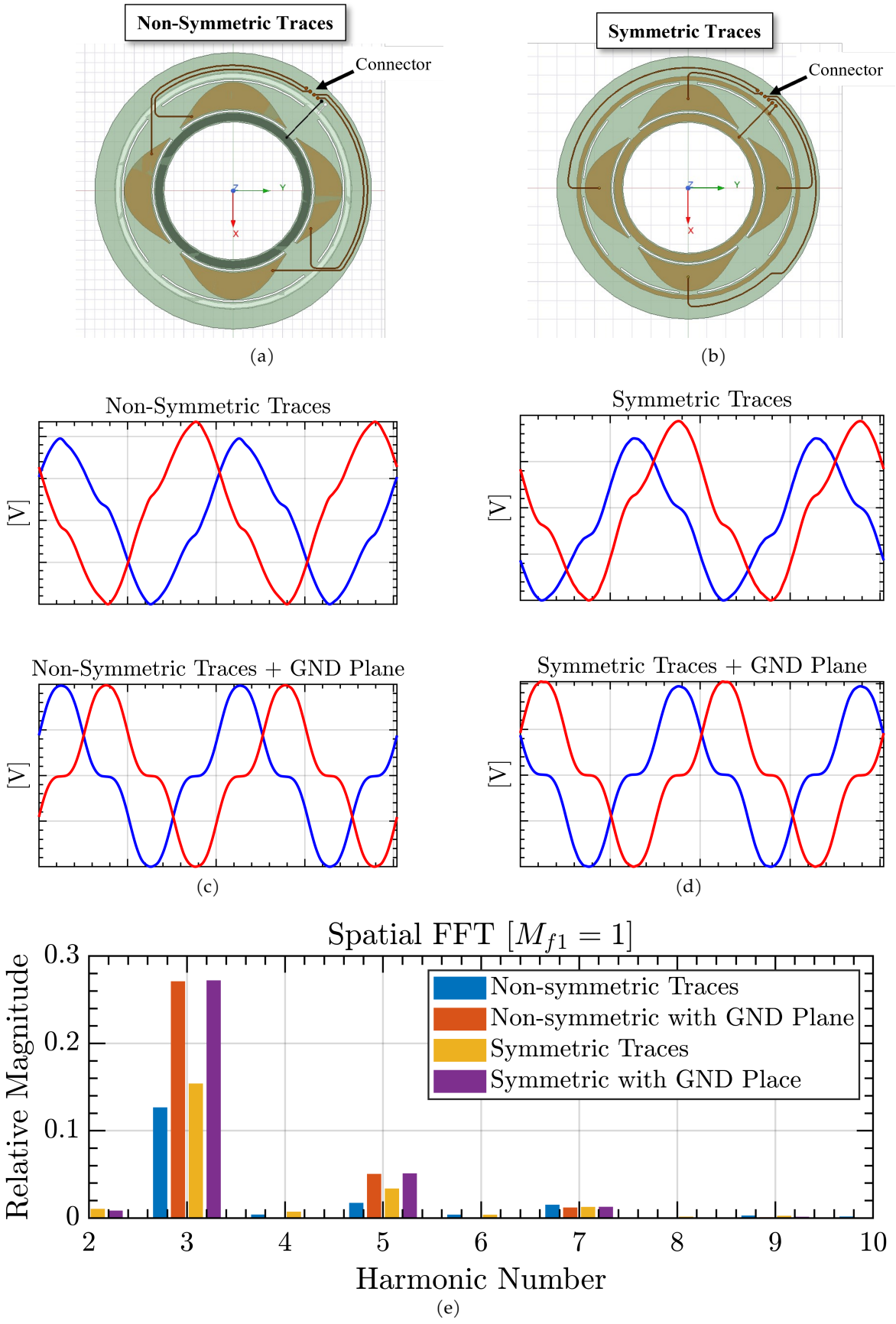

Figure 4.12: FEA results of simulations with connector traces

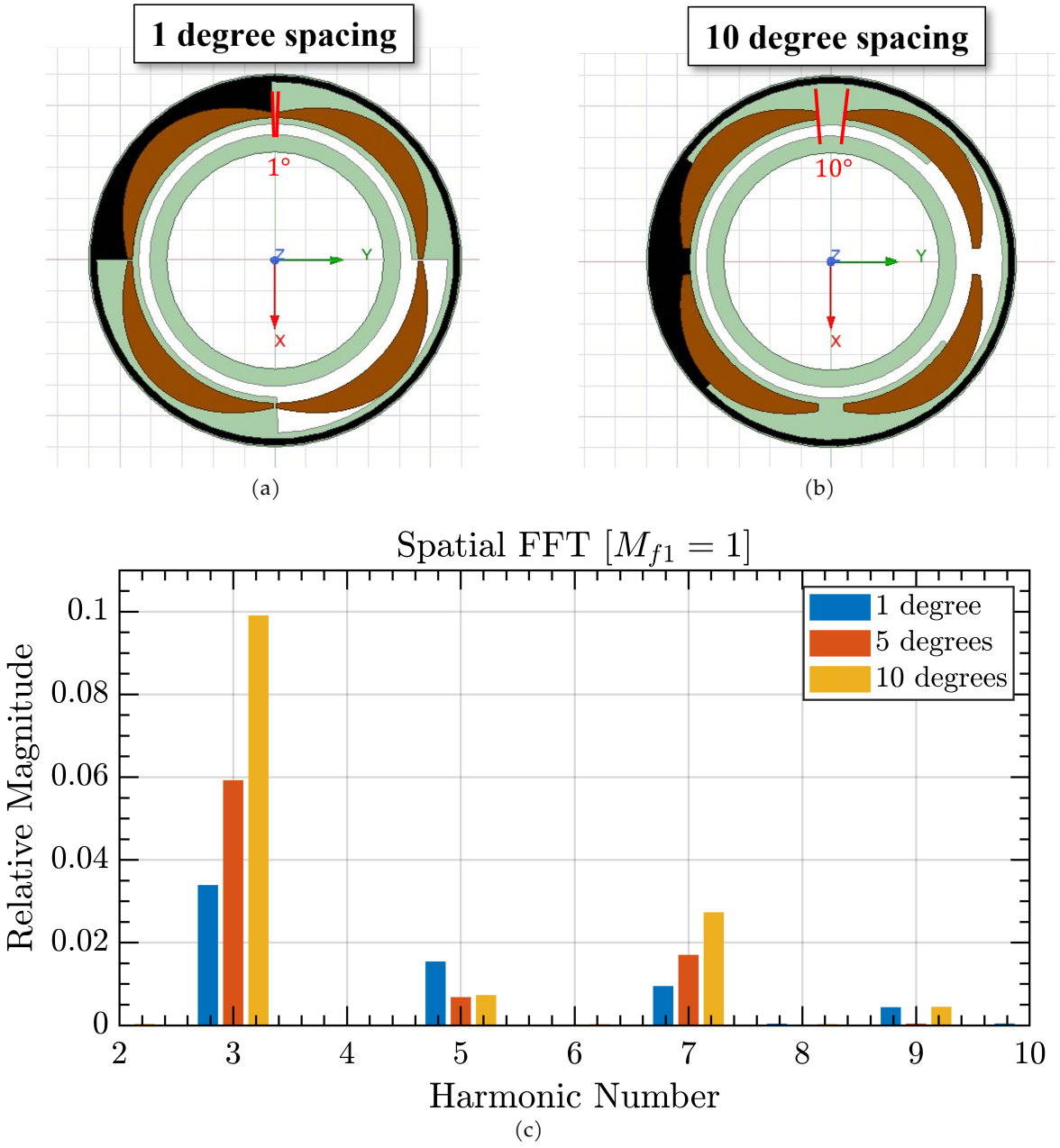

Figure 4.13: Summary of FEA results looking at different stator-side petal electrode spacing.

The next set of Maxwell FEA simulations look at removing the third harmonic stubbornly present to a large degree in all designs thus far. The third harmonic comes about from flat regions when crossing 0V on the x-axis that were predicted from the initial analytical calculations. The angle between the stator petals was originally set to 10 degrees to reduce the parasitic capacitance between neighboring petals. This gap could exasperate the flat regions present in the voltage waveforms.

Figure 4.13 looks at reducing the spacing from 10 degrees, to 1 degree of separation. It was easiest to quantify the spacing in terms of degrees instead of a distance measurement that would change with different electrode radii. It is clear from both the FFT that the harmonic magnitudes are higher as the stator petal separation increases. Table 4.4 shows the errors for each petal separation and confirms that the error reduces dramatically as the gap diminishes. From here on, all designs have a minimal stator petal gap.

1 Degree	**5 Degrees**	**10 Degrees**
$\pm 1.3^\circ$	$\pm 3.3^\circ$	$\pm 6.5^\circ$

Table 4.4: Calculated angle error, in degrees, from FEA simulations of different stator-side petal electrode spacing.

Numerous iterations and small adjusts of the stator electrodes produced the final, best case design with a predicted error of $\pm 0.32^\circ$. The optimal design is shown in Figure 4.14. The voltage waveform ends up looking like a cross between a perfect triangle wave and a sinusoid. The constant stator petal amplitude electrode, or triangle, design is shown on the right for comparison.

	Normal	**Shallow Curve**	**Triangle**
No Overhang	$\pm 1.3^\circ$	$\pm$**0.3**$^\circ$	$\pm 2.3^\circ$
Overhang	$\pm 2.2^\circ$	$\pm 0.7^\circ$	$\pm 0.7^\circ$

Table 4.5: Calculated angle error, in degrees, from FEA simulations of final stator petal configuration comparisons.

Only a few of the iterations are compared. The comparison of final electrode topologies in Figure 4.15 includes the overlapping and non-overlapping versions of the sinusoid as well as triangle wave shapes. Additionally, there is a "shallow" version that looks at decreasing the curvature of the stator petals to emulate the triangle wave. This is not unexpected as the initial analysis pointed out that a more triangle waveform would have lower error than the $\sin^2(\theta)$ counterpart. From the FFT comparison it is interesting to note that some of the designs have lower third-harmonic components than the labeled "best" design (sinusoid - exact shallow in the figure). It was a deliberate choice to use angle error as the measure for optimal electrode design, not necessarily reduction of total harmonics. Also note that only the first ten harmonics are shown for clarity and spacing.

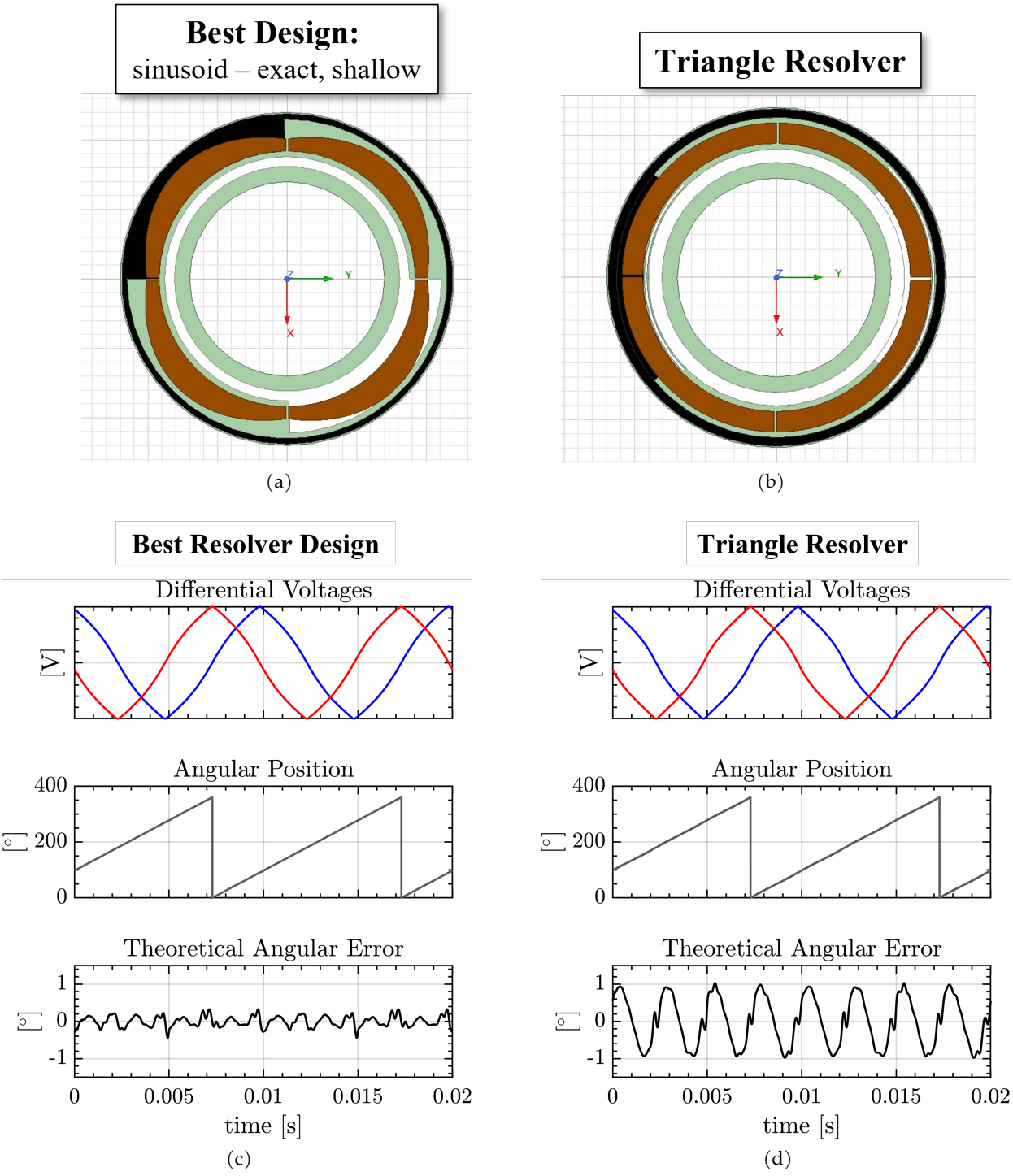

Figure 4.14: Summary of FEA results comparing the design with the lowest calculated error and the constant petal amplitude design.

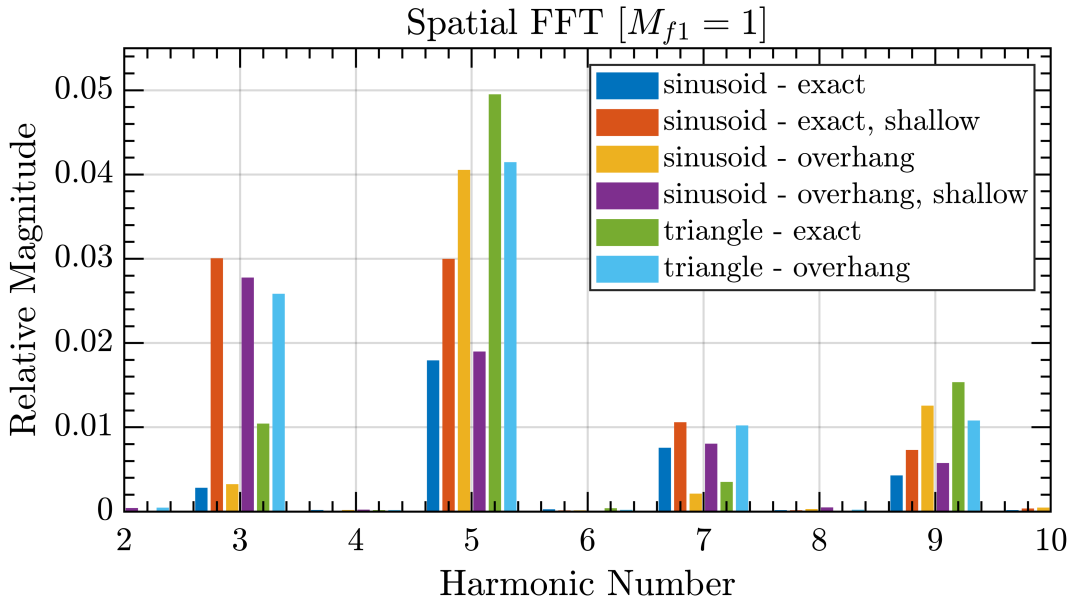

Figure 4.15: FFT comparing the spatial harmonics above the fundamental for sinusoidal and constant amplitude stator petal shapes.

While all of the designs thus far have been two pole designs, it is feasible to scale the resolver up to any number of poles. Figure 4.16 shows examples comparing the chosen two-pole resolver topology with four and eight-pole versions. The four and eight pole versions are drawn using eq. (4.21) as their designs were not optimized further. The FEA simulations were still carried out in 5 electrical degree increments. Table 4.6 shows the the peak angle error expected for the resolver extrapolated out to 2, 4, and 8-poles. The error is expected to get worse at higher pole counts.

2 Poles	**4 Poles**	**8 Poles**
±0.3°	±2.1°	±2.0°

Table 4.6: Peak angle error, in degrees, from FEA for resolvers with 2, 4, and 8 poles.

This resolver design is easily adapted for the CPC system. Figure 4.17 shows the rotor and stator for the CPC integrated resolver models used in Maxwell. Both excitation signals are able to come from the two electrodes on the rotor side for the forward and return path of the capacitive coupler. The radial height of the rotor and stator resolver electrodes are kept roughly the same, 9.5mm versus 11.5mm, with the general purpose resolver boards from above. The diodes of the rectifier are not shown on the FEA diagram but would be in the center of the rotor board as shown

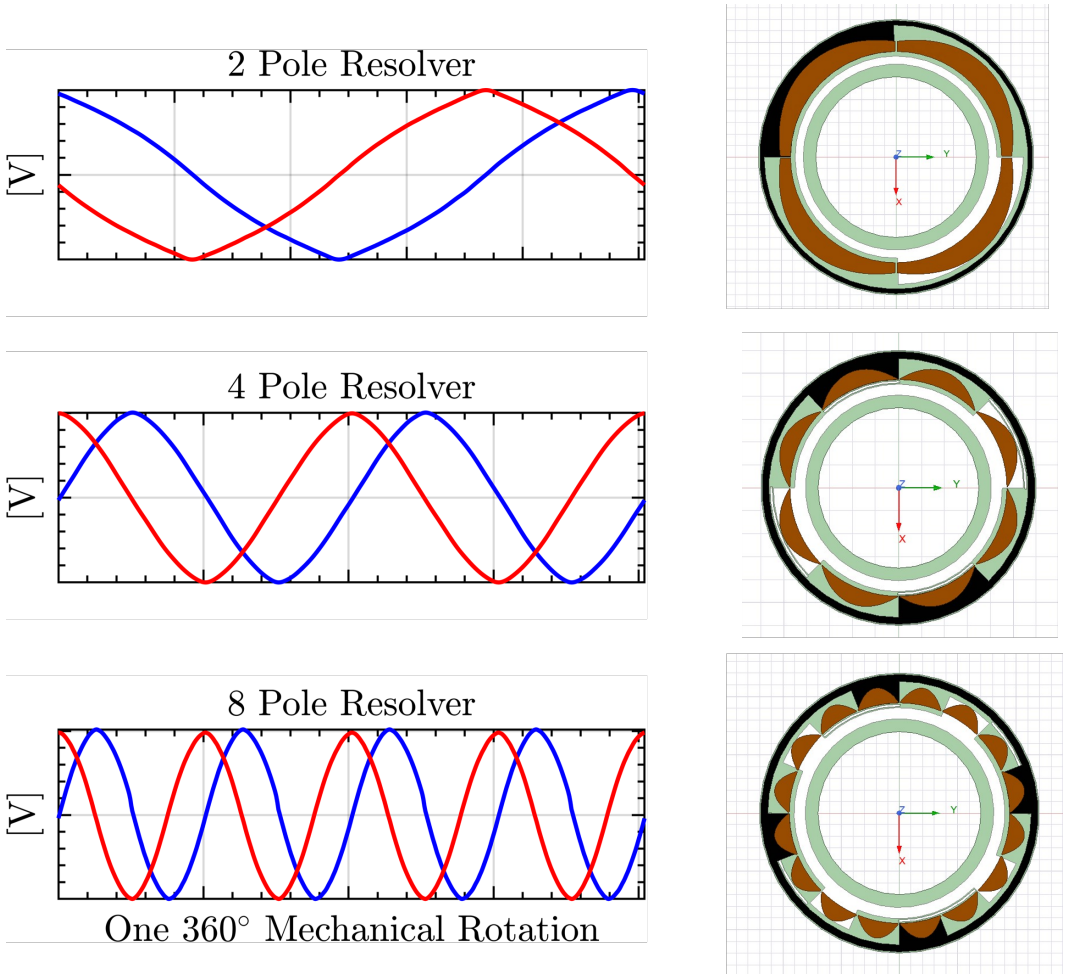

(a)

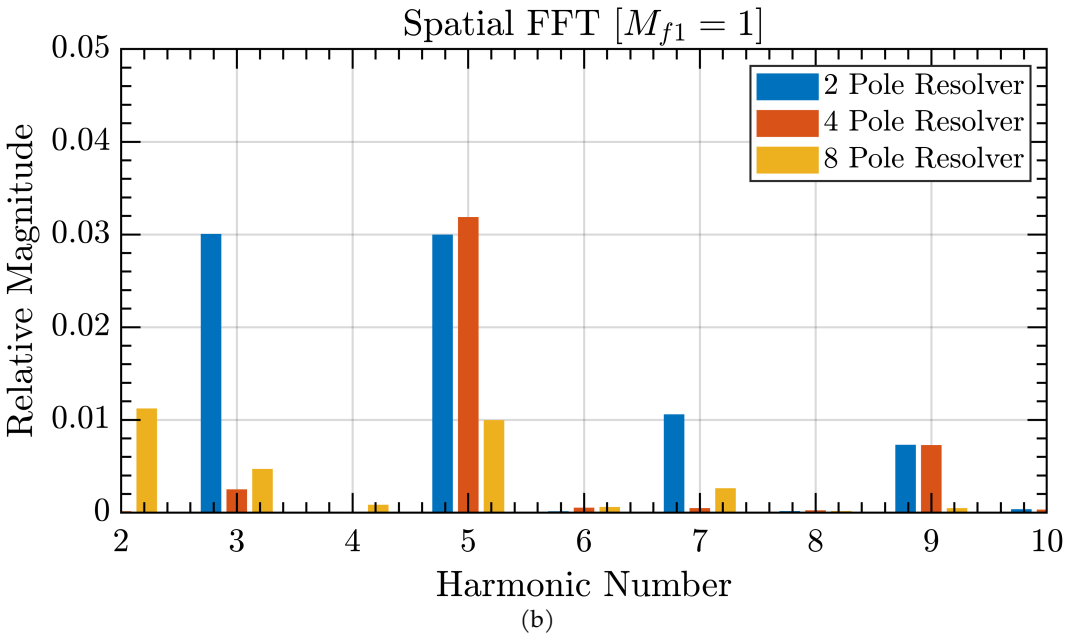

(b)

Figure 4.16: Ansys Maxwell FEA results of the resolver design extended to 2, 4, and 8-poles

in chapter 3. Additionally, the outer radius of the rotor and stator boards are kept the same for mounting purposes and the capacitive coupling area of the power path electrodes are shrunk in the radial direction to make room for the resolver functionality. For the testing in chapter 5, the CPC now has a lower capacitance resulting in a higher inductance required to maintain the same $\approx$ 6.78MHz LC resonance point.

Figure 4.18 shows the two-pole, four-pole, and eight-pole versions of the CPC boards with integrated resolver in FEA and their corresponding waveforms. The simulation took capacitance calculations at each five electrical degree step. Table 4.7 shows there resulting error for each version, as well. The lowest error condition ended up using the equations from eq. (4.21) and the adjusted lower amplitude no longer had the lowest error at the larger radius. There is an increase in error going to higher pole counts likely from adding an outer ring to the rotor-side board to connect the excitation electrodes together. However, as the pole count increases, the shaft angular error is expected to decrease. The CPC-resolver boards will be further analyzed in the context of the whole CPT system in chapter 5.

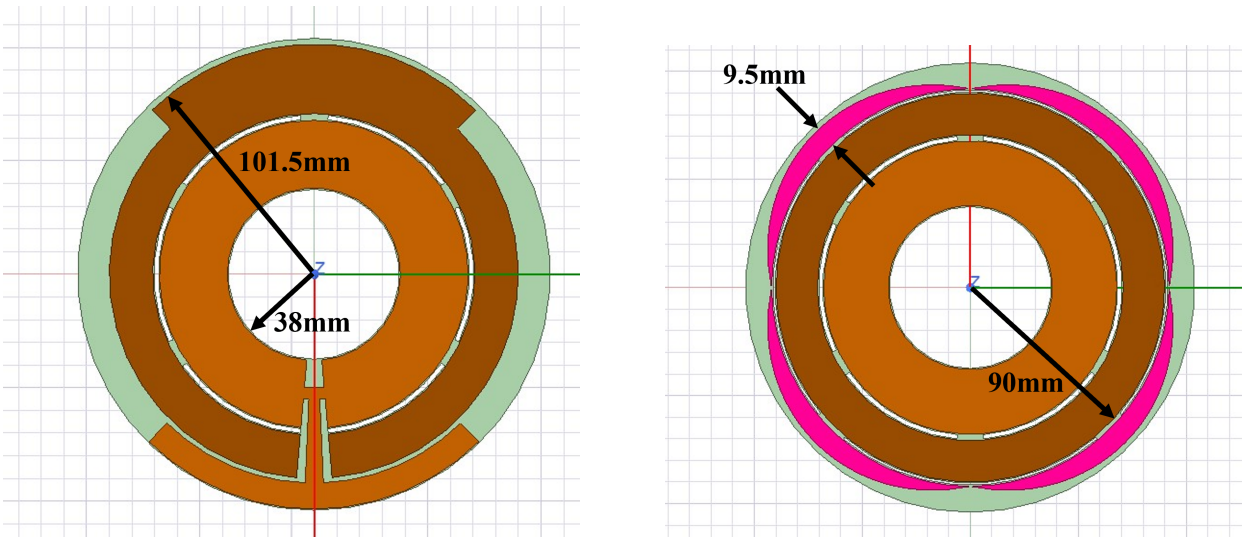

(a) (b)

Figure 4.17: Annotated diagrams of the CPC-integrated resolver (a) rotor board and (b) stator board. The stator petal electrodes are highlighted in pink.

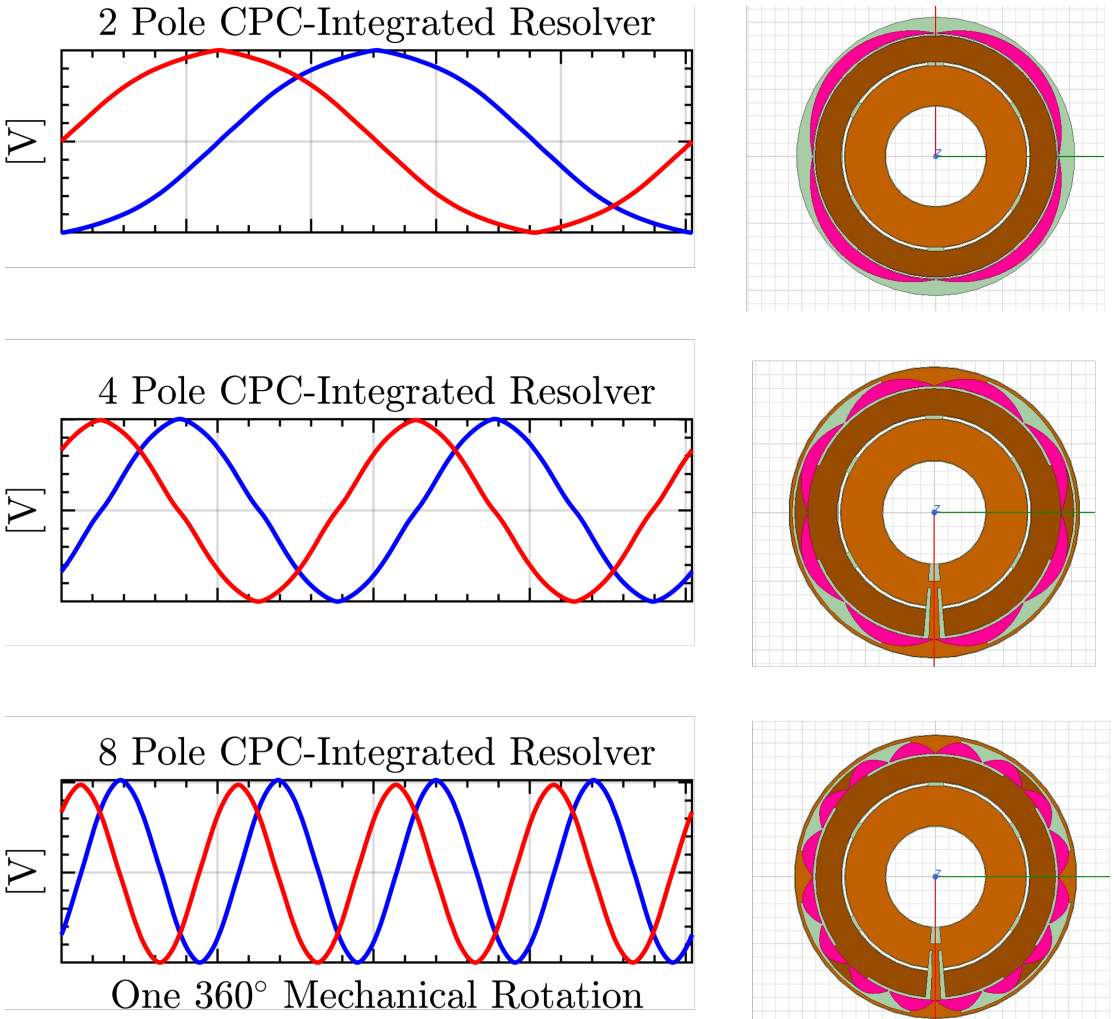

(a)

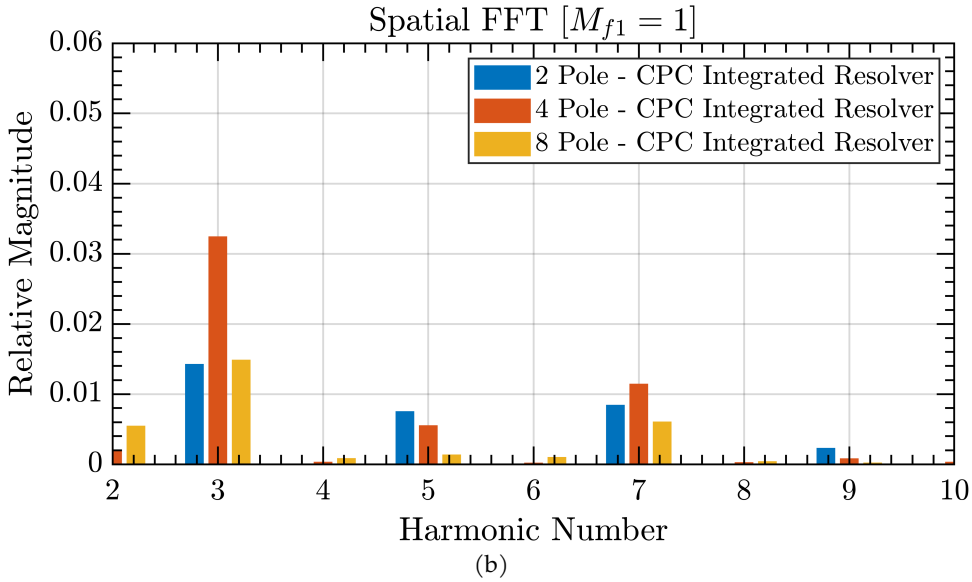

(b)

Figure 4.18: Ansys Maxwell FEA results of the CPC-integrated resolver design extended to 2, 4, and 8-poles

CPC - 2 Poles	CPC - 4 Poles	CPC - 8 Poles
$\pm 1.1^\circ$	$\pm 2.9^\circ$	$\pm 2.7^\circ$

Table 4.7: Peak angle error, in degrees, from FEA for CPC-integrated resolvers with 2, 4, and 8 poles.

4.4 Concluding Remarks

The proposed integrated resolver and rotating rectifier system serves as a further step to replace permanent magnet machines in traction applications with wound field synchronous machines. The capacitive resolver design is compatible with traditional magnetic resolvers in that it takes in a single-phase voltage waveform, and outputs two sinusoidallly modulated voltage waveforms 90° out-of-phase. The following are a list of design guidelines for designing the capacitive resolver:

- The two stator-to-rotor excitation electrode rings should be equal areas. This ensures that the capacitances C_{57} and C_{68} in Figure 4.4a will also be equal.
- Prioritize making the stator petal electrodes thicker instead of the stator-to-rotor excitation electrodes.
- Do not have traces routed on top of the electrodes on different board layers. The traces add enough picofarads of capacitance to significantly distort the modulated output voltage waveforms. Instead, add connectors or wires coming directly from each electrode on the stator board.
- Some amount of board misalignment is inevitable. Make sure the FEA simulations Include displacement and tilt in FEA simulations to see how it effects the resulting angle error.
- Keep the space between stator petal electrodes as small as possible to avoid having large sections of 0pF that create a large third spatial harmonic.

The capacitive resolver is theoretically expected to have a max shaft angle error of $\pm 0.3^\circ$ independent of rotor speed or excitation frequency. Conversely, the CPC-integrated resolver is expected to have a slightly worse shaft angle error of 1.1°. Both resolvers will be evaluated for their performance and accuracy in chapter 5.

Chapter Five

Capacitive Resolver Testing and Evaluation

5.1 Full System Overview

This chapter discusses the testing setup and results for the integrated capacitive resolver and rectifier to support the reduction in cost for wound field synchronous machines. The general integrated resolver and rectifier is a drop in solution for any rotor field wireless exciter application. This integration removes the need for a separate resolver component and is intended to be compatible with existing resolver demodulation algorithms. The first sections of this chapter show the results of the general resolver performance with an analog and digital demodulation, while the last section gives the results of the CPC-integrated resolver.

Figure 5.1 shows the overall diagram of the integrated resolver and rectifier. A rotary transformer example is shown, but this can represent any electromagnetic-based air-gap wireless exciter. Everything colored in blue is on the stationary board, and everything on the rotating board is green. A single-phase inverter provides the AC power on the stationary side and the rectifier converts back to DC and is connected directly to the terminals of the field winding. The two differential output signals, V_{sine} and V_{cosine} are the modulated signals going to separate filter circuitry not shown.

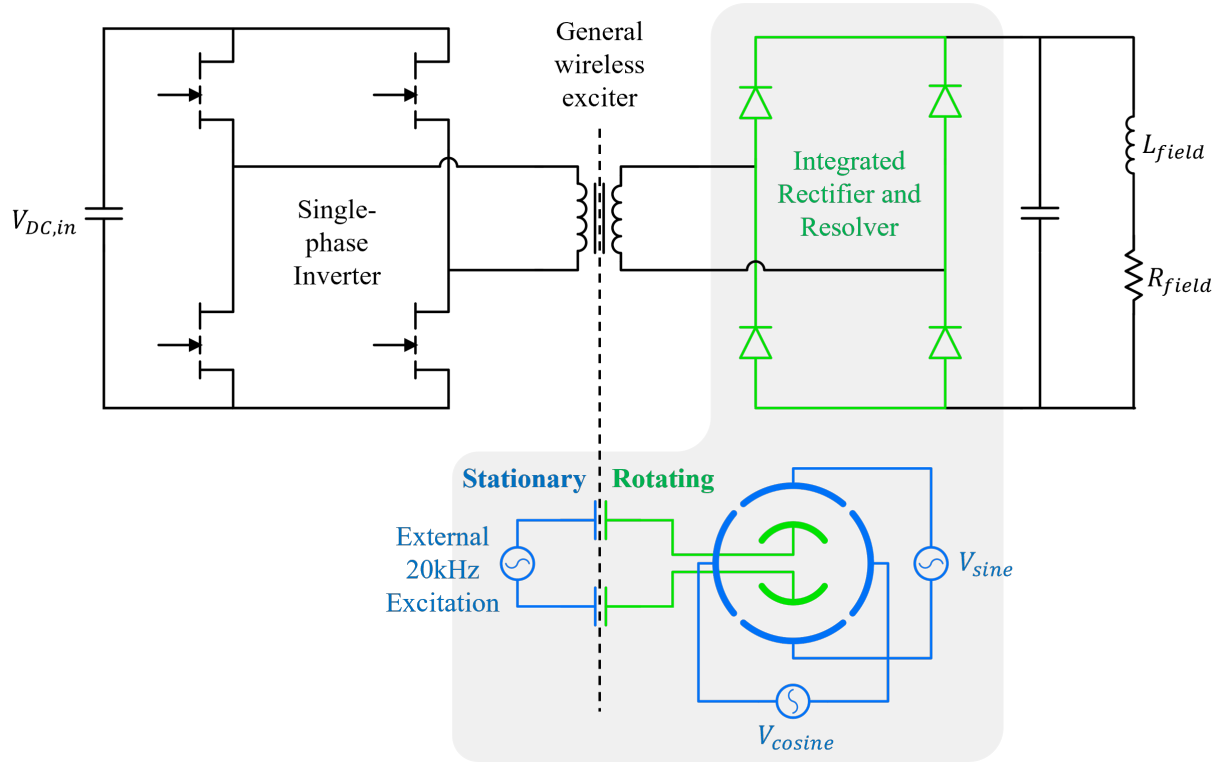

Figure 5.1: Diagram of general wireless excitation system showing the capacitive resolver integration and operation.

5.2 Initial Resolver Prototype

Figure 5.2 shows pictures of the first iteration of the capacitive resolver. There is no rectifier present on this revision and is intended only to test out the resolver functionality. Figure 5.2a and Figure 5.2b show the top and bottom sides of the two-layer stationary-side PCB. The return traces electrically connecting the stator petal electrodes to the connector are present on the bottom of the board. These boards correspond to the FEA shown in Figure 4.12. The connector provides the input excitation signals from a dual-output function generator, its ground reference, and the four output electrode voltages. In these pictures the two pairs of resolver differential output voltages would be across electrodes B and C, and electrodes A and D.

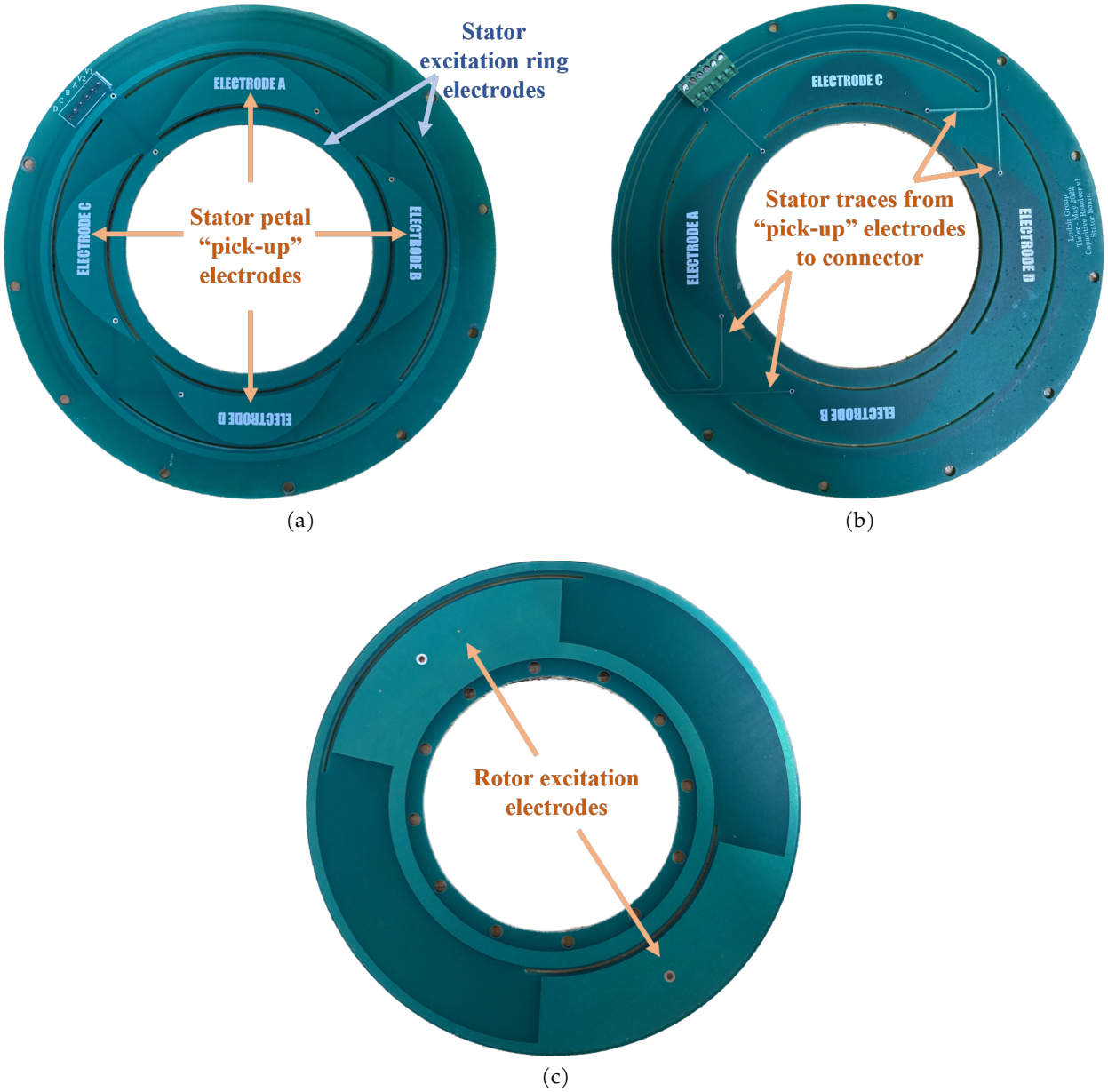

Figure 5.2: Annotated pictures of the (a) top-side and (b) bottom-side of the stator PCB, and the (c) rotor PCB.

The stationary and rotating resolver PCBs are intended to be parallel to each other at a distance of $\approx 1\text{mm}$. While the FEA results in Table 4.1 show that the resolver can handle small amounts of mechanical misalignment, it is ideal to test the resolver with perfect alignment. A lathe was used for resolver testing to provide a way to spin the rotor board at a constant speed with an accurate concentric and parallel reference. Figure 5.3 shows a side-view of the lathe setup. The rotor board on the left side is mounted on the chuck while the stator board is mounted on a 3D printed stand to

fit into the tail stock. During testing it was easy to adjust the parallel distance between the plates and the rotational speed as needed.

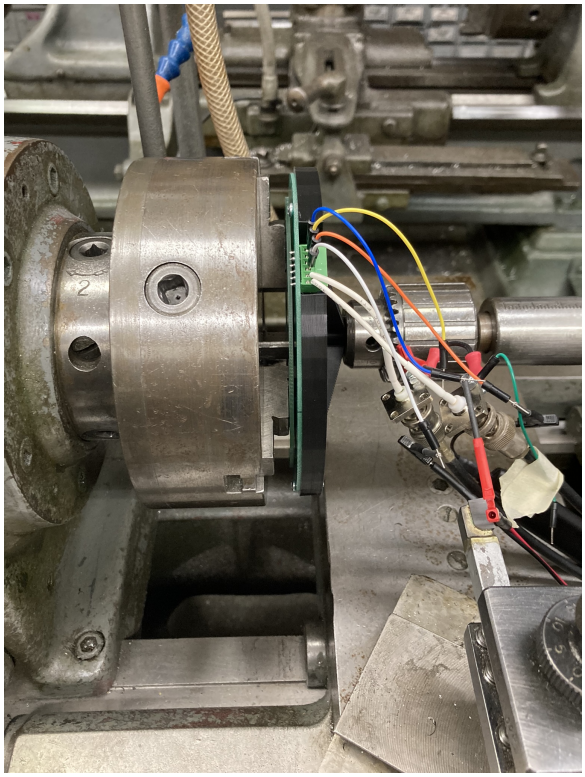

Figure 5.3: Resolver testing setup on the lathe.

The dual-output function generator is not pictured but supplies the $20V_{pk,pk}$ excitation voltages. Likewise, an oscilloscope reads the differential resolver output voltages across opposite-facing stator petal electrodes. Figure 5.4 shows example oscilloscope screen captures of the modulated differential voltages. It is clear that the waveforms are not symmetric and do not resemble sinusoidal waves.

Only the modulated waveforms were recorded and no analog modulation was applied to the signals during testing. However, in Figure 5.5a the differential resolver output voltages are demodulated in MATLAB using eq. (4.2) and envelope extraction. This gives an idea of what the sine and cosine waveforms would look like with demodulation. The resulting signal envelopes are not symmetrical about the x-axis and have a DC bias. This waveform is compared with Figure 5.5b which is taken from Figure 4.12 showing the FEA-generated waveforms of the same resolver design. The waveforms are not identical, but they follow similar trends with the waveforms both having

two different amplitudes. Testing on the lathe makes sure that any non-idealities in the resolver waveforms are solely a function of the electrode coupling geometries and not mechanical alignment issues. Therefore, it is inferred that the issue with the first resolver board revision comes from the presence of the connector traces as confirmed in FEA.

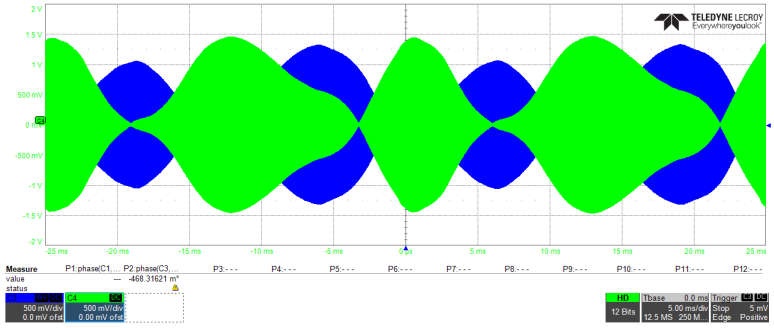

(a)

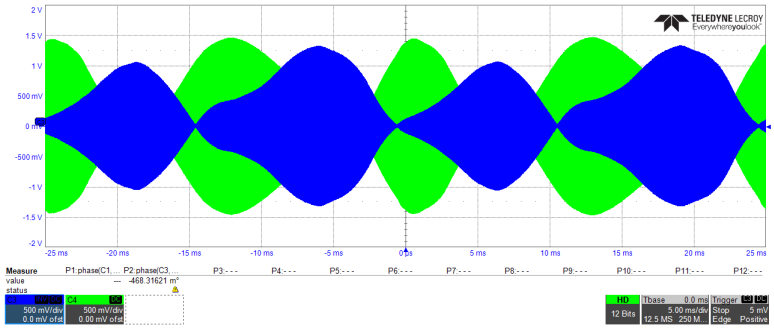

(b)

Figure 5.4: Example oscilloscope screenshots showing the modulated resolver output voltage waveforms.

The negative impact of additional traces on the stator PCB was first observed in the lab and later verified in FEA. A four-layer board was next proposed to reduce the effect of the traces by creating a quasi-Faraday cage within the PCB layers. The stack-up is described in Table 4.2. However, the FEA results in Table 4.3 show that the four-layer stack up may create symmetric waveforms, but it does not ultimately improve the expected resolver angular error. The four-layer board was fabricated and tested in the lab, but is not shown here because it did not improve the trace issue. Instead, the final version of the resolver removes the centralized connector and instead probes the resolver signals at the electrode pours directly. This removes the need for return traces that could add unintended capacitance.

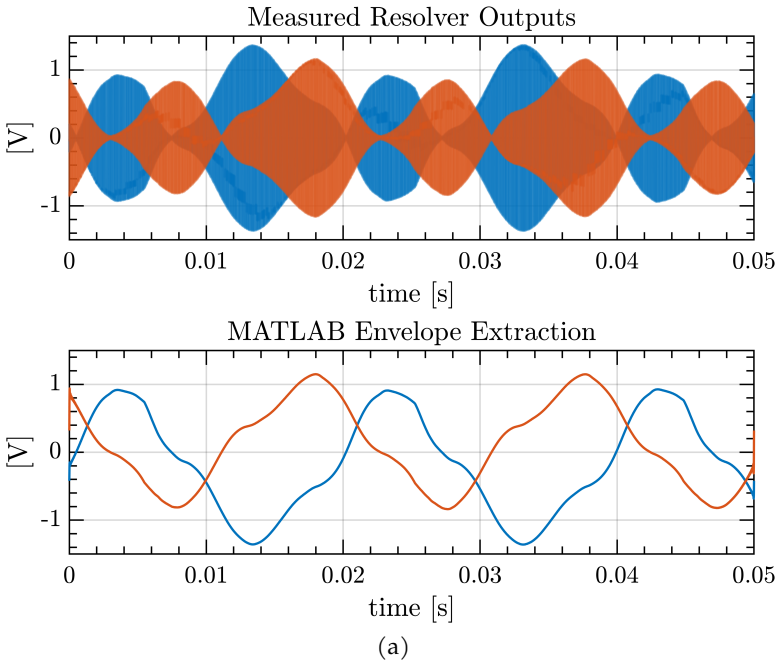

(a)

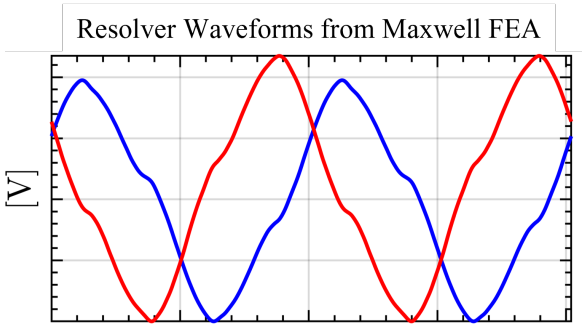

(b)

Figure 5.5: (a) Plots of resolver output waveforms and envelope extraction in MATLAB compared with (b) the sine and cosine waveforms derived from the Ansys Maxwell FEA simulation in fig. 4.12

5.3 Final Resolver Prototype with Integrated Rectifier

The peak coupling capacitances between the rotor and stationary electrodes are $< 30\text{pF}$ and are susceptible to even single picofarads of capacitance from electrically connected copper close to the main stator petals. Instead of making electrical connections parallel to the stator petal electrodes, the connections are via perpendicular board-to-board connectors. The stator board shown in Figure 5.6a has vias on each of the six electrodes connecting through to the bottom layer of the boards with pads for surface mount two-pin connectors. Only one pin is electrically needed for a single signal, but two pins are used for additional mounting stability considering they are surface-mount connectors.

For this final resolver prototype, the main connector interfacing with external hardware is on the filter board in Figure 5.6c.

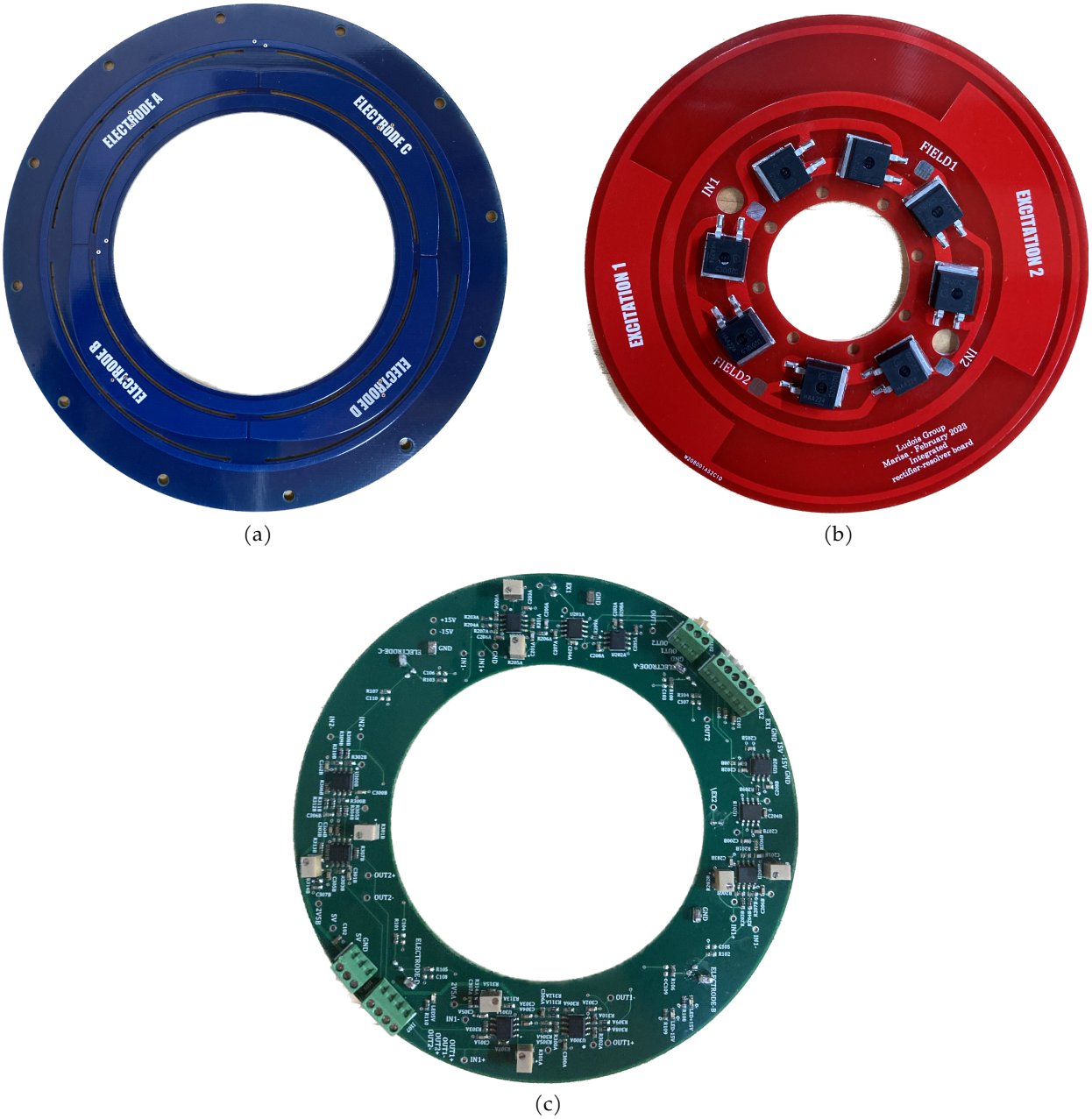

(a) (b)

(c)

Figure 5.6: Pictures of the final resolver boards: (a) stator board, (b) rotor board, and (c) filter and demodulation board.

Figure 5.6 shows the final iteration of the stator and rotor resolver boards and specifically includes the integration with the rotating rectifier. The pads for eight diodes are included on the rotating rectifier board to have two diodes in parallel for current sharing. The boards shown here

are the same as the best resolver design in Figure 4.14.

The lathe is again used to bench test this new three-board resolver prototype. During testing, the lathe did not exceed 1400 RPM. Figure 5.7 shows the three resolver boards mounted on the lathe. Again, the rotor board is mounted on the rotating chuck and a 3D printed part holds the stationary boards to the tail stock. The filter PCB, right-most board, is connected to the resolver stator board with six two-pin connectors.

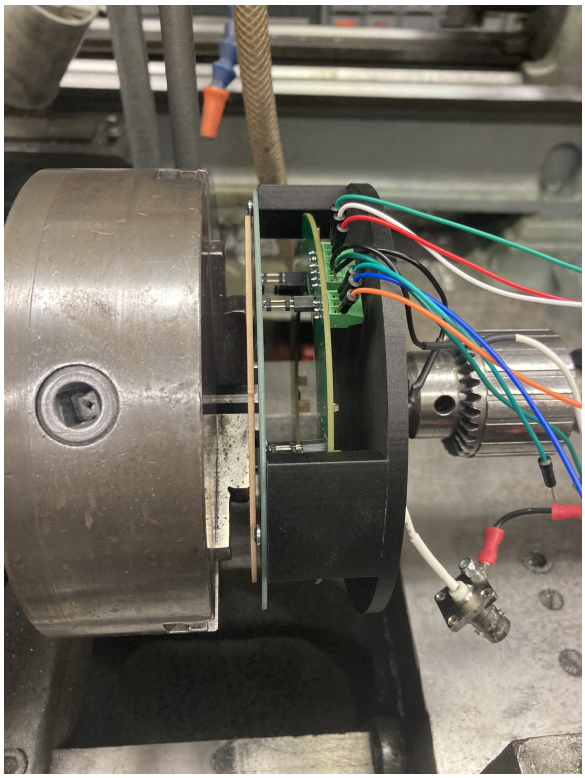

Figure 5.7: Picture of the test setup with the resolver and filter board mounted on the lathe.

$20V_{pk-pk}$ AC voltages are provided from the same dual output function generator as the original testing for the resolver excitation. The output signals from the resolver are captured on the oscilloscope. The filter circuitry and results from lathe testing are discussed in the following section.

The maximum standard resolver excitation frequency is 20kHz, and all measurements at various speeds were taken at this same frequency. However, it is important to understand how the carrier frequency affects the response of the resolver. A gain and phase plot of the capacitive resolver provides necessary for the gains and phase delays applied on all the filter circuitry.

Figure 5.8 shows the gain and phase information for the capacitive resolver. The gain is dependent on the gap distance, so this plot will not always be accurate, but gives a good trend in terms of carrier frequency. For example, the carrier excitation frequency should be as high as possible to avoid the signal significantly degrading and negatively affecting the shaft position derivation. Additionally, the gain peaks in the mega-hertz range which is convenient and useful for the CPC-integrated resolver version.

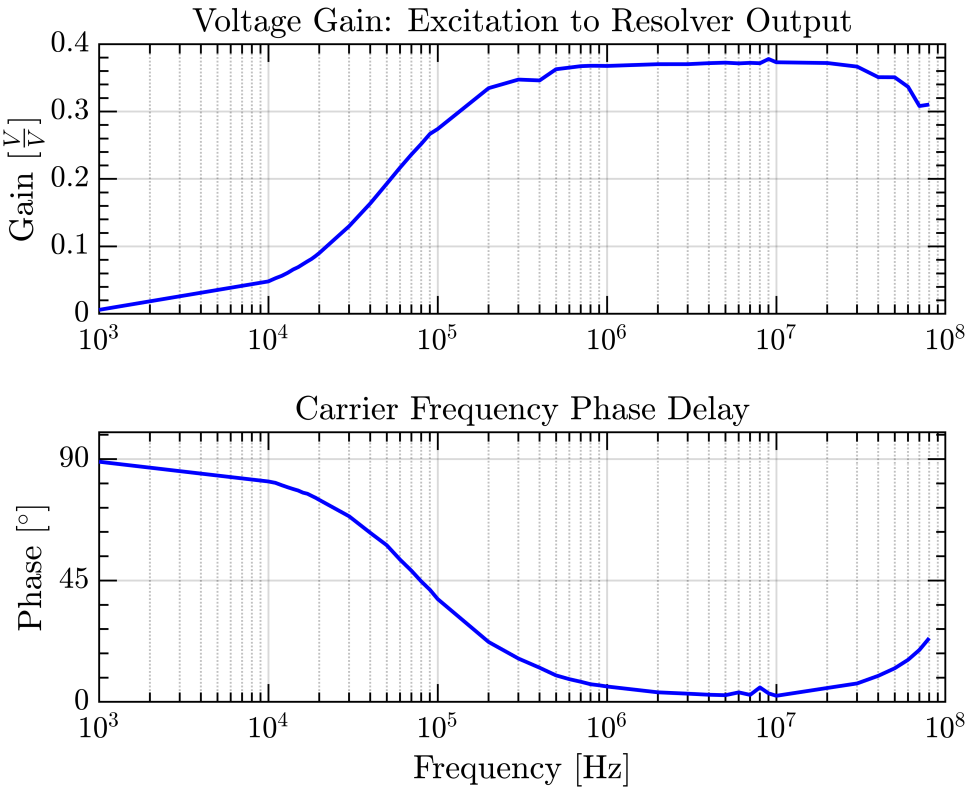

Figure 5.8: Plot of the voltage gain and phase of the resolver looking at $V_{sin,mod}(\theta)$ / $V_{carrier}$ from Figure 4.1b

5.4 Filtering and Demodulation circuits

5.4.1 Analog Multiplier

There are many different algorithms for resolver demodulation [143]. Analog multipliers offer a straightforward method for analog demodulation as explained in section 4.1. Figure 5.9 shows a block diagram of the analog multiplier circuitry processing the two sets of differential voltages to produce sine and cosine waveforms. This circuitry is included on the filter board shown in

Figure 5.6c. Each set of differential voltages are first converted to single-ended signals. A low pass filter is then used to apply a phase delay in order to bring the resolver output in phase with the excitation signal. According to Figure 5.8, the resolver will be phase shifted $\approx 80^{\circ}$ from the excitation voltage at 20kHz. A second-order filter is used to keep the cut-off frequency near the excitation voltage and avoid filtering it out. The 1MHz bandwidth Analog Devices AD633 IC can then multiply the two in-phase voltages with a post low pass filter set at the maximum shaft mechanical frequency. The final low pass filter is set at a single cut-off frequency of 160Hz, or 9600 RPM. This implies that there will be more harmonic content present at lower speeds than at speed near the cut off frequency.

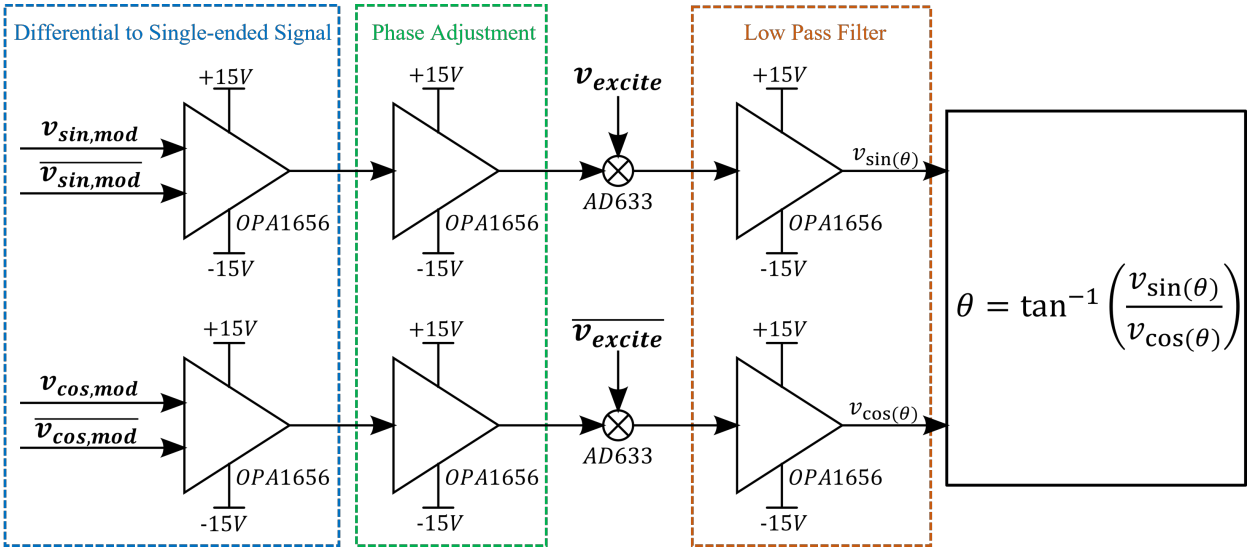

Figure 5.9: Block diagram of analog multiplier circuitry for demodulation

Figure 5.10 shows an example of the demodulated $v_{sine}(\theta)$ and $v_{cosine}(\theta)$ waveforms measured directly from the resolver filter board at a constant speed on the lathe. These waveforms are then used to determine the predicted shaft position. Instead of a microcontroller, MATLAB was used to take the inverse tangent of the two sine and cosine waveforms to calculate the angle directly.

Figure 5.11 summarizes the position information for a measurement point at $\approx$ 1400 RPM. The top plots shows the differential voltages directly measured across the outputs of the resolver. These signals are $130\text{m}V_{pk-pk}$ with a small DC offset. The gains on the filter circuitry are adjusted during testing to make sure the output signals have amplitudes on the order of volts for better signal to noise ratio and ease of interface.

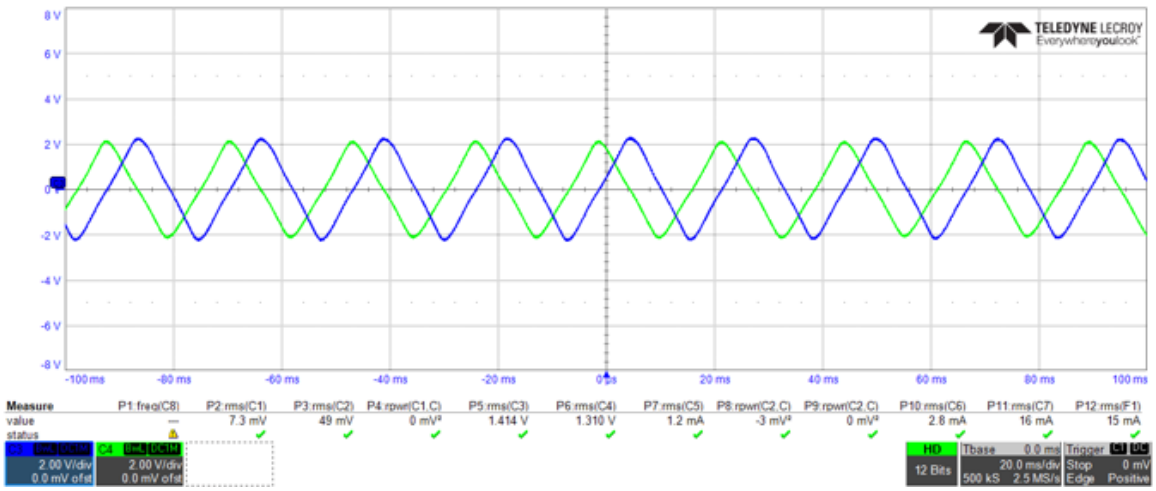

Figure 5.10: Capture oscilloscope waveform of demodulated sine and cosine waveforms. Taken from the outputs of the resolver filter board.

The plot in red and black compares the calculated rotor position with the actual rotor position interpolated from the constant rotational speed. The error between the calculated and actual position is additionally shown in magenta. It is apparent the the resolver error is periodic and reaches a maximum error of $\pm 12°$. Table 5.1 summarizes the peak resolver errors for different constant lathe speeds. In general, the absolute error is within the range of 10°-15° regardless of the speed of the rotor. Likewise, there does not appear to be a trend of the error changing significantly with rotor speed, and in general is consistent among all the tested speeds. There are no observers or other feedback circuitry that used that could otherwise improve the peak error. However, the analog multiplier demodulation circuitry is useful because it provides a straight-forward analog method to create sine and cosine waveforms for further microcontroller position processing.

Measured Speed	**Mechanical Frequency**	**Peak Angle Error**
62rpm	1.0Hz	$\pm 14.4°$
370rpm	6.2Hz	$\pm 12.6°$
828rpm	13.8Hz	$\pm 12.3°$
1020rpm	17Hz	$\pm 12.6°$
1408rpm	23.5Hz	$\pm 12.0°$

Table 5.1: Summary of results from testing resolver on the lathe with the analog multiplier demodulation circuitry.

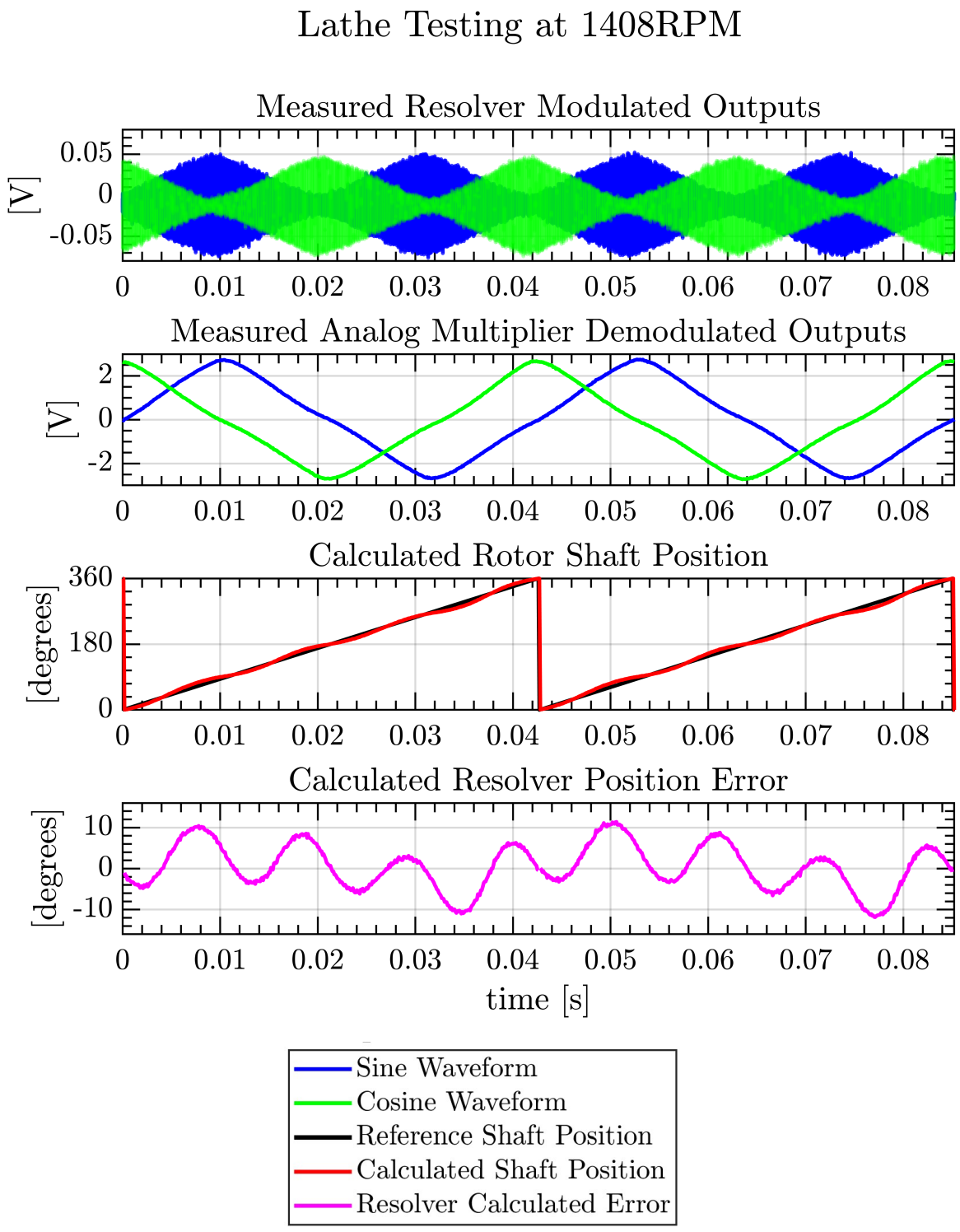

Figure 5.11: Figure of data captured during lathe testing at ≈ 1400 RPM and then the angle error calculated in MATLAB.

5.4.2 AD2S1210 Evaluation Board

In contrast to analog demodulation circuitry, many papers discuss purely digital algorithms for demodulation [147, 144, 145]. One common, commercially available device is the Analog Devices AD2S1210 resolver-to-digital converter. This device in particular is chosen for lab testing because it has a plug-and-play evaluation kit that is easy to interface with a laptop to measure and record rotational position and speed. Figure 5.12a shows a block diagram of the evaluation board electrical connections and interface with a general magnetic resolver [8]. From the user manual, the evaluation board can apply excitation voltages at R1 and R2 up to $10V_{pk-pk}$ and expects the resolver output signals to be a minimum of $4V_{pk-pk}$. The resolver output filtering is interesting in that it filters each of the four signals individually and not as a differential pair. Additionally, it expects each of the individual signals to be centered around 2.5V as well.

Figure 5.12b shows a block diagram of the filter circuitry in between the resolver outputs and the evaluation board inputs. This is necessary to make sure the output differential signals from the resolver are in the correct voltage range and amplitude for proper digital demodulation. The differential pairs are converted to single-ended signals centered at 0V, level-shifted up 2.5V, and then converted back to differential signals. This circuitry is also included on the filter board in Figure 5.6c. Each section stage of the filtering also includes potentiometers to fine tune the gains on the signals to achieve the minimum $4V_{pk-pk}$.

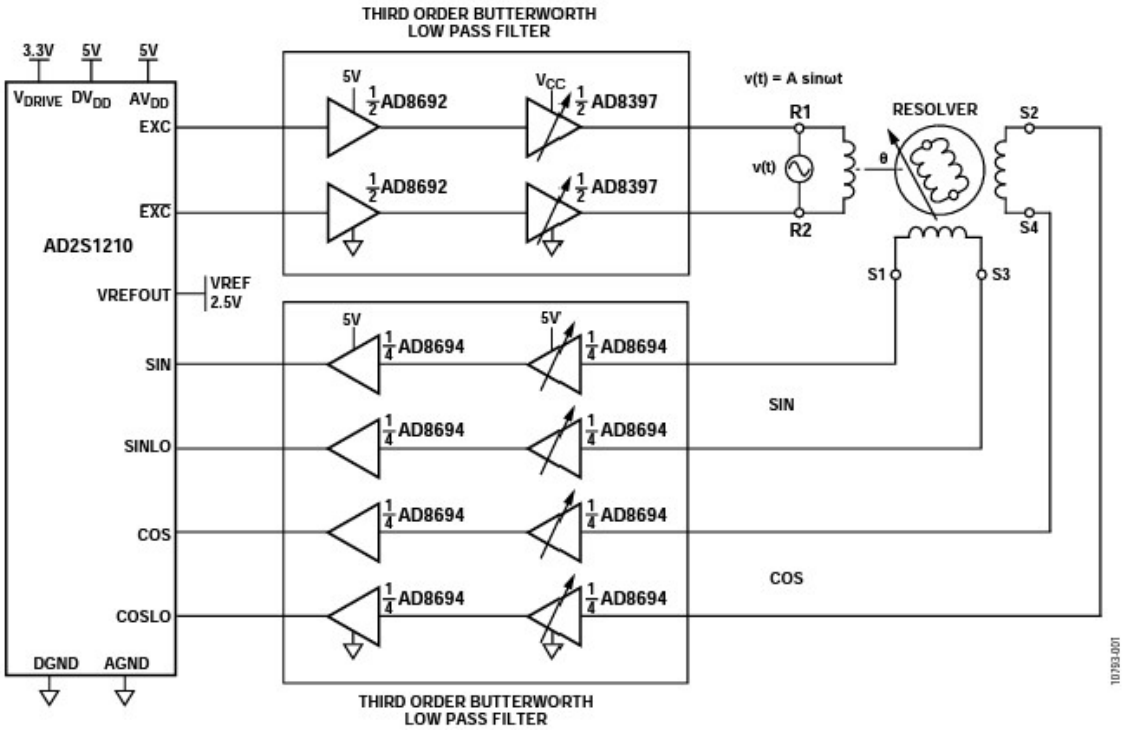

(a)

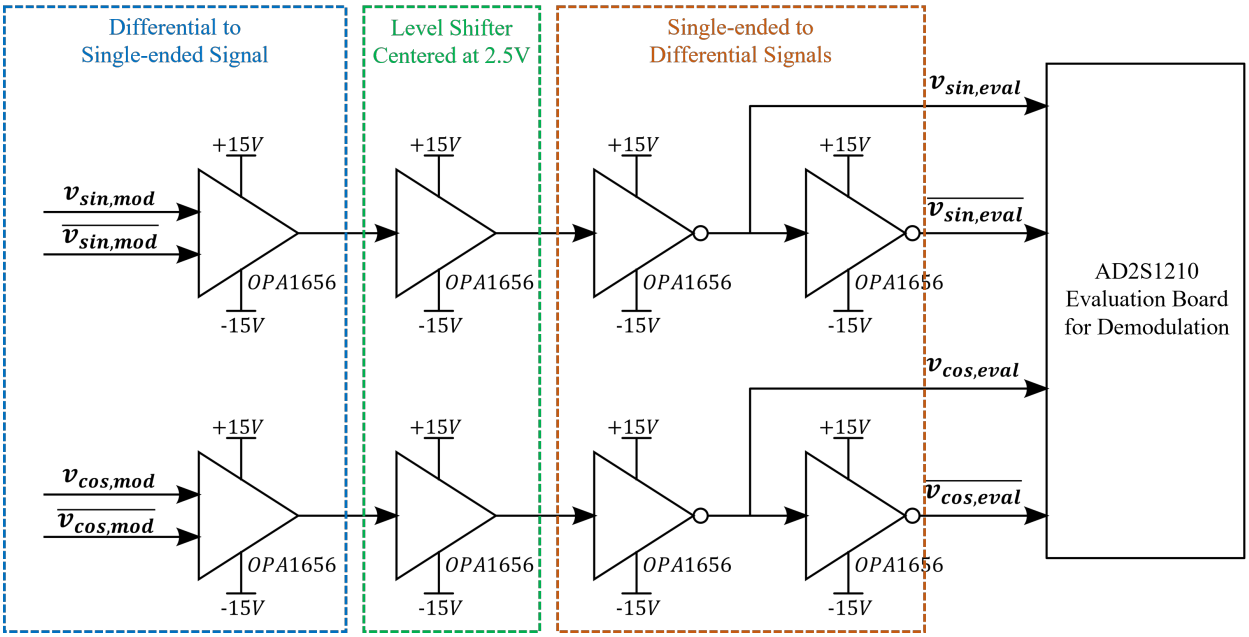

(b)

Figure 5.12: (a) Block diagram of AD2S1210 evaluation board taken from its datasheet [8]. (b) Block diagram of filter circuitry required to interface resolver with AD2S1210 evaluation board.

Figure 5.13 shows the bench testing setup with the AD2S1210 evaluation kit. The boards have a separate power supply and connect directly into a laptop. The resolver test stand is 3D printed to hold the stator board and allow the rotor board to rotate with a bearing. Since the resolver mounting is 3D printed, there is a good amount of mechanical tilt and offset expected. The filter board is mounted to the under-side of the blue stator PCB. All of the input and output connections from the evaluation board are connected to the filter board.

The red rotor board is spun to various speeds using compressed air. Spinning with compressed air does not produce a constant rotational speed, but allows the board to reach higher speeds than on the lathe. An optical tachometer was used during testing to give an estimate of the speed at the acquisition time and make sure the filter circuitry and evaluation board are giving reasonable position and speed results.

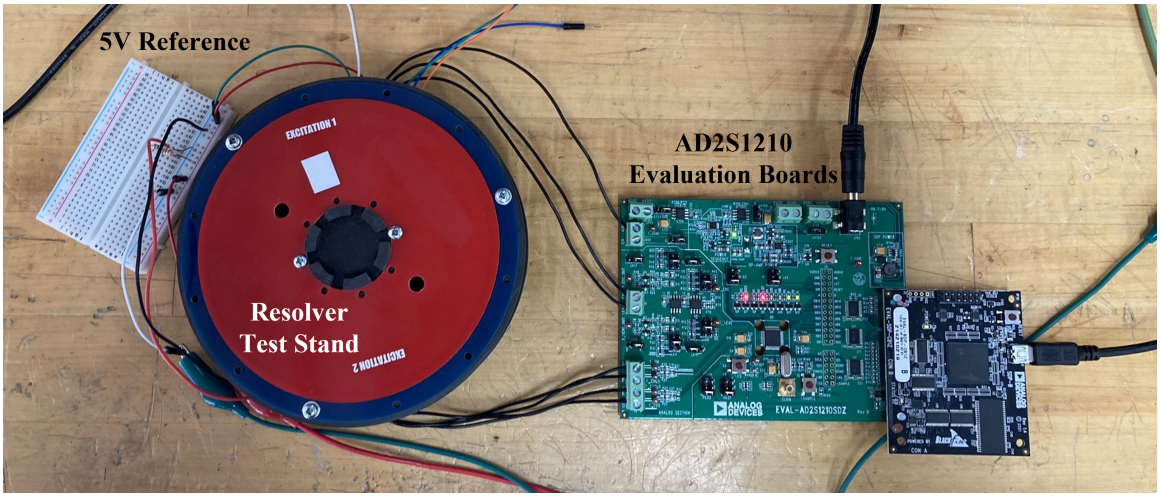

Figure 5.13: Picture of testing setup using 3D printed resolver stand and AD2S1210 evaluation board.

In the AD2S1210 evaluation software, the sampling frequency is fixed at 500kHz and the number of samples can be adjusted to change the amount of time to capture data. With the maximum number of samples, the acquisition time is 26ms. In the example in Figure 5.14, the compressed air is used to spin up the rotor board and the data collected is started when the air is removed and the rotor is coasting as it slows down. This approach attempts to have the speed as constant as possible. The display shows the rotor position angle over 360° and the speed is given in RPS which is equivalent to hertz. The speed range shown here is roughly between 2760 and 2800 RPM.

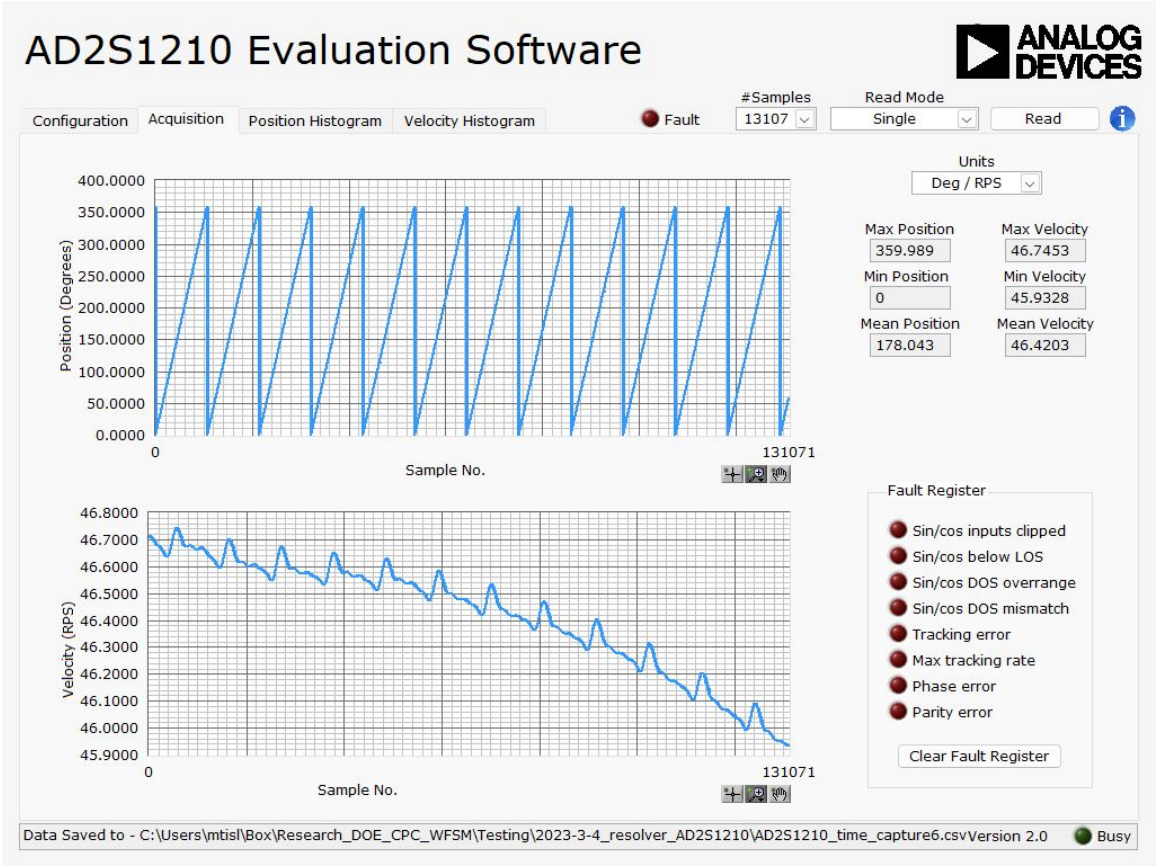

Figure 5.14: Sample picture of AD2S1210 graphical user interface showing measured resolver shaft position and speed. This measurement is taken when the resolver is coasting and slowing down.

The angle error from the example resolver data capture is shown in Figure 5.15. The speed within each 0-360° degree period is assumed to be constant and the reference position is interpolated linearly between each period. From the measurement taken in Figure 5.14, the predicted resolver error is $< 0.5°$ and a nearly two orders Table 5.2 summarizes the maximum errors calculated for different various different speeds. These results indicate an order of magnitude accuracy improvement over the multiplier demodulation sine it has no advanced signal processing. The resolver itself was not changed, only the demodulation algorithm.

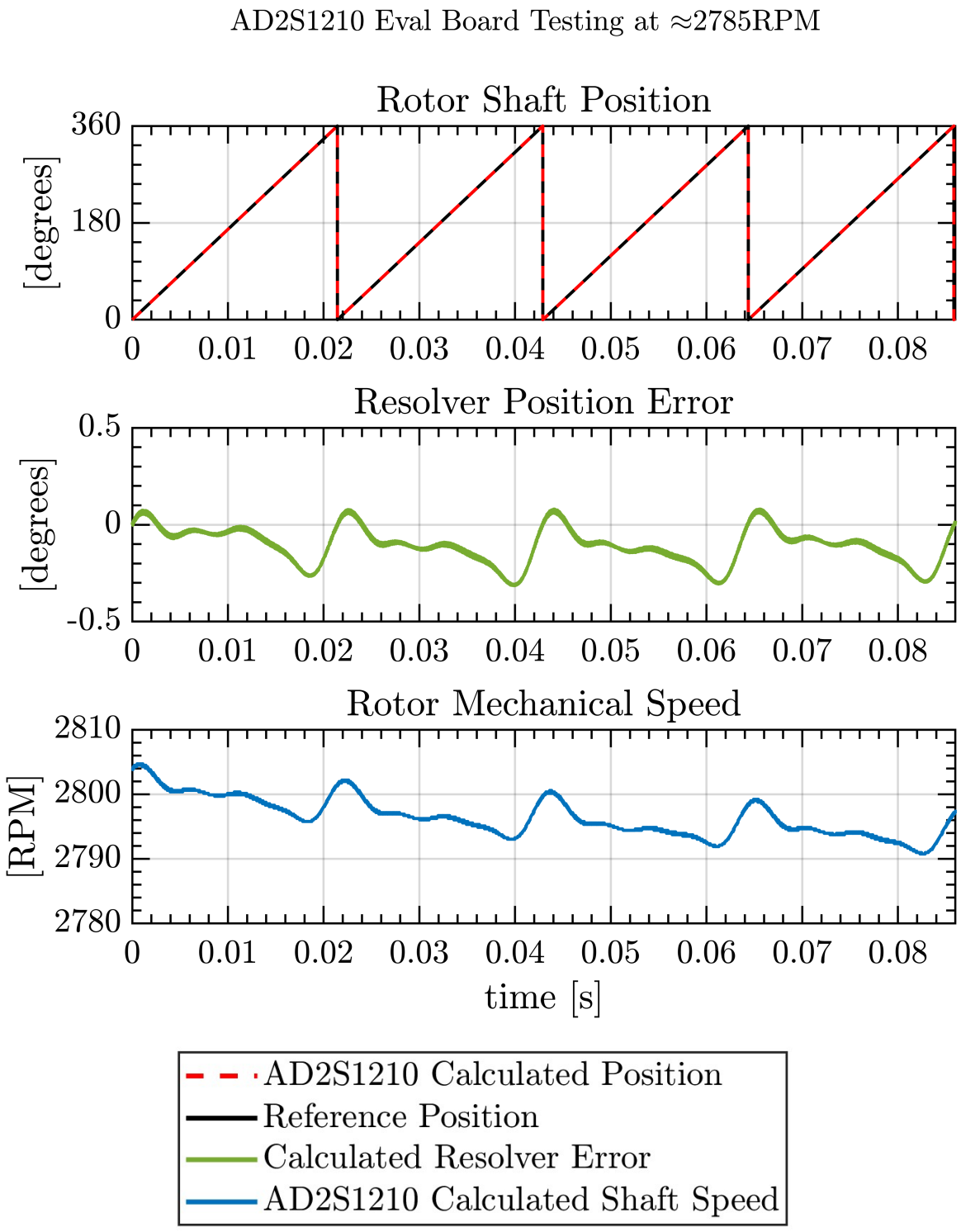

Figure 5.15: Plots showing the position and speed data captured from the AD2S1210 software and the resulting calculated angle error in MATLAB.

In Table 5.2 there is a trend that the resolver error improves at higher rotational speeds. The 3D printed part does not have the same concentricity and air-gap tolerance as the lathe setup, so

some of the error could come from the mounting setup itself. The centripetal acceleration flattens the board creating an even airgap between the stator and rotor. This effect contributes to the lower resolver error as the speed increases. Conversely, as the speed decreases it becomes less constant and there is less energy stored in the inertia. This would contribute to higher angle errors at lower speeds with this test setup.

Measured Speed	Mechanical Frequency	Max Angle Error
877rpm	14.6Hz	4.3°
1488rpm	24.8Hz	2.8°
2063rpm	34.4Hz	2.8°
2549rpm	42.5Hz	1.9°
2785rpm	46.4Hz	0.3°

Table 5.2: Summary of results for testing the resolver with a 3D printed stand using the AD2S1210 digital demodulation evaluation boards.

5.5 CPC-Integrated Resolver Testing

The capacitive resolver is integrated around the rotating rectifier circuitry, but it can also be integrated into and around the CPT coupler PCBs as well. Figure 5.16 gives a general diagram of the CPC-integrated resolver system. The 6.78MHz input voltages to the rectifier act as the excitation signals for the capacitive resolver. There is no need for an external sinusoidal generator. Additionally, the stationary parts of the resolver are again shown in blue while the rotating components are colored in green.

Figure 5.17 shows pictures of the CPC-integrated PCBs. The rotor board in Figure 5.17a shows the two excitation electrodes around the outside radius of the coupling electrodes. This matches the design simulated in FEA from Figure 4.17. The stator petal electrodes in Figure 5.17c are also located around the outer radius of the coupling electrodes with headers on the back of the board to connect to the filter board. The filter board and the mounting setup on the machine is shown in Figure 5.18.

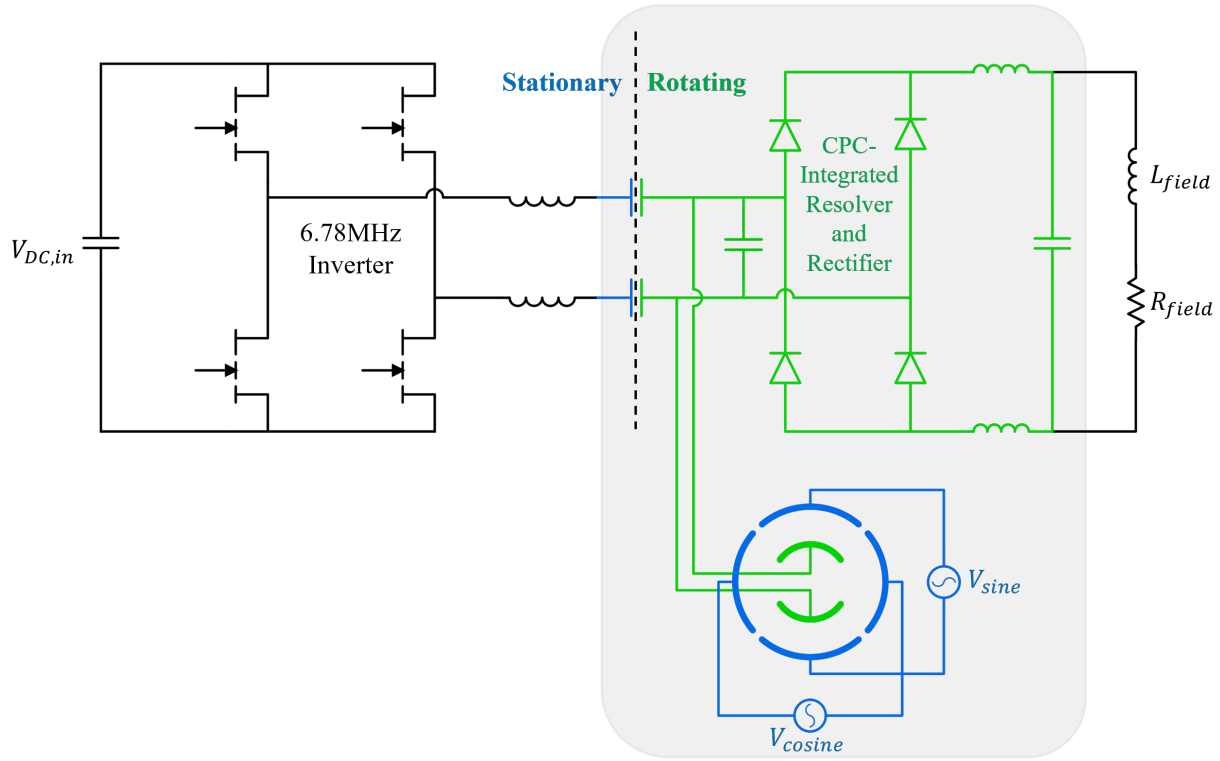

Figure 5.16: Diagram of the CPT system showing the CPC-integrated resolver operation.

The current-stiff rectifier is used for this CPC design with the same parts used in the high power testing in chapter 3. However, eight diodes are used in this rectifier instead of four in order to limit the amount of loss per device and mitigate diode thermal issues. While the rectifier takes up the same footprint as with the original CPC boards, the coupling electrodes are slightly smaller to maintain the same board diameter with the addition of the resolver functionality.

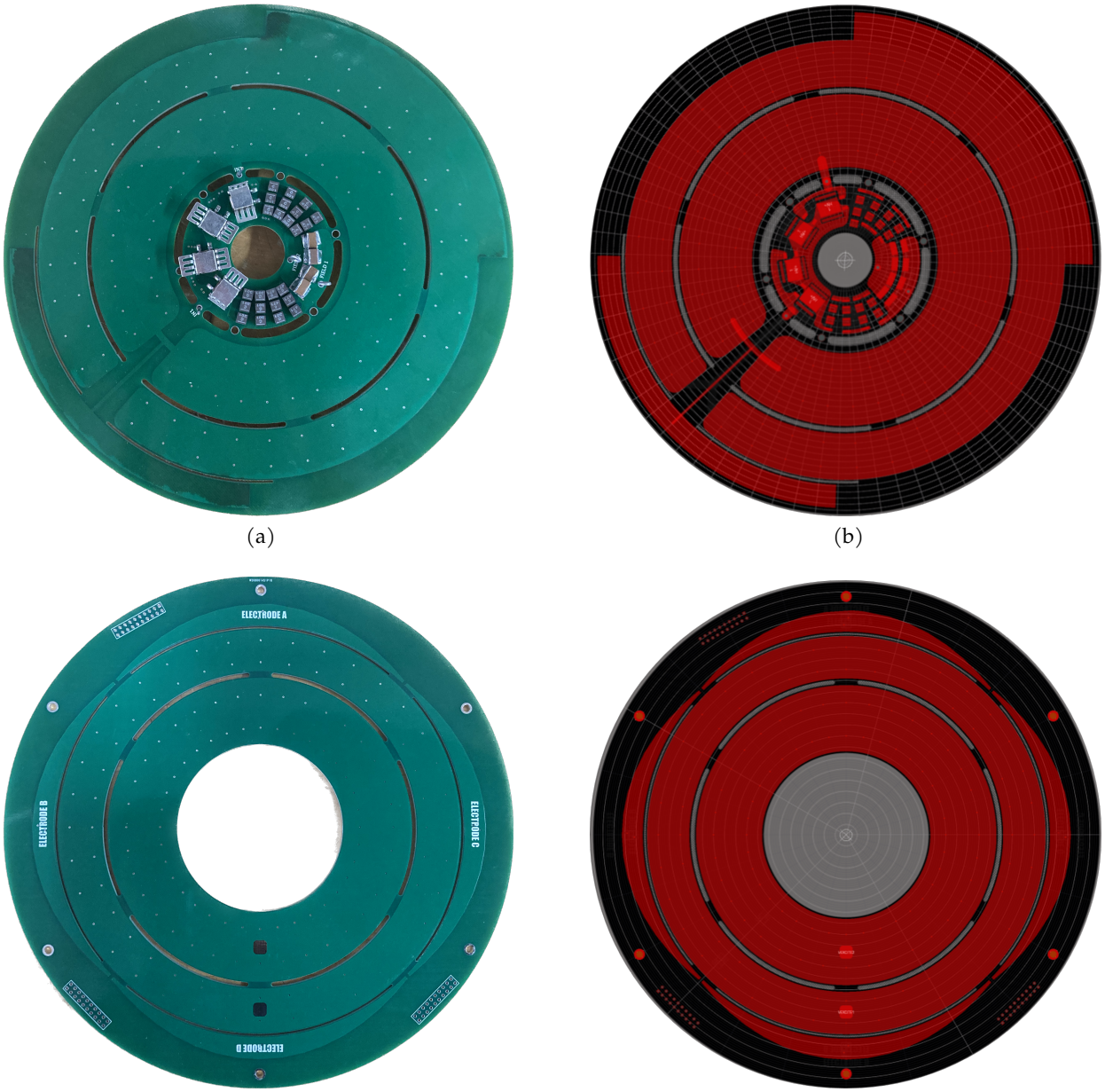

(a) (b)

(c) (d)

Figure 5.17: CPC-integrated resolver and rectifier boards with pictures of the (a) rotor board and (c) stator board and Altium renderings of the (b) rotor board and (d) stator board to clearly show the resolver functionality.

The three CPC boards are mounted in the same configuration as with the high power CPT testing. In order to keep the same approximate system frequency, the boards are mounted with slightly small air gaps closer to 0.6mm instead of 0.8mm. The filter board is added on the front facing side of the stator board and connected with tall connectors so as not to block the air flow

cooling to the rectifier diodes on the front-side. The filter circuitry follows the analog multiplier block diagram in Figure 5.9 except the multiplier is swapped out with the Analog Devices 250MHz bandwidth AD835 IC.

Since the machine is on the bench and signals are probed on the rotor board, the rotor cannot spin freely at a constant speed to evaluate the resolver. Instead, a rotary index head is used to rotate the shaft at discrete angle steps over one full revolution. The rotary index head provides very accurate discrete angle steps. Figure 5.18c shows the setup of the rotary head index on the back of the machine shaft with a wheel and many holes for accurate and consistent position steps. At each step the resolver output signals are captured on the oscilloscope and the resulting signal is demodulated in MATLAB. Measurements were taken at 9° increments.

One drawback for this setup is that the pick-up voltages in this system at high output power can be hundreds of volts. This means that high voltage is being applied to, and at the outputs of the resolver. In order to do any analog or digital filtering, all of these signals must be converted to low voltages. The AD835 has a voltage limit of $\pm 5V$. Therefore, all of the signals processed on this board have to be low voltage and within the same range. This is challenging considering that the applied rectifier voltage can be hundreds of volts and changes with the field power.

The filter board uses eight 1206 resistors in a voltage divider configuration to step down the $300V_{pk}$ excitation signal to a $2.1V_{pk}$ low voltage signal. Similarly, the resolver output waveforms are stepped down from a $120V_{pk}$ signal to a $2.4V_{pk}$ signal. Unfortunately, this means that the voltage divider gain is fixed regardless of how the output power changes. For all CPT testing the output power was kept at a constant bus voltage of 180V to achieve a relatively constant output power of $\approx 500W$.

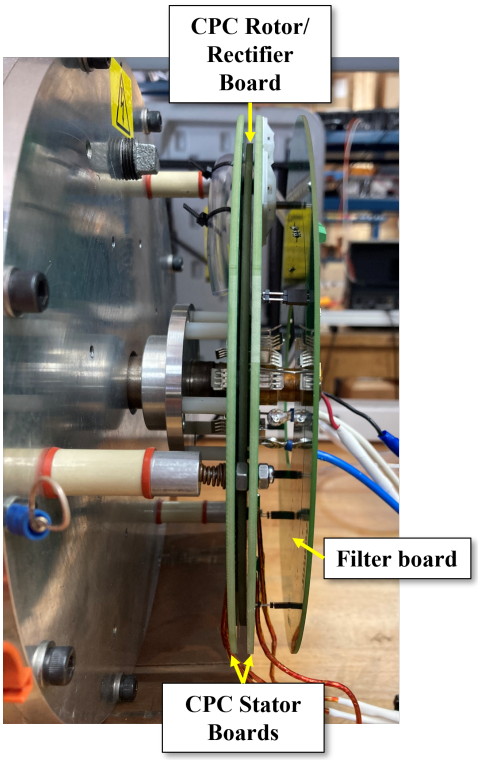

(a)

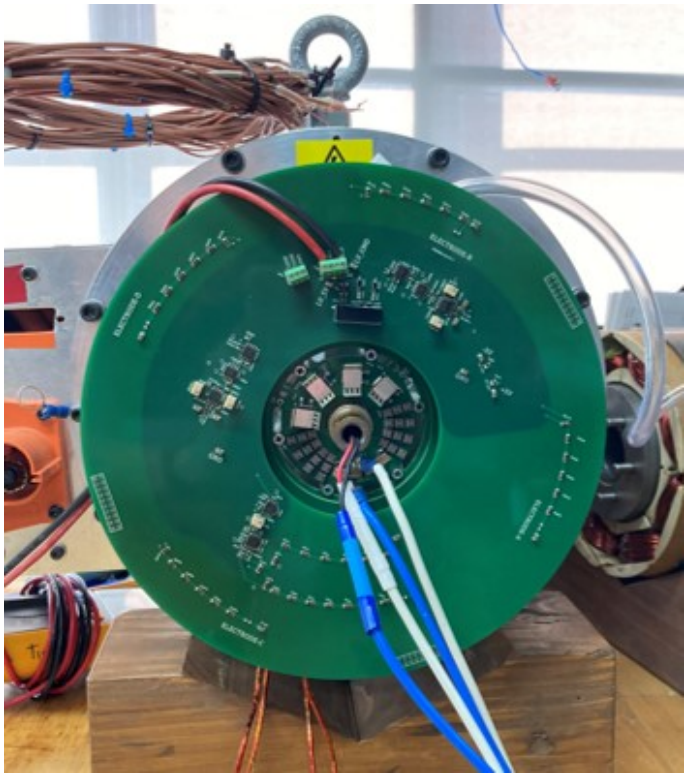

(b)

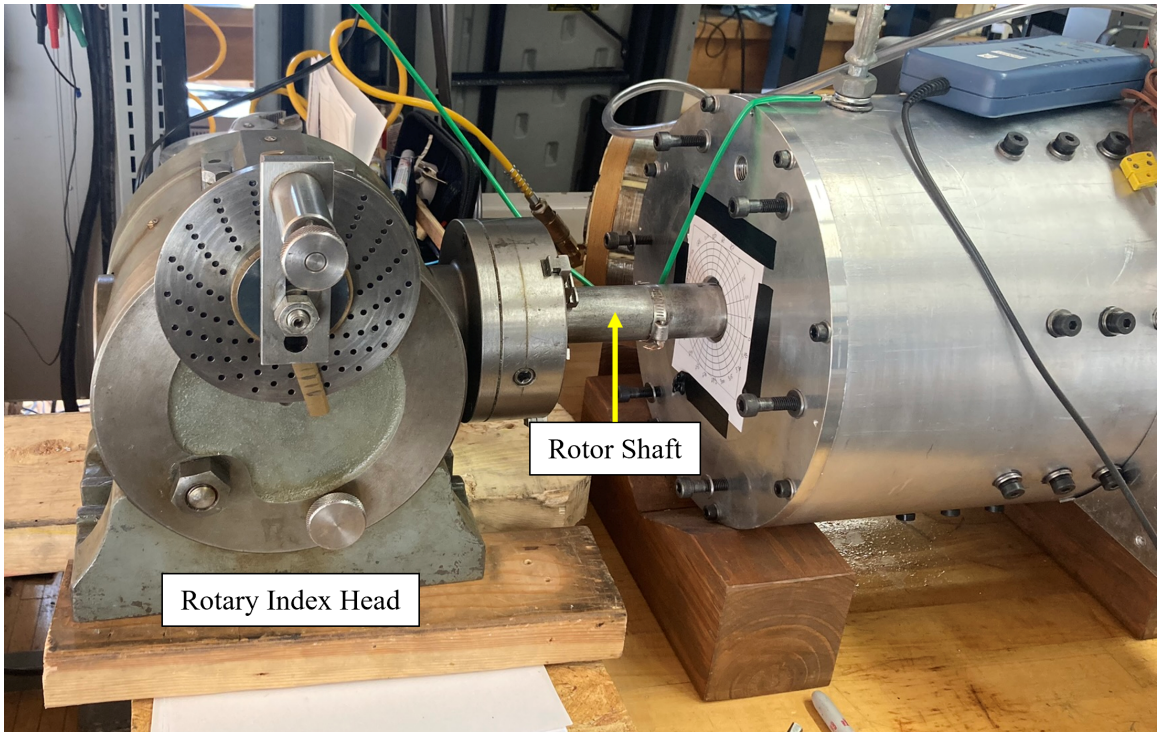

(c)

Figure 5.18: Pictures of testing the CPC-integrated resolver. (a) Side view of the CPC and filter boards, (b) front view of the filter board, and (c) rotary index head attached to the machine shaft.

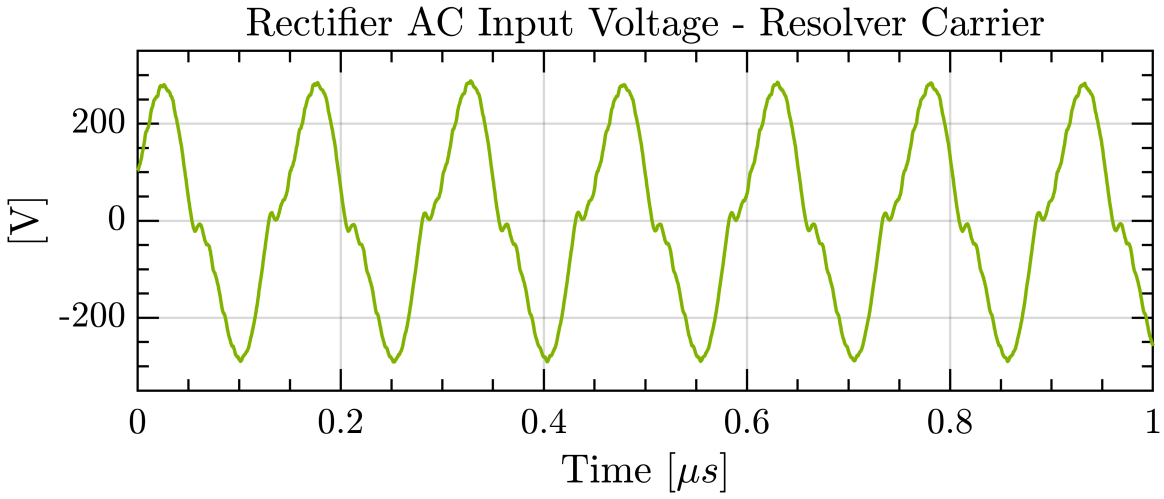

(a)

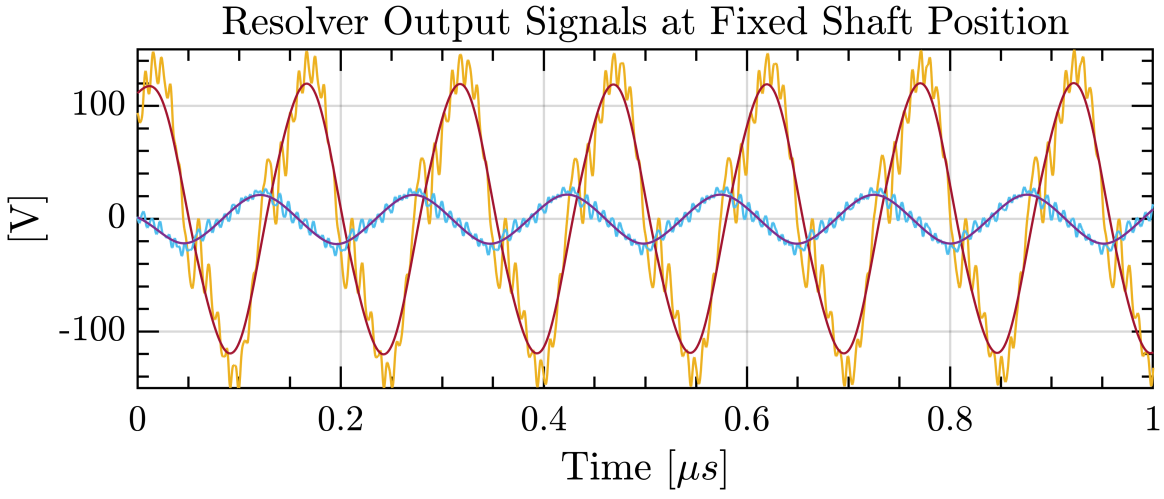

(b)

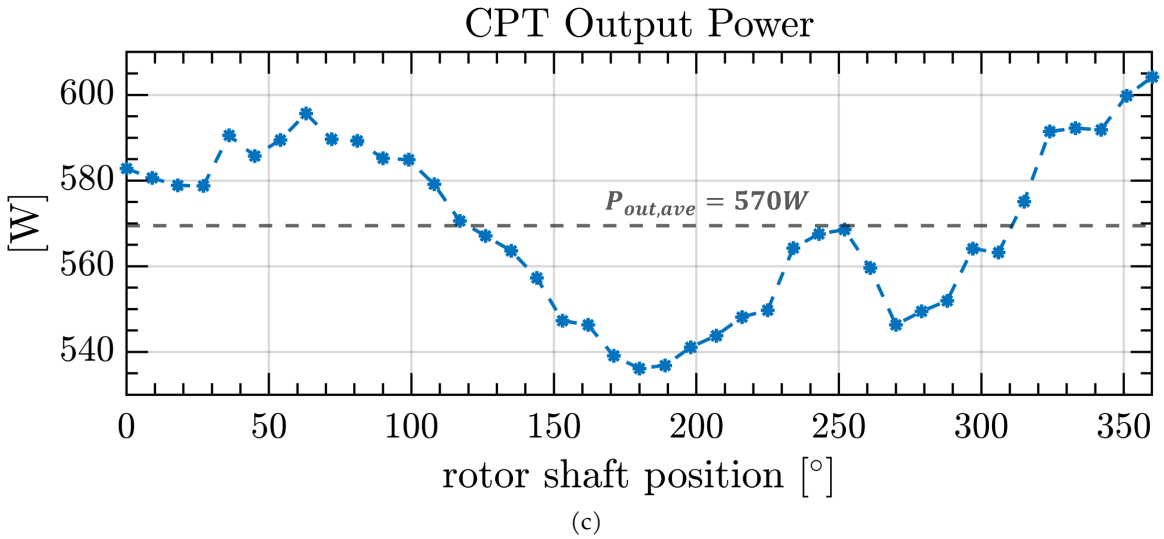

(c)

Figure 5.19: Plots showing the (a) input voltage to the CPC-integrated resolver, (b) sample raw and low-pass-filtered resolver output signals, and (c) the output power all as a function of shaft position.

Figure 5.19a shows an example waveform of the input rectifier voltage captured on the oscilloscope with an output power of 570W $\pm$5% at a 6.6MHz system frequency. The current stiff rectifier uses an input capacitor than filters the rectifier waveform and creates a sinusoidal waveform. This is ideal for the resolver excitation voltage. Additionally, Figure 5.19b shows an example of the two resolver output signals at a fixed shaft position. The carrier frequency is constant, but the amplitudes of the signals change with rotation. To demodulate the signals over the full rotation, the peak value of the filtered resolver signal is recorded and used to construct the sine and cosine waveforms.

Figure 5.20 shows the MATLAB analysis results of the 9° data points. The points in the blue and red curves plot show the peak magnitude of the modulated resolver output signals at each shaft position. High voltage differential probes were used to measure the resolver differential output voltages. Since they are rated for 1000V, their resolution at voltages < 10V is low. This data shows that the CPC-resolver can give the shaft position within a roughly $\pm 10°$. This is comparable to the general resolver results and confirms the capacitive resolver design is scalable to larger diameters and orders of magnitude higher frequencies.

Figure 5.19c plots the output DC power measured at each shaft position. There is a rough sinusoidal trend of the output power changing as a result of the coupler PCBs not being perfectly flat and likely having a slight tilt to prevent them being perfectly parallel. The coupling capacitance is sensitive to small changes in mechanical tolerances and misalignment. Therefore, as the rotor spins the coupling capacitance, and consequently the load on the inverter changes with rotation. As the load changes slightly, the inverter and rectifier voltage will also change slightly. This means that the voltage applied to the resolver is not going to be constant over a full rotation either. However, the angle derivation is a ratio of the sine and cosine, so any gain change from the rectifier voltage is applied equally and should not affect the final angle result.

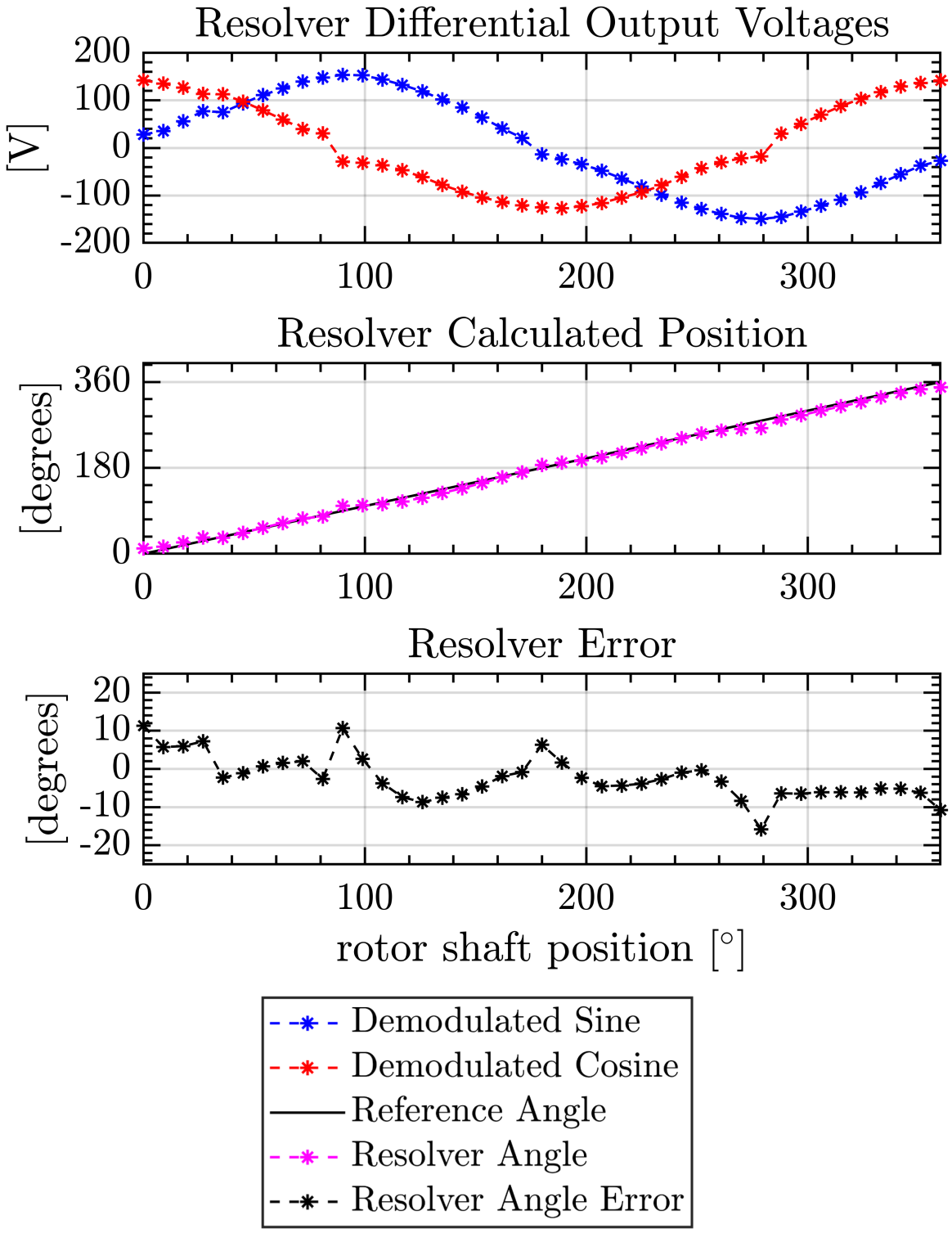

Figure 5.20: CPC-integrated resolver testing plots showing the demodulated sine and cosine waveforms as well as the shaft position error.

5.6 Concluding Remarks

The capacitive resolver is a simple and minimal design that is physically scalable and also maintains accuracy at various carrier frequencies. With basic analog demodulation the resolver design has a conservative error of $\pm 15°$. However, the accuracy can be improved down to $\pm 0.3°$ with sophisticated digital demodulation algorithms. These digital demodulation strategies are widely discussed in literature and have commercially available solutions so this is not a hindrance for the adoption of the design. Furthermore, the rectifier was in use during testing of the CPC-resolver with a >500W output power without significantly impacting the resolver error. Further work is needed for the CPC-resolver filter to be compatible with variable field power and signal processing at megahertz frequencies. Through this design, the technical and cost-related learning curves are eliminated associated with the adoption of the integrated capacitive resolver and rectifier. The resolver layout is able to be adapted for the space constraints in a machine design and overall provide an excellent solution for not only capacitive, but anytime of wireless rotor excitation method.

Chapter Six

Contributions, and Recommended Future Work

6.1 Contributions

Within this work, contributions were made to further the goal of increasing the viability of wound field synchronous machines (WFSM) in traction applications. Specifically, an emphasis was put on reducing the cost and complexity of rotor field excitation methods. These contributions are summarized in the following list and expanded upon in further detail afterwards.

1. Reduced CPT complexity with removal of the power coupler's rotor-side buck converter.
2. Achieved a new maximum output power, >3x from previous work, with air-gap CPT for synchronous machine rotor excitation.
3. Created closed form solution for determining resonant tank inductance in the series resonant converter.
4. Designed and manufactured integrated capacitive resolver with rotating rectifier for any WFSM excitation method.
5. Designed an integrated capacitive resolver and rectifier to be compatible with conventional resolver excitation and demodulation circuitry.
6. Developed capacitive resolver integrated around the capacitive power transfer coupler boards.

6.1.1 Contribution #1: Eliminating Rotor-Side Buck Converter

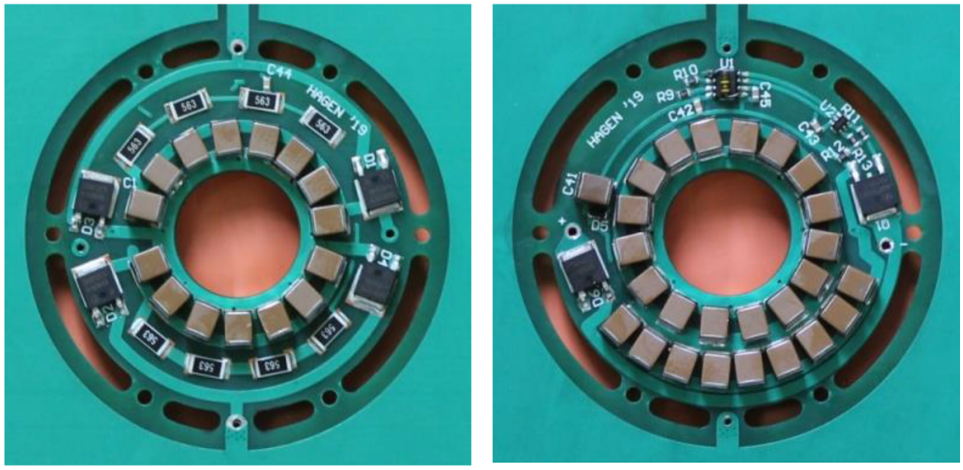

(a)

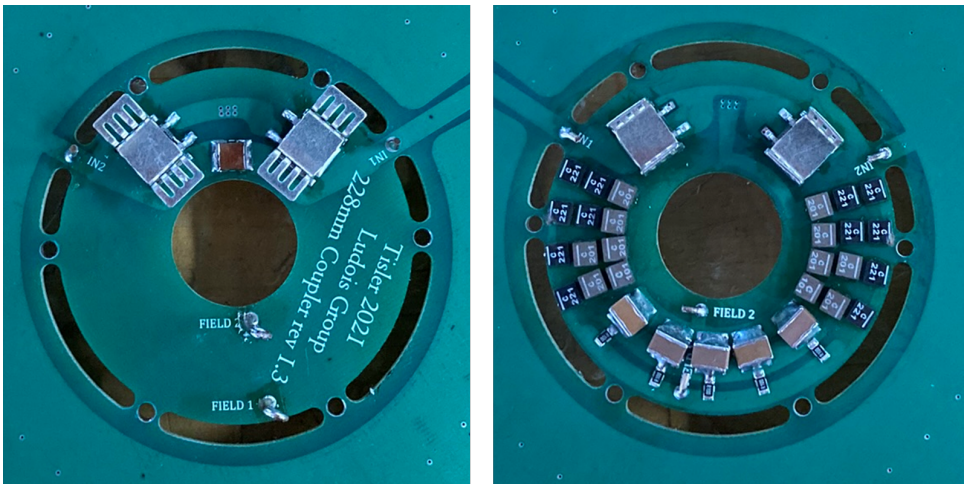

(b)

Figure 6.1: Pictures of the front and back sides of the rectifier board circuitry for the (a) 1.7MHz prototype with output buck converter and the (b) 6.78MHz prototype without any buck converter needed.

One barrier to WFSM adoption in traction applications is the total cost of the wireless excitation system. On the capacitive power coupler excitation system, one way to reduce cost is to the reduce the total number of unique components. The air-gap capacitive coupler's power capability is determined by its amps/hertz rating. In this work, the buck converter on the previous 1.7MHz prototype [84] was eliminated by increasing the system frequency to 6.78MHz. An increase in system frequency directly lowers the capacitive coupler impedance to achieve the same output power without requiring a buck converter for impedance matching to the load. Beyond a reduction

in the capacitive coupler impedance, 6.78MHz falls into the ISM band with fewer restrictions for pollution allowing for easier compliance to EMI/EMC standards. Likewise, a higher frequency requires less filter capacitance on the output of the rectifier, further reducing the part count as seen in Figure 6.1. The new rectifier board has 67% fewer unique components and 50% fewer total components.

6.1.2 Contribution #2: Achieved 2.3kW Output Power with Air-gap CPT and Current-Stiff Rectifier.

Previous air-gap capacitive power transfer systems for WFSM rotor excitation transferred a peak power of 675W to the field [84]. In this work, a peak power of 2.3kW was delivered to the load with an 88.5% efficiency for a 3.4x increase in output power. Increasing the system frequency >6.78MHz allowed the capacitive coupler to transfer higher current before voltage breakdown across the air gap. To achieve contributions #1 and #2, the following supporting contributions were made:

- Increased inverter frequency 4x from 1.7MHz to $\geqslant$ 6.78MHz

A class-D resonant inverter was designed with GaN HEMT switches to operate at and above 6.78MHz. To account for the shorter switching period, the deadtime was reduced by nearly 3x from 40ns to $\approx 15ns$. The deadtime reduction was realized via matching propagation delays among all IC components and tuning each GaN switch control pathway after assembling the inverter board. Likewise, care was taken to design and layout the gate drive circuitry with the fewest required parts and smallest gate loop to mitigate stray inductance to 4nH.

- Designed Current-Stiff Rectifier to Manage the Parasitics at $\geqslant$ 6.78MHz

The rotating rectifier board is necessary to put DC power on the field winding. Two different rectifier topologies were tested to reduce the stress and loss on the diodes to push their performance into the kilowatt output power range. The two topologies were the voltage stiff rectifier with a DC filter capacitor and the current stiff rectifier with a DC filter inductor. All prior work in this area used the voltage stiff rectifier. This rectifier featured an inductor across the input terminals to correct the power factor from the passive diode equivalent capacitance. Conversely, the current stiff

version featured a smoothing capacitor across the rectifier AC terminals to filter out higher order harmonics in the input voltage waveform.

The peak 2.3kW of output power was achieved using the current stiff rectifier. The design was shown to reduce the overshoot voltage seen by the passive diodes and produced the highest overall system efficiency. The parasitic inductance from the rectifier layout coupled with the diode equivalent capacitance created large amounts of ringing and voltage overshoot in the voltage-stiff design. However, the current-stiff rectifier specifically mitigated the effect of the nanohenry parasitic inductance, by adding the bulk microhenry inductance output filter. Additionally, the input capacitance to the rectifier creates a sinusoidal input voltage that is ideal for the CPT-integrated resolver excitation. The current-stiff rectifier is the preferred choice for megahertz operating frequencies as well as the integrated-resolver topology.

- Improved the Inverter Heat Sinks to Increase Inverter Output Power Capability

During preliminary testing, cooling of the inverter GaN switches was the limiting factor of the CPT system. To achieve >1kW of output power, small copper blocks were soldered directly onto the top-side thermal pad connected to the source of each switch to increase the thermal mass. A heatsink was placed across each half-bridge with a sheet of Kapton used to electrically isolate the two copper blocks. The pin fin heat sink featured an integrated fan that ensured equal airflow and a balanced temperature rise on each switch.

- Reduced Resonant System Equivalent Series Resistance for Improved Efficiency

The resonant system ESR was reduced nearly 3x from 1.56Ω to 0.55Ω, thus reducing a significant portion of avoidable loss in the system at higher frequencies. The ESR reduction came primarily from minimizing the total wire length in the system by decreasing the resonant tank inductor size from 27μH to 1.5μH. Additional vias connecting the top and bottom side copper pours of the CPC boards were also added to reduce system ESR.

6.1.3 Contribution #3: Closed-form solution for L_{tank}

The full series resonant DCDC converter was analyzed in steady state. The field winding load resistance and the capacitive coupler are fixed values. In the most simplified case, the series resonant

tank inductance is approximated in eq. (6.1) with a frequency set to 6.78MHz. This makes the assumption that the class-D resonant inverter is an ideal AC voltage source and the full-bridge rectifier is an ideal AC-to-DC converter. This simplification ignores the fact that the inverter must operate in a zero voltage switching, soft switching condition to mitigate switching losses.

$$L_{tank} = \frac{1}{\omega^2 C_{tank}} \tag{6.1}$$

Instead, the analysis in this work accounts for the non-idealities in the inverter and rectifier to give a more accurate approximation of the required tank inductance in eq. (6.2). It can also give insight into the sensitivity of system parameters. This new equation takes into account parameters such as the deadtime of the inverter, the equivalent diode capacitance of the rectifier, and equivalent series resistance of connection wires.

$$L_{tank} = \frac{C_{tank}\omega(C_e^2 R_e^2 R_{tank}\omega^2 + R_e + R_{tank})\tan(\frac{\omega}{2}t_d) + 2 + C_e R_e^2 (C_{tank} + 2C_e)\omega^2}{2\omega^2 C_{tank}(C_e^2 R_e^2 \omega^2 + 1)} \tag{6.2}$$

6.1.4 Contribution #4: Integrated capacitive resolver with rotating rectifier for any WFSM excitation method

This is the first capacitive resolver specifically designed for kilowatt-level electric machines. It is also easily scalable to match the rotor pole count. The development of an integrated resolver and rectifier board furthers the goal of reducing the system cost for any wound field synchronous machine excitation method. This design removes the need for an additional resolver component and helps to lower the cost of entry to replace WFSMs with permanent magnet machines for traction applications. Chapter 4 and Chapter 5 detail the design, analysis, and testing of a capacitive resolver integrated around a rotating rectifier.

The capacitive resolver is comprised of one stationary and one rotating PCB. The stationary board takes in two AC carrier excitation voltages 180° out of phase. The stator excitation electrodes capacitively couple to the rotor electrodes on the board that is mechanically connected to the rotor shaft. The rotor electrodes couple back to four petal-shaped "pick-up" electrodes on the stator. As the machine rotates, the differential voltages across the opposite electrodes inscribe sine and cosine envelopes on the input carrier voltage signal. Essentially, the goal is to create a sinusoidal

capacitance varying with the shaft angle. The rotating rectifier is placed on the inside radius of the resolver rotor board and directly connected to the field winding.

- Development of Closed-Form Analytical Resolver Model

Between the rotor and stator resolver boards, the eight separate electrodes form 36 unique capacitances. With simplifying assumptions, the full capacitance matrix is modeled in order to derive an analytical solution for the resolver modulated output voltages. With simplifying assumptions, the main coupling capacitance as a function of rotor position is derived between the rotor excitation electrodes and the stator pick up electrodes.

- Development of 3D FEA Capacitive Resolver Model

Ansys Maxwell was used to simulate a 3D FEA model of the capacitive resolver and evaluate different topologies. Figure 6.2 shows a few different resolver topologies that did not work well as resolvers. The capacitance matrix extracted from this model was analyzed in MATLAB and used to evaluate the harmonics and expected error from different capacitive resolver topologies. Additionally, the pattern between the stator and rotor electrodes is easily extrapolated out for higher pole machines. The capacitive resolver is a multi-purpose position sensing solution for any wireless excitation method.

In order to advance the goal of creating a low-cost wireless excitation method, an integrated capacitive resolver and rotating rectifier were proposed. The design is intended to act as a drop-in replacement for the rotating rectifier necessary in a WFSM wireless excitation system and the encoder or resolver present. Many rotating rectifiers already use printed circuit boards which naturally lends itself to a combined capacitive-based system.

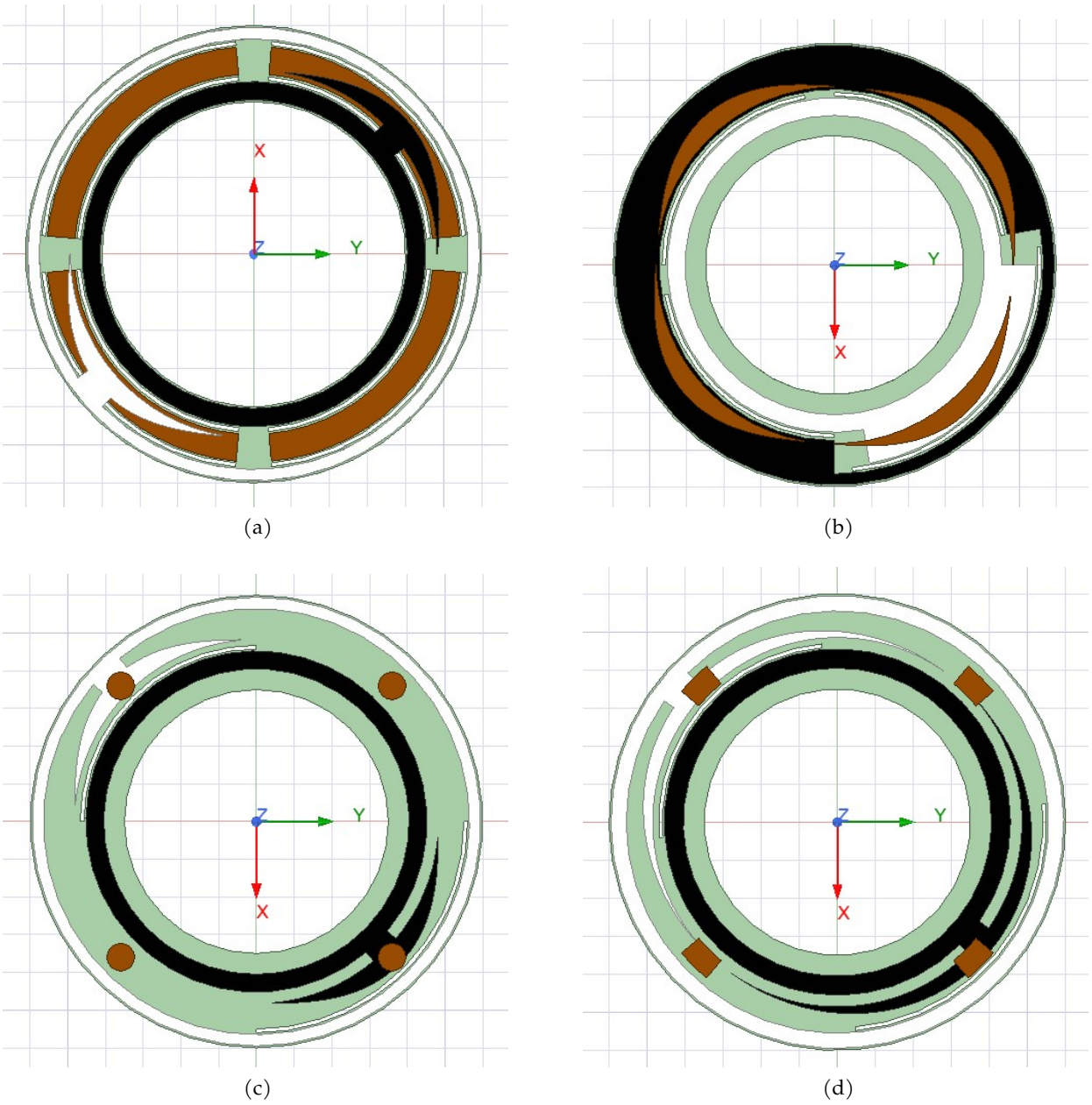

Figure 6.2: Screenshots from Ansys Maxwell simulations of different capacitive resolver topologies that did not work out. In brown are the stator board "pick-up" electrodes and the excitation electrodes are shown in black and white.

6.1.5 Contribution #5: Conventional Resolver Excitation and Demodulation Compatibility with Error $< 0.5°$

In the state of the art review in section 1.3, there are many different topologies of capacitive position sensors that have unique excitation and demodulation strategies. In order to lower the barrier for

the integrated design, the capacitive resolver is specifically made to be a drop-in replacement for traditional magnetic resolvers without the need for additional controls or circuitry. The capacitive resolver can take in two 10-20kHz carrier excitation voltages 180° out of phase, and output two pairs of differential voltages with sinusoidal envelopes.

During testing the sinusoidal envelope signals were demodulated using an analog multiplier to produce clean sine and cosine waves for the shaft position derivation. However, the differential voltages were also connected to a commercially available demodulation platform, the Analog Devices AD2S1210 resolver-to-digital converter platform. The resolver was spun at various speeds and the differential signals were digitally demodulated with a positional accuracy as low as 0.3°. This falls within the accuracy range of conventional magnetic resolver errors between 0.1° and 1° depending on the demodulation algorithm and software [140–142].

In order to interface directly with the AD2S1210 platform, a filter board was added between the output of the differential resolver signals and the evaluation board. The resolver filter board level shifts and applies a gain to each of the four output signals to be centered around 2.5V and $4V_{pk-pk}$. The AD2S1210 platform produced an order of magnitude lower positional error and gives an example of digital resolver demodulation that is widely available for drive system controllers.

6.1.6 Contribution #6: CPT System Integrated Resolver with Error $< 10°$

The design of the general capacitance resolver is a donut shape that is added at the outer radius of the rotating rectifier PCB. Likewise, the same capacitive resolver functionality is added around the outer radius of the CPC boards. The CPT system already has a sinusoidal voltage applied to the input of the current-stiff rectifier and is additionally used for the resolver excitation. The resolver excitation in this case is at 6.78MHz so it is not compatible with direct digital demodulation controllers that operate only up to 20kHz. However, analog multiplier demodulation circuitry can still be used successfully with an accuracy of $< 10°$.

6.2 Future Work

There are additional pathways to further the main goals of 1) improving the maximum continuous power capability of the capacitive wireless excitation system and 2) reducing the wound field

synchronous machine system costs to become a commercially viable permanent magnet alternative. Below is a list of suggested work followed by a detailed summary of each point.

1. Evaluate the EMI spectrum of the CPT system around 6.78MHz and determine its compatibility with automotive and other traction application standards.
2. Investigate alternate cooling strategies for CPT rectifier losses.
3. Investigate the use of an aluminum substrate for the rotating resolver board to increase diode thermal dissipation.
4. Scale the CPC-integrated-resolver filter circuitry gain with the rotor field power.
5. Characterize the general resolver and CPC-integrated resolver under dynamic power transients.
6. Add a ground plane for decoupling the stator-side resolver electrodes from filter circuitry on the back of the board.

6.2.1 Future Work #1: Evaluation of Capacitive Power Transfer EMI

The ISM band of reserved frequencies around 6.78MHz is only a 30kHz range between 6.765-6.795MHz. The CPT system is intended for use in traction applications, so it is important to understand the amount of EMI that is produced from parasitic resonances among the GaN HEMT and SiC Schottky diode equivalent capacitances and stray inductances. The natural frequency changes as the coupler boards rotate and the switching frequency is set to operate just above that natural resonant frequency. It is important to investigate if the rotor spinning and the changing output will affect the natural frequency enough to move out of the designated ISM band.

6.2.2 Future Work #2: CPT Rectifier Cooling

The CPT rectifier is confined to a small footprint on the center of the rotating coupler board. The machine rotor was stationary during CPT testing with forced air to mimic the natural airflow over the diodes when the rotor spins during normal motor operation. The limiting component of the system at 2.3kW was the rotating rectifier cooling. The diode heating at different speeds and powers

has not been measured. All rotor components must be rated for both the maximum field power as well as the maximum rotational speed and acceleration of the rotor. There is a need to investigate the diode placement and determine an optimal cooling configuration for continuous operation.

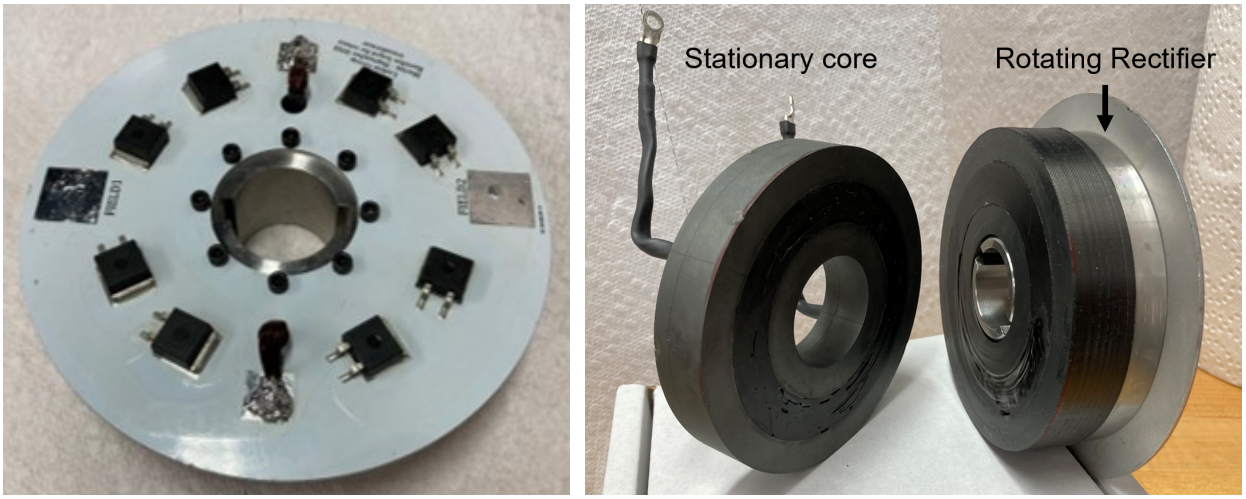

(a) (b)

Figure 6.3: (a) Picture of a rotating rectifier PCB and (b) rotary transformer core assembly.

6.2.3 Future Work #3: Aluminum Substrate PCB for Resolver Rectifier

Aluminum substrate PCBs are a highly thermally conductive alternative to standard FR4 substrate. Aluminum-clad boards are commonly used in applications where components are expected to generate a lot of localized heat, such as LEDs. Typically these are one layer boards where the bottom is attached to a heatsink for additional thermal dissipation. Figure 6.3 shows an example of a rotary transformer for wireless rotor excitation with a rotating rectifier. The rectifier is a single-layer aluminum PCB mounted onto the back of the spinning-side transformer core.

To further improve the power capability of the rectifier integrated with the capacitive resolver, it would be helpful to use an aluminum substrate PCB for the resolver rotor board. However, it would be necessary to investigate how a piece of solid aluminum would affect the coupling capacitances on the resolver. 3D FEA simulations could give insight into using alternative materials for the resolver PCB to aid in cooling the rectifier.

6.2.4 Future Work #4: CPC Resolver with Variable Filter Gain

The benefit of the CPC-integrated resolver is that the main power path provides the carrier frequency excitation for the resolver. No external AC supply is required as the input AC voltage to the rectifier is the excitation voltage. However, the rectifier voltage scales with the system output power and can reach well into the hundreds of volts. The resolver analog filter circuitry currently operates within a small voltage range of $\pm 5V$. Therefore, there is a need for a variable voltage gain between the resolver output voltages and the input to the filter circuitry to account for changing field power.

6.2.5 Future Work #5: Characterize Resolver under Dynamic Power Changes

Both versions of the integrated resolver and rectifier were tested in the lab and isolated from the dynamics of motoring operation. The CPC-integrated resolver was tested at a near-constant output power, 570W average, in order to avoid transient responses from dynamic changes in the load power. Dynamometer testing on a machine with dynamic rotor power changes will give a good understanding of how the resolver error is affected by transient events on the machine.

6.2.6 Future Work #6: Ground Plane for Circuitry on Resolver Stator Board

In this work, the resolver signals were measured from axial board-to-board connectors to avoid thin traces on the stator board other than the resolver electrodes. These traces introduced symmetry issues on the modulated output voltage signals as discussed in FEA in section 4.3 and confirmed during testing in section 5.2. Specifically, the connectors necessitated a third board for filtering and demodulating the resolver output signals.

Further work can be done to integrate the filter circuitry onto the stator resolver board specifically with the inclusion of ground planes. The ground planes were shown to remove symmetry issues from the traces but still had a large third spatial harmonic present. The ground planes also introduced additional leakage capacitance pathways that reduced the signal gain on the output modulated voltages. Additional filters and amplifiers could be used to remove the third spatial harmonic and create sinusoidal resolver output waveforms with only two total boards.

BIBLIOGRAPHY

[1] J. K. Nøland and S. Nuzzo, "Excitation System Technologies for Wound-Field Synchronous Machines : Survey of Solutions and Evolving Trends," *IEEE Access*, vol. 7, pp. 109 699–109 718, 2019.

[2] B. Reams, "New Brushes Aligned on Slip Rings," 2013. [Online]. Available: https://www.flickr.com/photos/brook-reams/9866702634/in/photostream/

[3] D. C. Ludois, J. K. Reed, and K. Hanson, "Capacitive power transfer for rotor field current in synchronous machines," *IEEE Transactions on Power Electronics*, vol. 27, no. 11, pp. 4638–4645, 2012.

[4] F. I. Lu, H. Zhang, and C. Mi, "A Review on the Recent Development of Capacitive Wireless Power Transfer Technology," 2017. [Online]. Available: www.mdpi.com/journal/energies

[5] S. Sinha, A. Kumar, B. Regensburger, and K. K. Afridi, "Design of High-Efficiency Matching Networks for Capacitive Wireless Power Transfer Systems," *IEEE Journal of Emerging and Selected Topics in Power Electronics*, vol. 2, no. c, pp. 1–1, 2020.

[6] R. W. Erickson and D. Maksimović, *Fundamentals of Power Electronics*, third edit ed. Springer International Publishing, 2020.

[7] M. B. Shamseh, I. Yuzurihara, and A. Kawamura, "A 3.2-kW 13.56-MHz SiC Passive Rectifier with 94.0% Efficiency Using Commutation Capacitor," *IEEE Transactions on Power Electronics*, vol. 31, no. 10, pp. 6787–6791, 2016.

[8] A. Devices, "CN-0276 (Rev 0)," Tech. Rep. [Online]. Available: www.analog.com/CN0276.

[9] S. Marcus, "U.S. House Bill Would Give Tax Credit for Rare Earth Magnets," *Reuters*, pp. 16–18, 2021. [Online]. Available: https://www.reuters.com/business/us-house-bill-would-give-tax-credit-rare-earth-magnets-2021-08-10/

[10] E. Onstad, "EU considers help for rare earth magnet production - sources," *Reuters*, pp. 1–5, 8 2021.

[11] D. Kramer, "US government acts to reduce dependence on China for rare-earth magnets," pp. 20–24, 2021.

[12] E. Alonso, A. M. Sherman, T. J. Wallington, M. P. Everson, F. R. Field, R. Roth, and R. E. Kirchain, "Evaluating rare earth element availability: A case with revolutionary demand from clean technologies," *Environmental Science and Technology*, vol. 46, no. 8, pp. 3406–3414, 2012.

[13] A. Leader, G. Gaustad, and C. Babbitt, "The effect of critical material prices on the competitiveness of clean energy technologies," *Materials for Renewable and Sustainable Energy*, vol. 8, no. 2, pp. 1–17, 2019. [Online]. Available: https://doi.org/10.1007/s40243-019-0146-z

[14] J. Nayar, "Not So "Green" Technology: The Complicated Legacy of Rare Earth Mining," *Harvard International Review*, 8 2021.

[15] M. Standaert, "China Wrestles with the Toxic Aftermath of Rare Earth Mining," *Yale Environment 360*, pp. 1–9, 7 2019.

[16] M. Penke, "Toxic and Radioactive: The Damage from Mining Rare Elements," *DW*, 2021. [Online]. Available: https://www.dw.com/en/toxic-and-radioactive-the-damage-from-mining-rare-elements/a-57148185

[17] D. Van Brusselen, T. Kayembe-Kitenge, S. Mbuyi-Musanzayi, T. Lubala Kasole, L. Kabamba Ngombe, P. Musa Obadia, D. Kyanika wa Mukoma, K. Van Herck, D. Avonts, K. Devriendt, E. Smolders, C. B. L. Nkulu, and B. Nemery, "Metal mining and birth defects: a case-control study in Lubumbashi, Democratic Republic of the Congo," *The Lancet Planetary Health*, vol. 4, no. 4, pp. e158–e167, 2020.

[18] A. Martin and A. Iles, "The ethics of rare earth elements over time and space," *Ethics Of Chemistry: From Poison Gas To Climate Engineering*, vol. 26, no. 2020, pp. 317–346, 2021.

[19] A. Home, "Cobalt, Congo and a mass artisanal mining experiment," *Reuters Investing News*, pp. 2–5, 5 2021.

[20] J. K. Noland, M. Giset, and E. F. Alves, "Continuous Evolution and Modern Approaches of Excitation Systems for Synchronous Machines," *Proceedings - 2018 23rd International Conference on Electrical Machines, ICEM 2018*, pp. 104–110, 2018.

[21] S. Nuzzo, M. Galea, P. Bolognesi, G. Vakil, D. Fallows, C. Gerada, and N. Brown, "A Methodology to Remove Stator Skew in Small-Medium Size Synchronous Generators via Innovative Damper Cage Designs," *IEEE Transactions on Industrial Electronics*, vol. 66, no. 6, pp. 4296–4307, 2019.

[22] S. Nuzzo, P. Bolognesi, C. Gerada, and M. Galea, "Simplified Damper Cage Circuital Model and Fast Analytical-Numerical Approach for the Analysis of Synchronous Generators," *IEEE Transactions on Industrial Electronics*, vol. 66, no. 11, pp. 8361–8371, 2019.

[23] Y. Q. Zhang and A. M. Cramer, "Unified model formulations for synchronous machine model with saturation and arbitrary rotor network representation," *IEEE Transactions on Energy Conversion*, vol. 31, no. 4, pp. 1356–1365, 2016.

[24] A. Di Gioia, I. P. Brown, Y. Nie, R. Knippel, D. C. Ludois, J. Dai, S. Hagen, and C. Alteheld, "Design and Demonstration of a Wound Field Synchronous Machine for Electric Vehicle Traction with Brushless Capacitive Field Excitation," *IEEE Transactions on Industry Applications*, vol. 54, no. 2, pp. 1390–1403, 2018.

[25] D. C. Ludois and I. Brown, "Brushless and permanent magnet free wound field synchronous motors for EV traction," University of Wisconsin – Madison, Illinois Institute of Technology, Madison, WI, Tech. Rep., 2017.

[26] C. Stancu, T. Ward, K. M. Rahman, R. Dawsey, and P. Savagian, "Separately Excited Synchronous Motor With Rotary Transformer for Hybrid Vehicle Application," *IEEE Transactions on Industry Applications*, vol. 54, no. 1, pp. 223–232, 2018.

[27] M. D. Bryant, A. Tewari, and J.-w. Lin, "Wear Rate Reductions in Carbon Brushes, Conducting Current, and Sliding Against Wavy Copper Surfaces," *Spring*, vol. 18, no. 2, 1995.

[28] A. M. El-Refaie, M. M. Abdel Aziz, S. A. Khorshid, and E. E. Abu Elzahab, "Effect of combined velocity and pressure on life time of carbon brushes," *IEEE Transactions on Energy Conversion*, vol. 15, no. 2, pp. 176–180, 2000.

[29] L. Brown, D. Kuhlmann-Wilsdorf, and W. Jesser, "Testing and evaluation of metal fiber brush operation on slip rings and commutators," *IEEE Transactions on Components and Packaging Technologies*, vol. 31, no. 2 SPEC. ISS., pp. 485–494, 2008.

[30] J. K. Skjølberg, H. F. Ohma, and M. Runde, "Wear rates and current distribution of carbon brushes on steel slip rings," *IEEE Transactions on Energy Conversion*, vol. 24, no. 4, pp. 835–840, 2009.

[31] R. D. Hall, F. Drive, R. P. Roberge, M. Am, and F. Drive, "CARBON BRUSH PERFORMANCE ON SLIP RINGS," 2010.

[32] J. Skooglund, W. South, T. Dillman, F. Keay, and C. Raczkowski, "Brushless Excitation," Westinghouse Electric Corporation, Tech. Rep., 1972.

[33] G. Laliberte, "A Comparison of Generator Excitation Systems," Cummins Power Generation, Tech. Rep., 2016.

[34] A. Griffo, R. Wrobel, P. H. Mellor, and J. M. Yon, "Design and characterization of a three-phase brushless exciter for aircraft starter/generator," *IEEE Transactions on Industry Applications*, vol. 49, no. 5, pp. 2106–2115, 2013.

[35] V. Ruuskanen, M. Niemelä, J. Pyrhönen, S. Kanerva, and J. Kaukonen, "Modelling the brushless excitation system for a synchronous machine," *IET Electric Power Applications*, vol. 3, no. 3, pp. 231–239, 2009.

[36] W. H. South, C. Raczkowski, T. L. Dillman, J. W. Skooglund, and F. W. Keay, "A High Initial Response Brushless Excitation System," no. February, pp. 2089–2094, 1971.

[37] T. A. Lipo, "Patent Application Publication Pub. No.: US 2012/0086381 A1," 2012.

[38] Q. An, X. Gao, F. Yao, L. Sun, and T. Lipo, "The structure optimization of novel harmonic current excited brushless synchronous machines based on open winding pattern," *2014 IEEE Energy Conversion Congress and Exposition, ECCE 2014*, no. 51277040, pp. 1754–1761, 2014.

[39] L. Sun, X. Gao, F. Yao, Q. An, and T. Lipo, "A new type of harmonic current excited brushless synchronous machine based on an open winding pattern," *2014 IEEE Energy Conversion Congress and Exposition, ECCE 2014*, no. 51277040, pp. 2366–2373, 2014.

[40] F. Yao, Q. An, X. Gao, L. Sun, and T. A. Lipo, "Principle of Operation and Performance of a Synchronous Machine Employing a New Harmonic Excitation Scheme," *IEEE Transactions on Industry Applications*, vol. 51, no. 5, pp. 3890–3898, 2015.

[41] F. Yao, Q. An, L. Sun, and T. A. Lipo, "Performance Investigation of a Brushless Synchronous Machine with Additional Harmonic Field Windings," *IEEE Transactions on Industrial Electronics*, vol. 63, no. 11, pp. 6756–6766, 2016.

[42] F. Yao, L. Sun, D. Sun, and T. Lipo, "Design and Excitation Control of a Dual Three-Phase Zero-Sequence Current Starting Scheme for Integrated Starter/Generator," *IEEE Transactions on Industry Applications*, vol. 57, no. 4, pp. 3776–3786, 2021.

[43] Q. Ali, T. A. Lipo, and B. I. Kwon, "Design and Analysis of a Novel Brushless Wound Rotor Synchronous Machine," *IEEE Transactions on Magnetics*, vol. 51, no. 11, pp. 1–4, 2015.

[44] M. Ayub, A. Hussain, G. Jawad, and B. I. Kwon, "Brushless Operation of a Wound-Field Synchronous Machine Using a Novel Winding Scheme," *IEEE Transactions on Magnetics*, vol. 55, no. 6, pp. 1–4, 2019.

[45] D. Fallows, S. Nuzzo, and M. Galea, "Exciterless Wound-Field Medium-Power Synchronous Machines: Their History and Future," pp. 2–9, 2021.

[46] K. Veszprémi, I. Schmidt, and M. Hunyár, "Optimal operation of the rotating transformer brushless excitation of synchronous machine," *IEEE International Symposium on Industrial Electronics*, vol. I, pp. 627–632, 2003.

[47] M. Ruviaro, F. Rüncos, N. Sadowski, and I. M. Borges, "Design and analysis of a brushless doubly fed induction machine with rotary transformer," *19th International Conference on Electrical Machines, ICEM 2010*, 2010.

[48] M. Ruviaro and F. Runcos, "A brushless doubly fed induction machine with flat plane rotary transformers," *Proceedings - 2012 20th International Conference on Electrical Machines, ICEM 2012*, pp. 23–29, 2012.

[49] M. Ruviaro, F. Rüncos, N. Sadowski, and I. M. Borges, "Analysis and test results of a brushless doubly fed induction machine with rotary transformer," *IEEE Transactions on Industrial Electronics*, vol. 59, no. 6, pp. 2670–2677, 2012.

[50] Y. Liu, D. Pehrman, O. Lykartsis, J. Tang, and T. Liu, "High frequency exciter of electrically excited synchronous motors for vehicle applications," *Proceedings - 2016 22nd International Conference on Electrical Machines, ICEM 2016*, pp. 378–383, 2016.

[51] M. Maier, N. Parspour, P. Kleemann, and M. Hagl, "Construction and measurements of an electrical excited synchronous machine with inductive contactless energy transfer to the rotor," *14th Brazilian Power Electronics Conference, COBEP 2017*, vol. 2018-Janua, pp. 1–6, 2017.

[52] J. Tang and Y. Liu, "Design and Experimental Verification of a 48 v 20 kW Electrically Excited Synchronous Machine for Mild Hybrid Vehicles," *Proceedings - 2018 23rd International Conference on Electrical Machines, ICEM 2018*, pp. 649–655, 2018.

[53] J. Tang, Y. Liu, and N. Sharma, "Modeling and Experimental Verification of High-Frequency Inductive Brushless Exciter for Electrically Excited Synchronous Machines," *IEEE Transactions on Industry Applications*, vol. 55, no. 5, pp. 4613–4623, 2019.

[54] S. Udema and C. Frager, "Rotary transformer for contactless excitation of synchronous machines fed through neutral conductor," *2019 IEEE International Electric Machines and Drives Conference, IEMDC 2019*, vol. 978, pp. 1724–1730, 2019.

[55] J. Veitengruber, F. Rinderknecht, and H. E. Friedrich, "Preliminary investigations of an inductive power transfer system for the rotor power supply of an electric traction drive," 2014.

[56] J. Veitengruber, "Design and characterization of a cost-effective and high-power density brushless rotor supply for mobile synchronous generators," pp. 12–17, 2015.

[57] H. Krupp, A. Mertens, and A. M. H. Krupp, "Rotary Transformer Design for Brushless Electrically Excited Synchronous Machines," *2015 IEEE Vehicle Power and Propulsion Conference, VPPC 2015 - Proceedings*, pp. 1–6, 2015.

[58] M. Maier, M. Zimmer, J. Heinrich, D. Maier, and N. Parspour, "Dimensioning of a contactless energy transfer system for an electrical excited synchronous machine," *2016 IEEE Wireless Power Transfer Conference, WPTC 2016*, vol. 2, no. 1, pp. 1–3, 2016.

[59] T. Raminosoa and R. Wiles, "Contactless Rotor Excitation for Traction Motors," *2018 IEEE Energy Conversion Congress and Exposition, ECCE 2018*, pp. 6448–6453, 2018.

[60] M. Maier and N. Parspour, "Operation of an Electrical Excited Synchronous Machine by Contactless Energy Transfer to the Rotor," *IEEE Transactions on Industry Applications*, vol. 54, no. 4, pp. 3217–3225, 2018.

[61] S. Kohler and B. Wagner, "Control of the excitation current of an externally excited synchronous machine supplied by an inductive energy transfer system," *2018 13th International Conference on Ecological Vehicles and Renewable Energies, EVER 2018*, pp. 1–8, 2018.

[62] D. Maier, J. Kurz, and N. Parspour, "Contactless Energy Transfer for Inductive Electrically Excited Synchronous Machines," *2019 IEEE PELS Workshop on Emerging Technologies: Wireless Power Transfer, WoW 2019*, pp. 191–195, 2019.

[63] J. P. Smeets, D. C. Krop, J. W. Jansen, M. A. Hendrix, and E. A. Lomonova, "Optimal design of a pot core rotating transformer," *2010 IEEE Energy Conversion Congress and Exposition, ECCE 2010 - Proceedings*, pp. 4390–4397, 2010.

[64] J. P. Smeets, L. Encica, and E. A. Lomonova, "Comparison of winding topologies in a pot core rotating transformer," *Proceedings of the International Conference on Optimisation of Electrical and Electronic Equipment, OPTIM*, no. 1, pp. 103–110, 2010.

[65] T. Raminosoa, R. H. Wiles, and J. Wilkins, "Novel Rotary Transformer Topology with Improved Power Transfer Capability for High-Speed Applications," *IEEE Transactions on Industry Applications*, vol. 56, no. 1, pp. 277–286, 2020.

[66] R. S. Yang, A. J. Hanson, B. A. Reese, C. R. Sullivan, and D. J. Perreault, "A Low-Loss Inductor Structure and Design Guidelines for High-Frequency Applications," *IEEE Transactions on Power Electronics*, vol. 34, no. 10, pp. 9993–10 005, 2019.

[67] J. Legrangerl, G. Friedrich, S. Vivierl, and J. C. Mipo, "Comparison of Two Optimal Rotary Transformer Designs for Highly Constrained Applications," 2007.

[68] S. A. Vip, J. N. Weber, A. Rehfeldt, and B. Ponick, "Rotary transformer with ferrite core for brushless excitation of synchronous machines," *Proceedings - 2016 22nd International Conference on Electrical Machines, ICEM 2016*, pp. 890–896, 2016.

[69] M. Maier, M. Hagl, M. Zimmer, J. Heinrich, and N. Parspour, "Design and construction of a novel rotating contactless energy transfer system for an electrical excited synchronous machine," *Proceedings - 2016 22nd International Conference on Electrical Machines, ICEM 2016*, pp. 709–714, 2016.

[70] H. Zhong, C. Wu, and Y. Wang, "Design and analysis of rotary transformer for brushless doubly fed induction generators," *Proceedings of the 13th IEEE Conference on Industrial Electronics and Applications, ICIEA 2018*, no. 1, pp. 1416–1419, 2018.

[71] J. Godbehere, A. Hopkins, and X. Yuan, "Design and thermal analysis of a rotating transformer," *2019 IEEE International Electric Machines and Drives Conference, IEMDC 2019*, no. Mdl, pp. 2144–2151, 2019.

[72] J. Haruna, T. Raminosoa, and J. Wilkins, "Enhanced Rotary Transformer-Based Field Excitation System for Wound Rotor Synchronous Motor," *2019 IEEE Energy Conversion Congress and Exposition, ECCE 2019*, pp. 1166–1173, 2019.

[73] X. Zu and Q. Jiang, "Study of High Frequency Rotary Transformer Structures for Contactless Inductive Power Transfer," pp. 1–5, 2019.

[74] D. C. Ludois, K. Hanson, and J. K. Reed, "Capacitive power transfer for slip ring replacement in wound field synchronous machines," *IEEE Energy Conversion Congress and Exposition: Energy Conversion Innovation for a Clean Energy Future, ECCE 2011, Proceedings*, pp. 1664–1669, 2011.

[75] C. Liu, A. P. Hu, and N. K. C. Nair, "Coupling study of a rotary capacitive power transfer system," *Proceedings of the IEEE International Conference on Industrial Technology*, 2009.

[76] C. Liu, A. P. Hu, and M. Budhia, "A generalized coupling model for Capacitive Power Transfer systems," *IECON Proceedings (Industrial Electronics Conference)*, pp. 274–279, 2010.

[77] F. Lu, H. Zhang, H. Hofmann, and C. Mi, "A Double-Sided LCLC-Compensated Capacitive Power Transfer System for Electric Vehicle Charging," vol. 30, no. 11, pp. 6011–6014, 2015.

[78] J. Dai and D. C. Ludois, "Capacitive Power Transfer Through a Conformal Bumper for Electric Vehicle Charging," *IEEE Journal of Emerging and Selected Topics in Power Electronics*, vol. 4, no. 3, pp. 1015–1025, 2016.

[79] S. Sinha, A. Kumar, B. Regensburger, and K. K. Afridi, "A New Design Approach to Mitigating the Effect of Parasitics in Capacitive Wireless Power Transfer Systems for Electric Vehicle Charging," *IEEE Transactions on Transportation Electrification*, vol. 5, no. 4, pp. 1040–1059, 2019.

[80] B. Regensburger, A. Kumar, S. Sinha, and K. Afridi, "High-Performance 13.56-MHz Large Air-Gap Capacitive Wireless Power Transfer System for Electric Vehicle Charging," *2018 IEEE 19th Workshop on Control and Modeling for Power Electronics, COMPEL 2018*, pp. 1–4, 2018.

[81] H. Zhang, F. Lu, H. Hofmann, W. Liu, and C. C. Mi, "A Four-Plate Compact Capacitive Coupler Design and LCL-Compensated Topology for Capacitive Power Transfer in Electric Vehicle Charging Application," *IEEE Transactions on Power Electronics*, vol. 31, no. 12, pp. 8541–8551, 2016.

[82] B. Regensburger, J. Estrada, A. Kumar, S. Sinha, Z. Popovic, and K. K. Afridi, "High-Performance Capacitive Wireless Power Transfer System for Electric Vehicle Charging with Enhanced Coupling Plate Design," *2018 IEEE Energy Conversion Congress and Exposition, ECCE 2018*, pp. 2472–2477, 2018.

[83] J. Dai and D. C. Ludois, "A Survey of Wireless Power Transfer and a Critical Comparison of Inductive and Capacitive Coupling for Small Gap Applications," *IEEE Transactions on Power Electronics*, vol. 30, no. 11, pp. 6017–6029, 2015.

[84] S. Hagen, M. Tisler, J. Dai, I. P. Brown, and D. C. Ludois, "Use of the Rotating Rectifier Board as a Capacitive Power Coupler for Brushless Wound Field Synchronous Machines," *IEEE Journal of Emerging and Selected Topics in Power Electronics*, vol. 6777, no. c, 2022.

[85] S. Hagen, J. Dai, I. P. Brown, and D. C. Ludois, "Low-cost, printed circuit board construction, capacitively coupled excitation system for wound field synchronous machines," *2019 IEEE Energy Conversion Congress and Exposition, ECCE 2019*, pp. 5358–5364, 2019.

[86] S. S. Hagen, "COUPLER AND PASSIVE COMPONENT DESIGN FOR SYNCHRONOUS MACHINES EXCITED WITH CAPACITIVE POWER TRANSFER," 2019.

[87] C. Liu and A. P. Hu, "Steady state analysis of a capacitively coupled contactless power transfer system," *2009 IEEE Energy Conversion Congress and Exposition, ECCE 2009*, pp. 3233–3238, 2009.

[88] K. Kamarudin, S. Saat, and Y. Yusmarnita, "Analysis and design of wireless power transfer: A capacitive based method," *ISIEA 2014 - 2014 IEEE Symposium on Industrial Electronics and Applications*, pp. 136–141, 2017.

[89] J. Heinrich, A. Lusiewicz, Q. Shen, and N. Parspour, "Fundamentals and Design Proposal for Capacitive Contactless Power Transfer Systems," *SPEEDAM 2018 - Proceedings: International Symposium on Power Electronics, Electrical Drives, Automation and Motion*, pp. 750–755, 2018.

[90] J. Kracek and M. Svanda, "Power balance of capacitive wireless power transfer," *Proceedings of European Microwave Conference in Central Europe, EuMCE 2019*, pp. 521–524, 2019.

[91] H. Funato, H. Kobayashi, and T. Kitabayashi, "Analysis of transfer power of capacitive power transfer system," *Proceedings of the International Conference on Power Electronics and Drive Systems*, pp. 1015–1020, 2013.

[92] Y. Yusop, Z. Ghani, S. Saat, H. Husin, and S. K. Nguang, "Capacitive power transfer with impedance matching network," *Proceeding - 2016 IEEE 12th International Colloquium on Signal Processing and its Applications, CSPA 2016*, no. March, pp. 124–129, 2016.

[93] S. Wang, J. Liang, and M. Fu, "Analysis and Design of Capacitive Power Transfer Systems Based on Induced Voltage Source Model," *IEEE Transactions on Power Electronics*, vol. 35, no. 10, pp. 10 532–10 541, 2020.

[94] S. Kuroda and T. Imura, "Derivation and comparison of efficiency and power in non-resonant and resonant circuit of capacitive power transfer," *2020 IEEE PELS Workshop on Emerging Technologies: Wireless Power Transfer, WoW 2020*, no. 1, pp. 152–157, 2020.

[95] J. Dai and D. C. Ludois, "Single active switch power electronics for kilowatt scale capacitive power transfer," *IEEE Journal of Emerging and Selected Topics in Power Electronics*, vol. 3, no. 1, pp. 315–323, 2015.

[96] S. Hagen, R. Knippel, J. Dai, and D. C. Ludois, "Capacitive coupling through a hydrodynamic journal bearing to power rotating electrical loads without contact," *2015 IEEE Wireless Power Transfer Conference, WPTC 2015*, pp. 1–4, 2015.

[97] J. Dai, S. Hagen, D. C. Ludois, and I. P. Brown, "Synchronous Generator Brushless Field Excitation and Voltage Regulation via Capacitive Coupling Through Journal Bearings," *IEEE Transactions on Industry Applications*, vol. 53, no. 4, pp. 3317–3326, 2017.

[98] W. C. Heerens, "Multi-terminal capacitor sensors," *Journal of Physics E: Scientific Instruments*, vol. 15, no. 1, pp. 137–141, 1982.

[99] ——, "Application of capacitance techniques in sensor design," *Journal of Physics E: Scientific Instruments*, vol. 19, no. 11, pp. 897–906, 1986.

[100] R. D. Peters, "Linear rotary differential capacitance transducer Linear rotary differential capacitance transducer," vol. 2789, 1989.

[101] X. Li, G. de Jong, and G. C. Meijer, "Effect of electric-field bending on the linearity of capacitive position sensors with various electrode structures," pp. 1348–1351, 1999.

[102] R. F. Wolffenbuttel and R. P. V. A. N. Kampen, "An Integrable Capacitive Angular Displacement Sensor with Improved Linearity," vol. 27, pp. 835–843, 1991.

[103] P. P. L. Regtien, "Capacitance-to-Phase Angle Conversion for the Detection of Extremely Small Capacities," vol. IM, no. 4, pp. 868–872, 1987.

[104] T. Fabian and G. Brasseur, "A measurement algorithm for capacitive speed encoder with a modified front-end topology," *IEEE Transactions on Instrumentation and Measurement*, vol. 47, no. 5, pp. 1341–1345, 1998.

[105] B. Hou, B. Zhou, X. Li, Z. Gao, and Q. Wei, "An Analog Interface Circuit for Capacitive Angle Encoder Based on a Capacitance Elimination Array and Synchronous Switch Demodulation Method," vol. c, 2019.

[106] B. Hou, B. Zhou, X. Li, B. Xing, Q. Wei, and R. Zhang, "Nonlinear Error Compensation of Capacitive Angular Encoder," *Proceedings of IEEE Sensors*, vol. 2019-Octob, pp. 2019–2022, 2019.

[107] G. W. D. Jong, G. C. M. Meljer, K. V. D. Lmgen, J. W. Spronck, A. M. M. Aalsma, and D. T. A. J. M. Bertels, "A smart capacitive absolute angular-position sensor," vol. 42, pp. 41–42, 1994.

[108] X. Li, G. C. M. Meijer, W. Gerben, and J. W. Spronck, "An Accurate Low-Cost Capacitive Abso Angular-Position Sensor with a Full-Circle," vol. 45, no. 2, pp. 516–520, 1996.

[109] M. Gasulla, X. Li, G. C. M. Meijer, L. V. D. Ham, and J. W. Spronck, "A Contactless Capacitive Angular-Position Sensor," vol. 3, no. 5, pp. 607–614, 2003.

[110] T. Fabian and G. Brasseur, "A robust capacitive angular speed sensor," *IEEE Transactions on Instrumentation and Measurement*, vol. 47, no. 1, pp. 280–284, 1998.

[111] G. Brasseur, "A Capacitive 4-Turn Angular-Position Sensor," vol. 47, no. 1, pp. 275–279, 1998.

[112] G. Brasseur, P. L. Fulmek, and W. Smetana, "Virtual rotor grounding of capacitive angular position sensors," *IEEE Transactions on Instrumentation and Measurement*, vol. 49, no. 5, pp. 1108–1111, 2000.

[113] R. M. Kennel and S. Basler, "New Developments in Capacitive Encoders for Servo Drives," pp. 190–195, 2008.

[114] D. Zheng, S. Zhang, Y. Zhang, and C. Fan, "Application of CORDIC in Capacitive Rotary Encoder Signal Demodulation," no. 60904094, pp. 17–21, 2012.

[115] D. Zheng, S. Zhang, S. Wang, C. Hu, and X. Zhao, "A Capacitive Rotary Encoder Based on Quadrature Modulation and Demodulation," vol. 64, no. 1, pp. 143–153, 2015.

[116] F. Kimura, M. Gondo, A. Yamamoto, and T. Higuchi, "Resolver compatible capacitive rotary position sensor," pp. 1923–1928, 2009.

[117] Bo Hou, Bin Zhou, Mingliang Song, Zhihui Lin, and Rong Zhang, "A Novel Single-Excitation Capacitive Angular Position Sensor Design," 2016.

[118] B. Hou, B. Zhou, L. Yi, B. Xing, X. Li, Q. Wei, and R. Zhang, "High-Precision Incremental Capacitive Angle Encoder Developed by Micro Fabrication Technology," vol. 68, no. 7, pp. 6318–6327, 2021.

[119] B. Hou, Z. Tian, C. Li, Q. Wei, B. Zhou, R. Zhang, and A. Structure, "A Capacitive Rotary Encoder with a Novel Sensitive Electrode," vol. 2, pp. 31–33, 2017.

[120] O. K. M. K. M. Karali, A. T. Karasahin and M. A. Erismis, "A new capacitive rotary encoder based on analog synchronous demodulation," *Electrical Engineering*, vol. 100, no. 3, pp. 1975–1983, 2018. [Online]. Available: https://doi.org/10.1007/s00202-018-0677-9

[121] X. Fan, Z. Yu, K. Peng, Z. Chen, and X. Liu, "A Compact and High-Precision Capacitive Absolute Angular Displacement Sensor," *IEEE Sensors Journal*, vol. 20, no. 19, pp. 11 173–11 182, 2020.

[122] H. Wang, K. Peng, X. Liu, Z. Yu, and Z. Chen, "Design and Realization of a Compact High-Precision Capacitive Absolute Angular Position Sensor Based on Time Grating," *IEEE Transactions on Industrial Electronics*, vol. 68, no. 4, pp. 3548–3557, 2021.

[123] E. Yavsan, M. Rojhat, M. Karali, and B. Gokce, "A novel high resolution miniaturized capacitive rotary encoder," *Sensors & Actuators: A. Physical*, vol. 331, p. 112992, 2021. [Online]. Available: https://doi.org/10.1016/j.sna.2021.112992

[124] E. Yavsan, M. Karali, B. Gokce, and M. A. Erismis, "The Effect of Rotor Plates on Capacitive Measurement in Capacitive Encoders," pp. 31–34, 2020.

[125] D. Rozario, N. A. Azeez, and S. S. Williamson, "Comprehensive review and comparative analysis of compensation networks for Capacitive Power Transfer systems," *IEEE International Symposium on Industrial Electronics*, vol. 2016-Novem, pp. 823–829, 2016.

[126] H. Zhang, F. Lu, H. Hofmann, and C. Mi, "An LC compensated electric field repeater for long distance capacitive power transfer," *ECCE 2016 - IEEE Energy Conversion Congress and Exposition, Proceedings*, 2016.

[127] F. Lu, H. Zhang, H. Hofmann, and C. C. Mi, "A Double-Sided LC-Compensation Circuit for Loosely Coupled Capacitive Power Transfer," *IEEE Transactions on Power Electronics*, vol. 33, no. 2, pp. 1633–1643, 2018.

[128] M. P. Theodoridis, "Effective capacitive power transfer," *IEEE Transactions on Power Electronics*, vol. 27, no. 12, pp. 4906–4913, 2012.

[129] F. Lu, H. Zhang, H. Hofmann, and C. Mi, "A CLLC-compensated high power and large air-gap capacitive power transfer system for electric vehicle charging applications," *Conference Proceedings - IEEE Applied Power Electronics Conference and Exposition - APEC*, vol. 2016-May, pp. 1721–1725, 2016.

[130] U. D. Kavimandan, G. S. Member, V. P. Galigekere, S. Member, B. Ozpineci, O. Onar, S. Member, S. M. Mahajan, and S. Member, "The Impact of Inverter Dead-Time in Single-Phase Wireless Power Transfer Systems," pp. 1–17, 2021.

[131] Y. Du, J. Wang, G. Wang, and A. Q. Huang, "Modeling of the high-frequency rectifier with 10-kV SiC JBS diodes in high-voltage series resonant Type DC-DC Converters," *IEEE Transactions on Power Electronics*, vol. 29, no. 8, pp. 4288–4300, 2014.

[132] S. S. Hagen, "An Integrated Capacitive Brushless Excitation System for Wound Field Synchronous Machines Using Low-Cost Printed Circuit Boards," 2019.

[133] F. E. Terman, *Radio Engineers' Handbook*. McGraw-Hill, 1943.

[134] MWS Wire Industries, "Litz Wire."

[135] J. Dai, "Power Electronics Design for High Power Capacitive Power Transfer," Ph.D. dissertation, 2017.

[136] G. Zulauf, S. Park, W. Liang, K. N. Surakitbovorn, and J. Rivas-Davila, "COSS Losses in 600 v GaN Power Semiconductors in Soft-Switched, High- and Very-High-Frequency Power Converters," *IEEE Transactions on Power Electronics*, vol. 33, no. 12, pp. 10 748–10 763, 2018.

[137] Z. Tong, L. Gu, K. Surakitbovorn, and J. M. Rivas-Davila, "Gate Drive for Very Fast Resonant Conversion using SiC Switch," *2019 IEEE Energy Conversion Congress and Exposition, ECCE 2019*, pp. 6647–6654, 2019.

[138] M. S. Nikoo, A. Jafari, N. Perera, and E. Matioli, "New Insights on Output Capacitance Losses in Wide-Band-Gap Transistors," *IEEE Transactions on Power Electronics*, vol. 35, no. 7, pp. 6663–6667, 2020.

[139] B. Regensburger and K. K. Afridi, "Challenges and Solutions to Passive Rectification in Multi-MHz Frequency Capacitive Wireless Power Transfer Systems for Electric Vehicle Charging," *ECCE 2020 - IEEE Energy Conversion Congress and Exposition*, pp. 5482–5486, 2020.

[140] TE Connectivity, "Angular Position Sensors - Hollow Shaft Resolvers," 4 2023.

[141] Minebea Mitsumi, "Motor Resolvers," 4 2023.

[142] L. Tamagawa Seiki Co., "R/D Converters," 4 2023.

[143] A. NAY LIN HTUN, "Analysis and Synthesis of Precision Resolver System," 2015.

[144] M. G. Tiapkin and A. P. Balkovoi, "High resolution processing of position sensor with amplitude modulated signals of servo drive," *Proceedings of the 2017 IEEE Russia Section Young Researchers in Electrical and Electronic Engineering Conference, ElConRus 2017*, pp. 1042–1047, 2017.

[145] H. Liu and Z. Wu, "Demodulation of angular position and velocity from resolver signals via chebyshev filter-based type III phase locked loop," *Electronics (Switzerland)*, vol. 7, no. 12, 2018.

[146] S. Sarma, V. K. Agrawal, and S. Udupa, "Software-based resolver-to-digital conversion using a DSP," *IEEE Transactions on Industrial Electronics*, vol. 55, no. 1, pp. 371–379, 2008.

[147] K. Bouallaga, L. Idkhajine, A. Prata, and E. Monmasson, "Demodulation methods on fully FPGA-based system for resolver signals treatment," *2007 European Conference on Power Electronics and Applications, EPE*, no. 1, 2007.

A.1 Integrated Position Sensor Topology

The integrated resolver and rectifier topologies use two boards: one stationary stator board and one rotating rotor board. The initial resolver design is shown in Figure A.1. These boards solely contain the position sensor and rectifier circuitry in order to be a multi-purpose solution for any wireless excitation system. The outer coupling electrode is used in order to provide the single-phase voltage excitation to the rotor electrode petal structure. Likewise, the petal structure is also electrically connected to the outer coupling electrode on the rotor. The resolver design is also adaptable to different pole/petal numbers for adjusting the desired resolution and shaft speed. The already-present capacitive coupler is able to integrate into exciting rotor electrode. Either the CPC PCBs can be made with a larger diameter to incorporate the resolver functionality, or the CPC can be shrunk slightly to fit with the same diameter.

As the rotor boards in the middle column spin about their center, the grey excitation electrode petals capacitively couple with different colorful stator "pick-up" electrodes. This creates the variable capacitance effect. The rotor board is wirelessly excited via capacitively coupling with the grey electrode of the stator. High frequency single-phase voltage is applied to the stator, coupled to the rotor, and is then modulated at the rotor frequency back to the stator electrodes. The “pick-up” electrodes are arranged in repeating patterns where the like-colored sections are electrically connected together. In this way, the position measurement can be distributed around the entirety of the board to reduce coupling disparities between warped or non-flat boards. Additionally, the mint green section on the rotor is designed for the rectifier circuit and is connected to the WFSM field windings.

The main capacitive coupling occurs between the petal shape on the rotor and the trapezoidal section of the “pick-up” electrodes. The petal shape on the rotor references [113, 117] where the outer radius of the shape follows a polar sinusoidal wave pattern that is easily mathematically defined. The rotor petal shape is defined by eq. (A.1) where r_o is the maximum outside radius and A is the amplitude of the petals, and N is the total number of petals as shown in A.2a.

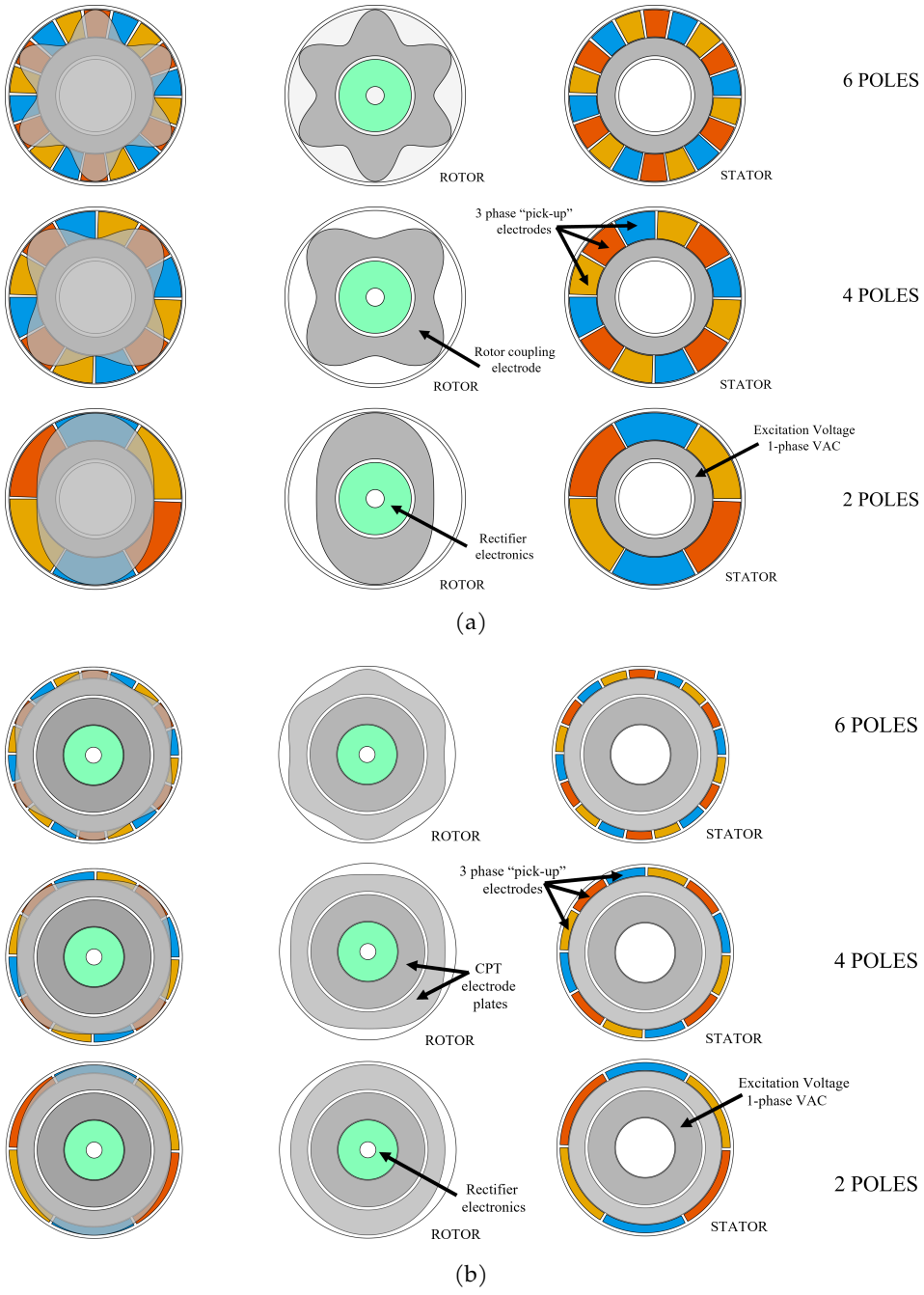

Figure A.1: (a) Diagrams of integrated resolver and rectifier designs with different numbers of poles for different resolution, and (b) diagrams of integrated resolver and rectifier designs added onto the CPT coupler with different number of poles.

$$r = (r_o - A) - A\cos(N\theta) \tag{A.1}$$

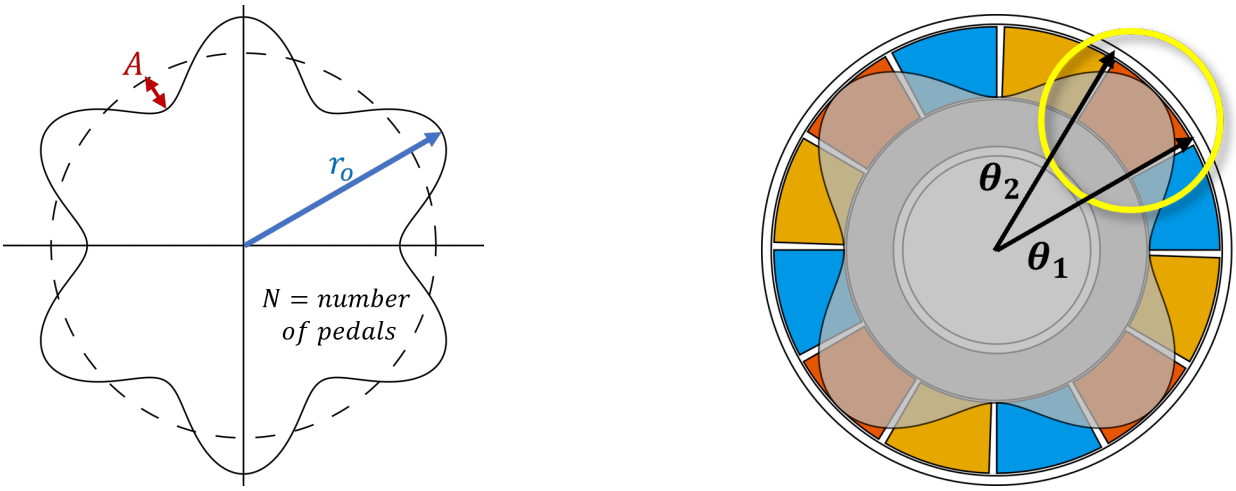

(a) (b)

Figure A.2: (a) Diagram of outer petal shape and (b) rotor petal shape overlapped with "pick-up" electrodes

where

$$0 \leqslant \theta \leqslant 2\pi$$

The overlapped area, SA, between the rotor and stator electrodes shown in A.2b is defined with the double integral in eq. (A.2) between angle θ_1 and θ_2. θ_1 and θ_2 align with the width of the stator "pick-up" electrodes.

$$SA = \int_{\theta_1}^{\theta_2} \int_{r_i - g}^{(r_o - A) - A\cos(N\theta) + g} r\,dr\,d\theta \tag{A.2}$$

In the calculation for the area, an extra fringing approximation is made in the petal radius by adding the $+g$ component on the outer radius and $-g$ on the inner radius where g is equal to the distance between the two plates. This approximation helps to account for electric fields in the gap curving out on the edges. In eq. (A.2), all variables except for the angles are constants. Furthermore, in a given resolver design, the stator electrode angles are fixed so that the area is solely a function of θ_1 as in eq. (A.3). The total capacitance is derived in eq. (A.4).

$$\theta_2 = \theta_1 + \frac{2\pi}{N} \tag{A.3}$$

$$C_{tot} = \frac{\varepsilon SA(\theta_1)}{d} N \tag{A.4}$$

A.1.1 Resolver Capacitance Calculations and Simulations

Finite element analysis (FEA) simulations were performed using Ansys Maxwell in order to evaluate how accurately the resolver calculations estimate the coupling capacitance. In Maxwell, the 3D electrostatic solver was used for the FEA. Figure A.3 shows two different cases with a two-pole and a four-pole resolver design each being rotated through 360 electrical degrees overlayed on top of the analytical calculations for capacitance. The FEA results are nearly identical to the calculations and follow the sinusoidal pattern closely; however, the FEA results show the resolver coupling capacitance to be slightly higher. This indicates the extra gap term in eq. (A.2) that accounts for fringing works well as an approximation.

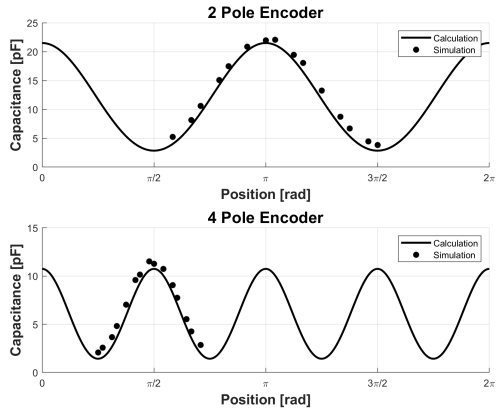

Figure A.3: FEA results compared to the analytical calculations for the two-pole and four-pole models

A.1.2 Resolver Performance

The proposed resolver is designed to operate in two modes depending on the application, as shown in Figure A.4. In A.4a, the stator side of the coupler is excited with a three-phase high frequency voltage on the three separate repeating "pick-up" electrodes. The voltage capacitively couples to the rotor petal shape and back to the "pick-up" electrodes where the modulated currents are measured and filtered. This first operating mode allows both the position and speed of the shaft to be measured. Specifically, the position at zero speed can be measured and used to align the motor shaft. As the rotor board rotates, the coupled stator electrode currents will modulate accordingly, creating an envelope around the relatively high frequency injected excitation. With an envelope

demodulator or other comparable filter, the overall envelope will be extracted from the raw current measurement. Additionally, this resolver configuration specifically differs from previous resolver designs described in the state-of-the-art review as it relies on current measurements within a three-phase system instead of differential voltage measurements amongst a four "pick-up" electrode configuration.

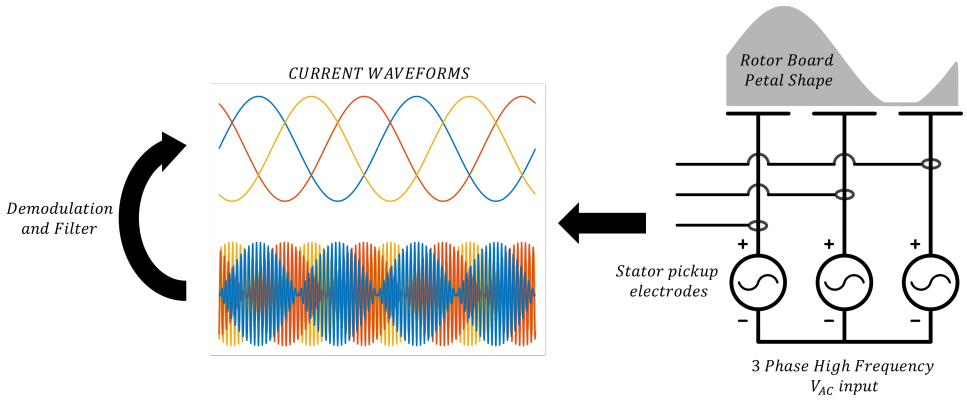

(a)

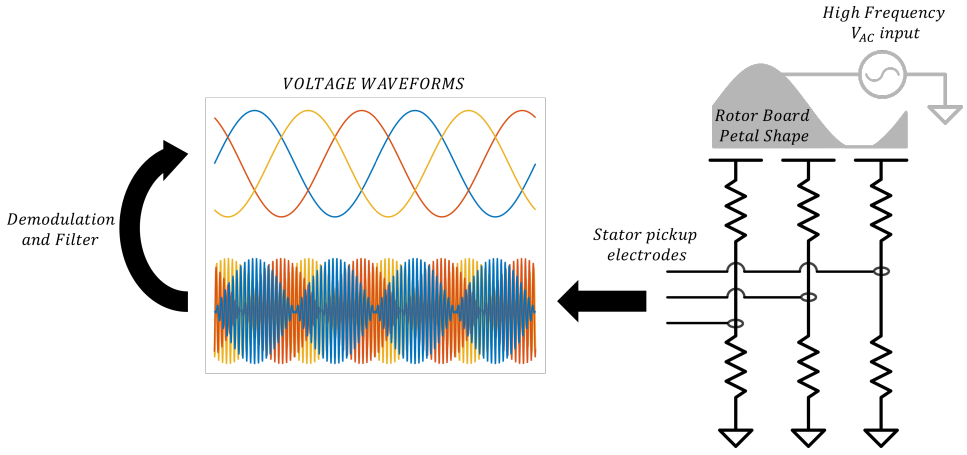

(b)

Figure A.4: (a) Three-phase excitation operation and (b) single-phase excitation operation.

The second mode in A.4b is excited by single-phase voltage from the WFSM rotor's wireless excitation system and coupled through the rotor. As the rotor rotates, it couples back to the "pick-up" electrodes on the stator and is converted to a measurable voltage via a voltage divider. This configuration works essentially in reverse from the first mode. The relatively high-frequency excitation voltage in conjunction with the relatively slow rotating rotor creates a sinusoidal measured voltage within an envelope.

A.1.3 Capacitive Position Sensor Design Limitations

For both operating modes, the position of the rotor is determined by calculating the resulting rotating spatial vector of the three-phase system. This will be able to provide the absolute electrical position, speed, and direction of the rotor. It will not be able to provide the absolute mechanical position of the rotor. This resolver cannot give absolute position unless it is just one lobe with three electrodes. This may be acceptable depending on the end user applications where the number of poles on the resolver is equivalent to the number of rotor poles. This design, however, is not a drop-in replacement for existing magnetic resolvers on the market as it requires one or three-phase excitation with three signals to filter and demodulate. This limitation might make it harder to adopt for the future.

A.1 Inverter Schematic

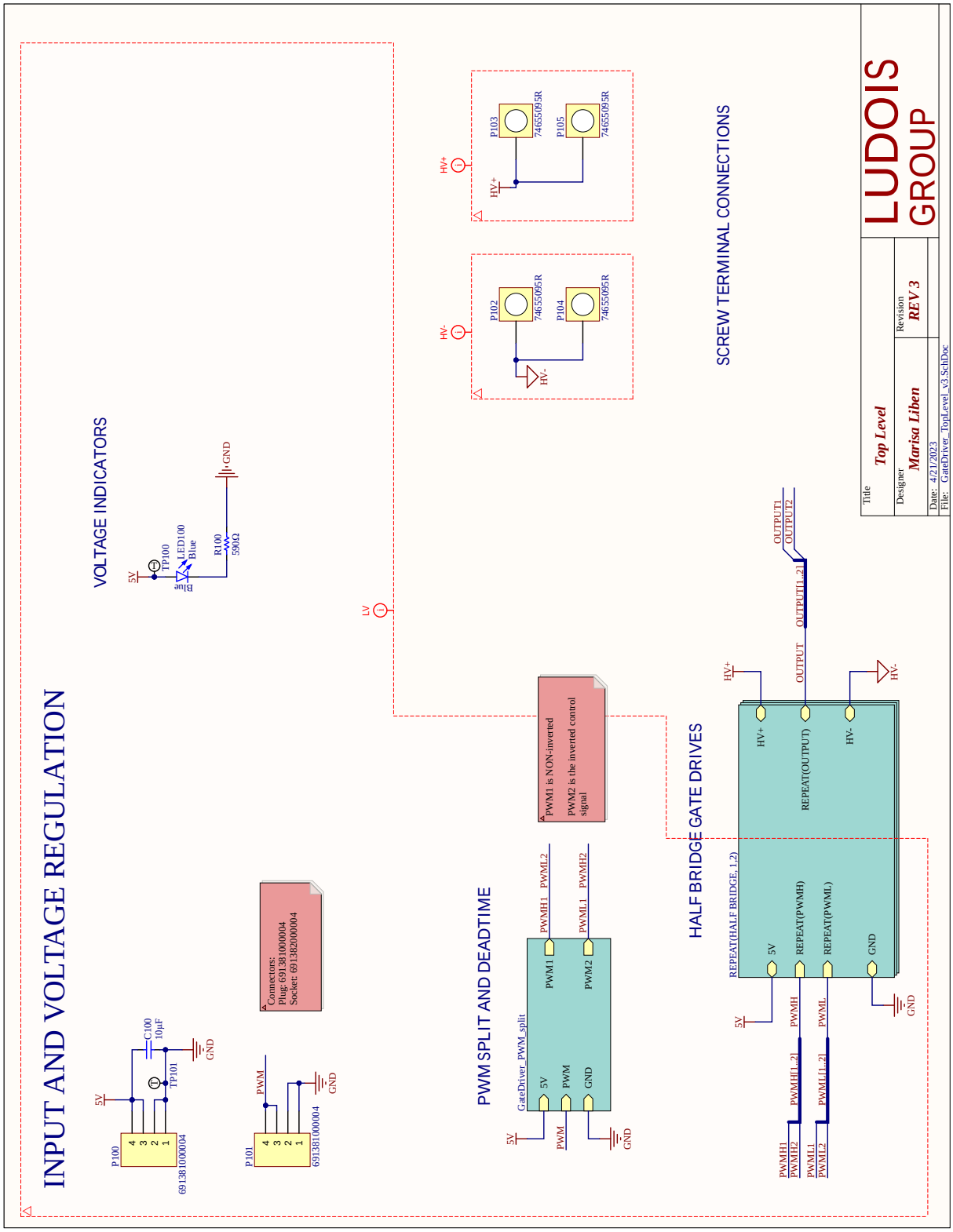
INPUT AND VOLTAGE REGULATION
VOLTAGE INDICATORS
5V
TP100
LED100
Blue
R100
590Ω
GND
LV
HV+
HV-
P103
74655095R
P105
74655095R
P102
74655095R
P104
74655095R
SCREW TERMINAL CONNECTIONS
P100
C100
10µF
TP101
6913810000004
P101
PWM
Connectors:
Plug: 691381000004
Socket: 691382000004
PWM1 is NON-inverted
PWM2 is the inverted control signal
PWM SPLIT AND DEADTIME
GateDriver_PWM_split
PWM1
PWM2
PWMH1
PWML2
PWML1
PWMH2
HALF BRIDGE GATE DRIVES
REPEAT(HALF BRIDGE, 1,2)
REPEAT(OUTPUT)
REPEAT(PWMH)
REPEAT(PWML)
OUTPUT
OUTPUT1
OUTPUT2
OUTPUT1..2
PWMH1..2
PWML1..2
LUDOIS GROUP
Title
Top Level
Designer
Marisa Liben
Revision
REV 3
Date: 4/21/2023
File: GateDriver_TopLevel_v3.SchDoc

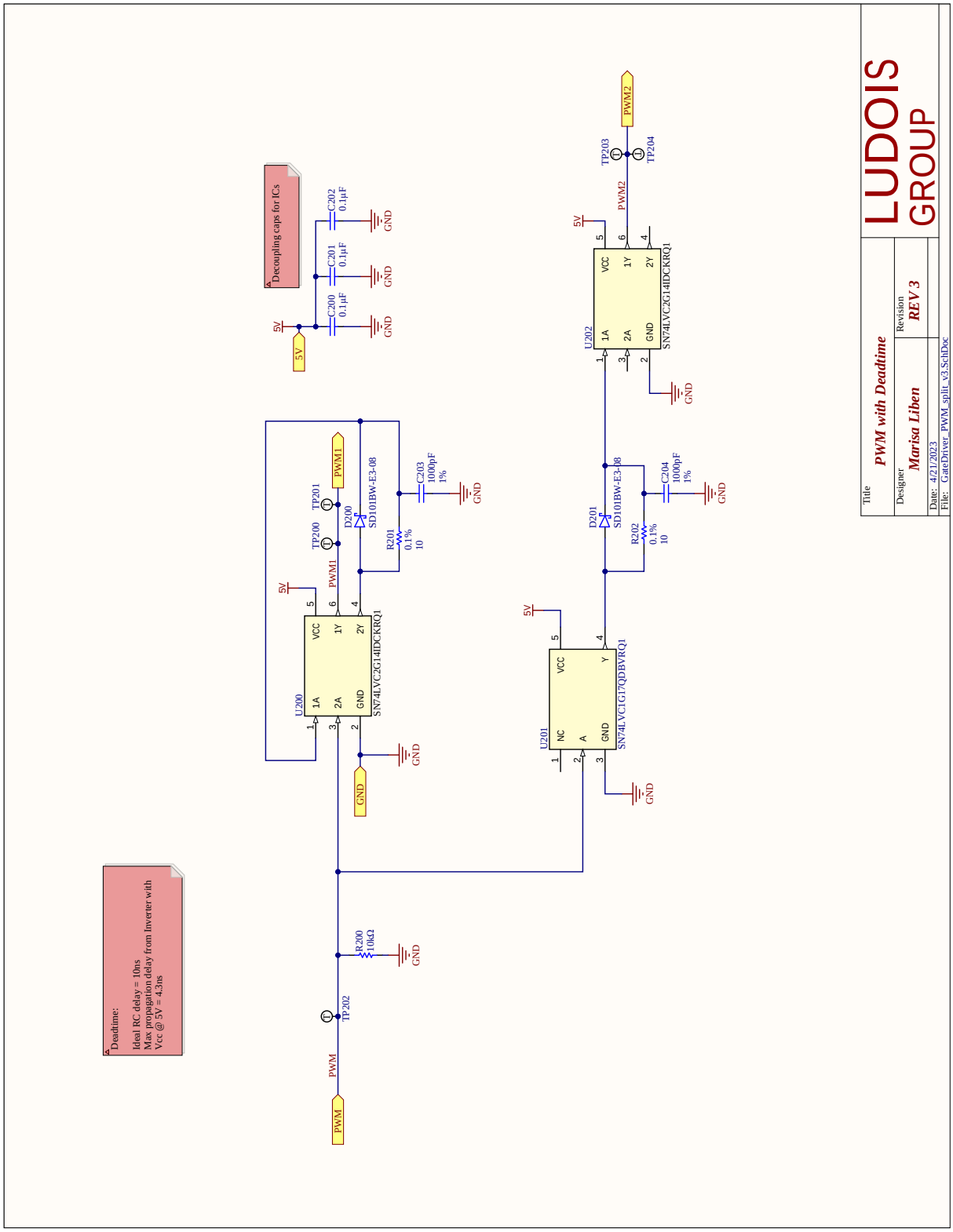
Deadtime:
Ideal RC delay = 10ns
Max propagation delay from Inverter with Vcc @ 5V = 4.3ns
Decoupling caps for ICs
C200 0.1µF
C201 0.1µF
C202 0.1µF
GND
5V
PWM
TP202
R200 10kΩ
U200
SN74LVC2G14IDCKRQ1
1A
2A
GND
VCC
1Y
2Y
TP200
TP201
PWM1
D200
SD101BW-E3-08
R201 0.1% 10
C203 1000pF 1%
U201
SN74LVC1G17QDBVRQ1
NC
A
Y
D201
R202 0.1% 10
C204 1000pF 1%
U202
TP203
TP204
PWM2
Title
PWM with Deadtime
Designer
Marisa Liben
Revision
REV 3
Date: 4/21/2023
File: GateDriver_PWM_split_v3.SchDoc
LUDOIS GROUP

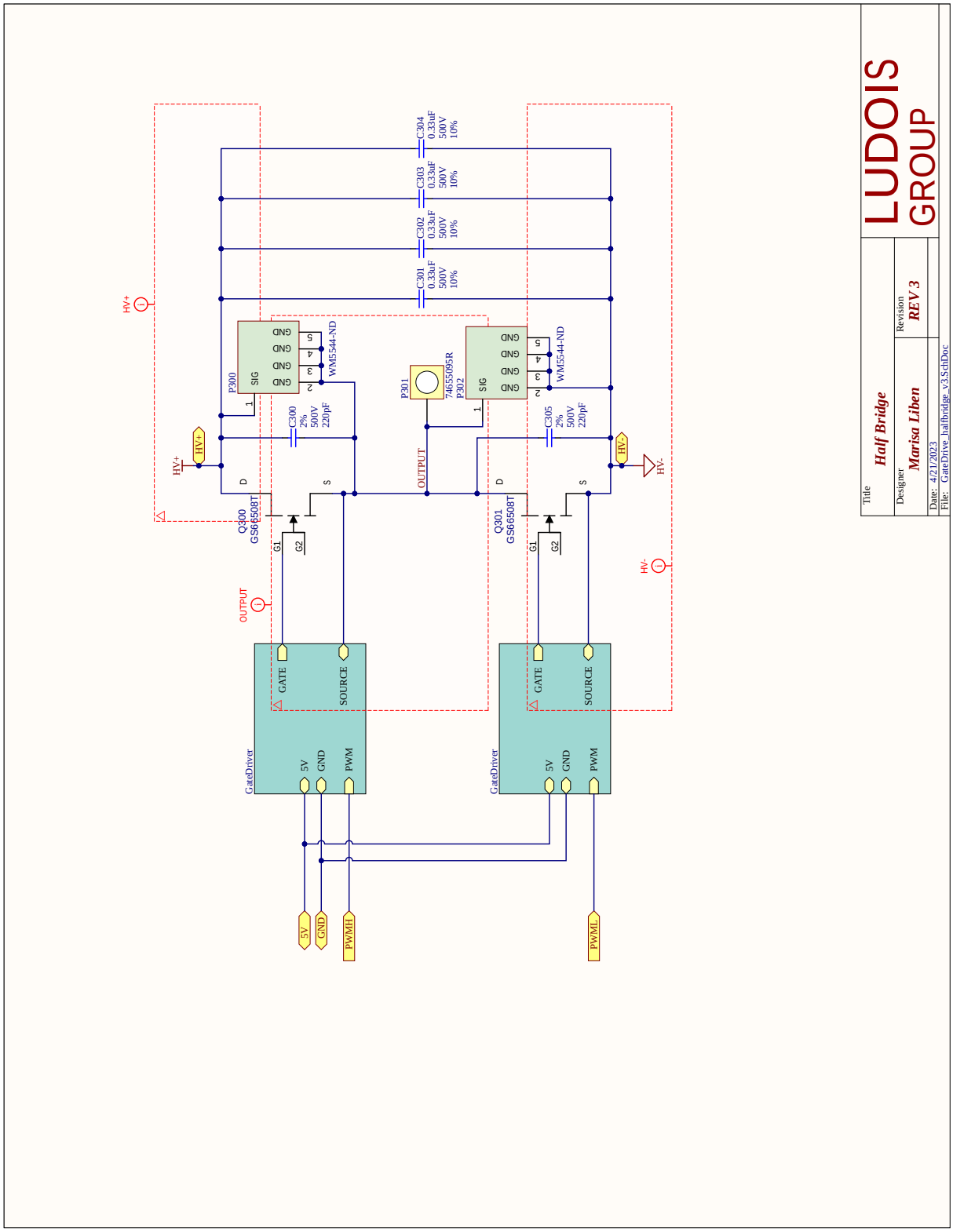
LUDOIS
GROUP
Title
Half Bridge
Designer
Marisa Liben
Revision
REV 3
Date: 4/21/2023
File: GateDrive_halfbridge_v3.SchDoc
HV+
HV-
OUTPUT
C304 0.33uF 500V 10%
C303 0.33uF 500V 10%
C302 0.33uF 500V 10%
C301 0.33uF 500V 10%
P300
P301
P302
74655095R
WM5544-ND
C300 2% 500V 220pF
C305 2% 500V 220pF
Q300 GS66508T
Q301 GS66508T
D
S
G1
G2
GateDriver
GATE
SOURCE
5V
GND
PWM
PWMH
PWML

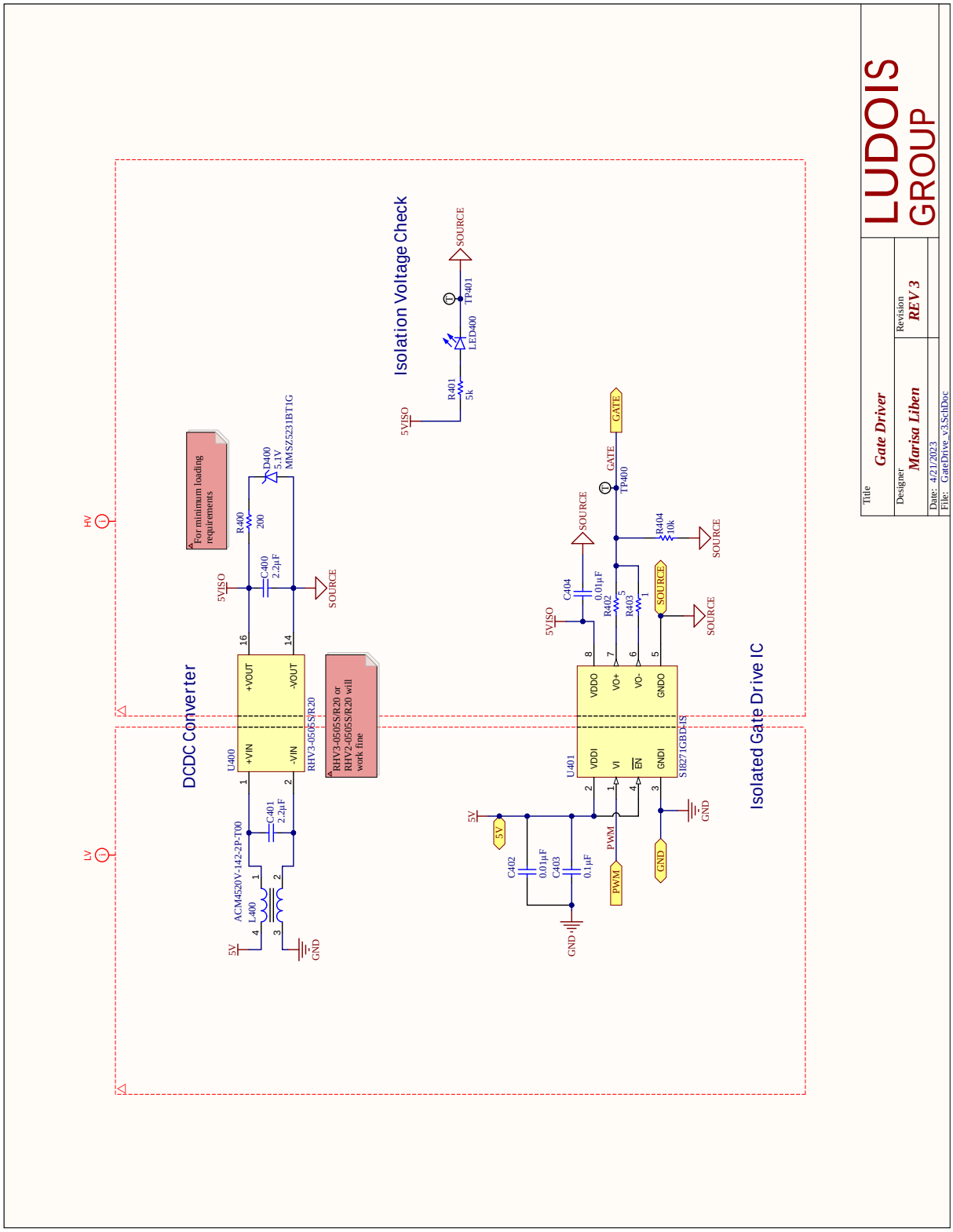
DCDC Converter
Isolated Gate Drive IC
Isolation Voltage Check
For minimum loading requirements
RHV3-0505S/R20 or RHV2-0505S/R20 will work fine
RHV3-0505S/R20
ACM4520V-142-2P-T00
SI8271GBD-IS
LUDOIS GROUP
Gate Driver
Marisa Liben
REV 3
4/21/2023
GateDrive_v3.SchDoc

A.2 Current-Stiff Rectifier Schematic

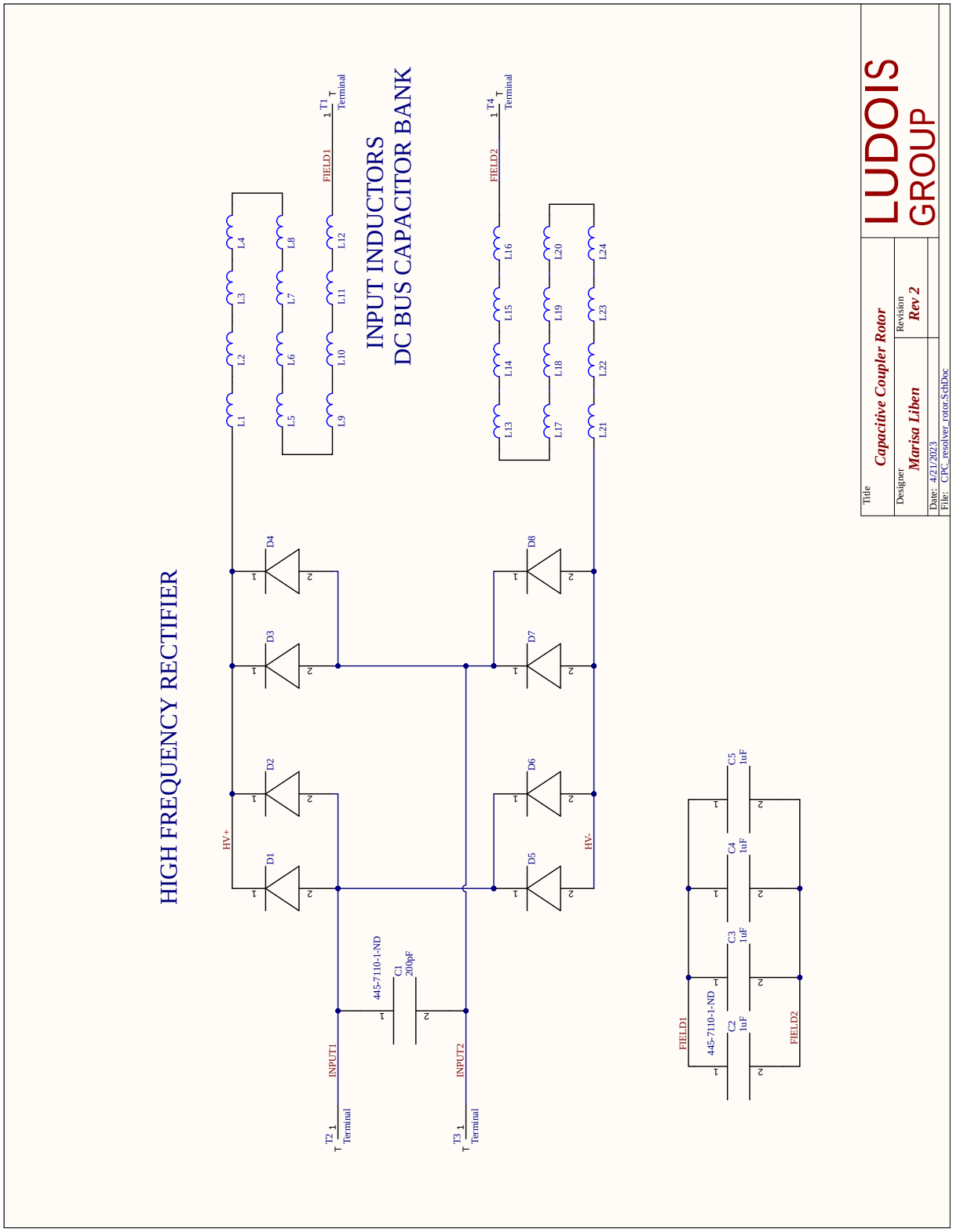
HIGH FREQUENCY RECTIFIER
INPUT INDUCTORS
DC BUS CAPACITOR BANK
HV+
HV-
INPUT1
INPUT2
FIELD1
FIELD2
T1 Terminal
T2 Terminal
T3 Terminal
T4 Terminal
D1
D2
D3
D4
D5
D6
D7
D8
L1
L2
L3
L4
L5
L6
L7
L8
L9
L10
L11
L12
L13
L14
L15
L16
L17
L18
L19
L20
L21
L22
L23
L24
C1 200pF
C2 1uF
C3 1uF
C4 1uF
C5 1uF
445-7110-1-ND
445-7110-1-ND
Title Capacitive Coupler Rotor
Designer Marisa Liben
Revision Rev 2
Date: 4/21/2023
File: CPC_resolver_rotor.SchDoc
LUDOIS GROUP

Connectors to Filter Board

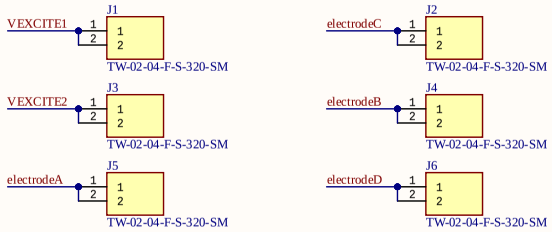

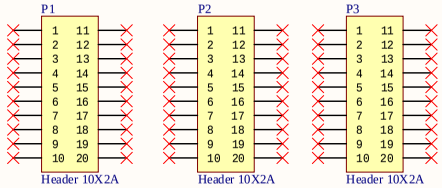

Structural Connectors

Title: *Capacitive Coupler Stator*	LUDOIS GROUP
Designer: *Marisa Liben* / Revision: *Rev 2*	
Date: 4/21/2023	
File: CPC_resolver_stator.SchDoc	

A.3 Resolver Filter Schematic

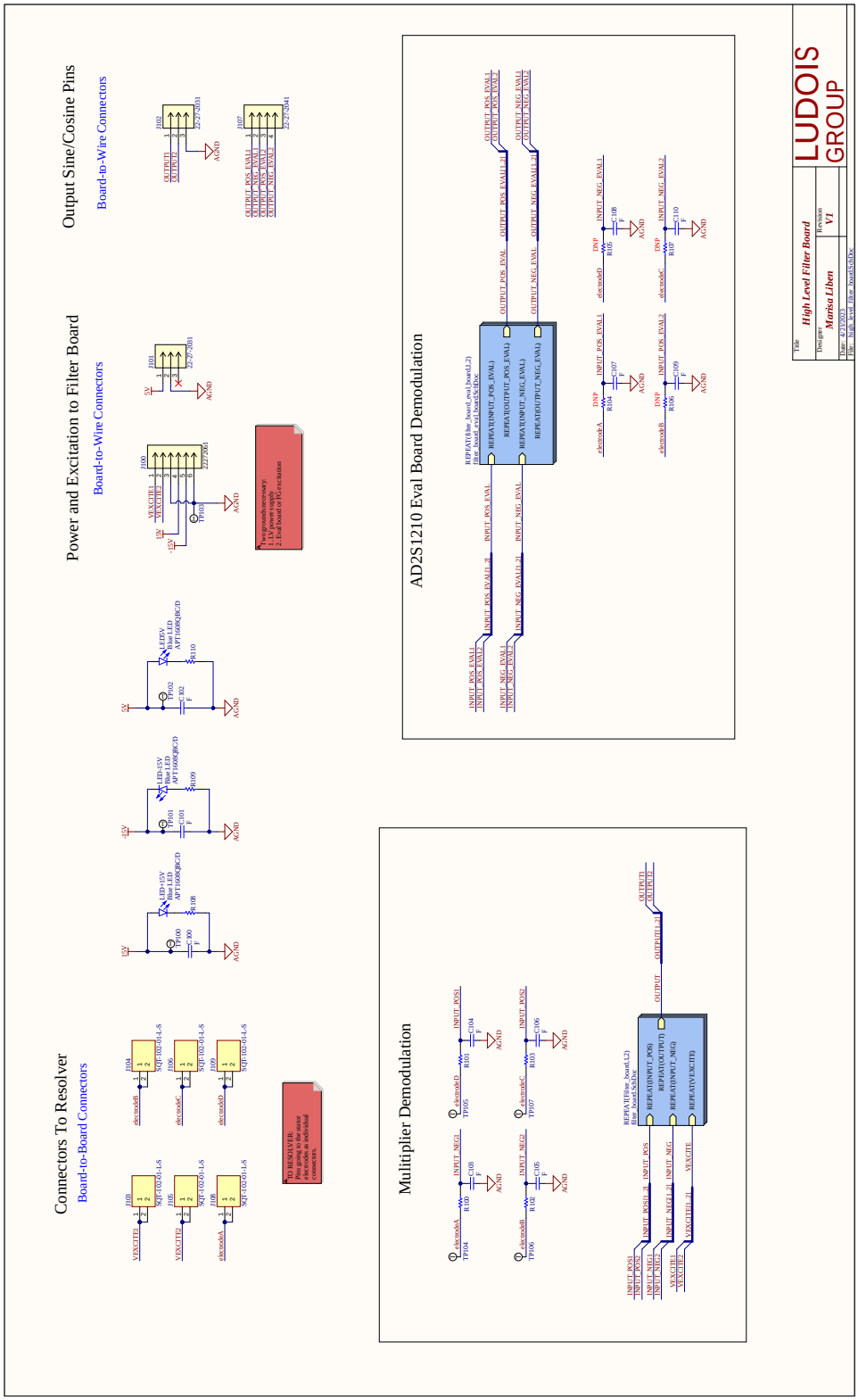
Connectors To Resolver
Board-to-Board Connectors
Power and Excitation to Filter Board
Board-to-Wire Connectors
Output Sine/Cosine Pins
Board-to-Wire Connectors
Multiplier Demodulation
AD2S1210 Eval Board Demodulation
High Level Filter Board
Marisa Litben
V1
LUDOIS GROUP

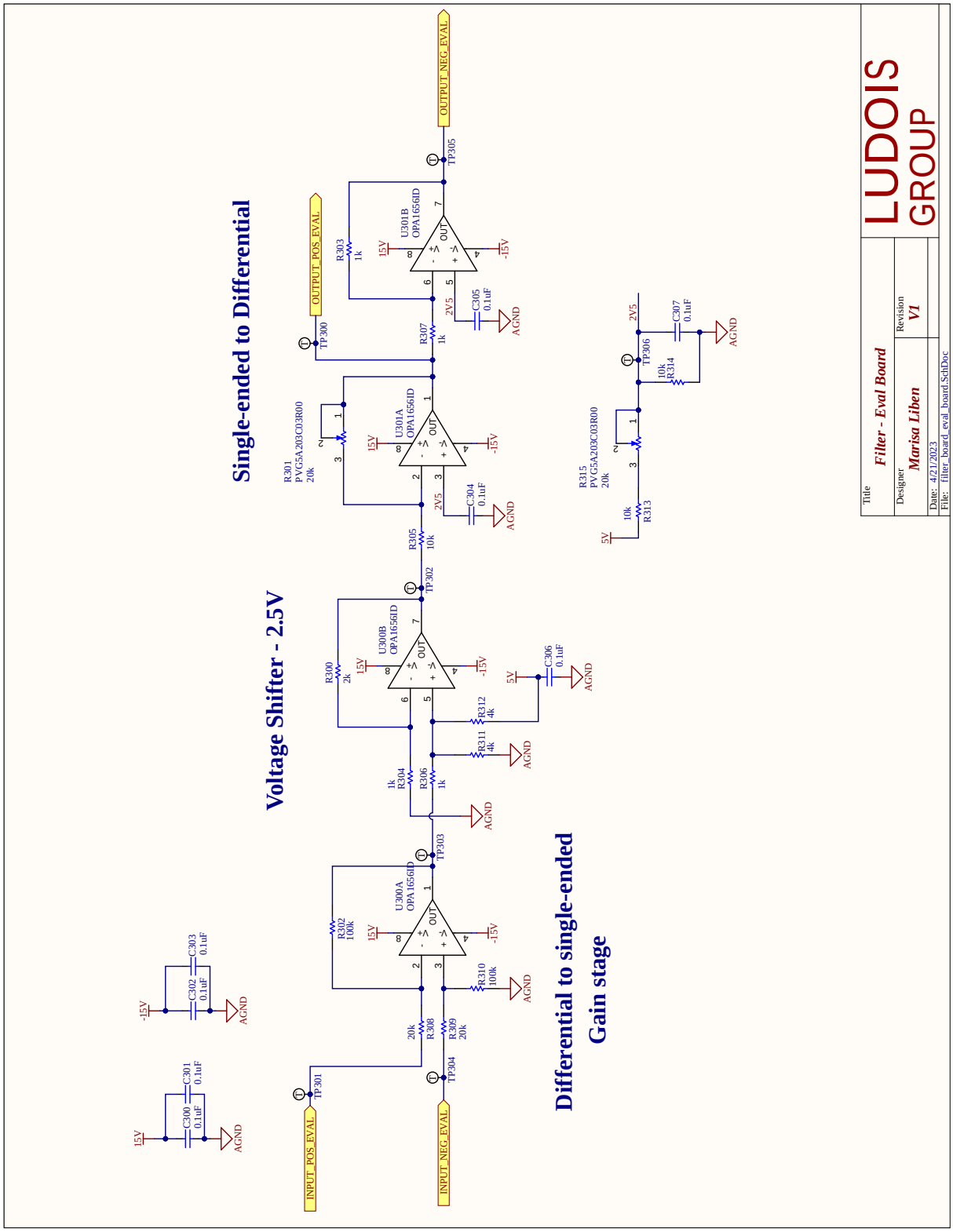
Single-ended to Differential
Voltage Shifter - 2.5V
Differential to single-ended
Gain stage
Title
Filter - Eval Board
Designer
Marisa Liben
Revision
V1
Date: 4/21/2023
File: filter_board_eval_board.SchDoc
LUDOIS
GROUP
INPUT_POS_EVAL
INPUT_NEG_EVAL
OUTPUT_POS_EVAL
OUTPUT_NEG_EVAL
TP301
TP302
TP303
TP304
TP305
TP306
TP300
U300A OPA1656ID
U300B OPA1656ID
U301A OPA1656ID
U301B OPA1656ID
R300 2k
R301 PVG5A203C03R00 20k
R302 100k
R303 1k
R304 1k
R305 10k
R306 1k
R307 1k
R308 20k
R309 20k
R310 100k
R311 4k
R312 4k
R313 10k
R314 10k
R315 PVG5A203C03R00 20k
C300 0.1uF
C301 0.1uF
C302 0.1uF
C303 0.1uF
C304 0.1uF
C305 0.1uF
C306 0.1uF
C307 0.1uF
15V
-15V
5V
2V5
AGND

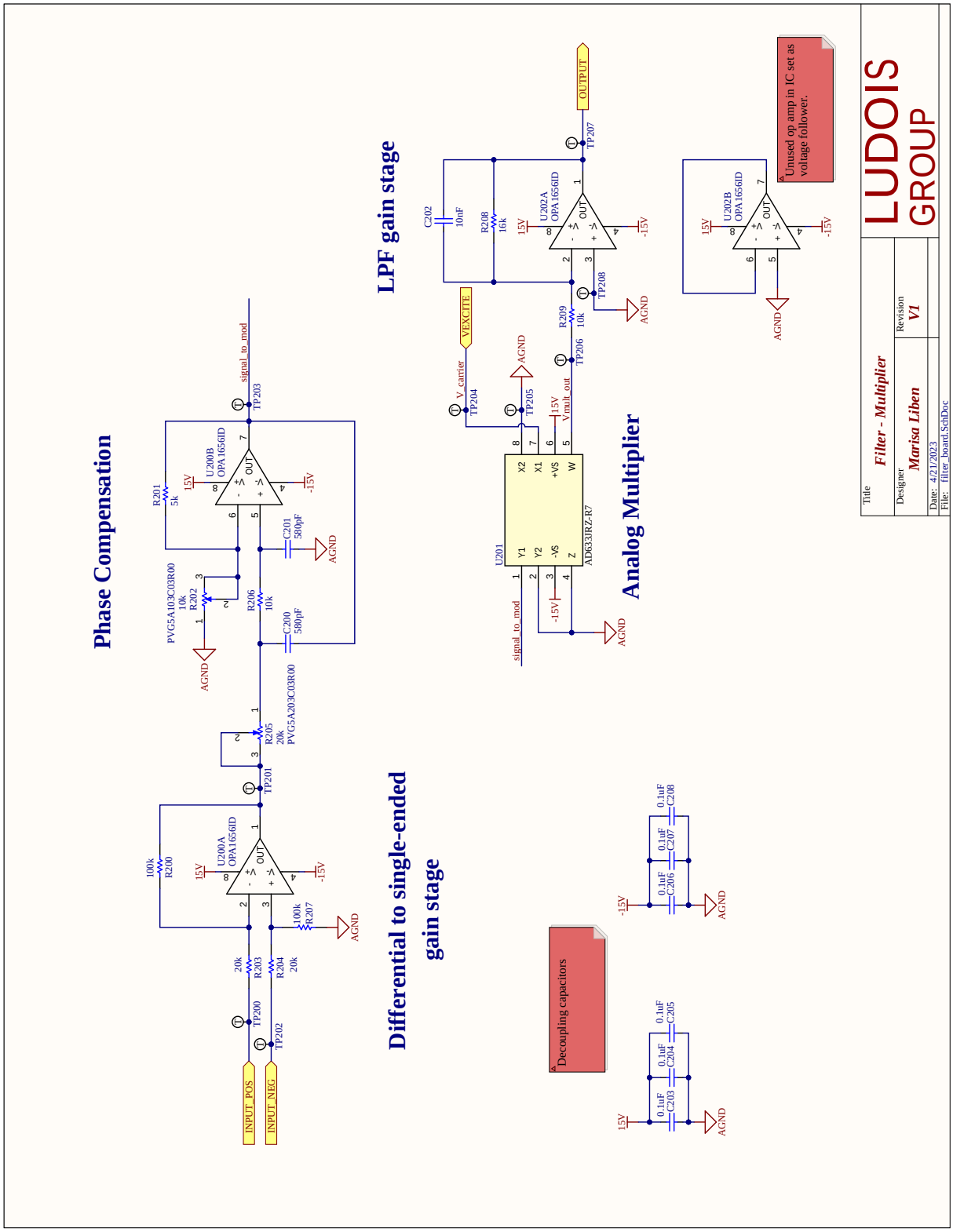
Phase Compensation
Differential to single-ended gain stage
LPF gain stage
Analog Multiplier
Decoupling capacitors
Unused op amp in IC set as voltage follower.
INPUT_POS
INPUT_NEG
signal_to_mod
VEXCITE
V_carrier
Vmult_out
OUTPUT
U200A OPA1656ID
U200B OPA1656ID
U201 AD633JRZ-R7
U202A OPA1656ID
U202B OPA1656ID
PVG5A103C03R00
PVG5A203C03R00
R200 100k
R201 5k
R202 10k
R203 20k
R204 20k
R205 20k
R206 10k
R207 100k
R208 16k
R209 10k
C200 580pF
C201 580pF
C202 10nF
C203 0.1uF
C204 0.1uF
C205 0.1uF
C206 0.1uF
C207 0.1uF
C208 0.1uF
TP200
TP201
TP202
TP203
TP204
TP205
TP206
TP207
TP208
15V
-15V
AGND
Title
Filter - Multiplier
Designer
Marisa Liben
Revision
V1
Date: 4/21/2023
File: filter_board.SchDoc
LUDOIS GROUP

A.4 CPC-Integrated Resolver Filter Schematic

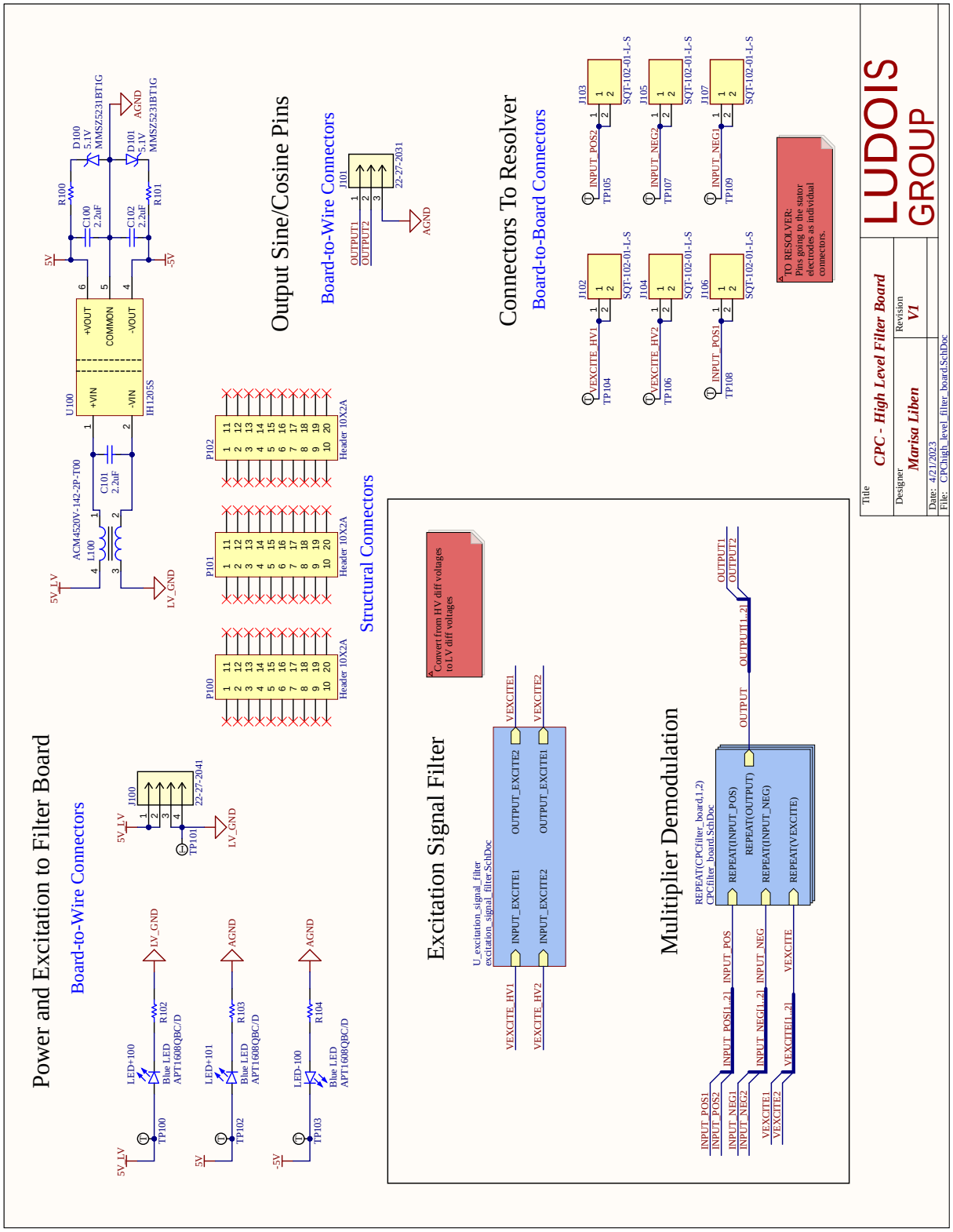
Power and Excitation to Filter Board
Board-to-Wire Connectors
Output Sine/Cosine Pins
Board-to-Wire Connectors
Structural Connectors
Connectors To Resolver
Board-to-Board Connectors
Excitation Signal Filter
Convert from HV diff volages to LV diff volages
Mulitiplier Demodulation
TO RESOLVER: Pins going to the stator electrodes as individual connectors.
Title
CPC - High Level Filter Board
Designer
Marisa Liben
Revision
V1
Date: 4/21/2023
File: CPChigh_level_filter_boardSchDoc
LUDOIS GROUP

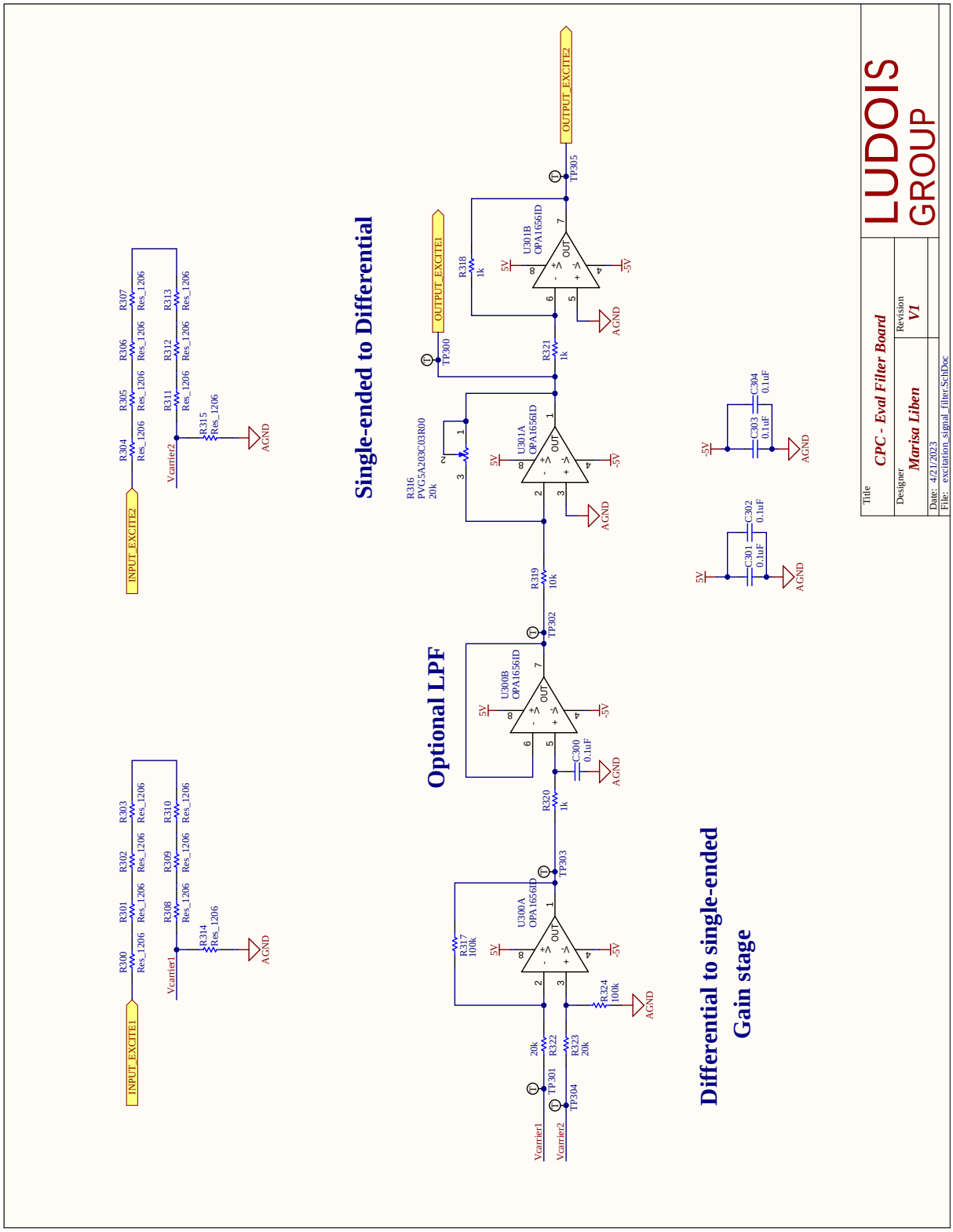
Single-ended to Differential
Optional LPF
Differential to single-ended
Gain stage
INPUT_EXCITE1
INPUT_EXCITE2
OUTPUT_EXCITE1
OUTPUT_EXCITE2
Vcarrier1
Vcarrier2
AGND
5V
-5V
U300A OPA1656ID
U300B OPA1656ID
U301A OPA1656ID
U301B OPA1656ID
R316 PVG5A203C03R00 20k
R317 100k
R318 1k
R319 10k
R320 1k
R321 1k
R322 20k
R323 20k
R324 100k
C300 0.1uF
C301 0.1uF
C302 0.1uF
C303 0.1uF
C304 0.1uF
TP300
TP301
TP302
TP303
TP304
TP305
Title
CPC - Eval Filter Board
Designer
Marisa Liben
Revision
V1
Date: 4/21/2023
File: excitation_signal_filter.SchDoc
LUDOIS GROUP

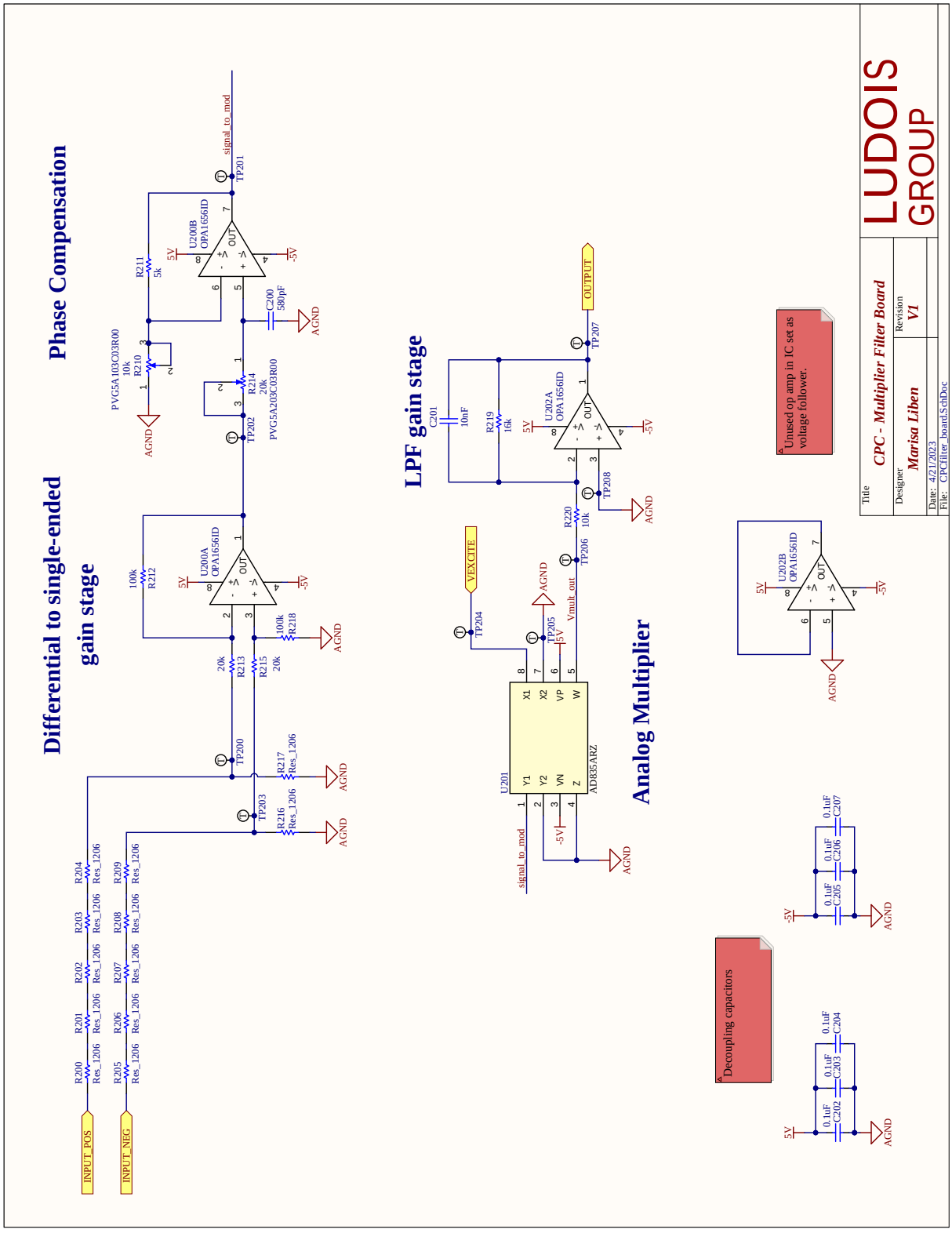
Differential to single-ended gain stage
Phase Compensation
LPF gain stage
Analog Multiplier
INPUT_POS
INPUT_NEG
signal_to_mod
VEXCITE
OUTPUT
Vmult_out
AD835ARZ
OPA1656ID
Decoupling capacitors
Unused op amp in IC set as voltage follower.
LUDOIS GROUP
CPC - Multiplier Filter Board
Marisa Liben
V1
4/21/2023
CPCfilter_board.SchDoc